



The University of
Nottingham

UNITED KINGDOM • CHINA • MALAYSIA

Fabrication of Nanostructured Inorganic and Carbon Porous Materials for Catalysis and Gas Storage Applications

Eric Masika

BSc (JKUAT) PGDE (MU) MSc-Nanoscience (UoN)

**Thesis submitted to the University of
Nottingham for the degree of Doctor
of Philosophy**

[September 2012]

Abstract

This thesis details the preparation and subsequent characterisation of novel nanostructured porous materials with tuneable porosity. The main focus is the development of inorganic and carbonaceous porous materials for catalysis, templating and gas storage applications. Three distinct methods of synthesis are investigated, namely: (i) hydrothermal synthesis of zeotype aluminosilicates, (ii) nanocasting techniques for templated carbons and (iii) sol-gel processes, with/without metal salt 'porogen', to carbon aerogels. Post-synthesis modification methods for carbonaceous materials include supercritical carbon dioxide mediated incorporation of palladium nanoparticles into zeolite templated carbons and chemical activation for carbon aerogels resulting in enhanced textural properties.

Chapter 1: Provides the foundation and background to the main themes of nanostructured porous materials investigated in this work. Information about fundamental properties and applications is emphasised.

Chapter 2: Gives a brief background of techniques used for characterisation of the porous materials generated in this research programme. Gas sorption techniques used to probe hydrogen storage and carbon dioxide uptake are also presented.

Chapter 3: Describes stepwise experimental techniques followed in the preparation of various porous materials. The chapter also describes the instrumentation used in these techniques.

Chapter 4 – 7: Each chapter reports a separate but sequential area of research in which appropriate additional theory and background is provided with associated literature review. This is followed by a results and discussion section, with a concluding summary for each chapter.

Chapter 4: Details the synthesis of ordered mesoporous aluminosilicates, which exhibit some zeolitisation, prepared from a recipe conventionally used for the synthesis of microporous zeolite BEA. The porosity of the aluminosilicates is modified by simple washing and/or refluxing (in water) of either on the as-synthesised mesophase or the calcined material. The aluminosilicates have excellent hydrothermal stability and strong acidity and thus combine the best properties from mesoporous materials and zeolites.

Chapter 5: Describes the preparation of zeolite templated carbons (ZTC) generated as replicas of zeolite Y via a hard template nanocasting process. In order to enhance hydrogen storage, the ZTCs are impregnated with Palladium nanoparticles using supercritical carbon dioxide solvent, scCO_2 , as environmentally benign reaction media. The Pd-doped ZTCs exhibit enhanced hydrogen storage due to optimised (with respect to metal content and particle size) incorporation of Pd.

Chapter 6: A two-step process for the generation of zeolite templated carbons (ZTCs) was investigated. In this case the nanocasting technique involves liquid impregnation of zeolite 13X with furfuryl alcohol followed by chemical vapour deposition (CVD) of ethylene at variable CVD temperatures. The two-step process was a successful attempt to optimise the replication of the zeolite structure in the carbons. The ZTCs had very high surface area and excellent mechanical stability, and achieved the highest hydrogen storage capacity (7.3 wt% at 77 K and 20 bar) ever reported for any carbon material.

Chapter 7: Organic Sol-gel chemistry is explored in the formation of carbon aerogels via conventional methods involving the use of resorcinol-formaldehyde resins and melamine-formaldehyde with or without metal

salt as a porogen and subcritical drying. Chemical activation is used to modify the porosity of aerogels for potential applications in carbon dioxide uptake.

Chapter 8: A brief overall conclusion to this research work is presented together with recommendations for future research.

Publications and conferences

Publications

1. E. Masika and R. Mokaya, 'Supercritical CO₂ Mediated Incorporation of Palladium Nanoparticles into Zeolite Templated Carbons with Enhanced Hydrogen Storage,' (submitted on 26th September 2012)
2. E. Masika and R. Mokaya, 'Hydrogen Storage in High Surface Area Carbons with Identical Surface Area but Different Pore Size: Direct Demonstration of the Effects of Pore Size', J. Phys. Chem. C, 2012, DOI: 10.1021/jp3100365
3. E. Masika and R. Mokaya, 'Mesoporous Aluminosilicates from a Zeolite BEA Recipe', Chem. Mater., 2011, **23**(9), 2491-2498. DOI: 10.1021/cm200706n

Conferences

Presentations:

1. Eric Masika, Richard Bourne, Thomas Chamberlain and Robert Mokaya, 34th Annual British Zeolite Association Conference, Edinburgh, 11 -13th April 2011, 'Supercritical CO₂ mediated Incorporation of Palladium Nanoparticles into Zeolite Templated Carbons with enhanced Hydrogen Storage.'
2. Eric Masika and Robert Mokaya, Chemistry Research Seminar 2010, The University of Nottingham, 23rd June 2011 'Templating Routes to New Type Nanostructured Porous Solids for Catalysis and Hydrogen Storage.'
3. Eric Masika and Robert Mokaya, Driving innovation in Chemistry and Engineering Workshop, The University of Nottingham, 12th March 2010, 'Templating Routes to Nanostructured and Mesostructured Porous Materials.'

Poster session:

1. Eric Masika and Robert Mokaya, 34th Annual British Zeolite Association Conference, Edinburgh, 11 -13th April 2011. 'Mesoporous Aluminosilicates via Molecular Templating.'

2. Eric Masika and Robert Mokaya, 'TA Instruments - UK Materials Characterisation seminar, University of Bradford, 13th and 14th September 2011 'Synthesis and Characterization of Pd-doped Zeolite Templated Carbons for Hydrogen Storage.'
3. Eric Masika and Robert Mokaya, 2010 Physical Chemistry Postgraduate Symposium, 9th July 2010. 'Synthesis and Characterization of Pd-doped Zeolite Templated Carbons for Hydrogen Storage.

Acknowledgements

First and foremost, I would like to thank most sincerely my supervisor, Prof Robert Mokaya for the opportunity to complete this PhD and especially for the kind support, encouragement and invaluable discussions which ensured that I remained sane and focused on the task at hand. I consider myself to have been very profoundly privileged to be under his supervision. I am greatly indebted to Prof Martyn Poliakoff for his wise counsel, kind support and advice.

I would like especially to thank Dr Marta Sevilla who patiently and in a very dedicated way offered undivided attention and advice. I am also grateful to the former and current colleagues in laboratories B11 and A30, especially Dr Yongde Xia, Dr Zhuxian Yang, Andrew Davies, Alex Greenway, Thomas Huddle, Dr Ingrida Lapenaite, Dr Sunil Joshi, Colin West, Dr Labet Marriane, Dr Nurul Alam, Afaf Almasoudi, Wantana Songchoom, and Beatrice Adeniran for their kind advice and friendship.

I would like to profoundly thank Prof Andrei Khlobystov and Alessandro La Torre for their immense help with transmission electron microscopy experiments. My gratitude also goes to Dr Wim Thielemans, Prof. Sandy Blake, Dr Jonathan Burley and Dr William Lewis (for combined efforts in X-ray diffraction training and data interpretation), Dr. Sihai Yang and Dr Illich A. Ibarra (for Intelligent Gravimetric Analysis training and constant advice on troubleshooting), Dane Toplis for Infrared Spectroscopy training and also Dr David Apperley of EPSRC Solid state NMR service based at University of Durham –UK for NMR analysis. My heartfelt thanks also go to Dr Richard Bourne and Dr Thomas Chamberlain for their collaboration during the supercritical carbon dioxide doping experiments. I also appreciate Dr Nigel Neate and Mr Martin Roe for their valued SEM training and data interpretation .

Many thanks go to Dr June McCombie, Dr Anna Bertram, Dr Kyle Galloway, Dr Samantha Tang and Prof Neil Champness for their endless kind support and encouragement. I would also like to thank Mr Neil Barnes, Mr Mark Guyler, Dr David Chambers-Asman, Mr Peter Morgan-Tansely, Mr Patrick Hutchinson and all the members of workshop and chemistry stores for their invaluable technical assistance. Likewise, I am grateful to Ms Dianne Mann, Ms Wend Kirkup, Ms Julie Dove, Ms Ruth Smith, Ms Nicola Gascoigne, Ms Rosemary Hart and Ms Amanda Wood for their assistance with administrative work. Special thanks go to Sue for her kind moral and

emotional support. Away from Chemistry, many thanks to International Office staff whose encouragement and support was invaluable. I also register my gratitude to Hannah Curnock, Jenny Wardrop, Rosemary Gibson, Nathalie Mortimer, Vincenzo Raimo, Jennifer Summerton, Claire Taylor, Stella Muthuri, Deborah Webb, Nina Taggart and Tim Bladon for the friendship and kind support.

I am deeply indebted to The Cornerstone Evangelical Church members and in particular the NG8 house group lead by the Rettie's and Miller's for creating a homely environment, kind support and love. Many thanks go to Bill and Rosemary Rettie for you were always there for me throughout my studies. The great friendship and visitations by the Taylor's, Gosrani's, Clemmet's, Janet Waters, Debbie Dickson, Margaret Shoukry and Val Boywer will always be treasured and memorable. Very special thanks to Jane and Richard Taylor together with their two little angels (Beth and Emily); I can't thank you enough for your kind support, love and prayers. Away from Nottingham, my life change friend Judy Machin. I do not have better words other than to dedicate this research to her for being instrumental and supportive since our first meeting over a decade ago. Moving overseas, I acknowledge Dr Masibo Lumala of Moi University and Elisha Wasike for your prayers and encouragement.

I would like in a very special way acknowledge the financial support of the International Office and School of Chemistry, The University of Nottingham and that of the Engineering and Physical Sciences Research Council (EPSRC). Likewise, I would like to thank Mountbatten Trust Fund and The University of Nottingham Risk Fund for their kind financial support during my write up period.

I would like to thank my wife and children for their continued prayers and sacrifice throughout my studies. Betty (spouse), Raquelle (daughter) and Zephan (son), your encouragement and moral support was immeasurable. Many thanks also go to my parents for your prayers and for being great role models. Likewise, Chris and Jane Mung'oma you get a mention for just being you especially your prayers and calls will always be treasured.

Finally, I reverently thank Almighty God for seeing me through this research and for bringing these wonderful and kind people, whether named or not across my path.

List of abbreviations and acronyms

AC – Activated carbon

AIP – Aluminium isopropoxide

ASAP – Accelerated Surface Area and Porosimetry Analyser

ATR – Attenuated Total Reflection

BET – Brunauer Emmett Teller

BDDT – Brunauer Deming Deming and Teller

BF – Bright field

BJH – Barrett-Joyner-Halenda

BOC – British Oxygen Company

CaCl₂ – Calcium chloride

CCD – Charge coupled device

CHA – Cyclohexylamine

CNFs – Carbon nanofibres

CTAB – Cetyltrimethylammonium Bromide

CVD – Chemical Vapour Deposition

DF – Dark field

DOE – Department of Energy, USA

DTA – Differential thermal analysis

EDX – Energy Dispersive X-rays

FA – Furfuryl alcohol

FTIR – Fourier Transform Infrared

HCl – Hydrochloric acid

HF – Hydrofluoric acid

HS – Hydrothermal synthesis

IGA – Intelligent Gravimetric Analyser

IUPAC – International Union of Pure and Applied Chemistry

KOH – Potassium hydroxide

LCT – Liquid Crystal Templating

LI – Liquid impregnation

MASNMR – Magic angle spin NMR

MF – Melamine – Formaldehyde resin

MCM-41 – Mobil Composition of Matter-41

MOFs – Metal Organic Frameworks

MWNT – Multi-walled carbon nanotube

NaOH – Sodium hydroxide

NLDFT – Non-local Density Function Theory

NMR – Nuclear Magnetic Resonance

Pd(hfa)_2 – Palladium hexafluoroacetylacetonate

PFA – Polyfurfuryl alcohol

PSD – Pore Size Distribution

RF – Resorcinol – Formaldehyde resin

TEAOH – Tetraethyl ammonium hydroxide

TEM – Transmission Electron Microscopy

TEOS – Tetraethyl orthosilicate

TGA – Thermogravimetric Analysis

TPD – Temperature Programmed Desorption

SDA – Structure directing agent

SE – Secondary electrons

SEM – Scanning Electron Microscopy

STP – Standard Temperature and Pressure

SWNT – Single-walled carbon nanotube

VOCs – Volatile Organic Compounds

XRD – X-Ray diffraction

XRF – X-Ray fluorescence

ZTC – Zeolite Templated Carbons

2D, 3D – 2 Dimensional, 3 Dimensional

List of structural formulae

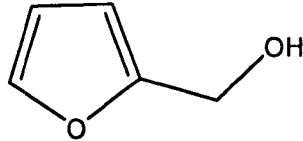
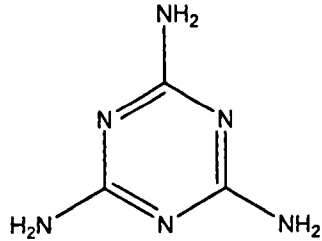
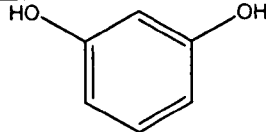
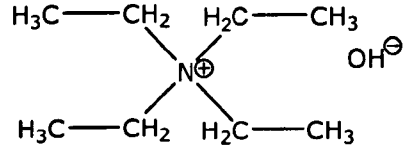
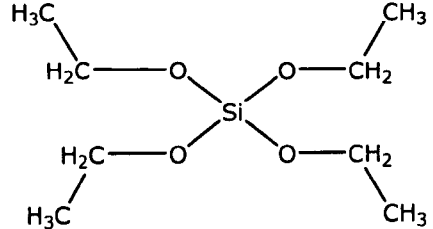
Structural formula	Common name	IUPAC name
	Furfuryl alcohol	2-furanmethanol
	Melamine	1,3,5-Triazine-2,4,6-triamine
	Resorcinol	Benzene-1,3-diol
	Tetraethyl ammonium hydroxide	Tetraethyl ammonium hydroxide
	Tetraethyl orthosilicate	tetraethoxysilane

Table of contents

Abstract	i
Publications and conferences	iv
Acknowledgements	vi
List of abbreviations and acronyms.....	viii
List of structural formulae.....	x
Table of contents	xi
Chapter 1. 0 Introduction: Nanotechnology and Nanostructured Porous Materials	1
1.1 Introduction	1
1.2 Nanoscience and nanostructured materials	1
1.3 Nanoporous materials.....	2
1.3.1 Classification based on pore dimensions.....	3
1.3.2 Classification based on accessibility to the surroundings....	3
1.3.3 Classification based on pore shape	4
1.4 Types of porous materials.....	5
1.4.1 Zeolites.....	6
1.4.2 Periodic mesoporous silicas (PMSs)	11
1.4.3 Porous carbonaceous nanomaterials	17
1.4.3.1 Nanocasting techniques to porous carbons.....	19
1.4.3.2 Porous carbon aerogels.....	22
1.4.3.3 Activated carbons.....	24
1.5 Metal-doping of carbons	25
1.6 Current and potential applications of nanostructured porous materials.....	28
1.7 Gas sorption/storage.....	29
1.7.1 Hydrogen storage.....	29
1.7.2 Carbon dioxide capture and storage.....	32

1.8 Bibliography.....	35
2.0 Complementary Analytical techniques.....	51
2.1 Powder X-ray diffraction (XRD) analysis.....	51
2.2 Nitrogen Physisorption	54
2.2.1 Nitrogen sorption isotherms.....	54
2.2.2 Specific surface area (BET)	56
2.2.3 Pore volume, Pore size and Pore size distribution.....	57
2.3 Thermogravimetric Analysis (TGA)	61
2.4 Temperature programmed desorption (TPD) of cyclohexylamine.....	61
2.5 Elemental analysis by X-ray fluorescence (XRF)	62
2.6 Fourier Transform Infrared (FTIR) Spectroscopy.....	63
2.7 Nuclear Magnetic Resonance Spectroscopy	64
2.8 Electron Microscopy	66
2.8.1 Scanning Electron Microscopy	66
2.8.2 Transmission Electron Microscopy	67
2.9 Gas adsorption	69
2.10 Bibliography	72
3.0 Experimental methodology.....	74
3.1 Introduction.....	74
3.2 Hydrothermal synthesis technique (HS)	74
3.2.1 Chemicals	75
3.2.2 Synthesis of porous aluminosilicates.....	75
3.2.3 Assessment of hydrothermal stability	77
3.3 Synthesis of nanostructured templated carbons via nanocasting routes	77
3.3.1 Chemicals	78

3.3.2 Porous carbon templating using zeolite Y	78
3.4 Supercritical carbon dioxide mediated incorporation of Palladium nanoparticles into zeolite templated carbon ZTC800A ..	79
3.4.1 Chemicals	80
3.4.2 Palladium loading procedure.....	80
3.5 Synthesis of high surface area carbons using a combination of liquid impregnation and chemical vapour deposition	82
3.5.1 Chemicals	83
3.5.2 Zeolite templated carbons prepared via two-step synthesis	83
3.5.3 Post-synthesis modification of FA-ZTCx : via compaction to assess mechanical stability.....	84
3.6 Inorganic metal salt templating of carbon aerogels	85
3.6.1 Chemicals	85
3.6.2 Preparation of carbon aerogels via metal salt templating.	85
3.7 Characterisation techniques.....	88
3.7.1 Characterisation techniques.....	88
I. Powder XRD analysis.....	88
II. Nitrogen sorption.....	88
III. Thermogravimetric analysis (TGA).....	89
IV. Elemental Analysis - X-ray Fluorescence (XRF)	89
V. Fourier Transform Infrared (FTIR) spectroscopy.....	89
VI. Nuclear Magnetic Resonance (NMR) spectra.....	90
VII. TPD of cyclohexylamine.....	90
VIII. Scanning Electron Microscopy images.....	90
IX Transmission Electron Microscopy (TEM) micrographs.....	90
3.7.2 Gas sorption measurements	91
I. Hydrogen uptake measurements	91

II. Carbon dioxide adsorption measurements.....	92
3.8 Summary	93
3.9 Bibliography.....	94
Chapter Four	96
Chapter 4.0: Preparation of Mesoporous Zeotype Aluminosilicates using Zeolite BEA recipe.....	97
4.1 Abstract.....	97
4.2 Introduction	97
4.3 Results and Discussion.....	100
4.3.1 Mesostructural and framework ordering	100
4.3.2 Silicate condensation in as-synthesised MZBN-100 sample and the washed derivatives.....	109
4.3.3 Aluminium content and acidity.....	110
4.3.4 Morphology of the as-synthesised and calcined MZBN-100 sample	113
4.3.5 Porosity.....	114
4.3.6 Effect of Hydrothermal Synthesis Temperature	118
4.3.7 Hydrothermal Stability of calcined MZBN-100 and its derivatives washed prior to calcination	134
4.3.8 Effect of SiO ₂ : TEAOH ratio on mesostructural framework	140
4.4 Summary	142
4.5 Bibliography.....	144
Chapter Five.....	150
Chapter 5.0: Supercritical CO₂ mediated Incorporation of Palladium Nanoparticles into Zeolite Templated Carbons: Structural Characterisation and Hydrogen Storage Properties.....	151
5.1 Abstract.....	151
5.2 Introduction	152
5.3 Results and discussions	156

5.3.1 Structural Analysis of Pd-free carbons.....	156
5.3.2 Thermal stability of templated carbons	159
5.3.3 Textural Properties and porosity of templated carbons ...	160
5.3.4 Effect of carbonisation environment	164
5.3.5 Effect of Pd loading in zeolite templated carbons.....	168
5.3.5.1 Structural and thermal analysis of Pd-doped carbons	169
5.3.5.2 Textural Properties and porosity of Pd-doped carbons	173
5.3.5.3 Electron microscopy analysis of Pd-free and Pd-doped carbons.....	175
5.4 Hydrogen uptake measurements of Pd-free and Pd-doped carbons.....	180
5.5 Summary	185
5.6 Bibliography.....	187
Chapter Six	192
Chapter 6.0 Two-Step Process Preparation of Ultrahigh Surface Area Porous Carbons Templated using Zeolite 13X for Enhanced Hydrogen Storage	193
6.1 Abstract.....	193
6.2 Introduction	193
6.3 Results and Discussion.....	195
6.3.1 Structural ordering and thermal stability.....	195
6.3.2 Porosity of zeolite templated carbons	199
6.3.3 Nanoscale ordering of zeolite templated carbons.....	202
6.3.4 Assessment of mechanical stability of FA-ZTCs	203
6.3.5 Hydrogen uptake storage.....	207
6.4 Summary	211
6.5 Bibliography.....	212

Chapter Seven	217
7.0 Preparation of Templated and Activated Carbon Aerogels for Carbon Dioxide Capture	218
7.1 Abstract	218
7.2 Introduction	218
7.2 Results and Discussion	222
7.2.1 Structure and porosity of CaCl ₂ -templated carbon aerogels	222
7.2.2 Thermogravimetric analysis	228
7.2.3 Chemical activation of CaCl ₂ -templated carbon aerogels	229
7.2.4 Effect of organic precursor on porosity on activated carbon aerogels	233
7.3 Measurement of Carbon dioxide uptake capacity	240
7.4 Summary	244
7.5 Bibliography	245
Chapter Eight	250
8.0 Conclusions and Outlook	250

Chapter 1. 0 Introduction: Nanotechnology and Nanostructured Porous Materials

1.1 Introduction

A key challenge in porous materials synthesis is the control of structure over several length scales. Length scales from molecular to bulk dimensions are being investigated with a view of designing materials with unique properties for targeted applications. This chapter will provide a foundation and background to the main themes explored in this thesis. The research area of nanoscience and nanostructured materials is introduced with subsequent classification of nanomaterials. Different types of porous materials are described with the main focus being on their fundamental properties and methods of fabrication. The known and potential applications of nanomaterials, with particular emphasis on hydrogen storage and carbon dioxide capture are also discussed.

1.2 Nanoscience and nanostructured materials

Nanostructured materials have attracted a great deal of attention in recent years due to their unique properties and potential interdisciplinary applications.¹ Developments in nanoscience are closely dependent on the possibilities of designing, synthesising and subsequently characterising new nanostructures with tailored applications. Nanomaterials are defined as materials of less than 100 nm in one or more dimensions and which exhibit novel properties that are different from those possessed by their bulk forms. Thus, 'nanoscience' is typically the study phenomena used to describe materials at nanometre length scale, i.e. on a scale of 1 billionth to several tens of billionths of a metre as illustrated in Figure 1.1.²

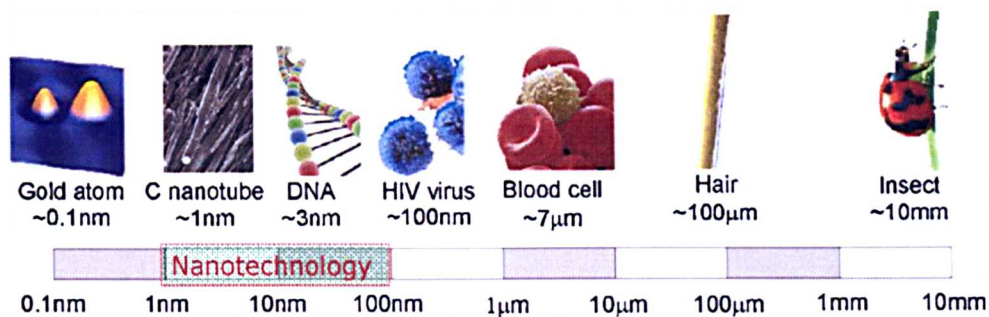


Figure 1.1 Schematic of nanometre scale domain relative to some physical and biological objects.²

Nanoporous materials as a subset of nanostructured materials are of scientific and technological importance due to their outstanding ability to adsorb and interact with atoms, ions and molecules not only on their large interior surfaces, but also throughout the bulk of the material.³ The wide range of potential applications for nanostructured porous materials dictate the current intensive research into methods of synthesis and characterisation. Porous materials have been investigated in a wide range of fields including, heterogeneous catalysis,⁴⁻⁶ gas hosts,⁷ sorption processes,⁸⁻¹⁰ molecular sieves,¹¹ air purification¹² and nanocasting.¹³⁻¹⁹ However, significant challenges remain regarding synthesis techniques for tailoring materials with defined pore size and morphology; and in particular, the control of properties such as pore size, pore shape, pore size distribution and surface area.

1.3 Nanoporous materials

Porous materials typically consist of voids, with either randomly distributed pores (disordered pore systems) or with long range ordering of the pores with high regularity (ordered pore systems).²⁰ Solids are generally considered porous if the pores (whether cavities, channels, or interstices)

have a greater depth than width.²¹ Porosity parameters, in particular the ratio between the pore volume and the total surface area, are vital in making a distinction between various porous systems. Conventionally, porous materials have porosity if the volume ratio of voids to the total volume of the material is in the range of 0.2 and 0.95.²² Therefore, classification of these porous systems has been achieved based on pore diameter dimensions along with type and shape of pores, classifications which are discussed below.

1.3.1 Classification based on pore dimensions

The classification according to pore diameter that is now widely used and accepted is based on International Union of Pure and Applied Chemistry (IUPAC) recommendations.²³ In this model, materials with pore diameters less than 2.0 nm are defined as microporous (most common examples of which are zeolites and activated carbons), greater than 50 nm are macroporous (such as amorphous silicates), and those of the intermediate range (2 to 50 nm) are mesoporous (with examples such as periodic mesoporous silica). Furthermore, the micropores are subdivided into two categories with those smaller than ca. 0.7 nm as narrow micropores or ultramicropores and those in the range of 0.7 to 2 nm as supermicropores.

1.3.2 Classification based on accessibility to the surroundings

Figure 1.2 illustrates a cross-section of a porous material with pores categorised according to their availability to external fluid.²¹ Based on this classification, some pores are described as closed, such as in (a) in which case the pores are totally isolated from their neighbours. Such pores are known to influence bulk density, mechanical strength and thermal stability, but they are of no great value to processes such as fluid flow and

adsorption of gases. In contrast, open pores like (b), (c), (d), (e), and ((f) consist of a continuous channel of communication with the external surface of the material and they are ideal for separation, catalysis and sensing applications.

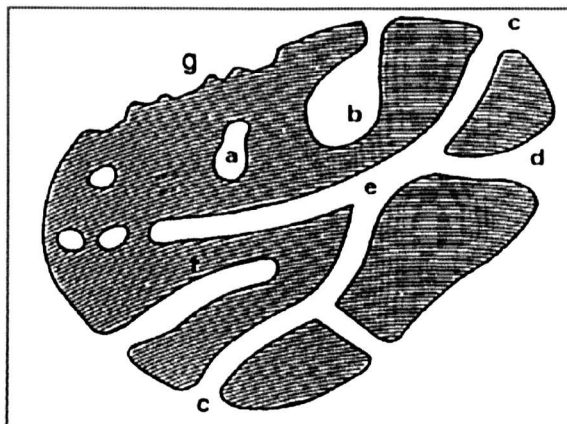


Figure 1.2 Schematic cross-section of a porous material illustrating closed pore (a), open pores (b-f) and roughness of the external surface represented around (g).²¹

1.3.3 Classification based on pore shape

This classification is based on the geometry of the pores, in which pore shapes may be cylindrical, spherical, slit-shape, ink-bottle or cone-shaped as illustrated in Figure 1.3.^{24, 25}

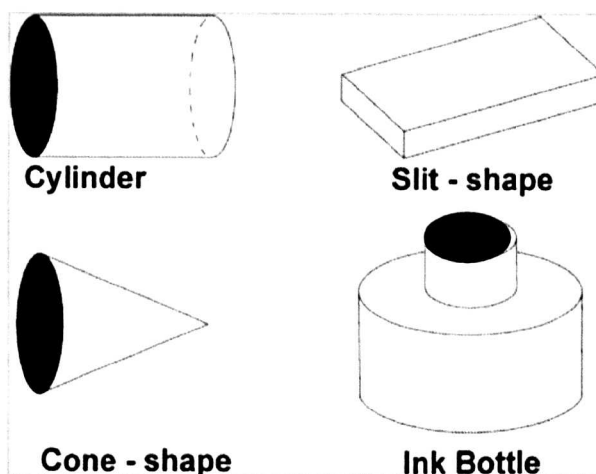


Figure 1.3 Pore shape classification based on geometry. ^{24, 25}

Pore size and pore size distribution are major factors in the applications of porous materials. This is evident in the significant development, as well as modification of current methods, the aim of which is to carry out pore size analysis. However, given the complexity and variety of porous materials, there is still no general agreement on the advantages and disadvantages of the various types of pore classification. Nevertheless, the IUPAC classification discussed in section 1.3.1 is most widely used. It is based largely on pore size determination from different mechanisms occurring in the pores during nitrogen adsorption at 77K and 1 atm. For example, multilayer adsorption, capillary condensation and micropore filling are processes that directly correlate to macropores, mesopores and micropores filling respectively. In this context, the focus of this research work is to investigate how porosity affects the application of porous solids in catalysis and gas adsorption.

1.4 Types of porous materials

Classification of porous materials into different categories as discussed in section 1.3 is without reference to their chemical composition. The level of

difficulty in pore size classification is also shared in the classification based on the chemical nature of the walls due to a large variety of constituent elements. Ozin and co-workers categorised nanoporous materials into three major classifications: organic, inorganic and hybrid porous systems.²⁶ The organic porous systems mainly differ from inorganic ones in having molecules stabilized by either hydrogen bond or Van der Waals interactions. In addition, the latter are characterised by a large number of covalent bonds in their structure making them chemically and thermally stable. Hybrid systems are generally as stable as inorganic systems though with potential use of functional organic groups as catalytic centres or adsorbing sites. In depth discussions of zeolites (including mesoporous aluminosilicates), and carbonaceous materials are presented in the following sections.

1.4.1 Zeolites

Currently, zeolites refer to all microporous silica-based solids presenting crystalline walls.²⁷ In recent years, there has been a significant increase in the synthesis, characterisation and applications of new microporous materials due to recently conceived frameworks, compositions and unique structural types.²⁸ To date there are more than 176 unique framework structures that have been approved and reported in the 6th edition of Atlas of Zeolite Framework Types by the International Zeolite Association Structure Commission (IZA-SC).²⁹

Structurally, zeolites are hydrated crystalline aluminosilicates constructed from TO_4 (where T = tetrahedral atom e.g. Si and Al).^{30, 31} The first class of nanoporous materials to be recognized as aluminosilicates had a general formula $\text{A}_{x/n}[\text{Si}_{1-x}\text{Al}_x\text{O}_2] \cdot m\text{H}_2\text{O}$, where A is typically a metal cation of valence n , and m is the number of water molecules.²⁸ Conventionally,

zeolitic architectures are based upon vertex-sharing $[\text{SiO}_4]$ and $[\text{AlO}_4]$ tetrahedra with Si/Al ratio ranging from a minimum of 1 to infinite. Thus, they contain well-ordered nanometre scale sized void spaces of ca. 3 – 15 Å in their structures. Figure 1.4 shows typical examples of zeolite structures. The consistency in nomenclature of zeolites is maintained by IZA-SC in accordance with IUPAC recommendations, in which a three letter code is assigned to each structure type.^{29, 32, 33} For example, the frameworks of zeolite β and faujasite-type structure which form the main area of study in this work are denoted *BEA and FAU, and are represented respectively in Figure 1.4.²⁹

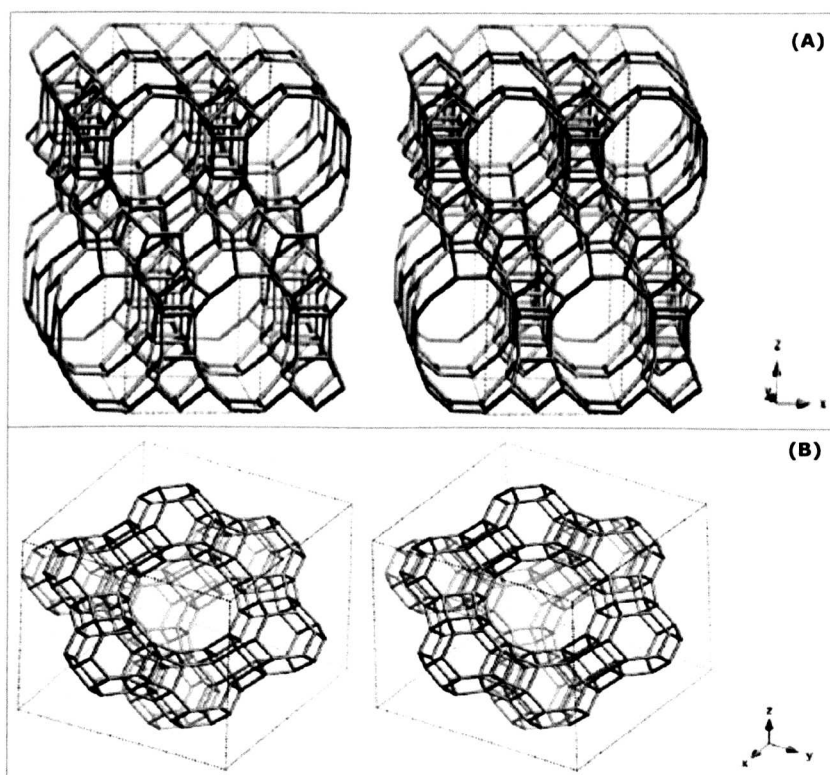


Figure 1.4 Zeolite framework for (A) BEA* viewed along $[010]$ with idealised tetragonal cell, $P4_122$, where $a = 12.6 \text{ Å}$, $c = 26.2 \text{ Å}$ and (B) FAU viewed along $[111]$ with cubic structure, $a = 24.3 \text{ Å}$.²⁹

Typically, zeolites are synthesised under hydrothermal conditions in which, after Si, Al and mineralisers such as NaOH or KOH are mixed in water, the resulting hydrogels are heated at prescribed temperatures and crystalized into zeolites. The resultant zeolites usually have a low Si/Al ratio framework ($\text{Si/Al} < 10$) and hydrophilic properties.³² This is because the framework contains a high proportion of anionic Al sites and charge compensating cation such as Na^+ or K^+ . The use of organic compounds such as quaternary ammonium salts often referred to as 'structure directing agents' (SDAs) was established in the 1960s resulting in zeolites with higher Si/Al ratio ($\text{Si/Al} > 10$).³⁴ In this case, the zeolite structures appear to form around the organic compounds via hydrophobic interactions, which results in hydrophobic frameworks in contrast to zeolites synthesised without SDAs. A schematic representation of the general synthesis process is shown in Figure 1.5.³⁵

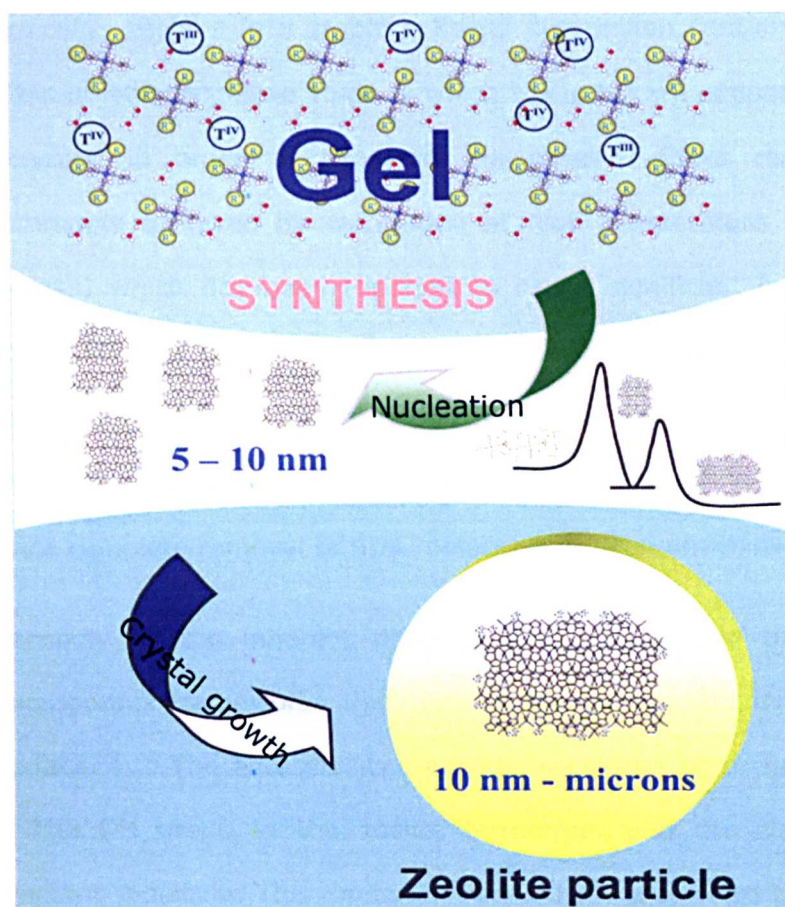


Figure 1.5 Scheme for hydrothermal synthesis of zeolite using organic molecules (such as amines or alkylammonium salts) as structure directing agents.³⁵

It is worth pointing out that variation of the gel composition (including incorporation of other metals or metal oxides), system pH, reaction temperature, gel ageing, seeding, reaction time and templates used determines the framework structure of the resultant zeolites.²⁸ In particular, zeolites with unique composition, morphology, particle size and particle size distribution are generated with changes in experimental parameters. However, the prepared zeolites by this method suffer the following limitations:

- Typically, zeolites in a stable colloidal suspension contain trapped SDAs in intracrystalline voids of which the latter are supposed to be removed in order to generate the pores.³⁶ SDAs removal is commonly achieved by calcination at high temperature in air or oxygen, which has been reported to cause significant irreversible aggregation of particles.³⁶⁻³⁸ In addition, calcination poses a great potential of destroying any previously grafted organic molecules. An alternative method would be solvent extraction, which is rarely used since complete removal of SDA molecules is often unachievable.³⁶
- Secondly, is the inherent diffusion limitations within the zeolite microporous frameworks that restrict accessibility to their internal surface.^{39, 40} The accessibility depends largely on both the location of the OH group in the zeolite framework and the size of the reactant molecule. This limitation has in turn prevented the use of zeolites not only in catalysis involving large molecule transformations, but in other areas of chemistry where large pore size is required.

In the quest to overcome these limitations, research efforts have focused on extending zeolitic dimensions to pores consisting of larger than 12 T-atoms (classified as extra-large pores).²³ In other research, the focus has been decreasing the zeolite's particle size thereby reducing the diffusion pathlength.^{19,41-44} There have also been efforts aimed at the introduction of networks of mesopores or macropores by chemical leaching³⁹ or nanocasting of zeolites within mesoporous templates.^{19, 43, 45} A seminal development in the templated synthesis of large-pore zeolites was the

discovery of the M41S family of mesoporous materials by researchers at the Mobil Corporation.^{46, 47}

These so-called periodic mesoporous silicas (PMSs) of the M41S type are discussed in detail in section 1.4.2 below, as they have become an area of intensive research due to their potential applications in a wide range of fields that require pore size greater than 2.0 nm.

1.4.2 Periodic mesoporous silicas (PMSs)

The development of porous materials with large surface areas and tuneable pore size is currently an area of extensive research particularly with regards to their potential applications in areas such as adsorption, chromatography, catalysis, sensor technology and gas storage.⁴⁸ Crystalline zeolites discussed in section 1.4.1 as well as PMSs are characterised by very large surface areas, ordered pore systems and well-defined pore size distribution. However, the M41S family of PMSs exhibit amorphous walls and do not possess acidity as high as some zeolites.⁴⁵

Typically, M41S family of materials are synthesised utilising SDAs in the form of lyotropic liquid-crystalline phases around which silica precursors can condense (i.e., sol-gel polymerisation) under basic conditions. The resultant mesostructured composite upon subsequent removal of the surfactant by extraction or calcination results in formation of mesoporous materials.^{46, 49} The most well-known representatives of this class consists of the silica solids MCM-41 (with a hexagonal packing arrangement of mesopores, space group $p6mm$), MCM-48 (with a cubic arrangement of mesopores, space group $Ia3d$) and MCM-50 (with a laminar structure, space group $p2$) as illustrated in Figure 1.6.⁴⁶⁻⁴⁸

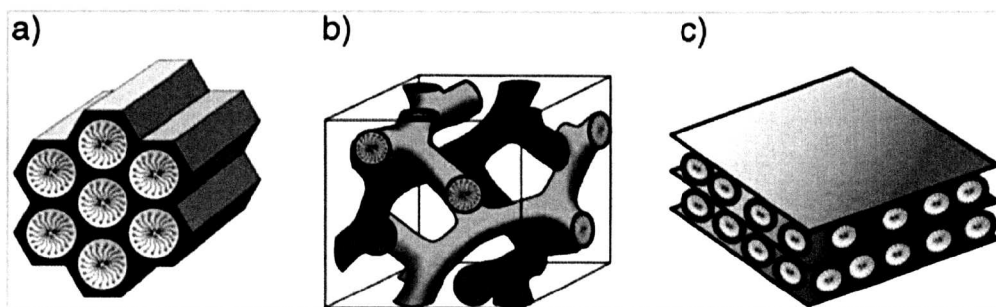


Figure 1.6 Framework structures of mesoporous M41S materials: (a) MCM-41 (2D hexagonal packing) (b) MCM-48 (cubic), (c) MCM-50 (lamellar) with space group of $p6mm$, $ia3d$ and $p2$ respectively.⁴⁸

A liquid-crystal templating mechanism for the formation of these materials as proposed by Beck and co-workers has two potential pathways illustrated in Figure 1.7.⁴⁶ On one hand, in true liquid-crystal templating (TLCT), the inorganic precursors are deposited and condensed on the micellar structure of a preformed lyotropic liquid crystal phase. This is due to the high concentration of the surfactants under the prevailing conditions (temperature and pH). On the other hand, a co-operative self-assembly between the SDA and the already added inorganic species initiates the ordering of silicate-encased surfactant micelles.

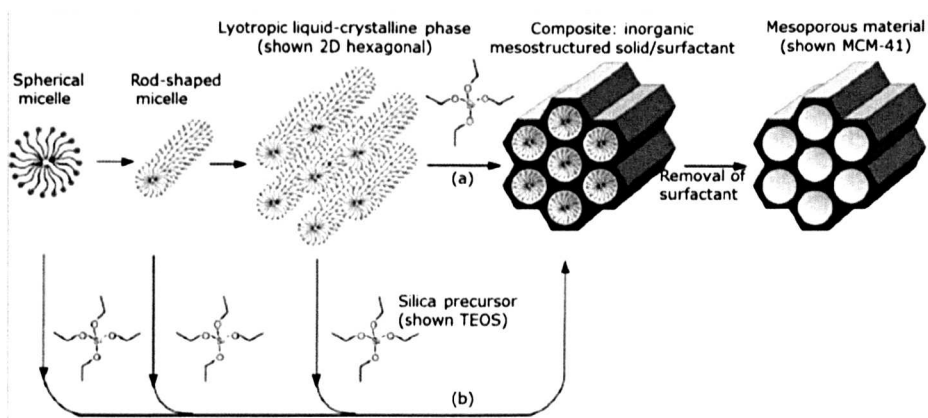


Figure 1.7 Synthesis of mesoporous materials by; (a) true liquid-crystal and (b) co-operative liquid-crystal templating mechanism.⁴⁸

The conventional mechanism of formation based on the electrostatic interaction between an inorganic precursor (**I**), and a SDA surfactant head group (**S**), as proposed by Huo *et al.*, is illustrated in Figure 1.8.^{48, 50, 51}

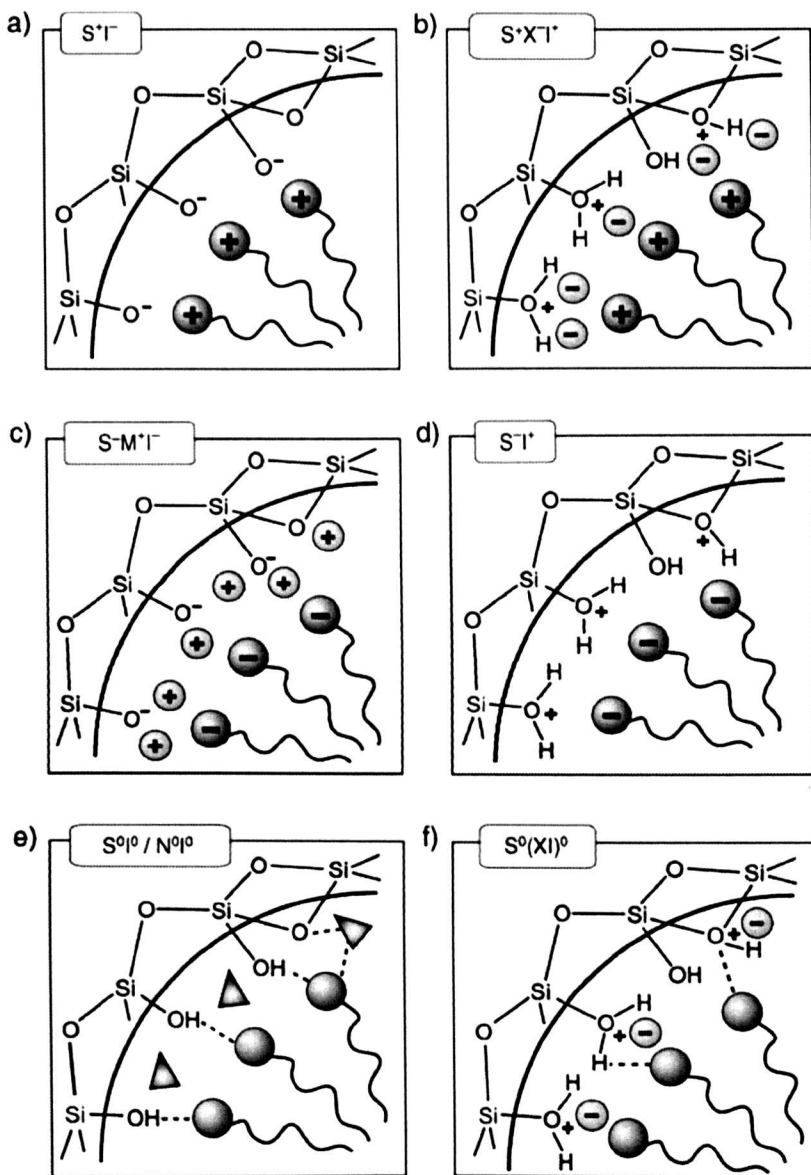


Figure 1.8 Inorganic – surfactant head group interactions with consideration of the possible synthetic pathways in acidic, basic or neutral media. Electrostatic: S^+I^- , S^+XI^- , $S-M^+I^-$, S^-I^+ ; through hydrogen bonds: S^0i^0/n^0i^0 , $S^0(XI)^0$.⁴⁸

Electrostatic interactions are classified as follows:

(a). S^+I^- pathway occurs under basic conditions whereby silica species are present as anions (I^-) with cationic ammonium surfactants (S^+) used as the SDAs.⁵²

(b). $S^+X^-I^+$ pathway if the synthesis occurs under acidic conditions whereby the silica species (I^+) are positively charged. In such a case a mediator ion (X^-) (typically a halide) is required to produce an interaction with the surfactant (S^+).⁵¹

(c). $S^-M^+I^-$ pathway occurs if negatively charged surfactant (S^-) are used as the SDA under basic conditions, requiring a mediator cation (M^+) to promote the interaction with the negatively charged silica species (I^-).⁵¹

(d). S^-I^+ pathway occurs under acidic conditions (silica species (I^+) are present as cations) with negatively charged surfactants (S^-).⁵¹

(e) and (f). In addition to the dominating electrostatic attractions in (a) to (d), hydrogen bond mediated interactions can also be a driving force for the formation of mesophase as illustrated in Figure 1.8 This is a case whereby non-ionic surfactants are used (e.g. S^0 a long-chained amine; N^0 : polyethylene oxide), whereby uncharged silica species (S^0I^0 ; pathway (e)) or ion pair ($S^0(XI^0)$; pathway(f)) can be present.^{48,53, 54}

To date, a wide range of well investigated periodic mesoporous silica materials have been reported with significant progress achieved in structural⁵⁵ and morphological control.^{56, 57} In addition, there has been remarkable advancement in compositional control,^{56, 58} functionalisation of pore walls,^{59, 60} formation of hybrid silica/organic frameworks⁶¹⁻⁶⁴ and improved stability of mesoporous materials.^{57, 65-69} Noteworthy is the

preparation of well-ordered hexagonal mesoporous silica structures (SBA-15) by Zhao and co-workers.⁷⁰ These materials exhibit uniform pore size up to approximately 30 nm.

The preparation of crystalline mesoporous aluminosilicas via supramolecular templating remains a challenge. This is because the preparation conditions required to generate mesoporosity do not favour the formation of crystalline aluminosilicate frameworks. Although the formation of supramolecular-templated crystalline silica-surfactant mesophases has been demonstrated in a number of studies,⁷¹⁻⁷⁶ their transformation to template free crystalline materials often fails. Alternatively, mesoporous silicate composites may be prepared using small organic molecules as 'structure directing agents' wherein the mesoporous structure formation is different from that which applies to supramolecular templates.⁷⁷⁻⁸¹ However, in most cases the resulting materials are composites made up of zeolite crystallites embedded in a disordered mesoporous matrix in which it has been suggested that such composites are generated via a nontemplating structure mechanism.⁷⁸

Part of the work presented in this thesis (chapter four) explores the preparation of mesoporous aluminosilicates using templating molecules and synthesis conditions that are typically used for the preparation of crystalline zeolites. The aim was to achieve the simultaneous formation of an ordered mesostructure that might also be crystalline. Such materials are expected to have larger pore sizes than conventional zeolites and simultaneously exhibit both higher hydrothermal and thermal stability because refluxing does not cause any dealumination.

1.4.3 Porous carbonaceous nanomaterials

A wide variety of carbon nanostructures have been reported, for example; carbon nanofibres,^{7, 82-84} activated carbon,⁸⁵⁻⁹² multi-walled and single-walled carbon nanotubes,⁹³⁻⁹⁶ templated carbons,^{14, 15, 97-102} and carbon aerogels,¹⁰³⁻¹⁰⁵ among many others. The wide range of forms in which carbon exists is attributed to its ability to bond to itself (catenation) via sp^3 (as in diamond) and sp^2 (as in graphite) hybridization. However, most porous carbons consist of benzene-like carbon hexagons with sp^2 – hybridised carbon atoms and differ from each other in the way these hexagons are arranged. The arrangement of the hexagons results in formation of carbons which are at the opposite ends of the spectrum; those that possess long-range ordering (well-ordered) like nanotubes or nanofibres and those with irregular shapes like activated carbons as illustrated in Figure 1.9.^{13, 106}

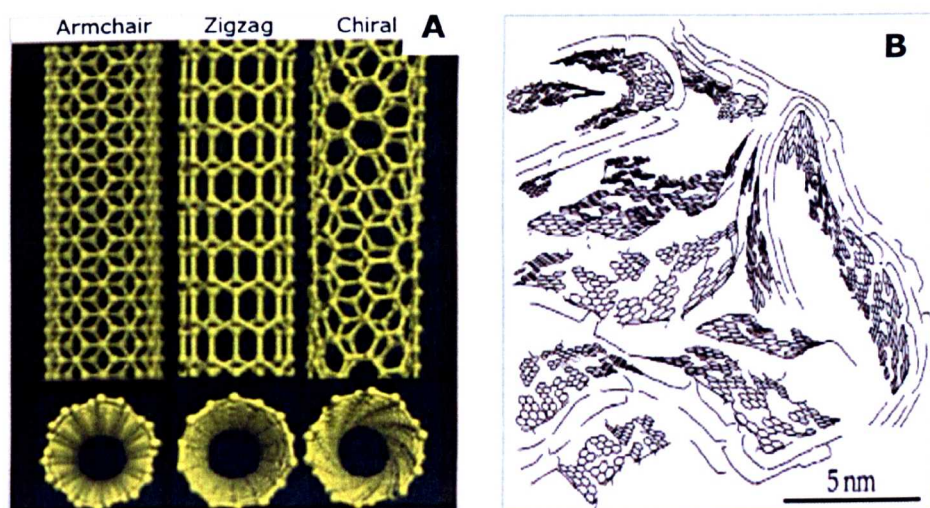


Figure 1.9 Schematic illustrations of the structures (A) single-walled carbon nanotubes with projections normal to the tube axis and perspective views on the top and bottom respectively; (B) molecular structure of activated carbon.^{13, 106}

Carbonaceous structures exhibit different structural properties and porosities that in turn dictate their applications. Their wide-spread application is a result of their remarkable properties, such as the hydrophobic nature of their surface, high specific surface area, large pore volume, chemical inertness, good thermal stability and good mechanical stability.¹⁰⁷ However, most porous carbons are microporous which implies that they are well-suited for many applications (section 1.6) involving small molecules as is the case for zeolites (section 1.4.1). There are still, however, many other applications for which the presence of larger pore size (i.e. mesopores or even macropores) would be preferred. The development of mesoporous as well as microporous carbons would therefore enhance their current and future applications (section 1.6 and 1.7).

Porous carbon materials are typically prepared by a process of pyrolysis or carbonisation of natural or synthetic carbon precursors with subsequent activation; a process involving a wide range of experimental conditions.¹⁰⁸ For instance, the carbonisation process may include a wide range of precursors, heating rates, final heat temperature, soaking time and reaction environment. Furthermore, activation constitutes an extra set of variables including reaction temperature, reacting gas, duration and extent of reaction.¹⁰⁸ The resultant activated carbons generally exhibit a broad pore size distribution (PSD) with a high proportion of micropores. The wide PSD is attributed to the etching processes that are difficult to control or by escaping gases during carbonisation of carbon precursors with subsequent activation. To control the porosity of carbons, the template carbonisation route (section 1.4.3.1) has attracted much attention because it allows

preparation of carbon materials with controlled architecture and narrow pore size distribution.¹⁰⁹

1.4.3.1 Nanocasting techniques to porous carbons

In 1986, Knox and co-workers pioneered the template synthesis of a porous carbon material for liquid chromatography by the impregnation of porous silica with phenolic resin and subsequent carbonisation.¹¹⁰ Since then, template carbonisation has been extensively studied and employed to prepare ordered porous carbon materials^{15, 16, 99, 101, 102, 111-113} Figure 1.10 illustrates a typical nanocasting technique using zeolite Y as a hard template.¹¹⁴

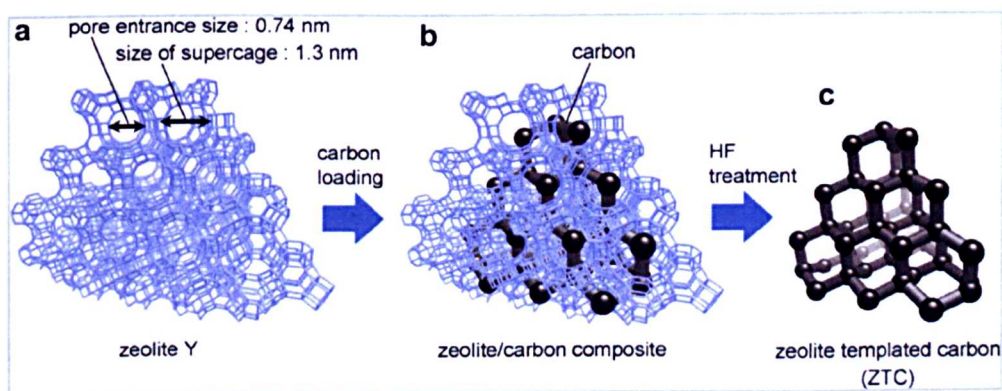


Figure 1.10 Scheme for the synthesis of microporous carbons; (a) crystal structure of zeolite y template, (b) zeolite/carbon composite and (c) framework structure of liberate carbon after zeolite etching in HF acid.¹¹⁴

Template carbonisation conventionally involves the following four main stages:

- I. Preparation of porous inorganic template.

- II. Introduction of a suitable carbon source into the pores of the template either by liquid impregnation or chemical vapour deposition.
- III. Carbonisation of the inorganic-organic composite at a specific temperature.
- IV. Removal of the template by dissolution in an alkali (NaOH) or acidic media (HF or HCl).

A variety of inorganic porous templates including zeolites^{14, 15, 99, 102, 113, 115} and mesoporous silicas^{16, 74, 110, 116-120} have been used to prepare porous carbons. Likewise, the wide range of carbon precursors includes: sucrose,¹⁶ furfuryl alcohol,^{14, 15, 97, 121, 122} acrylonitrile,^{15, 121} propylene,^{14, 115} pyrene,¹²¹ acetonitrile,^{119, 123} and vinyl acetate¹²¹ have been used. Generally, the use of microporous zeolites and mesoporous silicas as hard templates results in microporous and mesoporous carbon materials respectively.^{15, 99, 111, 124, 125} It is noteworthy that the structural ordering of mesoporous carbons in most cases is a faithful inverse replica of the corresponding pore ordering of silica template. In contrast, it still remains a great challenge to replicate the zeolite pore structural ordering.

Poor inverse replication in carbons templated by zeolites has been attributed to a number of factors including low carbon loading due to the small pores in the zeolites or disordered/inappropriate symmetry of the zeolite ordering. Moreover, close replication of pore ordering of zeolite β and zeolite Y is considered challenging due to the disordered structure of zeolite β and high symmetry cubic space in zeolite Y respectively.^{14, 126} In order to address these limitations, Parmentier and co-workers employed the use of zeolitic material which combines a 2D or 3D with non-cubic

[20]

systems such as zeolite EMC-2 to successfully prepare porous carbons with significant levels of zeolite-like ordering and thus exhibiting more than one XRD diffraction peak.¹²⁶

Working independently, Kyotani *et al.*^{101, 102} and Mokaya *et al.*⁹⁹ successfully prepared microporous carbon materials using zeolite Y and zeolite β respectively as templates. The resultant carbons in both cases were exclusively microporous exhibiting high surface area and large pore volume up to 3600 m²/g and 1.5 cm³/g respectively. There are, however, limitations in that, only a few zeolites may be used to give a faithful inverse replica. In addition, the desirable mesopore size range is not obtainable in this process limiting the applications of these materials.

In contrast to zeolites, mesoporous silicas tend to result in faithful inverse replica carbon. This is because the mesoporous silicas have larger pores and pore wall thicknesses that allow the formation of mesoporous carbon materials. Ryoo *et al.*¹⁶ and Hyeon *et al.*,¹¹⁶ working independently reported the first synthesis of ordered mesoporous carbon CMK-1 and SNU-1 respectively using mesoporous silica as hard template. Since then, a wide range of mesoporous silicas such as MCM-48,¹¹⁶ SBA-15,^{109, 118, 119} and hexagonal mesoporous silica (HMS),¹¹⁷ among others, have been investigated as templates to prepare ordered mesoporous carbons.

It is desirable to control the pore size and/or morphology of mesoporous carbons given the diverse range of porosity. The possibility of pore size control for mesoporous carbons was first reported by Ryoo and co-workers.¹²⁷ This was achieved by varying the ratio of SDAs cetyltrimethylammonium bromide (CTAB) and polyoxyethylene hexadecylether-type C₁₆H₃₃(C₂H₅O)₈OH (C₁₆EO₈) in the synthesis of

mesoporous silica template. It was noted that the wall thickness in mesoporous silica varied between 1.4 nm and 2.2 nm which resulted in mesoporous carbons with pore sizes in the range of 2.2 to 3.3 nm.

In this thesis, commercial zeolites Y and 13X are explored as hard templates for porous carbon formation. In particular the replication of the template's structural regularity in the resultant carbons is investigated. The main focus will be on tailoring porosity to the desired applications especially in catalysis and gas adsorption.

1.4.3 2 Porous carbon aerogels

Another form of porous carbonaceous materials that has been intensively studied in recent years is carbon aerogels due to their high surface-to-volume ratios, high electrical conductivity and tuneable porosities at nanometre scale^{104, 105, 128, 129} Although new precursors and solvents have been reported in literature,¹³⁰⁻¹³² most organic aerogels are prepared by sol-gel polycondensation of resorcinol with formaldehyde (RF hydrogel) as initially proposed by Pekala.¹³³ This is because the sol-gel process allows better control of the composition, homogeneity and structural properties of the resulting materials.¹³⁴

Typical synthesis of carbon aerogels is achieved in two main steps. The first step involves preparation of organic aerogels via sol-gel process followed by supercritical drying to remove liquid from the delicate gel structure without collapse or shrinkage. A wide range of organic monomers/resin systems have been reported; namely, melamine-formaldehyde (MF),^{104, 135} resorcinol-formaldehyde (RF),¹³³ polyurethane-dichloromethane¹³⁶ and phenolic-furfuryl (PF),¹³⁷ among many other precursors. In the second step the dry organic aerogels are pyrolysed in an

inert atmosphere at temperatures between 500 °C and 2500 °C to yield mesoporous/macroporous aerogels/monoliths.¹³⁸

The RF hydrogel has been widely investigated and its two-step reaction mechanism is illustrated in Figure 1.11.¹³⁸ The first step involves the addition of formaldehyde to resorcinol conventionally catalysed by a base to form mono-, di-, and tri-hydroxymethylated derivatives (-CH₂OH). In step two the condensation of -CH₂OH groups forms ether linkages (CH₂-O-CH₂-) or with unsubstituted site of the phenyl ring, forms methylene (CH₂).¹³⁸ Several factors have been investigated in order to optimise the experimental conditions. For example, Pekala *et al*^{104, 105, 133} and Shen *et al*.¹³⁹ independently reported that the resorcinol/catalyst (R/C) ratio plays a major role in deciding the size and porosity of carbon aerogels. Moreover, Job and co-workers linked this ratio with pH of the solution which is usually adjusted by the catalyst.¹⁴⁰ However, as the pH changes throughout the experiment, it is more useful to use the R/C ratio as the controlling parameter.

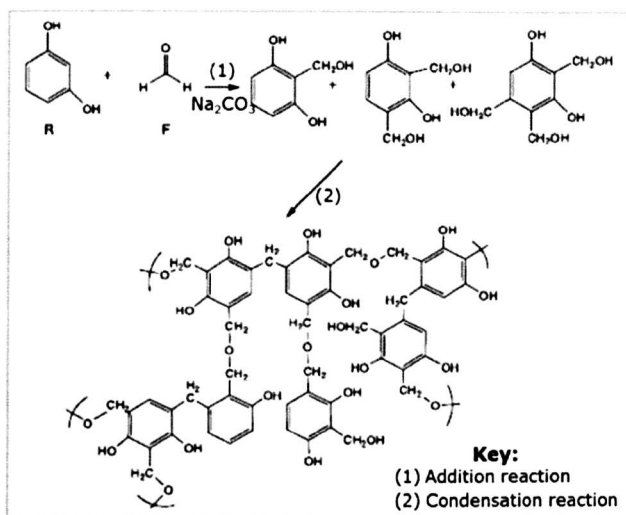


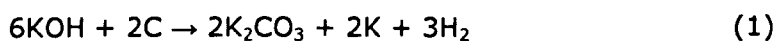
Figure 1.11 Reaction mechanism of the sol-gel polymerization of resorcinol with formaldehyde.¹³⁸

In contrast to zeolite templated carbons, aerogels do not exhibit an ordered pore size structure or a narrow PSD. However, the disordered framework of the aerogels has been demonstrated to be advantageous with respect to certain applications. In particular, the pore size extends to the larger end of the mesoporous regime and into the macroporous regime thus enhancing molecular diffusion.¹³⁸ In addition, the pores in these materials are interconnected allowing multiple points of entrance and egress.

1.4.3.3 Activated carbons

Chemical and physical activation of carbonaceous materials constitutes a well-established route for the preparation of carbons with high surface area.^{87-89, 91, 92, 141} In recent years, chemical activation has been investigated as a tool for enhancing the textural properties of advanced carbon materials such as templated carbon, carbide-derived carbons (CDCs) or carbon nanotubes.^{86, 88, 89, 142} In particular, activated carbons produced using KOH as activating agent exhibit attractive properties such as: (i) high surface areas and pore volumes, (ii) a significant proportion of the porosity arises from uniform micropores in the 1 – 2 nm range, (iii) the pore structure can be tailored by varying the activating parameters such as activation temperature and KOH/carbon ratio and (iv) activation may be performed via an easy one-step process.^{91, 141}

During the chemical activation process, the reaction which takes place between KOH and carbon is primarily as follows,^{90, 143}



The carbon framework is etched to generate pores due to the oxidation of the carbon into carbonate ions and intercalation of the resulting potassium

compounds which are removed during subsequent washing steps. On the other hand, the production of CO₂ from the decomposition of K₂CO₃ at temperatures above 700 °C can contribute to further porosity development through gasification with simultaneous formation of atomic potassium according to reaction (2).¹⁴⁴ Thus the atomic K expands the interlayers of adjacent hexagonal network planes consisting of carbon atoms resulting in enhanced pore formation.¹⁴⁵



In this thesis (Chapter 7), chemical activation is explored as a route of tailoring the porosity of carbon aerogels for gas adsorption. The effect of using a metal salt as a 'porogen' in polycondensation of melamine-formaldehyde resins on the pore texture is investigated. Furthermore, the effect of chemical activation on porosity of carbon aerogels is assessed in reference to RF and MF (with or without a porogen). The pore texture is studied before and after activation in order to determine which synthesis parameters and/or pyrolysis variables have a significant influence on the final textural properties of the resultant carbons.

1.5 Metal-doping of carbons

The combination of metal nanoparticles and porous carbons is an interesting research area. The dispersion of metal nanoparticles within high surface area support has been suggested as one way of enhancing hydrogen storage via the so-called 'spillover' mechanism.¹⁴⁶ It has been demonstrated that by using Palladium nanoparticles, that degree of Pd-carbon contact, pore size and the state of hydrogen receptor surfaces are key factors that enhance H₂ spillover.^{82, 146-152} The spillover mechanism employs metals that can adsorb hydrogen dissociatively, thus acting as a

source of H atoms that may spill over the metal-support interface.¹⁴⁷ However synthesis of metal nanoparticles with subsequent dispersion into the high surface area carbons is yet to be optimised. This often involves the use of volatile organic compounds (VOCs) which are highly hazardous. For instance halogenated solvents being photochemically active, result in the formation of smog which is considered toxic.¹⁵³ In recent years supercritical fluids (SCFs) have been intensively investigated for incorporation of metal nanoparticles into the carbon substrates.

The 'green' benefits of using supercritical fluids are due to elimination of VOCs and replacement with non-toxic fluids such as carbon dioxide. Supercritical fluids have been defined by Darr and Poliakoff as:

*"Any substance, the temperature and pressure of which are higher than their critical values, and which has a density close or higher than its critical density."*¹⁵⁴

Figure 1.12 illustrates the phase changes of a pure substance.¹⁵⁴ The critical point marked C is approached (from the liquid-vapour phase region) as the meniscus between the liquid and the vapour gradually disappear. All the properties of the vapour and the liquid become identical resulting in a homogeneous single phase.¹⁵⁵ This implies that SCFs could be easily described as having properties between those of a gas and a liquid; for instance, SCFs tend to have low viscosity and high heat capacities enhancing heat and mass transfer but also intermediate density giving them ability to dissolve other liquid and solid compounds.¹⁵⁶⁻¹⁵⁸ One such SCF that has been under intensive investigation in recent years is supercritical carbon dioxide (scCO₂) due to attractive properties such as non-toxicity, non-flammability and thermodynamic stability.¹⁵⁵

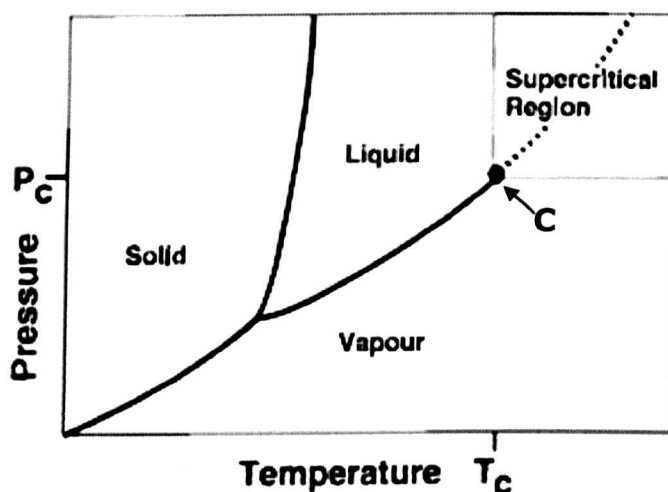


Figure 1.12 Schematic pressure-temperature phase diagram for a pure component showing supercritical fluid region with the critical point marked C.¹⁵⁴

In recent years, scCO_2 has been extensively studied as a green medium for chemical reactions and separations.^{69, 152, 154, 159} This is due to the uniquely attractive properties of scCO_2 such as delivering molecules to areas with high aspect ratios, complicated surfaces and poorly wettable substrates.¹⁵¹ Moreover, unreacted materials and by-products from scCO_2 processes can be readily removed from the system by flushing with CO_2 fluids. In this thesis (Chapter five) zeolite templated carbons were first prepared using nanocasting techniques and then doped with Pd in supercritical scCO_2 . The aim was to provide further insights into optimising experimental parameters that would result in homogeneously dispersed metal nanoparticles in porous carbons with potential for enhanced hydrogen storage.

1.6 Current and potential applications of nanostructured porous materials

The diverse range of nanostructured porous materials with tuneable textural properties and morphology allows their use in a wide range of fields. Some of the applications have already been in existence for a long time (such as ion exchange for separation and catalysis),¹¹ while others are still under intensive investigations for possible scale up (for example as hydrogen storage media). Some applications are outlined in this section, while hydrogen uptake and carbon dioxide capture, which are the main focus of this work, will be discussed in section 1.7. The remarkable use of porous materials is evident in Breck's statement on zeolites as follows:

*"Rarely in our technological society does the discovery of a new class of inorganic materials result in such a wide scientific interest and kaleidoscopic development of applications as has happened on zeolite molecular sieves."*¹⁶⁰

Applications of porous materials have been dictated mainly by their porosity. For example, traditional applications such as ion exchange, adsorption for separation and catalysis all benefit from well-ordered materials such as zeolites.^{3 28} The characteristic 3D frameworks of zeolites that typically form channels are useful as molecular sieves and adsorbents because their pore sizes are comparable to molecular dimensions.^{160, 161} Also, zeolites have been successfully used as supports on different materials including metals, ceramics and polymers.¹⁶¹⁻¹⁶³ However, the use of materials of a mesoporous nature, beyond the 2 nm range remained elusive until pioneering synthesis methods were reported in the early 1990's by researchers from the Mobil Corporation.⁴⁷

The diverse range of mesostructured materials with tuneable textural properties and morphologies are highly desirable for applications in sorption and size-selective separation,³ or as hard templates for nanocasting of new mesoporous materials.^{16, 111} Furthermore, as catalyst supports and catalysts, they overcome size selection and diffusion limitations associated with microporous materials. However, for catalytic applications the amorphous nature of silica frameworks results in low hydrothermal stability and reactivity (e.g. acidity) when compared with crystalline zeolites. Thus, substantial study is directed to the synthesis of mesoporous materials with crystalline frameworks; for example, addition of molecular zeolite templates to the precursor for mesoporous aluminosilicate synthesis.¹⁶⁴⁻¹⁶⁶

In recent years, there has been extensive study into the use of porous carbon materials as a hydrogen reservoir (section 1.7) and in supercapacitors¹⁶⁷ among many other applications. Therefore, with the ever increasing broad range of applications of porous materials, there is the need to optimise the conditions for their syntheses with a view of enhancing reproducibility. Despite the outstanding challenges in the preparation of ordered porous materials, the rate of advancement in this area in the recent past has been impressive.

1.7 Gas sorption/storage

1.7.1 Hydrogen storage

Hydrogen is an ideal alternative to finite fossil fuels from an environmental point of view. The availability of hydrogen is potentially unlimited and combustion does not generate pollutants and particularly not carbon dioxide (a greenhouse gas).¹⁶⁸⁻¹⁷⁰ A particularly daunting challenge facing the use of hydrogen as a transportation fuel or in power generation is the

development of safe and practical storage systems. The current research on hydrogen storage is mainly guided by United States Department of Energy (DoE) which has set target systems for hydrogen storage for gravimetric (5.5 wt %) and volumetric (40 gL⁻¹) densities to be achieved by the end of 2017.¹⁷¹ In addition, the storage systems should show no decay for 1500 consecutive fuelling cycles and allow filling to full capacity in less than 3.0 minutes for a 5.0 kg hydrogen charge, over the lifetime of the system.

At the present time there are essentially four main systems being investigated for hydrogen storage, namely: Liquefaction, compressed gas, metal hydrides, and adsorption on porous materials.^{98, 99, 170, 172-175} The high energy cost for liquefaction coupled with the low energy efficiency due to continuous boil-off of hydrogen make liquid systems impractical for application in hydrogen fuel cell powered vehicles. The compressed gas systems involve high pressure cylinders which engender safety issues. The remaining systems which are potentially attractive may be categorised into chemisorption (in metal and complex hydrides) and physisorption (in porous materials).

Metal hydrides work by using a metal alloy that can store hydrogen by bonding with it to form hydrides. Different types of materials including LaNi₅H₆, TiFe, Mg₂Ni, Mg-based materials among others have been investigated for improved hydrogen storage density, kinetics and life cycle.¹⁷⁶ LaNi₅ is the most studied metal hydride with the parent compound absorbing ca. 1.0H/LaNi₅ (1.5 wt %). It is easy to activate to 5 bar at a temperature of 100 °C in order to achieve maximum hydrogen capacity.¹⁷⁶ Other widely investigated hydrides are complex hydrides, for example

lithium borohydrides (LiBH_4) with a promising potential for on-board applications as it yields 13.8 wt % of hydrogen through decomposition into LiH and B .¹⁷⁷ However, the strong bonding of atoms in LiBH_4 results in high thermodynamic stability and it also suffers from sluggish decomposition kinetics due to its multi-step decomposition reactions at a temperature above 400 °C. Also, despite the good reversibility of LiBH_4 system reported by Walker and co-workers, its destabilisation reaction was kinetically limited which was attributed to the formation of a passivating boride layer.¹⁷⁸

Extensive studies have been performed on physisorption of hydrogen on porous solids, such as zeolites,¹⁷⁹⁻¹⁸² metal organic frameworks (MOFs)¹⁸³⁻¹⁸⁶ and nanostructured carbons (e.g. carbon nanotubes, carbon fibres, and nanoporous carbons)^{94, 95, 98, 99, 113, 184, 187, 188}. Nanostructured carbons have received much attention due to their highly desirable properties in gas sorption as discussed in section 1.4.3. Besides carbon nanotubes and nanofibres, nanoporous carbon materials such as activated carbons and templated carbons (microporous and mesoporous)^{98, 120, 175, 188} have been extensively studied. It is now well established that the hydrogen sorption capacity of porous carbons and other types of porous materials generally increases with increase in surface area.^{120, 173, 175, 189-191} A number of studies have suggested that micropore below 1.0 nm^{87-89, 192-195} and preferably 0.6 to 0.8 nm are the most efficient for hydrogen uptake.¹⁹¹⁻¹⁹³

Despite continuing extensive research efforts into hydrogen as an alternative source of energy, the targets set by the US DoE are yet to be achieved in any known material. Recently, the embedment of metal nanoparticles into the porosity of ordered porous materials with controlled

pore size distribution has been extensively explored.^{152, 196-198} The resulting material is a hybrid with the combined advantages of adsorption on the high surface of the porous substrate and hydrogenation of metal nanoparticles forming metal hydrides.¹⁹⁹ Moreover, the presence of metal nanoparticles inside the pores is considered to increase hydrogen uptake of different porous materials via the spillover mechanism.¹⁴⁶ This mechanism proceeds via catalysed formation of monoatomic hydrogen followed by migration to the surface of the support.

Most routes employed for doping metal nanoparticles onto porous substrates are typically post-synthesis implantations with inevitable challenges in controlling metal particle size and distribution.^{82, 149} In addition, metals can readily agglomerate into fewer larger particles. The use of supercritical fluids in recent years to deposit metal nanoparticles onto the surface of porous materials has shown the potential to eliminate the disadvantages posed by conventional solvents.^{151, 159} Furthermore, most of the supercritical fluid mediated doping processes are performed at modest temperature and pressure with considerable flexibility of experimental conditions. This thesis (Chapter five) investigated the effect of SCF-mediated metal doping on the textural properties of zeolite templated carbons. Hydrogen storage capacity for Pd-doped and Pd-free carbons as a function of textural properties was analysed in an effort to determine effect of Pd-doping.

1.7.2 Carbon dioxide capture and storage

The use of fossil fuels is expected to increase worldwide as part of a diverse energy mix in 21st century²⁰⁰ with a corresponding rise in

greenhouse gases (i.e. CO₂, CO, SO₂ and NO_x) and especially CO₂ which is associated with global warming.^{168, 201} Strategies, such as CO₂ capture and storage, which help to reduce the global atmospheric concentration of greenhouse gases, can reverse this trend. To date, most commercial CO₂ capture use aqueous amine scrubbers.^{202, 203} However, regarding flue gases, these strategies need significant modification and this ultimately leads to high capital and running costs. Thus the development of low cost technologies is critical in providing a more cost and environmentally benign route to reduce CO₂ on a global scale.

In recent years, the development of solid adsorbents has been considered as one of the more promising technologies for efficient CO₂ capture.^{204, 205} A wide range of porous materials under investigation include supported amines,^{206, 207} immobilised amines,²⁰⁸ carbons,^{97, 204, 209, 210} zeolites (with or without surface modification)²¹¹ and inorganic-organic hybrid materials such as MOFs.²¹² For example, Siriwardane and co-workers reported that the CO₂ adsorption capacity for zeolite 13X, zeolite 4A and activated carbon was ca. 160, 135 and 110 mg/g-adsorbent respectively at 25 °C and 1 atmosphere CO₂ partial pressure.²¹³ However, the adsorption capacities rapidly decrease with increasing temperature making them unsuitable for practical use because many separations are operated at higher temperatures of up to ca. 150 °C.²⁰⁶

Among the wide range of porous sorbents under investigations for CO₂ capture and storage, carbon-based materials are considered to be most promising due to the low cost, high surface area, tuneable pore size among other textural properties. For example, Lu *et al*²¹⁴ and Zhao *et al*²¹⁵ independently reported a high CO₂ adsorption capacity of 3.13 and 2.90

mmol/g respectively for N-doped carbons. This demonstrates that high nitrogen content may result in enhanced CO₂ uptake. It is therefore of interest to explore materials (such as carbon aerogels) generated using nitrogen rich precursors. This thesis (Chapter seven) has studied the fabrication of carbon aerogels using a nitrogen rich precursor (melamine). In addition, the use of a metal salt as 'porogen' in the synthesis of carbon aerogels using nitrogen rich precursor is explored.

1.8 Bibliography

1. A. S. Arico, P. Bruce, B. Scrosati, J.-M. Tarascon and W. van Schalkwijk, *Nat Mater*, 2005, **4**, 366-377.
2. E. Serrano, G. Rus and J. García-Martínez, *Renewable and Sustainable Energy Rev.*, 2009, **13**, 2373-2384.
3. M. E. Davis, *Nature*, 2002, **417**, 813-821.
4. M. Fujita, Y. J. Kwon, S. Washizu and K. Ogura, *J. Am. Chem. Soc.*, 1994, **116**, 1151-1152.
5. J. S. Seo, D. Whang, H. Lee, S. I. Jun, J. Oh, Y. J. Jeon and K. Kim, *Nature*, 2000, **404**, 982-986.
6. Y. Xia and R. Mokaya, *Angew. Chem. Int. Ed.*, 2003, **42**, 2639-2644.
7. A. C. Dillon, K. M. Jones, T. A. Bekkedahl, C. H. Kiang, D. S. Bethune and M. J. Heben, *Nature*, 1997, **386**, 377-379.
8. C. Janiak, *Dalton Trans.*, 2003, 2781-2804.
9. R. Kitaura, S. Kitagawa, Y. Kubota, T. C. Kobayashi, K. Kindo, Y. Mita, A. Matsuo, M. Kobayashi, H.-C. Chang, T. C. Ozawa, M. Suzuki, M. Sakata and M. Takata, *Science*, 2002, **298**, 2358-2361.
10. O. M. Yaghi, M. O'Keeffe, N. W. Ockwig, H. K. Chae, M. Eddaoudi and J. Kim, *Nature*, 2003, **423**, 705-714.
11. A. Corma, *Chem. Rev.*, 1997, **97**, 2373-2420.
12. T. J. Barton, L. M. Bull, W. G. Klemperer, D. A. Loy, B. McEnaney, M. Misono, P. A. Monson, G. Pez, G. W. Scherer, J. C. Vartuli and O. M. Yaghi, *Chem. Mater.*, 1999, **11**, 2633-2656.
13. T. Kyotani, *Bull. Chem. Soc. Jpn.*, 2006, **79**, 1322-1337.
14. T. Kyotani, Z. Ma and A. Tomita, *Carbon*, 2003, **41**, 1451-1459.

15. T. Kyotani, T. Nagai, S. Inoue and A. Tomita, *Chem. Mater.*, 1997, **9**, 609-615.
16. R. Ryoo, S. H. Joo and S. Jun, *J. Phys. Chem. B*, 1999, **103**, 7743-7746.
17. F. Schüth and W. Schmidt, *Adv. Eng. Mater.*, 2002, **4**, 269-279.
18. Y. Xia, Z. Yang and R. Mokaya, *Nanoscale*, 2010, **2**, 639-659.
19. Z. X. Yang, Y. D. Xia and R. Mokaya, *Adv. Mater.*, 2004, **16**, 727-732.
20. Y. Mastai, S. Polarz and M. Antonietti, *Adva. Func. Mater.*, 2002, **12**, 197-202.
21. J. Rouquerol, D. Avnir, C. W. Fairbridge, D. H. Everett, J. M. Haynes, N. Pernicone, J. D. F. Ramsay, K. S. W. Sing and K. K. Unger, *Pure Appl. Chem.*, 1994, **66**, 1739 - 1758.
22. K. Ishizaki, S. Komarneni and M. Nanko, *Porous Materials - process technology and applications* Kluwer Academic Publishers, Boston, 1998.
23. K. S. W. Sing, D. H. Everett, R. A. W. Haul, L. Moscou, R. A. Pierotti, J. Rouquerol and T. Siemieniowska, *Pure Appl. Chem.*, 1985, **57**, 603-619.
24. K. Kaneko, *J. Membr. Sci.*, 1994, **96**, 59-89.
25. B. Zdravkov, J. Čermák, M. Šefara and J. Janků, *Cent. Eur. J. Chem.*, 2007, **5**, 385-395.
26. G. A. Ozin, A. C. Arsenault and L. Cademartini, *Nanochemistry : A Chemical Approach to Nanomaterials*, 2nd ed., RSC Publishing, Cambridge, UK, 2008.
27. F.-S. Xiao, S. Qiu, W. Pang and R. Xu, *Adv. Mater.*, 1999, **11**, 1091-1099.

28. A. K. Cheetham, G. Férey and T. Loiseau, *Angew. Chem. Int. Ed.*, 1999, **38**, 3268-3292.
29. C. Baerlocher, L. B. McCusker and D. H. Olson, *Atlas of Zeolite Framework Types (6th Edition)*, Elsevier Science & Technology, Amsterdam, NLD, 2007.
30. R. M. Barrer, *"Hydrothermal Chemistry of Zeolites"*, Academic Press, London, UK, 1982.
31. C. S. Cundy and P. A. Cox, *Chem. Rev.*, 2003, **103**, 663-702.
32. T. Wakihara and T. Okubo, *Chem. Lett.*, 2005, **34**, 276-281.
33. L. B. McCusker, F. Liebau and G. Engelhardt, *Pure Appl. Chem.*, 2001, **73**, 381 - 394.
34. R. M. Barrer and P. J. Denny, *J. Chem. Soc.*, 1961, 971-982.
35. A. Corma and M. E. Davis, *ChemPhysChem*, 2004, **5**, 304-313.
36. B. Gautier and M. Smaïhi, *New J. Chem.*, 2004, **28**, 457-461.
37. B. Zhang, S. A. Davis, N. H. Mendelson and S. Mann, *Chem. Commun.*, 2000, 781-782.
38. L. Huang, Z. Wang, J. Sun, L. Miao, Q. Li, Y. Yan and D. Zhao, *J. Am. Chem. Soc.*, 2000, **122**, 3530-3531.
39. S. van Donk, A. H. Janssen, J. H. Bitter and K. P. de Jong, *Catal. Rev. Sci. Eng.*, 2003, **45**, 297-319.
40. Z. Yang, PhD Thesis, The University of Nottingham, 2007.
41. S. Mintova and T. Bein, *Adv. Mater.*, 2001, **13**, 1880-1883.
42. I. Schmidt, C. Madsen and C. J. H. Jacobsen, *Inorg. Chem.*, 2000, **39**, 2279-2283.

43. I. Schmidt, A. Boisen, E. Gustavsson, K. Ståhl, S. Pehrson, S. Dahl, A. Carlsson and C. J. H. Jacobsen, *Chem. Mater.*, 2001, **13**, 4416-4418.
44. M. Yamamura, K. Chaki, T. Wakatsuki, H. Okado and K. Fujimoto, *Zeolites*, 1994, **14**, 643-649.
45. C. J. H. Jacobsen, C. Madsen, J. Houzvicka, I. Schmidt and A. Carlsson, *J. Am. Chem. Soc.*, 2000, **122**, 7116-7117.
46. C. T. Kresge, M. E. Leonowicz, W. J. Roth, J. C. Vartuli and J. S. Beck, *Nature*, 1992, **359**, 710-712.
47. J. S. Beck, J. C. Vartuli, W. J. Roth, M. E. Leonowicz, C. T. Kresge, K. D. Schmitt, C. T. W. Chu, D. H. Olson, E. W. Sheppard, S. B. McCullen, J. B. Higgins and J. L. Schlenker, *J. Am. Chem. Soc.*, 1992, **114**, 10834-10843.
48. F. Hoffmann, M. Cornelius, J. Morell and M. Fröba, *Angew. Chem. Int. Ed.*, 2006, **45**, 3216-3251.
49. T. Yanagisawa, T. Shimizu, K. Kuroda and C. Kato, *Bull. Chem. Soc. Jpn.*, 1990, **63**, 988-992.
50. Q. Huo, D. I. Margolese, U. Ciesla, P. Feng, T. E. Gier, P. Sieger, R. Leon, P. M. Petroff, F. Schuth and G. D. Stucky, *Nature*, 1994, **368**, 317-321.
51. Q. Huo, D. I. Margolese, U. Ciesla, D. G. Demuth, P. Feng, T. E. Gier, P. Sieger, A. Firouzi and B. F. Chmelka, *Chem. Mater.*, 1994, **6**, 1176-1191.
52. J. S. Beck, J. C. Vartuli, G. J. Kennedy, C. T. Kresge, W. J. Roth and S. E. Schramm, *Chem. Mater.*, 1994, **6**, 1816-1821.
53. P. T. Tanev and T. J. Pinnavaia, *Science*, 1995, **267**, 865-867.
54. S. A. Bagshaw, E. Prouzet and T. J. Pinnavaia, *Science*, 1995, **269**, 1242-1244.
55. K. J. Edler, A. Goldar, A. V. Hughes, S. J. Roser and S. Mann, *Microporous Mesoporous Mater.*, 2001, **44-45**, 661-670.

56. Q. Huo, D. Zhao, J. Feng, K. Weston, S. K. Buratto, G. D. Stucky, S. Schacht and F. Schüth, *Adv. Mater.*, 1997, **9**, 974-978.
57. C. Yu, J. Fan, B. Tian, D. Zhao and G. D. Stucky, *Adv. Mater.*, 2002, **14**, 1742-1745.
58. U. Ciesla and F. Schüth, *Microporous Mesoporous Mater.*, 1999, **27**, 131-149.
59. G. Kickelbick, *Angew. Chem. Int. Ed.*, 2004, **43**, 3102-3104.
60. B. Hatton, K. Landskron, W. Whitnall, D. Perovic and G. A. Ozin, *Acc. Chem. Res.*, 2005, **38**, 305-312.
61. S. Inagaki, S. Guan, Y. Fukushima, T. Ohsuna and O. Terasaki, *J. Am. Chem. Soc.*, 1999, **121**, 9611-9614.
62. S. Guan, S. Inagaki, T. Ohsuna and O. Terasaki, *J. Am. Chem. Soc.*, 2000, **122**, 5660-5661.
63. Y. Xia, W. Wang and R. Mokaya, *J. Am. Chem. Soc.*, 2005, **127**, 790-798.
64. T. Asefa, M. J. MacLachlan, N. Coombs and G. A. Ozin, *Nature*, 1999, **402**, 867-871.
65. J. M. Kim, S. Jun and R. Ryoo, *J. Phys. Chem. B*, 1999, **103**, 6200-6205.
66. R. Mokaya, *J. Phys. Chem. B*, 1999, **103**, 10204-10208.
67. E. Masika and R. Mokaya, *Chem. Mater.*, 2011, **23**, 2491-2498.
68. Y. Liu and T. J. Pinnavaia, *J. Mater. Chem.*, 2002, **12**, 3179-3190.
69. A. S. O'Neil, R. Mokaya and M. Poliakoff, *J. Am. Chem. Soc.*, 2002, **124**, 10636-10637.
70. D. Zhao, J. Feng, Q. Huo, N. Melosh, G. H. Fredrickson, B. F. Chmelka and G. D. Stucky, *Science*, 1998, **279**, 548-552.

71. S. C. Christiansen, D. Zhao, M. T. Janicke, C. C. Landry, G. D. Stucky and B. F. Chmelka, *J. Am. Chem. Soc.*, 2001, **123**, 4519-4529.
72. L.-Q. Wang and G. J. Exarhos, *J. Phys. Chem. B*, 2002, **107**, 443-450.
73. R. Mokaya, *Chem. Commun.*, 2001, 1092-1093.
74. Y. Xia, R. Mokaya and J. J. Titman, *J. Phys. Chem. B*, 2004, **108**, 11361-11367.
75. Y. Xia and R. Mokaya, *Microporous Mesoporous Mater.*, 2006, **94**, 295-303.
76. Y. Xia and R. Mokaya, *J. Phys. Chem. B*, 2006, **110**, 9122-9131.
77. J. C. Jansen, Z. Shan, L. Marchese, W. Zhou, N. von der Puil and T. Maschmeyer, *Chem. Commun.*, 2001, 713-714.
78. J. Wang, J. C. Groen and M. O. Coppens, *J. Phys. Chem. C*, 2008, **112**, 19336-19345.
79. J. Wang, J. C. Groen, W. Yue, W. Zhou and M. O. Coppens, *Chem. Commun.*, 2007, 4653-4655.
80. J. Wang, J. C. Groen, W. Yue, W. Zhou and M. O. Coppens, *J. Mater. Chem.*, 2008, **18**, 468-474.
81. J. Wang, W. B. Yue, W. Z. Zhou and M. O. Coppens, *Microporous Mesoporous Mater.*, 2009, **120**, 19-28.
82. A. D. Lueking and R. T. Yang, *Appl. Catal., A*, 2004, **265**, 259-268.
83. H.-J. Liu, X.-M. Wang, W.-J. Cui, Y.-Q. Dou, D.-Y. Zhao and Y.-Y. Xia, *J. Mater. Chem.*, 2010, **20**, 4223-4230.
84. M. A. de la Casa-Lillo, F. Lamari-Darkrim, D. Cazorla-Amorós and A. Linares-Solano, *J. Phys. Chem. B*, 2002, **106**, 10930-10934.

85. B. Weinberger and F. D. Lamari, *Int. J. Hydrogen Energy*, 2009, **34**, 3058-3064.
86. M. J. Illán-Gómez, A. García-García, C. Salinas-Martínez de Lecea and A. Linares-Solano, *Energy Fuels*, 1996, **10**, 1108-1114.
87. M. Sevilla, N. Alam and R. Mokaya, *J. Phys. Chem. C*, 2011, **114**, 11314 - 11319.
88. M. Sevilla, R. Foulston and R. Mokaya, *Energy Environ. Sci.*, 2010, **3**, 223-227.
89. M. Sevilla, R. Mokaya and A. B. Fuertes, *Energy Environ. Sci.*, 2011, **4**, 2930-2936.
90. M. A. Lillo-Ródenas, J. P. Marco-Lozar, D. Cazorla-Amorós and A. Linares-Solano, *J. Anal. Appl. Pyrolysis*, 2007, **80**, 166-174.
91. D. Lozano-Castelló, D. Cazorla-Amorós and A. Linares-Solano, *Fuel Process. Technol.*, 2002, **77-78**, 325-330.
92. J. A. Maciá-Agulló, B. C. Moore, D. Cazorla-Amorós and A. Linares-Solano, *Carbon*, 2004, **42**, 1367-1370.
93. E. Poirier, R. Chahine, P. Bénard, D. Cossement, L. Lafi, E. Mélançon, T. K. Bose and S. Désilets, *Appl. Phys. A*, 2004, **78**, 961-967.
94. H.-M. Cheng, Q.-H. Yang and C. Liu, *Carbon*, 2001, **39**, 1447-1454.
95. C. Liu, Y. Y. Fan, M. Liu, H. T. Cong, H. M. Cheng and M. S. Dresselhaus, *Science*, 1999, **286**, 1127-1129.
96. A. La Torre, G. A. Rance, J. El Harfi, J. Li, D. J. Irvine, P. D. Brown and A. N. Khlobystov, *Nanoscale*, 2010, **2**, 1006-1010.
97. Y. Xia, R. Mokaya, G. S. Walker and Y. Zhu, *Adv. Energy Mater.*, 2011, **1**, 678-683.
98. Y. Xia, G. S. Walker, D. M. Grant and R. Mokaya, *J. Am. Chem. Soc.*, 2009, **131**, 16493-16499.

99. Z. Yang, Y. Xia and R. Mokaya, *J. Am. Chem. Soc.*, 2007, **129**, 1673-1679.
100. N. Alam and R. Mokaya, *Energy Environ. Sci.*, 2010, **3**, 1773-1781.
101. Z. Ma, T. Kyotani, Z. Liu, O. Terasaki and A. Tomita, *Chem. Mater.*, 2001, **13**, 4413-4415.
102. Z. Ma, T. Kyotani and A. Tomita, *Chem. Commun.*, 2000, 2365-2366.
103. Y. Hanzawa, K. Kaneko, N. Yoshizawa, R. W. Pekala and M. S. Dresselhaus, *Adsorption*, 1998, **4**, 187-195.
104. R. W. Pekala, C. T. Alviso, F. M. Kong and S. S. Hulsey, *J. Non-Cryst. Solids*, 1992, **145**, 90-98.
105. R. W. Pekala, J. C. Farmer, C. T. Alviso, T. D. Tran, S. T. Mayer, J. M. Miller and B. Dunn, *J. Non-Cryst. Solids*, 1998, **225**, 74-80.
106. R. H. Baughman, A. A. Zakhidov and W. A. de Heer, *Science*, 2002, **297**, 787-792.
107. B. Sakintuna and Y. Yürüm, *Ind. Eng. Chem. Res.*, 2005, **44**, 2893-2902.
108. J. W. Patrick, ed., *Porosity in Carbons*, Edward Arnold, a division of Hodder, London, UK, 1995.
109. A. B. Fuertes, *J. Mater. Chem.*, 2003, **13**, 3085-3088.
110. J. H. Knox, B. Kaur and G. R. Millward, *J. Chromatogr. A*, 1986, **352**, 3-25.
111. R. Ryoo, S. H. Joo, M. Kruk and M. Jaroniec, *Adv. Mater.*, 2001, **13**, 677-681.
112. R. Srivastava, M. Choi and R. Ryoo, *Chem. Commun.*, 2006, 4489-4491.

113. Z. X. Yang, Y. D. Xia, X. Z. Sun and R. Mokaya, *J. Phys. Chem. B*, 2006, **110**, 18424-18431.
114. H. Nishihara, Q.-H. Yang, P.-X. Hou, M. Unno, S. Yamauchi, R. Saito, J. I. Paredes, A. Martínez-Alonso, J. M. D. Tascón, Y. Sato, M. Terauchi and T. Kyotani, *Carbon*, 2009, **47**, 1220-1230.
115. J. Rodriguez-Mirasol, T. Cordero, L. R. Radovic and J. J. Rodriguez, *Chem. Mater.*, 1998, **10**, 550-558.
116. J. Lee, S. Yoon, T. Hyeon, S. M. Oh and K. Bum Kim, *Chem. Commun.*, 1999, 2177-2178.
117. J. Lee, S. Yoon, S. M. Oh, C. H. Shin and T. Hyeon, *Adv. Mater.*, 2000, **12**, 359-362.
118. S. Jun, S. H. Joo, R. Ryoo, M. Kruk, M. Jaroniec, Z. Liu, T. Ohsuna and O. Terasaki, *J. Am. Chem. Soc.*, 2000, **122**, 10712-10713.
119. Y. Xia and R. Mokaya, *Adv. Mater.*, 2004, **16**, 1553-1558.
120. Y. Xia and R. Mokaya, *J. Phys. Chem. C*, 2007, **111**, 10035-10039.
121. C. J. Meyers, S. D. Shah, S. C. Patel, R. M. Sneeringer, C. A. Bessel, N. R. Dollahon, R. A. Leising and E. S. Takeuchi, *J. Phys. Chem. B*, 2001, **105**, 2143-2152.
122. F. Su, X. S. Zhao, L. Lv and Z. Zhou, *Carbon*, 2004, **42**, 2821-2831.
123. Z. Yang, Y. Xia and R. Mokaya, *Microporous Mesoporous Mater.*, 2005, **86**, 69-80.
124. J. Lee, S. Han and T. Hyeon, *J. Mater. Chem.*, 2004, **14**, 478-486.
125. J. Lee, J. Kim and T. Hyeon, *Adv. Mater.*, 2006, **18**, 2073-2094.
126. F. O. M. Gaslain, J. Parmentier, V. P. Valtchev and J. Patarin, *Chem. Commun.*, 2006, 991-993.

127. J.-S. Lee, S. H. Joo and R. Ryoo, *J. Am. Chem. Soc.*, 2002, **124**, 1156-1157.
128. C. du Fresne von Hohenesche, D. F. Schmidt and V. Schädler, *Chem. Mater.*, 2008, **20**, 6124-6129.
129. M. Mirzaeian and P. J. Hall, *Electrochimica Acta*, 2009, **54**, 7444-7451.
130. V. G. Pol, M. Motiei, A. Gedanken, J. Calderon-Moreno and M. Yoshimura, *Carbon*, 2004, **42**, 111-116.
131. J. Shen, J. Li, Q. Chen, T. Luo, W. Yu and Y. Qian, *Carbon*, 2006, **44**, 190-193.
132. L. Xu, J. Liu, J. Du, Y. Peng and Y. Qian, *Carbon*, 2005, **43**, 1560-1562.
133. R. W. Pekala, *J. Mater. Sci.*, 1989, **24**, 3221-3227.
134. C. S. Sharma, M. M. Kulkarni, A. Sharma and M. Madou, *Chem. Eng. Sci.*, 2009, **64**, 1536-1543.
135. S. S. Kistler, *J. Phys. Chem.*, 1931, **36**, 52-64.
136. G. Biesmans, A. Mertens, L. Duffours, T. Woignier and J. Phalippou, *J. Non-Cryst. Solids*, 1998, **225**, 64-68.
137. R. W. Pekala, C. T. Alviso, X. Lu, J. Gross and J. Fricke, *J. Non-Cryst. Solids*, 1995, **188**, 34-40.
138. K. J. Klabunde and R. M. Richards, eds., *Nanoscale Materials in Chemistry (2nd Edition)*, John Wiley & Sons Inc., Hoboken, NJ, USA, 2009.
139. J. Shen, J. Hou, Y. Guo, H. Xue, G. Wu and B. Zhou, *J. Sol-Gel Sci. Technol.*, 2005, **36**, 131-136.
140. N. Job, A. Théry, R. Pirard, J. Marien, L. Kocon, J.-N. Rouzaud, F. Béguin and J.-P. Pirard, *Carbon*, 2005, **43**, 2481-2494.

141. M. Wu, Q. Zha, J. Qiu, Y. Guo, H. Shang and A. Yuan, *Carbon*, 2004, **42**, 205-210.
142. C. Guan, K. Wang, C. Yang and X. S. Zhao, *Microporous Mesoporous Mater.*, 2009, **118**, 503-507.
143. C. Portet, M. A. Lillo-Rodenas, A. Linares-Solano and Y. Gogotsi, *Phys. Chem. Chem. Phys.*, 2009, **11**, 4943-4945.
144. Y. Guo, S. Yang, K. Yu, J. Zhao, Z. Wang and H. Xu, *Mater. Chem. Phys.*, 2002, **74**, 320-323.
145. K. Okada, N. Yamamoto, Y. Kameshima and A. Yasumori, *J. Colloid Interface Sci.*, 2003, **262**, 179-193.
146. L. Wang and R. T. Yang, *Energy Environ. Sci.*, 2008, **1**, 268-279.
147. V. V. Bhat, C. I. Contescu and N. C. Gallego, *Nanotechnology*, 2009, **20**, 204011.
148. A. Lueking and R. T. Yang, *J. Catal.*, 2002, **206**, 165-168.
149. L. Wang and R. T. Yang, *J. Phys. Chem. C*, 2008, **112**, 12486-12494.
150. F. H. Yang, A. J. Lachawiec and R. T. Yang, *J. Phys. Chem. B*, 2006, **110**, 6236-6244.
151. X. Ye, Y. Lin, C. M. Wang, M. H. Engelhard, Y. Wang and C. M. Wai, *J. Mater. Chem.*, 2004, **14**, 908-913.
152. X. R. Ye, Y. Lin and C. M. Wai, *Chem. Commun.*, 2003, 642-643.
153. B. M. Knudsen, N. R. P. Harris, S. B. Andersen, B. Christiansen, N. Larsen, M. Rex and B. Naujokat, *Atmos. Chem. Phys.*, 2004, **4**, 1849 - 1856.
154. J. A. Darr and M. Poliakoff, *Chem. Rev.*, 1999, **99**, 495-542.

155. G. P. Jessop and W. Leitner, eds., *Chemical Synthesis Using Supercritical Fluids*, Wiley-VCH, Weinheim, 1999.
156. D. Reinhardt, F. Ilgen, D. Kralisch, B. König and G. Kreisel, *Green Chem.*, 2008, **10**, 1170-1181.
157. A. Baiker, *Chem. Rev.*, 1998, **99**, 453-474.
158. P. G. Jessop, T. Ikariya and R. Noyori, *Chem. Rev.*, 1999, **99**, 475-494.
159. F. Cansell, B. Chevalier, A. Demourgues, J. Etourneau, C. Even, V. Pessey, S. Petit, A. Tressaud and F. Weill, *J. Mater. Chem.*, 1999, **9**, 67-75.
160. D. W. Breck, *Zeolite Molecular Sieves*, Wiley & Sons, New York, 1974.
161. Y. Wei, Q. Feng, J. Xu, H. Dong, K. Y. Qiu, S. A. Jansen, R. Yin and K. K. Ong, *Adv. Mater.*, 2000, **12**, 1448-1450.
162. N. Alam and R. Mokaya, *J. Mater. Chem.*, 2008, **18**, 1383-1391.
163. J. García-Martínez, D. Cazorla-Amorós, A. Linares-Solano and Y. S. Lin, *Microporous Mesoporous Mater.*, 2001, **42**, 255-268.
164. Y. Xia and R. Mokaya, *J. Phys. Chem. B*, 2003, **107**, 6954-6960.
165. Y. Xia and R. Mokaya, *J. Mater. Chem.*, 2003, **13**, 3112-3121.
166. K. Richard Klotstra and J. C. Jansen, *Chem. Commun.*, 1997, 2281-2282.
167. C. Vix-Guterl, E. Frackowiak, K. Jurewicz, M. Friebe, J. Parmentier and F. Béguin, *Carbon*, 2005, **43**, 1293-1302.
168. J. A. Turner, *Science*, 1999, **285**, 687-689.
169. G. W. Crabtree, M. S. Dresselhaus and M. V. Buchanan, *Phys. Today*, 2004, **57**, 39-44.

170. C.-J. Winter, *Int. J. Hydrogen Energy*, 2009, **34**, 1-52.
171. Fuel Cell Technologies Program Multi-Year Research, Development and Demonstration Plan, <http://www1.eere.energy.gov/hydrogenandfuelcells/mypp/>, Accessed 20/08/2012.
172. L. Schlapbach and A. Züttel, *Nature*, 2001, **414**, 353-358.
173. M. Armandi, B. Bonelli, C. O. Areán and E. Garrone, *Microporous Mesoporous Mater.*, 2008, **112**, 411-418.
174. A. W. C. van den Berg and C. O. Arean, *Chem. Commun.*, 2008, 668-681.
175. N. Texier-Mandoki, J. Dentzer, T. Piquero, S.-E. Saadallah, P. David and C. Vix-Guterl, *Carbon*, 2004, **24**, 2744-2747.
176. M. Bououdina, D. Grant and G. Walker, *Int. J. Hydrogen Energy*, 2006, **31**, 177-182.
177. T. Sun, H. Wang, Q. Zhang, D. Sun, X. Yao and M. Zhu, *J. Mater. Chem.*, 2011, **21**, 9179-9184.
178. M. Meggouh, D. M. Grant and G. S. Walker, *J. Phys. Chem. C*, 2011, **115**, 22054-22061.
179. L. Regli, A. Zecchina, J. G. Vitillo, D. Cocina, G. Spoto, C. Lamberti, K. P. Lillerud, U. Olsbye and S. Bordiga, *Phys. Chem. Chem. Phys.*, 2005, **7**, 3197-3203.
180. A. Zecchina, S. Bordiga, J. G. Vitillo, G. Ricchiardi, C. Lamberti, G. Spoto, M. Bjørgen and K. P. Lillerud, *J. Am. Chem. Soc.*, 2005, **127**, 6361-6366.
181. H. W. Langmi, D. Book, A. Walton, S. R. Johnson, M. M. Al-Mamouri, J. D. Speight, P. P. Edwards, I. R. Harris and P. A. Anderson, *J. Alloys Compd.*, 2005, **404-406**, 637-642.
182. H. W. Langmi, A. Walton, M. M. Al-Mamouri, S. R. Johnson, D. Book, J. D. Speight, P. P. Edwards, I. Gameson, P. A. Anderson and I. R. Harris, *J. Alloys Compd.*, 2003, **356-357**, 710-715.

183. A. G. Wong-Foy, A. J. Matzger and O. M. Yaghi, *J. Am. Chem. Soc.*, 2006, **128**, 3494-3495.
184. Y. Yan, X. Lin, S. Yang, A. J. Blake, A. Dailly, N. R. Champness, P. Hubberstey and M. Schroder, *Chem. Commun.*, 2009, 1025-1027.
185. D. J. Tranchemontagne, K. S. Park, H. Furukawa, J. Eckert, C. B. Knobler and O. M. Yaghi, *J. Phys. Chem. C*, 2012, **116**, 13143-13151.
186. H. K. Chae, D. Y. Siberio-Perez, J. Kim, Y. Go, M. Eddaoudi, A. J. Matzger, M. O'Keeffe and O. M. Yaghi, *Nature*, 2004, **427**, 523-527.
187. P. Chen, X. Wu, J. Lin and K. L. Tan, *Science*, 1999, **285**, 91-93.
188. X. B. Zhao, B. Xiao, A. J. Fletcher and K. M. Thomas, *J. Phys. Chem. B*, 2005, **109**, 8880-8888.
189. E. Terrés, B. Panella, T. Hayashi, Y. A. Kim, M. Endo, J. M. Dominguez, M. Hirscher, H. Terrones and M. Terrones, *Chem. Phys. Lett.*, 2005, **403**, 363-366.
190. Y. Gogotsi, C. Portet, S. Osswald, J. M. Simmons, T. Yildirim, G. Laudisio and J. E. Fischer, *Int. J. Hydrogen Energy*, 2009, **34**, 6314-6319.
191. M. Rzepka, P. Lamp and M. A. de la Casa-Lillo, *J. Phys. Chem. B*, 1998, **102**, 10894-10898.
192. Y. Gogotsi, R. K. Dash, G. Yushin, T. Yildirim, G. Laudisio and J. E. Fischer, *J. Am. Chem. Soc.*, 2005, **127**, 16006-16007.
193. G. Yushin, R. Dash, J. Jagiello, J. E. Fischer and Y. Gogotsi, *Adv. Funct. Mater.*, 2006, **16**, 2288-2293.
194. M. Sevilla, A. B. Fuertes and R. Mokaya, *Energy Environ. Sci.*, 2011, **4**, 1400-1410.
195. A. Pacula and R. Mokaya, *J. Phys. Chem. C*, 2008, **112**, 2764-2769.

196. C.-Y. Chen, J.-K. Chang, W.-T. Tsai and C.-H. Hung, *J. Mater. Chem.*, 2011, **21**, 19063-19068.
197. D. Giasafaki, A. Bourlinos, G. Charalambopoulou, A. Stubos and T. Steriotis, *Microporous Mesoporous Mater.*, 2012, **154**, 74-81.
198. T. Hasell, C. D. Wood, R. Clowes, J. T. A. Jones, Y. Z. Khimyak, D. J. Adams and A. I. Cooper, *Chem. Mater.*, 2009, **22**, 557-564.
199. C. Zlotea, F. Cuevas, V. r. Paul-Boncour, E. Leroy, P. Dibandjo, R. Gadiou, C. Vix-Guterl and M. Latroche, *J. Am. Chem. Soc.*, 2010, **132**, 7720-7729.
200. T. C. Drage, C. E. Snape, L. A. Stevens, J. Wood, J. Wang, A. I. Cooper, R. Dawson, X. Guo, C. Satterley and R. Irons, *J. Mater. Chem.*, 2012, **22**, 2815-2823.
201. D. M. D'Alessandro, B. Smit and J. R. Long, *Angew. Chem. Int. Ed.*, 2010, **49**, 6058-6082.
202. R. Steeneveldt, B. Berger and T. A. Torp, *Chem. Eng. Res. Des.*, 2006, **84**, 739-763.
203. G. T. Rochelle, *Science*, 2009, **325**, 1652-1654.
204. T. C. Drage, A. Arenillas, K. M. Smith, C. Pevida, S. Piippo and C. E. Snape, *Fuel*, 2007, **86**, 22-31.
205. J. D. Figueroa, T. Fout, S. Plasynski, H. McIlvried and R. D. Srivastava, *Int. J. Greenhouse Gas Control*, 2008, **2**, 9-20.
206. X. Xu, C. Song, J. M. Andresen, B. G. Miller and A. W. Scaroni, *Energy Fuels*, 2002, **16**, 1463-1469.
207. T. C. Drage, A. Arenillas, K. M. Smith and C. E. Snape, *Microporous Mesoporous Mater.*, 2008, **116**, 504-512.
208. P. J. E. Harlick and A. Sayari, *Ind. Eng. Chem. Res.*, 2006, **46**, 446-458.

- 209. C. Pevida, T. C. Drage and C. E. Snape, *Carbon*, 2008, **46**, 1464-1474.
- 210. C. Shen, J. Yu, P. Li, C. Grande and A. Rodrigues, *Adsorption*, 2011, **17**, 179-188.
- 211. G. Li, P. Xiao, P. Webley, J. Zhang, R. Singh and M. Marshall, *Adsorption*, 2008, **14**, 415-422.
- 212. A. Torrisi, R. G. Bell and C. Mellot-Draznieks, *Crystal Growth & Design*, 2010, **10**, 2839-2841.
- 213. R. V. Siriwardane, M.-S. Shen, E. P. Fisher and J. A. Poston, *Energy & Fuels*, 2001, **15**, 279-284.
- 214. G.-P. Hao, W.-C. Li, D. Qian and A.-H. Lu, *Adv. Mater.*, 2010, **22**, 853-857.
- 215. Q. Li, J. Yang, D. Feng, Z. Wu, Q. Wu, S. Park, C.-S. Ha and D. Zhao, *Nano Research*, 2010, **3**, 632-642.

2.0 Complementary Analytical techniques

Methods for the synthesis of nanostructured porous materials have received substantial attention in recent years. Simultaneously their characterisation has been extensively investigated in an attempt to fully appraise these nanostructures. To fully characterise the materials, a combination of chemical, structural and surface characterisation techniques are used. This chapter will provide a brief overview of the equipment and techniques used for the characterisation of the materials prepared during this research programme.

2.1 Powder X-ray diffraction (XRD) analysis

Powder XRD is an efficient and rapid analytical technique for revealing the structure of crystals i.e. it allows the identification and characterisation of unknown crystalline materials. Plotting the angular positions and intensities of the resultant peaks of radiation produces a pattern that is characteristic of the material. If different phases exist in a given material, then the resultant diffractogram is formed by the addition of individual patterns. Recent improvements in instrumentation and algorithm development coupled with greater computing power, have made this technique indispensable, increasingly more complex structures now being solved and/or identified.

X-rays are a form of energetic electromagnetic radiation of wavelength ca. $10^{-10} - 10^{-11}$ m, of comparable size to the spacing of atoms within a crystal, ca. 100pm.¹ They are produced when high-energy charged particles such as accelerated electrons collide with matter. A typical X-ray source consists of a metal target, often Cu which is bombarded with electrons with energy capable of ionizing some of the Cu 1s electrons. An electron in an outer shell (either 2p or 3p) then fills the vacant 1s level and the energy released

in the transition appears as X-radiation. The resultant 2p to 1s transition in Cu, referred to as Cu K α radiation, has a characteristic wavelength of 1.5418 Å and an energy of 8.04 keV.² The beam created by the X-ray generator strikes the sample and is diffracted and then detected by either photographic film or movable counter.

The most simplified explanation of X-ray principle was described by Bragg, in which a crystal structure is considered to consist of lattice planes, i.e. planes or families of parallel planes which intersect the crystal with 2D periodicity. The comparable size of the X-ray wavelength and the interplanar spacing (d) causes a crystal to diffract an X-ray passing through it. Diffracted radiation reflected from the surface of a crystalline material may be in phase, or out of phase which corresponds to constructive and destructive interference respectively, depending on the angle of incidence (θ) and interplanar spacing (see figure 2.1). The regular array of lattice points that make up the crystal structure provides the conditions for constructive interference that are described by Bragg's equation.³

$$n\lambda = 2d_{hkl}\sin\theta, \quad (\text{where } n = 1, 2, 3\dots)^3 \quad (1)$$

where λ is the X-ray wavelength, d_{hkl} is the lattice distance (hkl refers to Miller indices) and θ is Bragg's angle as illustrated in Figure.2.1.

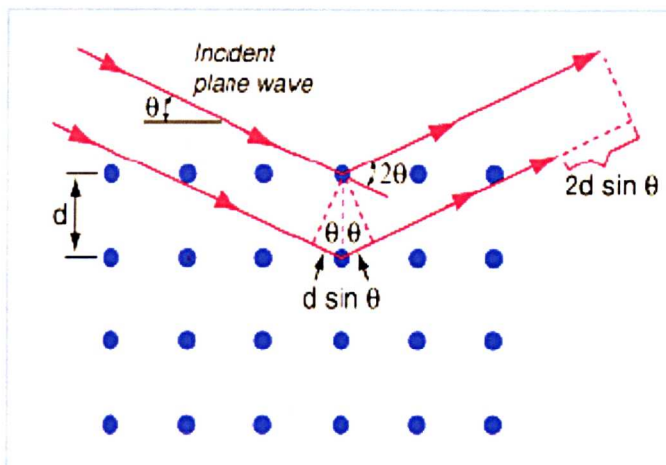


Figure 2.1 Diagram illustrating diffraction of X-rays from a crystal surface indicating the Bragg's law.

The intensity of diffracted X-rays will always be zero value except at those angles where Bragg's Law is satisfied with the strongest peak being assigned an intensity value of 100 and the others are scaled relative to this value. In addition, the scattered X-rays must be in phase and a reflection is observed. This only occurs at specific angles and it is dependent on the symmetry of the sample's crystal structure, as the symmetry and the unit cell dimensions will determine the number of different lattice planes and their separation. Therefore, the position (2θ value) of the peak is used for indexing the pattern which then allows the crystallographic structure of the material to be determined. Other information that can be determined from the data provided by XRD includes the size of the unit cell and interplanar spacing (d). Hence XRD analysis provides a characteristic fingerprint of a crystalline sample and in particular can be used to identify how atoms in the material pack as well as their inter-atomic distances and angles.

2.2 Nitrogen Physisorption

2.2.1 Nitrogen sorption isotherms

Nitrogen sorption is a routine technique used for the characterisation of porous (and nonporous) materials allowing measurements of specific surface area, pore size, pore size distribution (PSD), pore wall thickness (in combination with XRD) and pore volume. Data collection is achieved by exposing the sample in a closed space to a gas (Nitrogen) while recording adsorbed/desorbed gas as a function of the applied pressure. The adsorbed and desorbed amount of gas gives rise to adsorption and desorption isotherms respectively, whose shape is suggestive of the texture of the solid measured. The International Union of Pure and Applied Chemistry has categorised the physisorption isotherms according to Brunauer-Deming-Deming-Teller (BDDT) into six types (I to VI) as illustrated in Figure 2.2A, which corresponds to materials with different types of porosity.⁴

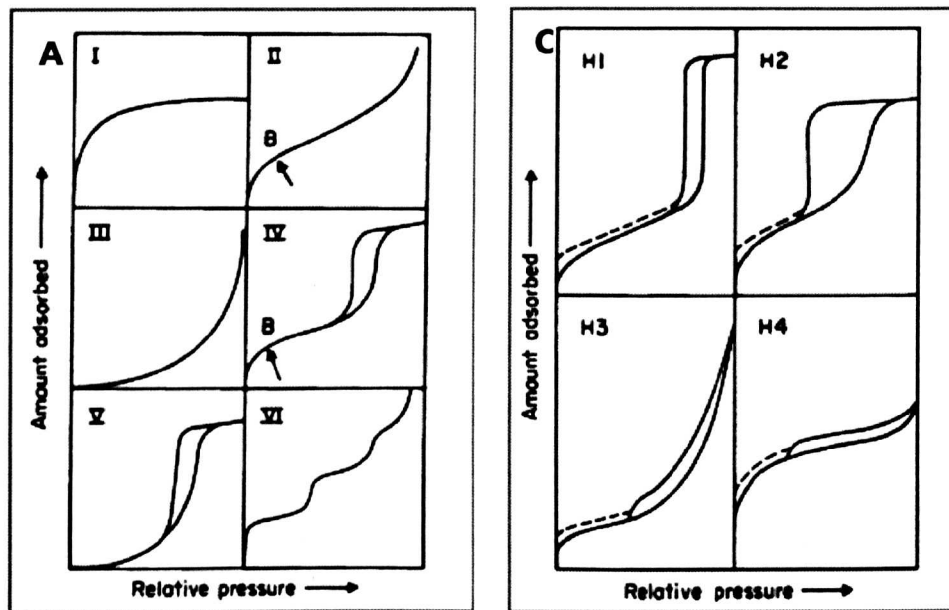


Figure 2.2 (A) The six types of adsorption and desorption isotherms, (B) point indicating the end of monolayer with simultaneous onset of multilayer coverage and (C) four types of hysteresis loops; H1 – typical for type iv isotherms, H2 – characteristic for 'ink-bottle' pores, H3 and H4 – for slit pores.⁴

The reversible Type I isotherms are characteristic of microporous materials such as zeolites with the adsorbed amount (n^a) approaching a limiting value as the relative pressure (P/P_0) approaches 1.0. Nanostructured and non-porous materials exhibit Type II isotherms, while Type III is suggestive of macroporous materials. Type III gives a gradual curvature and indistinct Point B, implying adsorbate-adsorbate interactions play an important role. Type IV, typically mesoporous materials, is characterised by the presence of hysteresis loop, which is associated with capillary condensation taking place in the mesopores. Type V isotherms are obtained with certain porous adsorbents in which the adsorbate-adsorbate interaction is weak. Type VI represents non-porous material which has uniform surface.⁴

Adsorption on mesoporous materials is achieved via surface monolayer adsorption of the adsorbate, then multilayer adsorption with onset at point B shown in Type IV isotherm, followed by capillary condensation. The desorption branch of the isotherm exhibits capillary evaporation that does not take place at the same pressure as capillary condensation resulting in isotherms with hysteresis loops. Hysteresis is typically attributed to thermodynamic or network effects or both.⁵ According to the IUPAC recommendations, adsorption-desorption loops are categorised in four types (denoted H1 – H4) as illustrated in Figure 2.2B.⁴ Given that hysteresis loops are related to adsorption and desorption mechanisms from particular pore shapes, textural properties including PSD, pore geometry and connectivity may be deduced from their shapes.^{4, 6} For example:

- Type H1 loop shows nearly vertical parallel lines and is characteristic of cylindrical pores with hexagonal or other well-

ordered pore geometries with a narrow PSD. These have been associated with porous materials known to consist of agglomerates.

- Type H2 is attributed to the presence of pores with narrow mouth (the so called “ink bottle” shaped pores).
- Type H3 does not level off at high P/P_0 and has been attributed to plate-like particles forming slit-like pores.
- Type H4 shows parallel but horizontal branches and this could be attributed to narrow slit-like pores. This loop may also show large mesopores in a micropore matrix.

2.2.2 Specific surface area (BET)

The Brunauer Emmett and Teller (BET) model is currently a standard in the determination of specific surface area. This model is based on a number of major assumptions; the key one being that the heats of adsorption for all the layers except the first one, are equal to the heat of condensation (evaporation).⁴ The BET surface area is calculated from a multilayer adsorption theory based on several assumptions and is derived from equation (2).⁴

$$\frac{P_s}{V_A (P_0 - P_s)} = \frac{1}{V_M C} + \left[\frac{C - 1}{V_M C} \right] * \frac{P_s}{P_0} \quad (2)$$

where V_A is the volume of the gas adsorbed, P_s is the pressure of the gas, P_0 is the saturation pressure at a given temperature (101.3kPa for N_2 at 77K), V_m is the volume equivalent of adsorbed monolayer and C is the constant related to the enthalpy of adsorption.

A specified partial pressure (P/P_0 0.02 – 0.25) range of the isotherm is selected and the isotherm data is used to calculate the BET surface area

from equation 2 which assumes straight shape in that partial pressure range ($y = mx \pm c$ where m and c are constants). The resultant straight line with m (slope) and c (y-intercept) correspond to $(C-1)/V_m C$ and $(1/V_m C)$ respectively. The BET surface area expressed in m^2/g is then determined from equation 3.

$$S_{\text{BET}} = \frac{V_M * N_A * A_M}{M_v} \quad (3)$$

where S_{BET} is the BET surface area, N_A is Avogadro's constant (6.02×10^{23}), A_M is the cross sectional area occupied by each adsorbed nitrogen molecule ($1.62 \times 10^{-1} \text{ nm}^2$) and M_v is the molar volume (22414 mL).

2.2.3 Pore volume, Pore size and Pore size distribution

The total pore volume is calculated from the amount adsorbed at a relative pressure close to the saturation vapour pressure when the pores are completely filled. By using the total quantity adsorbed, the density of condensed adsorbate and its total volume, the pore volume of the sample can be determined. For nitrogen at 77 K, the conversion factor from the amount adsorbed to the volume of liquid adsorbate is 0.0015468 at standard temperature and pressure (STP).

The thickness-plot (t -plot) method is used for the estimation of micropore volume and area, in which the volume of gas adsorbed, is plotted against the adsorbate molecular film thickness. The thickness of the film is calculated from either the Halsey equation⁷ (4) or Harkins and Jura equation⁸ (5).

$$t = \left[\frac{13.99}{\log \frac{P_o}{P_s} + 0.034} \right]^{\frac{1}{2}} \quad (4)$$

$$t = 3.54 \times \left[\frac{5}{2.303 \times \log \frac{P_o}{P_s}} \right]^{\frac{1}{3}} \quad (5)$$

where P_s is the sample pressure and P_o is the saturation pressure.

The t -plot data is used to calculate y -intercept which when converted from a gas volume to liquid volume results in micropore volume. The gradient of the linear section is used to determine the micropore volume and surface area based on equations (6) to (8).

$$V_{\text{micropore}} = (0.001547) \times (t\text{-plot intercept}) \quad (6)$$

$$S_{\text{mesopore}} = 1.547 \times (t\text{-plot slope}) \quad (7)$$

$$S_{\text{micropore}} = S_{\text{BET}} - S_{\text{mesopore}} \quad (8)$$

The pore size distribution (PSD) of a material can also be determined from the condensation within the narrow pores at a pressure less than the saturated vapour pressure of the adsorbate. The Kelvin equation equation (9) describes the relationship between the changes in vapour pressure above the interface of a liquid cylindrical capillary with its radius (r).⁵

$$\ln \frac{P}{P_o} = \frac{2\gamma V_M}{rRT} \quad (9)$$

where P is the sample vapour pressure, P_o is saturated vapour pressure, γ is surface tension, V_M is molar volume, R is universal gas constant (8.3145 J K⁻¹mol⁻¹), T is temperature and r is radius of droplet/meniscus.

For nitrogen adsorbed at 77 K, the following values may be used; $\gamma = 8.85 \text{ m Nm}^{-1}$, density = 0.807 g cm^{-3} , molecular mass = 28.01 g cm^{-3} and $V_m = 34.71 \text{ cm}^3 \text{ mol}^{-1}$ resulting in equation (10).⁵

$$\frac{r_k}{nm} = - \frac{0.415}{\log_{10}(P/P_0)} \quad (10)$$

where r_k is Kelvin radius, P and P_0 are sample and saturated pressure respectively.

However, the Kelvin equation cannot be used directly to calculate the pore size as it does not take into account that adsorption within mesoporous materials occurs via multilayer adsorption followed by capillary condensation. The Barrett, Joyner and Halenda method (BJH) is based on the Kelvin equation and can be applied to calculated PSD with the assumptions that the pores are cylindrical and the equilibrium between the gas phase and adsorbed phase during desorption occurs via two possible mechanisms: (i) by physisorption on the pore walls and (ii) adsorbate-adsorbate capillary condensation within the inner capillary volume. At P_0 all the pores are saturated, on decreasing pressure to P_1 capillary evaporation and a reduction of layer thickness occurs in the largest pore. On further decreasing pressure to P_2 , capillary evaporation occurs in the second largest pore with simultaneous reduction of layer thickness in both pores, this process occurs repeatedly until all the pores are empty. Based on this idea the BJH equation is developed where the first term on the right hand side of equation (11) is capillary evaporation and the second term describes the correction term.

$$V_{pn} = \frac{r_{pn}^2}{(r_{kn} + \Delta t_n)^2} \cdot \Delta V_n - \frac{r_{pn}^2}{(r_{kn} + \Delta t_n)^2} \cdot \Delta t_n \cdot \sum_{j=1}^{n-1} \frac{r_{pj} - t_j}{r_{pj}} A_{pj} \quad (11)$$

where V_{pn} is pore volume corresponding to the n^{th} desorption step; r_{pn} is pore radius corresponding to n^{th} desorption step; r_{kn} is inner capillary radius (Kelvin radius) corresponding to n^{th} desorption step; Δt_n is reduction in thickness of the adsorbed layer corresponding to n^{th} desorption step; ΔV_n is desorption volume of adsorbed gas corresponding to n^{th} desorption step; t is thickness of adsorbed layer on the pore surface; A_p is area of each pore given by ($A_p = 2V_p/r_p$).

For each desorption step, the average diameter of the pore which undergoes capillary condensation is calculated from Kelvin equation and t -plot equation:

$$r_p = r_k + t \quad (12)$$

where r_p is average pore radius, r_k is inner capillary (Kelvin radius) and t is thickness of adsorbed layer on the pore surface.

$$\log \frac{P}{P_0} = 0.034 - \frac{13.99}{t^2} \quad (13)$$

where t is thickness of adsorbed layer on the pore surface, P is vapour pressure and P_0 is saturation pressure.

$$\log \frac{P}{P_0} = \frac{-4.14}{r_k} \quad (14)$$

where r_k is inner capillary radius (Kelvin radius), P is sample pressure and P_0 is saturation pressure.

2.3 Thermogravimetric Analysis (TGA)

TGA is based on the very simple principle of monitoring the change in weight of a sample as the temperature is varied.⁹ The heating of a sample is usually done in an inert or oxidising atmosphere, the resultant weight changes over specific temperature ranges providing an indication of the composition of the sample and thermal stability. The changes in temperature can be programmed to include heating or cooling at a specified rate, which can be fixed or varied and/or having an isotherm. Thus, a tailored temperature program can be designed to specifically test the material and the environment can be controlled by varying the atmosphere (argon, nitrogen or air) under either static or flow conditions.

While the changes in mass can be linked to a particular thermal event, such as oxidation, or loss of water of crystallisation, the step size on a curve can easily be used for quantitative analysis. However, for more complex thermograms or when changes are subtle, Differential Thermal Analysis (DTA), i.e. the first derivative of the weight loss can be valuable in interpretation.

The simultaneous use of TGA/DTA is advantageous and can be used for determining properties such as oxidation, heat resistance, the amount of water, compositional analysis and ash content in a sample.

2.4 Temperature programmed desorption (TPD) of cyclohexylamine

Acidity was measured using established procedures in which thermally programmed desorption of cyclohexylamine is used.¹⁰ The method involves thermogravimetric analysis following adsorption of the base on the catalysts. The number of acid sites capable of interacting with the base after heat treatment at either 80 or 250 °C was thus determined. In a

typical analysis the sample is exposed to liquid cyclohexylamine at room temperature and kept overnight. One half of the sample is then put in an oven at 80 °C for 2 h to allow the base to permeate the sample. The remaining half is transferred to an oven at 250 °C for 2 h. Thermal treatment at 250 °C removes the base from the weak acid sites and is therefore performed to determine the population of the medium and strong acid sites.

TGA curves are then obtained for the cyclohexylamine containing samples thermally pre-treated at either 80 or 250°C. The weight loss associated with desorption of the base from acid sites (between 280 and 450°C) is used to calculate the acid content in mmol of cyclohexylamine per gram of the sample, assuming that each mole of cyclohexylamine corresponds to one mol of the protons (H⁺).^{11, 12} The following equation is used to calculate the acid content:

$$Acidity = \left(\frac{M_{280} - M_{450}}{M_{280}} \right) * \frac{1000}{99.18} \text{ mmol/g} \quad (15)$$

where M_{280} and M_{450} is the percentage mass at 280 and 450 °C respectively, and 99.18 is the molecular mass of cyclohexylamine in g/mol.

2.5 Elemental analysis by X-ray fluorescence (XRF)

XRF is a non-destructive technique that is widely used for quantitative and elemental analysis of materials. The technique works on the principles of characteristic X-rays being emitted from transitions involving K and L electrons.⁹ This transition gives off an X-ray of fixed characteristic energy that can be detected by a fluorescence detector. Because each element has a unique set of energy levels, each element therefore produces X-rays at a unique set of energies, allowing a non-destructive determination of the elemental composition of the sample.

Typically the lightest element that can be analysed is Be ($Z=4$), but due to instrumental limitations and low X-ray yields for light elements, it is often difficult to quantify elements lighter than sodium ($Z=11$). The instrument in an XRF machine and its set up is able to measure minute shifts in the position and the strength of the aluminium band in the spectrum. The associated computer software is pre-calibrated to show Si/Al ratios directly but repeat readings are taken to improve the accuracy of the results.

The fluorescent radiation can then be analysed based either on the energies of the photons (energy-dispersive analysis) or by sorting out the wavelengths of the radiation (wavelength-dispersive analysis). The separated intensities are typical characteristic radiation for a given element and the radiation is directly related to the amount of each element in a material.

2.6 Fourier Transform Infrared (FTIR) Spectroscopy

The Infrared region broadly refers to that part of the electromagnetic spectrum between the visible and microwave regions. However, mid-infrared radiation with wavenumber range of 4000 and 400 cm^{-1} (30 – 2.5 μm) is generally used in this spectroscopic analysis due to the presence of characteristic vibrational modes.¹³ Such bands provide useful structural information by simple inspection and reference to the generalised charts of characteristic group frequencies. Thus utilisation of IR spectra in conjunction with other spectral data is a useful tool for determining molecular structure. This technique is based on the possibility of separating the energies of a molecule into three additive components associated with the rotation of the molecule as a whole, the vibration of the constituent atoms and finally, the electrons in a molecule.¹⁴

Conventionally, if a molecule of the material under investigation is placed in an electromagnetic field, for instance light, a transfer of energy from the molecule will occur in accordance to Bohr's frequency equation (16). The resultant signal (interferogram) is usually converted from time-domain to frequency-domain via Fourier Transform.

$$\Delta E = h\nu \quad (16)$$

where ΔE is the difference between two quantized states, h is Planck's constant and ν is the frequency of the light.

The frequency or wavelength of absorption is dependent on the relative masses of atoms, the force constant of bonds and the geometry of the atoms. Assignment of frequencies can be approximated by application of Hooke's Law in which two atoms and their connecting bonds are treated as a simple harmonic oscillator consisting of two masses joined by a spring. This is represented in equation (17), derived from Hooke's Law.¹³

$$\bar{\nu} = \frac{1}{2\pi c} \sqrt{\frac{f}{(M_x M_y)/(M_x + M_y)}} \quad (17)$$

where $\bar{\nu}$ is the vibrational frequency (cm^{-1}), c is the velocity of light (cm/s), f is the bond force constant (dyne/cm), M_x and M_y refers to mass of atom x and atom y respectively. The force constant can be thought as a measure of bond "stiffness" which correlates with properties such as bond order and bond strength.

2.7 Nuclear Magnetic Resonance Spectroscopy

Nuclear magnetic spectroscopy (NMR) technique is now regarded as a standard tool for probing the structure of compounds and also in obtaining more information such as oxidation states, co-ordination number and bond

angles in a static magnetic field.¹⁵ The signal multiplicity and internal ratios are pivotal in the identification of the structures of pure crystalline materials. The remarkably high resolution spectra especially for carbon and hydrogen are attributed to the use of high speed magic-angle spinning (MAS) and multidimensional NMR.¹⁵

Typically, MAS-NMR is used to perform experiments in solid-state materials. This is because of the elimination of anisotropic effects such as dipole – dipole interactions between the magnetic moments of nearby nuclei which lead to broadening in the spectra. For such interactions, a physical rotation of the macroscopic sample around an axis inclined at an angle of 54.74°, the so-called magic angle, to the external field is required. The mobility of the nuclei in liquid samples also creates an averaging process, leading to an intrinsic elimination of line broadening related to dipolar interactions. In addition, a wide variety of radio frequency patterns allows decoupling of interactions in spin space. In this technique the spinning speed is critical in increasing the MAS frequency in order to obtain narrowed lines of the spectra.

²⁷Al and ²⁹Si solid state NMR spectroscopy are very useful techniques in studying position of Al ions and condensation of siloxane units respectively. Also, the latter technique is used in the identification of the structure of silica, silicate and organo-silica compounds. They are classified according to the number of oxygen atoms that are grouped around the silicon core. The silicon atom can form four siloxane bridges whereby mono-, di-, tri- and tetra-substitution are named with letters M, D, T and Q respectively allowing measurement and comparison of the local structures of the network forming cation Si⁴⁺ (i.e. Qⁿ groups). In which n represents the number of oxygen atoms, linked to the silicon that are hydroxyl group(s).

Due to different chemical environment, namely: $\text{Si}(\text{OH})_2(\text{OR})_2$, $\text{Si}(\text{OH})_1(\text{OR})_3$ and $\text{Si}(\text{OR})_4$ designated Q^2 , Q^3 and Q^4 respectively, each type of the silicon shows a distinctive peak in a specific ppm range.

2.8 Electron Microscopy

Electron microscopy makes use of a beam of highly energetic electrons to examine materials on a very fine scale. In this thesis, scanning electron microscopy and transmission electron microscopy have been used to characterise the prepared porous materials. SEM is mainly used to obtain images of external morphology, quite similar to those formed by the eye. In contrast, TEM probes the internal structure of solids and gives access to microstructural or ultra-structural details.³

2.8.1 Scanning Electron Microscopy

A scanning electron microscope operates by accelerating a fine beam of electrons (incident beam) ca. $1.0\ \mu\text{m}$ in diameter onto a sample mounted within a vacuum, specifically by scanning across the sample using scan coils. When a focused beam of electrons is incident on a thick specimen, it will be scattered many times until it effectively comes to rest. The strength of scattering depends on its atomic number and is usually described in terms of its atomic scattering factor, f .³ A number of signals are produced including secondary electrons (SE), backscattered electrons (BSE) and X-rays of which the first two can be collected by special detectors to form SEM images.

The most widely used signal in SEM is that from SE (10 eV- 50 eV). Due to their low energy, only the SE near the surface (<10 nm) can exit from the specimen making it possible to investigate the topography of the surface features of the sample. Meanwhile, BSE imaging shows the spatial distribution of the elements or compounds with the surface of the sample.

BSE are not usually as numerous as SE but most of them carry very high energies and because of this they are able to escape from deeper within the interaction volume.

X-rays, which are also produced by the interaction of electrons with the sample, may also be detected in an SEM equipped with energy-dispersive or wave-length dispersive X-ray spectroscopic detector (EDX). The emitted X-rays, after excitation on bombardment with high energy electrons, possess elemental characteristic energies as the atoms return to their ground state. However, this technique has limitations. It cannot detect elements with atomic number lower than that of carbon and also X-rays of similar energies such as nitrogen and oxygen result in overlapping spectra.

2.8.2 Transmission Electron Microscopy

In transmission electron microscopy, electrons are transmitted through the sample (typically < 100 nm thick), including elastic, inelastic and unscattered electrons. Thus when an electron beam emerges from the sample, it carries information about its structure. The obtained spatial variation information is viewed by projecting the magnified electron image onto a fluorescent viewing screen coated with phosphor/scintillator material such as zinc sulphide or a charged couple device (CCD).³ Images can be recorded on photographic film or digitised to be stored on computer.

Resolution of TEM is inherently limited primarily by spherical aberration. However, a new generation of aberration correctors have been able to partially overcome spherical aberration to increase its resolution. For example, development of high resolution TEM (HRTEM) has allowed processing of images with resolution below 5 nm at magnifications above 50 million times.¹⁶

Images in TEM can be obtained either by using directly transmitted or scattered electrons. The regions imaged with the transmitted beam are termed as bright field (BF), while those obtained by aligning a diffracted beam down the optic axis of the microscope are referred to as dark field (DF) as illustrated in Figure 2.3.¹⁷

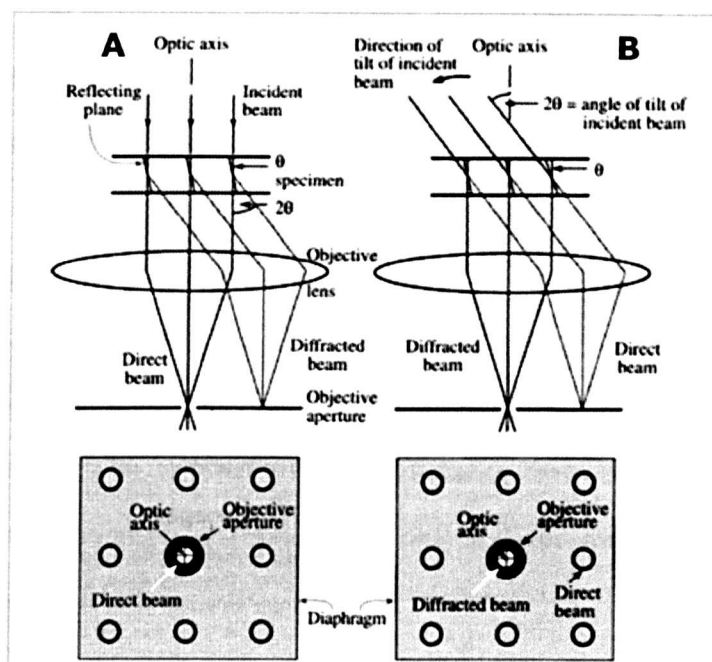


Figure 2.3 Schematic illustrations for the formation of (A) a bf diffraction contrast image using directly transmitted beam and (B) a DF diffraction contrast image, with the incident beam titled so that the scattered beam remains on the optic axis.¹⁷

There are three modes of contrast in TEM images, namely: (i) mass thickness contrast, e.g. in amorphous samples, thick regions of the sample and areas with a higher atomic number appear dark, (ii) diffraction contrast, e.g. low index crystalline orientations of crystalline samples that satisfy Bragg's diffraction also appear dark and (iii) phase contrast, this is if the objective aperture is removed resulting in formation of images with

contrast arising from constructive and destructive interference of electron waves.

2.9 Gas adsorption

Physical adsorption of a gas on a solid substrate can be described in terms of enrichment of gaseous molecules at the interface between the solid surface and the gas phase. This process is governed by a combination of attractive dispersive (or Van der Waals) interactions and short-range repulsive interactions between the adsorbent and the adsorbate. These forces arise from fluctuations in the electron density of one atom which then induces another atom with order of magnitude in the range of between 1.0 and 10.0 kJ/mol, which is approximately ten times lower than for chemisorption.¹⁸ Figure 2.4 shows the potential energy curves for a hydrogen molecule as a function of the distance from the adsorbent, both for dissociative adsorption (chemisorption) and for molecular adsorption (physisorption).^{5, 19}

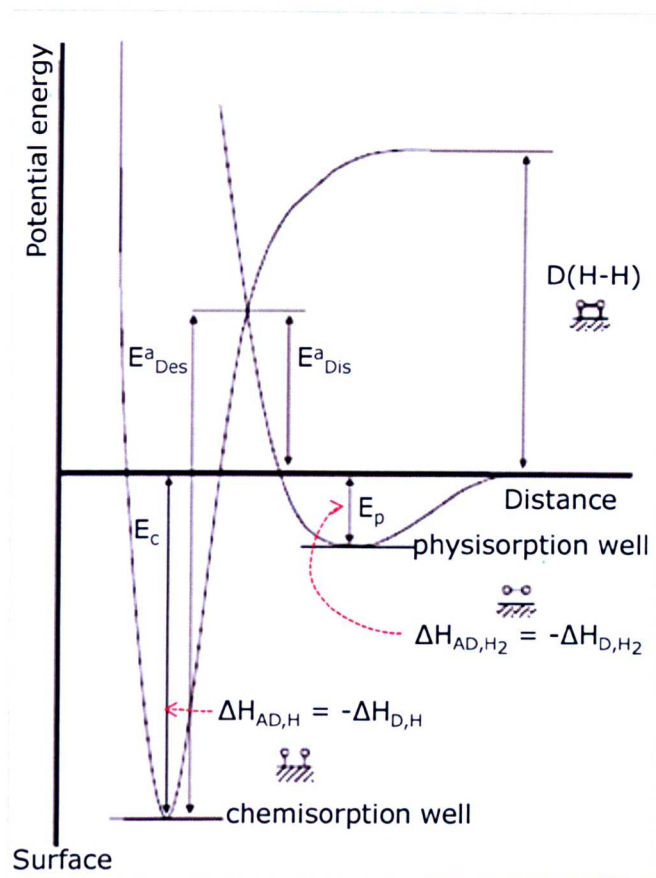


Figure 2.4 Potential energy curve for chemisorbed and physisorbed hydrogen as a function of the distance from the adsorbent surface with the two minima curves corresponding to equilibrium distances for chemisorbed (E_c) physisorbed (E_p).¹⁹

In physisorption there is no energy barrier to prevent the molecule approaching the surface from entering the E_p well. This implies that if no diffusional barriers are presents, then this process is non-activated and therefore physical adsorption is characterised by fast kinetics. However, in order for the hydrogen molecule to enter into chemisorbed atomic state, it must overcome activation energy barrier, E^a_D is formed at the crossing of physisorption and chemisorption curves as illustrated in Figure 2.4. Based on the fast kinetics, this thesis explores physisorption of hydrogen and carbon dioxide on porous carbons. Hydrogen is currently being studied

intensively as an alternative energy carrier. This is because hydrogen is considered environmentally benign. While the current intensive research on carbon dioxide capture and storage is tailored towards prevention of CO₂ concentration in the atmosphere rising to unacceptable levels.

2.10 Bibliography

1. B. E. Warren, *X-ray Diffraction*, Dover, New York, 1990.
2. B. D. Cullity, *Elements of X-ray Diffraction, 2nd Edition*, Addison-Wesley Publishing Company, Inc., London, UK, 1978.
3. P. J. Goodhew, F. J. Humphreys and R. Beanland, *Electron Microscopy and Analysis*, Taylor & Francis, London, GBR, 2000.
4. K. S. W. Sing, D. H. Everett, R. A. W. Haul, L. Moscou, R. A. Pierotti, J. Rouquerol and T. Siemieniewska, *Pure Appl. Chem.*, 1985, **57**, 603-619.
5. F. Rouquerol, J. Rouquerol and K. S. W. Sing, *Absorption by Powders and Porous Solids*, Academic Press, London, GBR, 1998.
6. M. Kruk and M. Jaroniec, *Chem. Mater.*, 2001, **13**, 3169-3183.
7. G. Halsey, *J. Chem. Phys.*, 1948, **16**, 931-937.
8. W. D. Harkins and G. Jura, *J. Am. Chem. Soc.*, 1944, **66**, 1362-1366.
9. F. W. Fifield and G. Kealey, *Principles and Practice of Analytical Chemistry, 4th Edition*, Blackie Academic and Professional; an Imprint of Chapman and Hall, Glasgow, UK, 1995.
10. R. Mokaya, *Angew. Chem. Int. Ed.*, 1999, **38**, 2930-2934.
11. R. Mokaya, *J. Catal.*, 2000, **193**, 103-107.
12. R. Mokaya, W. Jones, S. Moreno and G. Poncelet, *Catal. Lett.*, 1997, **49**, 87-94.
13. R. M. Silverstein, F. X. Webster and D. J. Kiemle, *Spectroscopic Identification of Organic Compounds, 7th Edition*, Wiley, Hoboken, NJ, USA, 2005.
14. K. Nakamoto, *Infrared and Raman Spectra of Inorganic and Coordination Compounds, Theory and Applications in Inorganic Chemistry*, Wiley, Hoboken, NJ, USA, 2009.

15. M.-M. Titirici, R. J. White, C. Falco and M. Sevilla, *Energy Environ. Sci.*, 2012, **5**, 6796-6822.
16. D. B. Williams and C. B. Carter, *Transmission electron microscopy : a textbook for materials science, 2nd edition*, Springer Science+Business Media, 2009.
17. C. Binns, *Introduction to Nanoscience and Nanotechnology*, Wiley, Hoboken, NJ, USA, 2010.
18. A. Züttel, *Naturwissenschaften*, 2004, **91**, 157-172.
19. G. Attard and C. Barnes, *Surfaces*, Oxford University Press, Oxford, 1998.

3.0 Experimental methodology

The aim of this chapter is to introduce and explain the experimental pathways followed in the preparation of the study materials and describe the protocols for the analytical techniques used to characterise the prepared materials.

3.1 Introduction

The experimental procedures used for the synthesis, modification and characterisation of the nanostructured porous materials presented in this thesis are described in this chapter. Section 3.2 covers the hydrothermal methods used for the synthesis of porous aluminosilicates, and provides details of the equipment, chemical precursors and conditions of the experimental procedures. Section 3.2 also describes the methods used to assess hydrothermal stability of the porous aluminosilicates. Section 3.3 describes nanocasting procedures and focuses on the use of zeolites as hard templates for the fabrication of porous carbons. Section 3.4 outlines the procedure for incorporation of palladium nanoparticles into zeolite templated carbons to generate Pd-doped carbons.

Section 3.5 describes a two-step templating method that combines Liquid Impregnation (LI) and chemical vapour deposition (CVD) in an attempt to prepare high surface area carbons. Section 3.6 describes a chemical activation technique used to modify carbon aerogels. Finally, section 3.7 provides details of the techniques used for chemical, structural and surface characterisation and gas sorption measurements of the study materials.

3.2 Hydrothermal synthesis technique (HS)

Nucleation of precipitates from an aqueous precursor solution is the ultimate stage in the reaction stages of HS, apart from induction period and crystal growth. Therefore, the whole process of HS can most

adequately be described as a mechanism based on the solution-mediation model with or without having a visible liquid phase. Consequently, this section will provide a detailed stepwise procedure for the synthesis of porous aluminosilicates. To enhance preparation of consistent reaction products, a standard 200 ml capacity stainless steel pressure autoclave lined with Teflon autoclave was used in all the reactions.

3.2.1 Chemicals

The following chemicals were used as supplied: Sodium hydroxide (NaOH) from Fisher Scientific, aluminium isopropoxide (AIP) 98+% from Aldrich, tetraethyl ammonium hydroxide (TEAOH) 20 wt% in water from Sigma-Aldrich and tetraethyl orthosilicate $\geq 98.0\%$ from Fluka.

3.2.2 Synthesis of porous aluminosilicates

The aim of this part of the thesis was to prepare mesoporous aluminosilicates from recipes that are typically used for the synthesis of zeolite BEA. In a typical synthesis¹, 0.3 g of NaOH and 2.7 g of aluminium isopropoxide were dissolved in 33 mL of water by stirring at room temperature, followed by addition of 71 g of tetraethyl orthosilicate and 84 g of tetraethyl ammonium hydroxide (20 wt% in water) to give a gel of molar composition $0.57 \text{ NaOH} : 9 \text{ TEAOH} : \text{Al} : 25 \text{ Si} : 420 \text{ H}_2\text{O}$, which was placed in a Teflon-lined autoclave and heated at 100 °C for 8 days. The solid product was obtained, without washing, by drying in a fume hood under atmospheric conditions and then either directly calcined in static air at 550 °C for 4 h, or washed (stirred) in boiling water for 3 or 5 h and dried before calcination. The synthesis scheme is shown in Figure 3.1. The sample prepared and calcined directly without washing was designated as MZBN-x (where x is the aging temperature). Three samples were washed (stirred) in boiling water before calcination and designated as follows: MZBN-xw3h (washed in 200 ml water for 3 h); MZBN-xw3hd (washed in

[75]

100 ml water for 3 h) and MZBN-xw5h (washed in 200 ml water for 5 h). Five more sets of samples were prepared as described above but at crystallisation temperature of 25, 50, 80, 135 and 150 °C in order to elucidate the effect of crystallization temperature on the properties of the materials. The direct calcination and washing/calcination regime was as described above. The sample prepared at 100 °C and its derivatives are herein denoted as MZBN-100 for calcined without washing, MZBN-w3h for washed for 3h in 200 ml water, MZBN-w3hd for washed for 3h in 100 ml water and MZBN-w5h for washed for 5 h in 200 ml water.

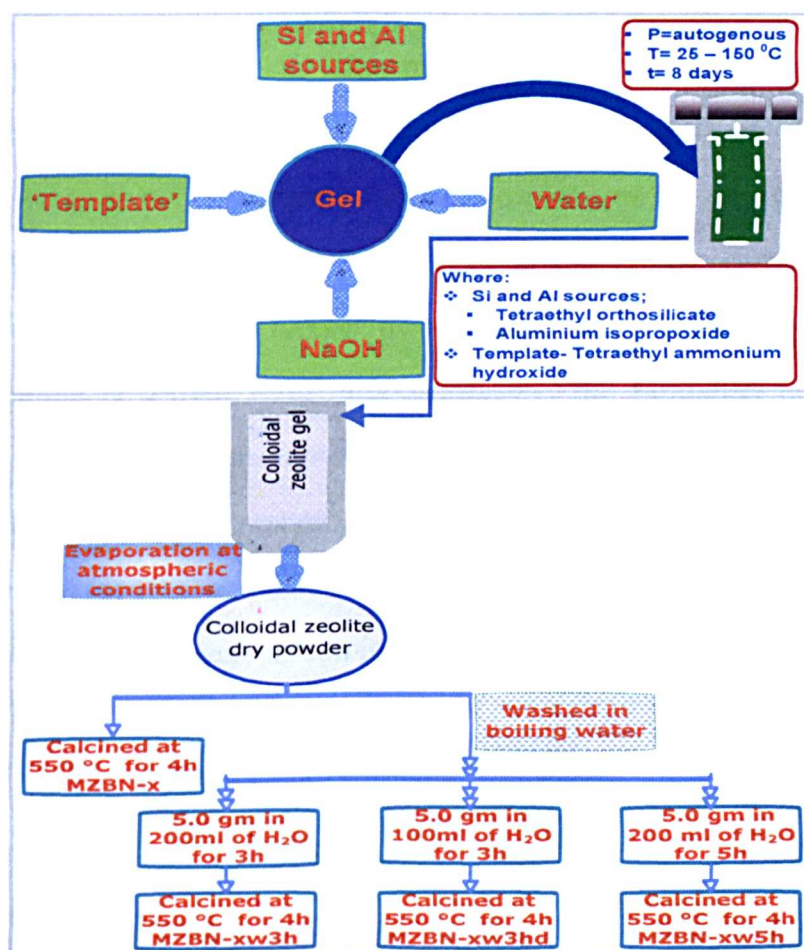


Figure 3.1 Reaction schemes for the hydrothermal synthesis of porous aluminosilicates using a zeolite BEA recipe.

3.2.3 Assessment of hydrothermal stability

The hydrothermal stability of calcined MZBN-x materials prepared at 100 °C was tested by refluxing the samples in boiling water for 6 or 120 h at a water-to-sample ratio of 1L/g. The designation of the refluxed samples was prefixed with R; for example refluxed MZBN-100 was designated as RMZBN-100. Subsequent samples washed prior to calcination followed by refluxing as above were designated RMZBN-100w3hd and RMZBN-100w5h.

3.3 Synthesis of nanostructured templated carbons via nanocasting routes

The concept of hard template carbonization has been used to investigate two synthesis strategies for the preparation of porous carbonaceous materials which are described in detail in respective sections below. The reaction setup shown in Figure 3.2 is a typical scheme for chemical vapour deposition. The apparatus consists of an alumina tube (1-2 inches in diameter) inserted into a tubular furnace capable of maintaining ± 1 °C over a range of 25 cm zone². Conventionally, the formation of carbons involves an inert gas saturated with a hydrocarbon flowing through the tube with or without a catalytic substrate inside. The high temperature in this reaction causes activation and decomposition of the hydrocarbon feedstock and subsequent carbon deposition.

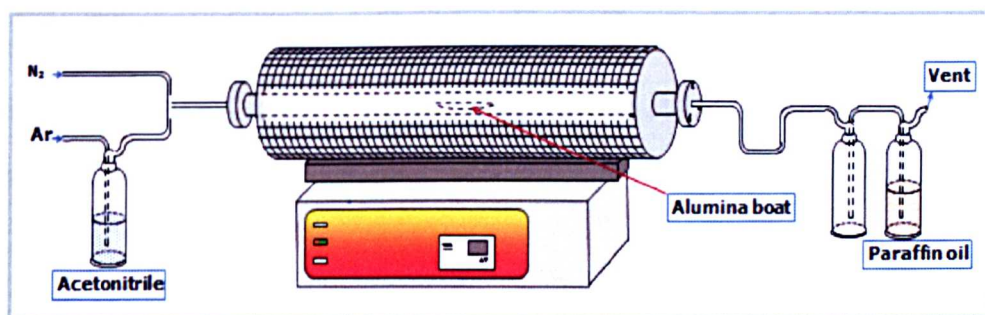


Figure 3.2 Reaction setup for chemical vapour deposition (CVD) and chemical activation procedures.

3.3.1 Chemicals

Zeolite Y with a Si : Al ratio of 2.55, commercially known as CBV100, from Zeolyst International and acetonitrile (Fisher Scientific) were used as received as a hard template for carbon fabrication. Other chemicals were: hydrofluoric acid (48-51%, Acros Organics) and hydrochloric acid (36.5%, Fisher Scientific). Nitrogen and Argon cylinders for the chemical vapour deposition process were procured from BOC Ltd and used as received.

3.3.2 Porous carbon templating using zeolite Y

The templating of porous carbons using zeolite Y followed established procedures as follows.^{3, 4} Briefly, 0.5 g of Zeolite Y in an alumina boat was placed in a flow through tube furnace, which was then heated to 800, 850 or 900 °C at a ramp rate of 5 °C/min under nitrogen or argon flow. Once the target temperature was reached, a flow of N₂/Ar saturated with acetonitrile as carbon precursor was passed through the furnace for 3 h. In order to improve the structural organisation, as evidenced by Ma and Co-workers,⁵ a final step of heat treatment at 900 °C for 3 h under a flow of N₂/Ar was performed. The temperature regimes and gas flow conditions are summarised in Figure 3.3 The resultant zeolite/carbon composites were allowed to cool down to room temperature under N₂/Ar flow and then washed with 10% HF for 24 h. The resulting carbon was filtered and washed with copious amounts of distilled water and then further refluxed in excess HCl (35%) at 60 °C for 6h to ensure complete removal of the zeolite framework followed by washing with distilled water and air-drying at 120 °C.

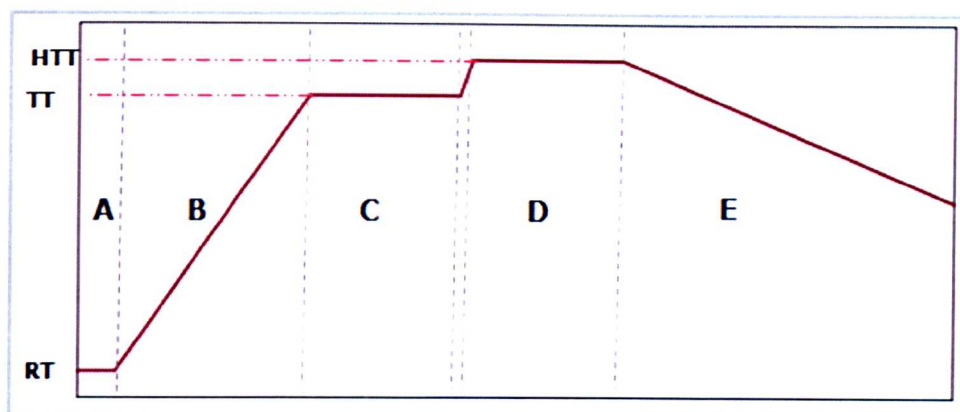


Figure 3.3 A plot representing the temperature programme used for the nanocasting of porous carbons; A (purge with Ar/N₂ for 30 min.), B (ramp at 5 °C up to the target temperature under Ar/N₂), C (target temperature – carbonisation process for 3 h), D (heat treatment temperature for 3 h under Ar/N₂) and finally E (cooling under Ar/N₂ environment). Key: RT (Room Temperature), TT (Target Temperature) and HHT (Heat-Treatment Temperature).

Carbons samples inversely generated from zeolite Y were designated ZTC_{xy} where x is the CVD temperature (800, 850, and 900 °C) and y is the carrier gas (Argon or Nitrogen). An extra sample derived from zeolite Y at CVD temperature of 800 °C following the procedure described above but with step B in figure 3.3 having a ramp rate of 15 °C/min instead of 5 °C/min was denoted ZTC800A*

3.4 Supercritical carbon dioxide mediated incorporation of Palladium nanoparticles into zeolite templated carbon ZTC800A

Pd incorporation into high surface area zeolite templated carbons was investigated as a way of enhancing hydrogen storage. The introduction of Pd nanoparticles into the ZTCs should ensure that the high surface area and pore size/distribution of the ZTCs remain unchanged so as to provide better understanding of the mechanism through which any enhancement of

hydrogen storage is achieved without reference to changes in textural properties.

3.4.1 Chemicals

ZTC800A carbon (prepared in section 3.3.2) and Palladium hexafluoroacetylacetonate, Pd(hfa)_2 (Sigma Aldrich) were used as a substrate and Pd nanoparticle precursor, respectively. Other chemicals used in this section include Hydrogen gas (research grade (BOC)) and carbon dioxide (BOC).

3.4.2 Palladium loading procedure

In order to introduce Pd nanoparticles into zeolite templated carbons prepared in section 3.3.2, a procedure previously reported by Wai and co-workers⁶ for the deposition of metal nanoparticles on functionalised multi-walled carbon nanotubes *via* supercritical hydrogenation of CO_2 -phillic precursor was followed. Thus, ZTC800A and ZTC800A* were impregnated with palladium nanoparticles using the experimental set-up illustrated in Figure 3.4.

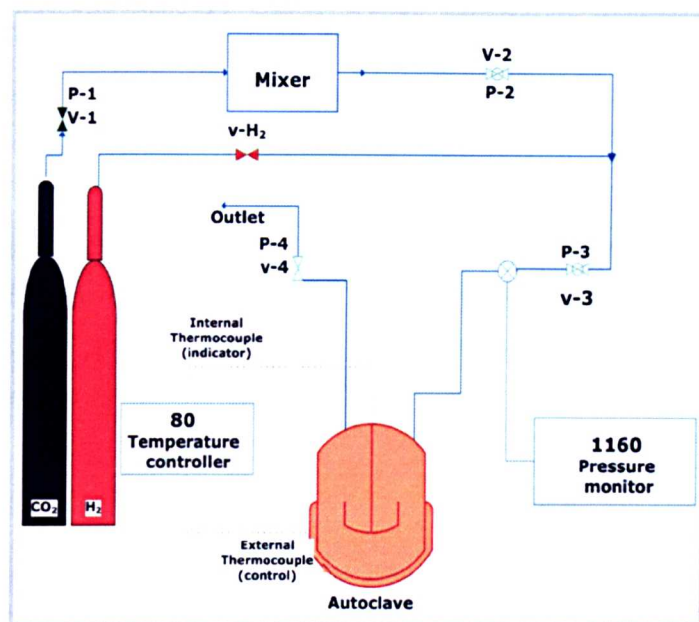


Figure 3.4 Schematic representation of the experimental set-up for the introduction of palladium nanoparticles in the ZTC using scCO₂ as a solvent and Pd(hfa)₂ as precursor.

In detail, ZTC (prepared as described in section 3.3.2) were mixed with Pd(hfa)₂ complex and loaded in glass vials and transferred into a high pressure stainless steel autoclave. The target loading of Pd nanoparticles in was varied between 0.2 mg and 4.0 mg range as shown in Table 3.1. The autoclave was heated to 40 °C, closing valve v-1 and opening the rest. Hydrogen gas at 80 psi was allowed to flow through the system for 30 min to expel any air inside. After flowing through hydrogen, valves v-H₂ and v-3 were closed and the reactor evacuated. Afterwards, valve v-4 was closed and simultaneously v-1 opened to add CO₂ to the mixer (H₂+CO₂) at 40 °C and a pressure of 1160 psi. Then valve v-2 and v-3 were opened in order to force the mixture into the reactor, which was left undisturbed for 30 min. The temperature was raised to 80 °C and maintained at this temperature for 10 min to allow the Pd(hfa)₂ reduction process. The heater

was then turned off, allowed to cool down, and flushed with CO₂ for a further 10 min. The Pd-doped carbons were then recovered.

Table 3.1 summary of Pd-loaded zeolite templated carbons prepared using pd(hfa)₂ as pd precursor and scCO₂ as a solvent, ^aZTCs designated as ZTC8 and ZTC8* are in section 3.3.2 previously denoted as ZTC800A and ZTC800A*, respectively.

Sample	Pd/wt (mg)
ZTC8 ^a	-
ZTC8Pd-0.2	0.2
ZTC8Pd-0.4	0.4
ZTC8Pd-0.8	0.8
ZTC8Pd-2.0	2.0
ZTC8* ^a	-
ZTC8*Pd-4.0	4.0

3.5 Synthesis of high surface area carbons using a combination of liquid impregnation and chemical vapour deposition

Zeolites provide a great variety of unique nanochannels as well as well-defined nanospaces that may be utilized for generating inverse replica carbon materials with controlled textural properties and morphologies. Previous work by the groups of Mokaya and Kyotani focused on the preservation of the structural regularity of zeolite in the generated carbons. The concept of template carbonisation is represented in Figure 3.5. ⁷

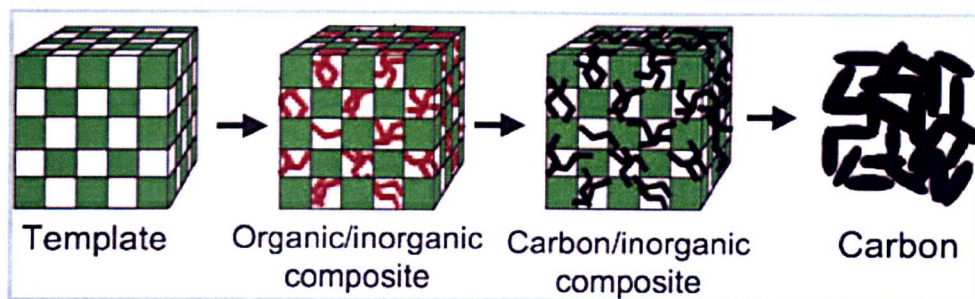


Figure 3.5 Schematic representation of the hard template carbonisation route for the synthesis of porous carbons.⁷

In this section, the main focus is the generation of high surface area carbons through the combined advantage of LI and CVD. In addition the mechanical stability of the resultant carbons was assessed by mechanical compaction and compared with commercially activated carbon (AX21) as a baseline material for compaction.

3.5.1 Chemicals

The following chemicals were used as supplied without modification; zeolite 13X and furfural alcohol. All the other reagents are as described in previous sections.

3.5.2 Zeolite templated carbons prepared via two-step synthesis

Three carbon samples were prepared using different heating ramp rates.⁸

In summary, 0.6 g zeolite 13X was dried in the furnace at 300 °C for 12 h before being impregnated (incipient wetness method) with furfuryl alcohol. The resulting FA/zeolite composite was placed on an alumina boat and transferred into the flow through tube furnace and polymerised under argon flow at 80 °C for 24 h followed by 150 °C for 8 h. In order to allow the carbonisation of polymerised furfural alcohol (polyfurfuryl alcohol), the temperature was ramped at 5 °C/min to 700 °C and held for 3 h under Ar

flow. The resulting zeolite/carbon composite was then exposed to ethylene gas (10% in Argon by volume) at 700 °C for 3 h. The gas flow was then switched to Ar flow only and the temperature of the furnace was raised to 900 °C and held for 3 h followed by cooling under Ar to room temperature. The heating regime is illustrated in Figure 3.6. The resulting zeolite/carbon composite was treated in 10% HF for 24 h, washed and then refluxed in 36.5% HCl for 6 h. The final carbon was then washed with deionised water and dried at 120 °C for 12 h. Here after the resulting carbon sample is denoted as FA-ZTC1. Two other samples designated as FA-ZTC2 and FA-ZTC3 were prepared as described above except for a heating ramp rate of 10 and 15 °C /min, respectively.

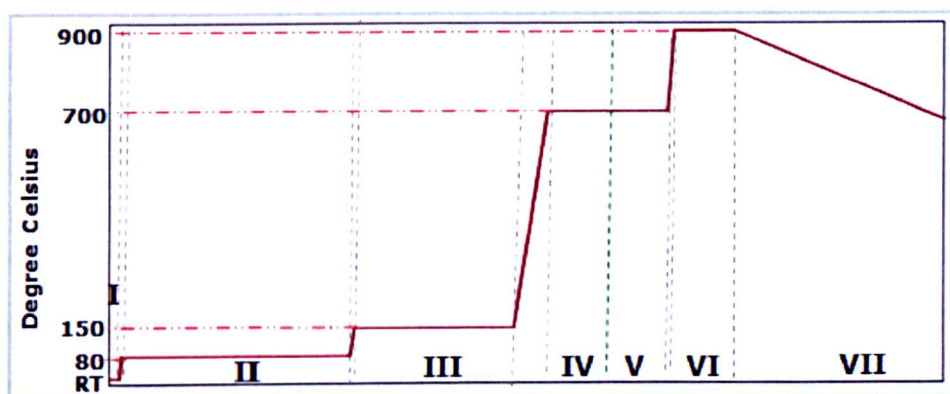


Figure 3.6 A plot illustrating the heating regime for synthesis of FA-ZTCx carbon samples: I - purge with Ar at room temperature for 30 minutes, II - treatment at 80 °C followed by III - at 150 °C to polymerise furfuryl alcohol in the zeolite channels, IV - first step carbonisation of polyfurfuryl alcohol, V - second step carbonisation via CVD with ethylene gas, VI - heat treatment and finally VII -cooling step under argon.

3.5.3 Post-synthesis modification of FA-ZTCx : via compaction to assess mechanical stability

To probe the effect of pressure on the textural properties and morphology of the zeolite templated carbons, they were compacted at two different

pressures (5 or 10 Tons) for 10 min. Briefly, ca 35 mg of the carbon was loaded into a pressing unit which was then compacted at 5 or 10 Tons. The compacted samples were denoted as C5-FA-ZTCx and C10-FA-ZTCx for compaction at 5 and 10 Tons, respectively. Commercially available activated carbon (AX21) was also compacted and used as a baseline material for compaction studies under similar conditions. The compacted AX21 samples were denoted C5-AX21 and C10-AX21.

3.6 Inorganic metal salt templating of carbon aerogels

The effect of metal salt templating on the morphology and textural properties of carbon aerogels before and after activation was investigated. The textural properties of the CaCl₂-templated and activated carbon aerogels were compared with the properties of conventionally synthesised and activated aerogels.

3.6.1 Chemicals

The following chemicals were used as supplied without any modification: 2,4,6-Triamino-1,3,5-triazine (Melamine), hydrochloric acid and sodium carbonate from Fisher Scientific while formaldehyde (37%) and calcium chloride were obtained from Sigma-Aldrich.

3.6.2 Preparation of carbon aerogels via metal salt templating

The salt templating procedure is described stepwise in Table 3.2. Chemical activation of the aerogels was performed by mixing the carbon aerogel with KOH at a carbon/KOH weight ratio of 1 : 4. The mixture was ground together to attain a homogeneous sample which was loaded on an alumina boat and placed in a flow-through tube furnace followed by heat-treatment at heating ramp rate of 3 °C/min under nitrogen gas flow to the activation temperature (600, 700, and 800 °C) and held for 1h. The synthesis and

3.0 Experimental methodology

activation procedure is illustrated in Figure 3.7. After cooling down under nitrogen flow, activated samples were obtained and washed with 2M HCl under stirring at room temperature to remove any inorganic salts formed during the activation stage, followed by copious deionised water until a neutral pH was attained. Solid materials were obtained by filtration and finally dried in the oven at 120 °C. The samples obtained were denoted as 14AC-Ca-CAMF800-x (where x is 6, 7 and 8 corresponding to activation at 600, 700 and 800 °C, respectively).

Table 3.2 Metal salt (CaCl₂) templating step-wise procedure of carbon aerogels derived from melamine-formaldehyde (MF) resin.

Chemicals	Quantity	Procedure	
Melamine	4.2 g	The mixture with pH of 8.5 was heated at 40 °C to obtain a clear solution in which hexamethylome lamine (MF) was formed.	CaCl₂/MF ratio of 2. Condensation reaction was initiated by adjusting pH to 4.5 by HCl addition. The solution was then heated at 60 °C for 1h, during which a MF resin/calcium chloride composite was formed. The resin was dried and cured at 180 °C for 6h then carbonised at 700, 800 and 900 °C for 2h under nitrogen gas flow. The products were washed with water to remove the template. The products were denoted as Ca-CAMFx (x = temperature of carbonisation)
37% Formaldehyde	19.4 g		
Water	15.0 g		
Na ₂ CO _{3(aq)}	0.1M		
CaCl ₂ (Template)	33.6 g		
HCl _(aq)	1.0M		

The resultant carbon aerogels carbonised at 700, 800 and 900 °C were designated as Ca-CAMF700, Ca-CAMF800 and Ca-CAMF900, respectively. The use of CaCl_2 as a 'porogen' in this work is advantageous in that, it is cheap and soluble in water. Therefore, the metal salt template is easily removed by washing with deionised water at ambient conditions, resulting in nanostructured porous materials.

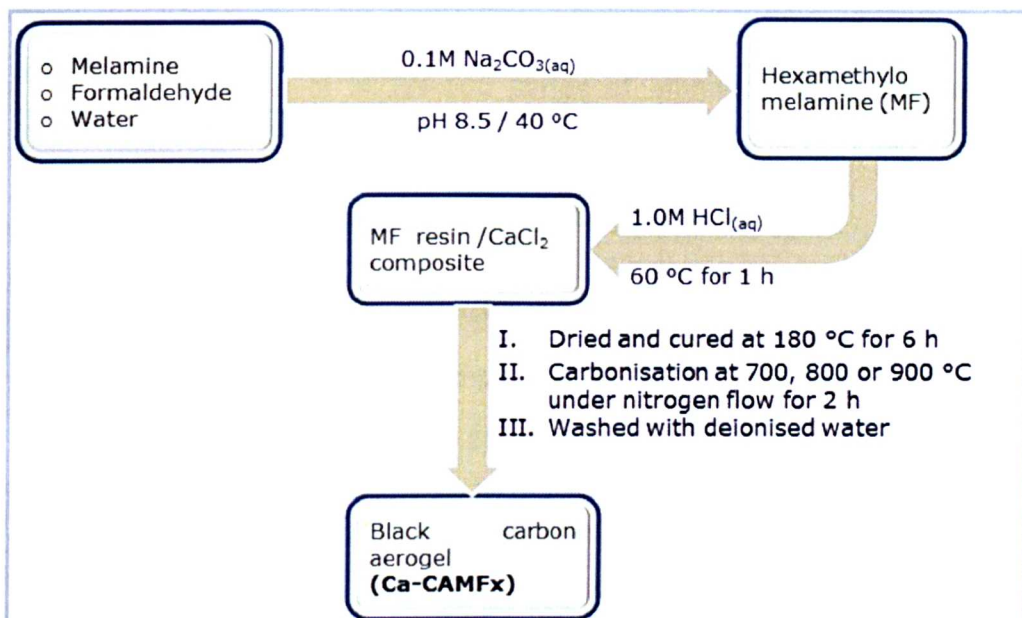


Figure 3.7 Schematic representation of metal salt templated preparation of carbon aerogels.

In order to assess the effect of salt templating on the textural properties and morphology on the resultant activated carbon aerogels, a second set of activated carbons were prepared from the conventional melamine-formaldehyde and resorcinol-formaldehyde resins. The carbon samples prepared from resorcinol-formaldehyde resin (CACR) were designated 12AC-CACRx while those from melamine-formaldehyde resin were denoted 12AC-CAMFx (where x is the activation temperature of 600, 700, 800 or 900 °C while 12 means carbon : KOH ratio of 1:2).

3.7 Characterisation techniques

The first part of this section outlines the experimental setup used in material characterisation, while the second part concentrates on gas sorption measurements of the prepared porous solids.

3.7.1 Characterisation techniques

I. Powder XRD analysis was performed using three different diffractometers:

- XRD analysis of MZBN-100 series of aluminosilicates and zeolite templated carbons was performed with a Phillips 1830 powder diffractometer with a 0.02 step size and 2 s step time.
- In order to elucidate structural ordering in the low angle region XRD analysis was done on a Bruker AXS D8 Advance with 0.007° step size, and 2 s step time for 2θ between 0.5 and 5°.
- Pd-loaded ZTCs and carbon aerogels were analysed on a PANalytical X'Pert PRO diffractometer with Cu-K α . Powder samples were mounted on silicon coated zero background holder and placed on a pinner stage (rotation of 2 cycles per second) with measurements in the $2\theta = 0.65 - 60^\circ$ range.

All the three power diffractometer used Cu-K α radiation ($\lambda = 1.5418 \text{ \AA}$) with the standard operating power of X-ray tube set at 40kV and 40mA.

II. Nitrogen sorption isotherms and textural properties of the prepared materials were analysed at 77 K and 87 K using nitrogen gas on a conventional volumetric gas adsorption equipment namely Micrometrics ASAP 2020 sorptometer. Before analysis, the samples were oven dried at 100 °C and evacuated overnight at 160 and 200 °C for aluminosilicates and carbonaceous materials respectively under a vacuum. The surface area was

calculated using the BET method based on adsorption data in the relative pressure (P/P_0) range 0.02-0.25 while the total pore volume was determined from the amount of nitrogen adsorbed at $P/P_0 = ca\ 0.99$.^{9, 10} For calculation of the surface area range, the partial pressure range selection was based on reports which indicate that using $P/P_0 = 0.01-0.05$ overestimates the surface area while $P/P_0 = 0.1-0.3$ can underestimate the surface area.^{4,70} Pore size distribution (PSD) was determined using the Barrett-Joyner-Halenda (BJH) method applied to the adsorption branch of the isotherm. The PSD was also assessed via a Non Local Density Functional Theory (NLDFT) method using nitrogen adsorption data, and assuming a slit pore model. The microporosity was determined by performing t -plot analysis of the sorption data.

III. Thermogravimetric analysis (TGA) was performed using a SDT Q600 TGA Analyser (from room temperature up to 1000 °C at a heating rate of 10 °C/min) in static-air environment. The acquired data were converted to Microsoft excel by in built TA Instruments Universal Analysis software.

IV. Elemental Analysis - X-ray Fluorescence (XRF) was used to determine silica to alumina ratio in the aluminosilicate samples on a Philips MiniPal PW4025 XRF instrument.

V. Fourier Transform Infrared (FTIR) spectroscopy spectra were obtained on a Bruker optics TENSOR 27 series FT-IR spectrometer. The samples for analysis were prepared at an aluminosilicate: KBr weight ratio of 1: 300 and pressed briefly at 5 Tons into a thin disk suitable for IR analysis.

VI. Nuclear Magnetic Resonance (NMR) spectra were obtained on a Varian Unity Inova 300 MHz spectrometer run by EPSRC Solid-State NMR service at the Durham University (UK). ^{29}Si MASNMR spectra were acquired at silicon-29 frequency of 59.56 MHz, acquisition time of 30 – 50 ms, total spectral width of 30 kHz, recycle delay of 30 s, and a MAS rate of 5.1 kHz. ^{27}Al MASNMR spectra were acquired at a frequency of 104 MHz, acquisition time of 10 ms, recycle delay of 0.1 s, spectral width of 416 kHz and a MAS rate of 14.0 kHz.

VII. TPD of cyclohexylamine was used to probe the acidity of calcined aluminosilicates. Approximately 10 mg of calcined aluminosilicates were exposed to liquid cyclohexylamine (CHA) at room temperature and kept overnight. The CHA-containing materials were transferred into an oven at 80 °C for 2 h so as to allow the base to permeate into the samples. TGA curves were then obtained for the CHA-containing samples. The mass loss associated with desorption of the base from acid sites was used to calculate the acid content in mmol of CHA per gram of sample. The main assumption is that each acid site $[\text{H}^+]$ ¹¹⁻¹³ interacts with one base molecule. To obtain the content of strong acid sites, the CHA-containing samples dried at 80 °C, were further heated in an oven at 250 °C for 2h prior to TGA analysis.

VIII. Scanning Electron Microscopy images were recorded using an FEI XL30 Microscope. The samples were mounted using a carbon double-sided conductive sticky tape. A thin (ca. 10 nm) coating of platinum sputter was deposited onto the samples to reduce the effects of charging.¹⁰

IX Transmission Electron Microscopy (TEM) micrographs were recorded on photographic films, developed and fixed on a JEOL 2000-FX with a LaB_6 filament operating at 200 kV. The plate negatives were then

rinsed in water, dried at room temperature followed by scanning on an EPSON scanner. The scanned black and white images at a resolution of 1200 dpi were saved as JPEG files. In addition, High Resolution Transmission Microscopy (HRTEM) images were taken on a JEOL 2100F equipped with a Gatan Imaging Filter (GIF) and Gatan double tilt heating holder (field emission electron gun source, information limit 0.19 nm)¹⁴ at room temperature and recorded using a CCD camera, processed using Gatan Digital Micrograph¹⁵ software and saved as DM3. Sample preparation involved ultrasonic dispersion of the solid powders in ethanol followed by several drops being cast onto copper-grid mounted 'holey' carbon films.

3.7.2 Gas sorption measurements

I. Hydrogen uptake measurements were gravimetrically obtained on an Intelligent Gravimetric Analyser (IGA-003 Analyser Hiden Analytical; UK). The hydrogen storage capacities for porous carbonaceous materials were analysed using established procedures.^{10, 16, 17} Typically, 20 to 40 mg of the sample was loaded in the analyser represented in Figure 3.9 capable of measuring weights with a resolution of $\pm 0.02 \mu\text{g}$ over the pressure range of 0-20 bar. Pd-free and Pd-loaded samples were degassed at 200 °C and 160 °C respectively for 12 h under vacuum (10^{-6} up to 10^{-8} bar) before analysis. Ultra high pure hydrogen (BIP 99.9999%) uptake was then gravimetrically determined by measuring wt% increase with increase in pressure from 0 bar to a maximum of 20 bar (adsorption) followed by desorption on decreasing pressure from 20 bar to 0 bar at 77K (under a liquid nitrogen bath). The hydrogen uptake data were rigorously corrected for the buoyancy of the system and the samples using carbon density (1.5 g/cm^3) and hydrogen density (0.04 g/cm^3). In addition, the Isosteric heat of adsorption (Q_{st} , kJ/mol) was determined from hydrogen adsorption [91]

isotherms under liquid nitrogen (77 K) and liquid argon (87 K) temperatures based on the Clausius-Clapeyron equation:

$$Q_{st} = -R \left[\frac{\partial \ln(P)}{\partial (1/T)} \right]_{\theta} \quad (1)$$

where θ is the fraction of the adsorbed sites at a pressure P and temperature T ; R is the universal gas constant.

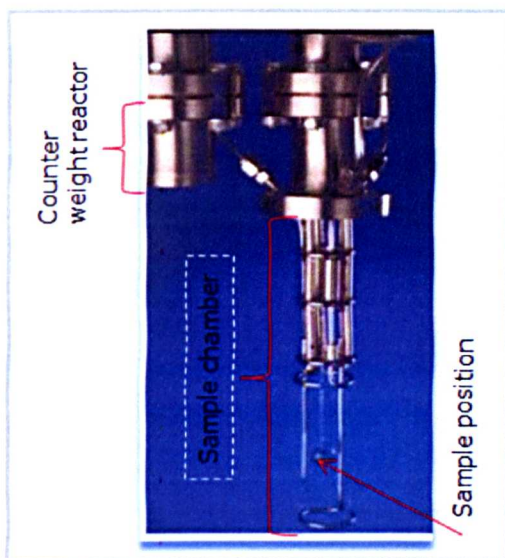


Figure 3.8 Schematic representation of IGA-003 sample chamber and counter weight.

Langmuir plots were used to estimate the maximum hydrogen (%wt) at 77K using the equation;

$$\frac{P}{W} = \frac{1}{W_0} P + \frac{1}{W_0 \cdot K} \quad (2)$$

where W is the degree of adsorption at Pressure P , W_0 is the saturated adsorption and K is a coefficient constant.

II. Carbon dioxide adsorption measurements were performed using an SDT Q600 Thermogravimetric Analyser under a stream of CO_2 at

25 °C. The samples (ca. 10 mg) were heated at a ramp rate of 15 °C/min under a stream of nitrogen gas (flow rate of 50 ml/min) up to 250 °C (AB in Figure 3.9) and held for 2 h (BC) in order to remove adsorbed gaseous molecules including water. The sample was then allowed to cool down (CD) under nitrogen flow to 25 °C and held for 10 min after which the gas was switched from N₂ to CO₂ for 3 h (DE) to allow CO₂ uptake to be recorded according to the weight variation.

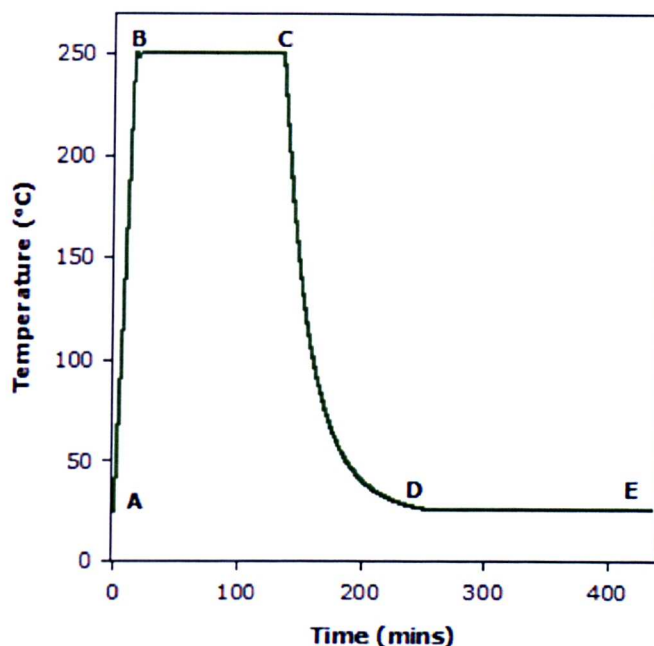


Figure 3.9 A plot representing temperature programmes for CO₂ adsorption measurements at 1 atmosphere.

3.8 Summary

The experimental methods discussed in this chapter were the actual protocols followed for the synthesis, post-synthesis decoration/modification and characterisation of aluminosilicates and carbonaceous materials. Also, the procedures followed for gas sorption measurements have been described in detail outlining the key parameters.

3.9 Bibliography

1. B. Gautier and M. Smaïhi, *New J. Chem.*, 2004, **28**, 457-461.
2. M. Meyyappan, ed., *Carbon Nanotubes Science and Applications*, CRC Press LL, London, 2005.
3. Z. X. Yang, Y. D. Xia and R. Mokaya, *Adv. Mater.*, 2004, **16**, 727-732.
4. Z. Yang, Y. Xia and R. Mokaya, *J. Am. Chem. Soc.*, 2007, **129**, 1673-1679.
5. Z. Ma, T. Kyotani, Z. Liu, O. Terasaki and A. Tomita, *Chem. Mater.*, 2001, **13**, 4413-4415.
6. X.-R. Ye, Y. Lin, C. Wang, M. H. Engelhard, Y. Wang and C. M. Wai, *J. Mater. Chem.*, 2004, **14**, 908-913.
7. T. Kyotani, *Bull. Chem. Soc. Jpn.*, 2006, **79**, 1322-1337.
8. Y. Xia, G. S. Walker, D. M. Grant and R. Mokaya, *J. Am. Chem. Soc.*, 2009, **131**, 16493-16499.
9. N. Alam and R. Mokaya, *J. Mater. Chem.*, 2008, **18**, 1383-1391.
10. Z. X. Yang, Y. D. Xia, X. Z. Sun and R. Mokaya, *J. Phys. Chem. B*, 2006, **110**, 18424-18431.
11. R. Mokaya, *J. Catal.*, 2000, **193**, 103-107.
12. R. Mokaya, W. Jones, S. Moreno and G. Poncelet, *Catal. Lett.*, 1997, **49**, 87-94.
13. Z. Yang, PhD Thesis, The University of Nottingham, 2007.
14. A. La Torre, G. A. Rance, J. El Harfi, J. Li, D. J. Irvine, P. D. Brown and A. N. Khlobystov, *Nanoscale*, 2010, **2**, 1006-1010.
15. M. V. Landau, L. Vradman, V. Valtchev, J. Lezervant, E. Liubich and M. Talianker, *Ind. Eng. Chem. Res.*, 2003, **42**, 2773-2782.

3.0 Experimental methodology

16. M. Sevilla, A. B. Fuertes and R. Mokaya, *Energy Environ. Sci.* , 2011, **4**, 1400-1410.
17. M. Sevilla, R. Mokaya and A. B. Fuertes, *Energy Environ. Sci.*, 2011, **4**, 2930-2936.

Chapter Four

Chapter 4.0: Preparation of Mesoporous Zeotype Aluminosilicates using Zeolite BEA recipe.....97

4.1 Abstract	97
4.2 Introduction	97
4.3 Results and Discussion	100
4.3.1 Mesostructural and framework ordering.....	100
4.3.2 Silicate condensation in as-synthesised MZBN-100 sample and the washed derivatives.....	109
4.3.3 Aluminium content and acidity.....	110
4.3.4 Morphology of the as-synthesised and calcined MZBN-100 sample.....	113
4.3.5 Porosity.....	114
4.3.6 Effect of Hydrothermal Synthesis Temperature.....	118
4.3.7 Hydrothermal Stability of calcined MZBN-100 and its derivatives washed prior to calcination.....	134
4.3.8 Effect of SiO ₂ : TEAOH ratio on mesostructural framework.....	140
4.4 Summary	142
4.5 Bibliography.....	144

Chapter 4.0: Preparation of Mesoporous Zeotype Aluminosilicates using Zeolite BEA recipe

4.1 Abstract

This chapter explores the preparation of mesoporous aluminosilicates using synthesis conditions that are normally used for preparation of crystalline zeolites. The key to the formation of a mesostructured material is the use of a relatively low crystallisation temperature and in particular the Si/TEAOH ratio in the synthesis gel. Careful setting of these key synthesis parameters allowed the formation of aluminosilicate materials that possess tuneable mesoporosity with surface areas of 500 to 850 m²/g, pore volumes in the range of 0.35 – 1.5 cm³/g and pore size between 2.5 and 14.0 nm. Depending on the synthesis conditions, the resultant aluminosilicates exhibit strong acidity and are hydrothermally stable with potential applications in catalysis.

4.2 Introduction

Zeolites and zeotype molecular sieves belong to the microporous class of porous materials. Since their discovery, as discussed in chapter 2.2, they have continually attracted attention in the fields where molecular recognition is required, e.g. catalysis, ion-exchangers, chemical sensing and separation among the growing list of applications. The extensive usage in acid-catalysed reactions for the production of petrochemicals and fine chemicals is due to their attractive features such as high thermal and hydrothermal stability as well as tuneable acidity and pore size. However, the pore size of zeolites (pore diameters 0.4 - 1.0 nm with 12 T-atoms)¹ has been a great barrier in reactions involving bulky reactants or those generating bulky products. This raises the need for zeolitic materials that extend pore dimensions beyond the current shape/size selectivity limits.

Mesoporous materials, with larger pores than conventional zeolites can be prepared via a variety of supramolecular templating methods where arrays of surfactant molecules are used as structure directors.² For example, UTD-1 (14-membered ring size) reported by Davis and co-workers possesses good acidity and thermal/hydrothermal stability.³ This is attributed to their crystalline pore walls (frameworks) that are ordered at the atomic level, which contrasts with most of the mesoporous aluminosilicas that have amorphous pore walls.^{4, 5} The amorphous mesoporous aluminosilicas have relatively low acidity and hydrothermal stability which limits their industrial applications in catalytic reactions.

In order to enhance acidity and hydrothermal stability of mesoporous materials, several strategies for introducing some crystallinity into the pore walls have been developed, including dual templating⁶ and secondary crystallisation of mesoporous molecular sieves.^{7,8} Furthermore, the use of preorganised zeolite building blocks has been a centre of focus. For example Pinnavaia and co-workers reported steam stable aluminosilicate mesostructures assembled from zeolite (Y, ZSM-5) seeds.^{9, 10} Post-synthesis treatment of conventionally prepared zeolites and zeotype aluminosilicates provides a different route to achieve the desired framework composition and properties.¹¹ Given that no method has so been identified that generates all the required properties, the search for new types of materials which combine the advantages of mesoporous molecular sieves and zeolites is on-going.

The main difficulty encountered in the preparation of aluminosilicas via supramolecular templating is inability to generate crystalline aluminosilicate frameworks. Although the formation of crystalline supramolecular-templated silica-surfactant mesophases has been reported

in a number of studies¹²⁻¹⁷ their transformation into template free crystalline materials often fails. The formation of mesoporous silicate materials is, however, not limited to supramolecular templating. Mesoporous silicate composites may be prepared using small organic molecules as "structure-directing agents", wherein the mesoporous structure formation mechanism is different from that which applies for supramolecular templates.¹⁸⁻²² However, in most cases the resulting materials are composites made up of zeolite crystallites embedded in a disordered mesoporous matrix.

Given the large number of variables to explore, zeolite synthesis is expected to be an expanding field for high quality zeolite and zeotype crystals preparation. The modification of existing methods as well as the development of new compositional and synthesis methods will play a vital role in the discovery of new zeolite and other nanostructured porous materials. Such new ideas will result in zeolites that have distinct framework types. However, simple methods to control the parameters in zeolite synthesis have remained as one of the major challenges. The current scientific and technological effort into zeolite synthesis is therefore directed towards understanding how zeolites crystallise, to characterise their structures and invent new methods to modify properties. This will increase their utility and produce an ever growing list of new applications for these fascinating materials.

The work presented in this chapter explores the preparation of mesoporous aluminosilicates using template molecules and synthesis conditions that are conventionally used for the preparation of crystalline zeolites. The aim is to achieve the formation of mesostructured aluminosilicates that exhibit properties associated with zeolites such as strong acidity and

thermal/hydrothermal stability. The composition of the synthesis gel and preparation conditions (i.e. recipe) used are similar to those known to generate zeolite BEA²³ as detailed in section 3.2. This chapter describes the successful preparation of strongly acidic and hydrothermally stable mesoporous aluminosilicates designated as MZBN-x (where x is the crystallisation temperature in °C). The synthesised aluminosilicate materials exhibit properties that suggest that they have potential for use as acid catalysts or catalyst supports.

4.3 Results and Discussion

This section reports the synthesis of mesoporous aluminosilicates at variable crystallisation temperatures with subsequent post-synthesis modification by washing. Also reported here is the use of a higher ratio of SiO₂ : TEOH i.e. ratio of 4 instead of 2.8.

4.3.1 Mesostructural and framework ordering

The powder XRD patterns of mesoporous aluminosilicates synthesised at 100 °C (designated MZBN-100) before and after calcination are shown in Figure 4.1 A and respective basal spacing (d_{100}) is given in Table 4.1. The XRD patterns of as-synthesised MZBN-100 shows a peak at low 2θ value (ca. 1.7°) which is attributed to mesostructural ordering with a basal spacing of 5.2 nm. Moreover, a further weak peak is observed at $2\theta = 7^\circ$, which is a position similar to that of (100) and (101) diffractions of zeolite β . The presence of this latter peak indicates either the formation of zeolite β crystallites or the presence of zeolite building units in the as-synthesised MZBN-100 sample. Likewise, the XRD pattern of calcined MZBN-100 indicates retention of the mesostructural ordering (peak at 2θ value of 1.8°) with a d_{100} of 4.9 nm. Thus calcination induces slight contraction of ca. 5% of the as-synthesised sample. This represents a very low level of

calcination-induced contraction, which is ascribed to a high level of silica condensation for as-synthesised silicate framework. On the contrary, the peak at $2\theta = 7^\circ$ for the calcined MZBN-100 sample is not well resolved, which suggests the thermal destruction or diminution of any zeolite β crystallites or zeolite building units. However, it has been reported that zeolite β crystallites are stable upon calcination,²⁴⁻²⁸ thus the absence of a well resolved peak at $2\theta = 7^\circ$ appears to rule out the presence of such crystallites in the MZBN-100 samples.

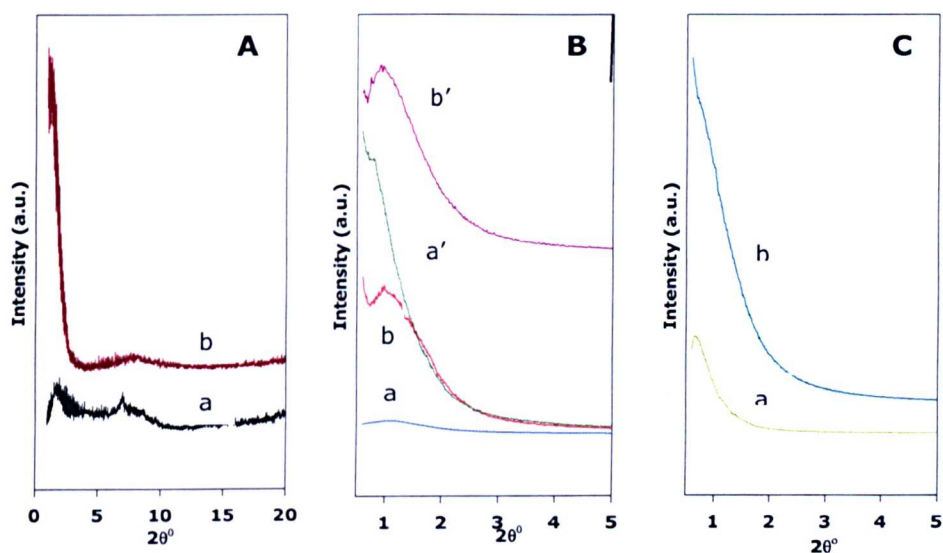


Figure 4.1 Powder XRD patterns of (a) as-synthesised and (b) calcined MZBN-100 aluminosilicate materials prepared from a zeolite BEA recipe at 100 °C; (A) directly calcined (sample MZBN-100), (B) washed for 3 h before calcination (MZBN-100w3h) and (C) washed for 5 h before calcination (MZBN-100w5h). (a') and (b') in (b) are for sample MZBN-100w3hd which was washed in 100 ml water.

Table 4.1 Composition, textural properties and acidity of mesoporous aluminosilicate materials prepared from a zeolite BEA recipe at a crystallisation temperature of 100 °C.

Sample	Si/Al ratio	Basal spacing (nm) ^a	Surface area (m ² g ⁻¹)	Pore volume (cm ³ g ⁻¹) ^b	Pore size (nm) ^c	Acidity (mmol CHA/g) ^d
MZBN-100	18.6	4.9 (5.2)	527	0.37 (0.06)	2.5 (3.5)	0.28 (0.28)
RMZBN-100	13.8		541	0.43 (0.05)	3.4 (4.6)	0.47 (0.47)
MZBN-100w3h		9.4 (10.0)	667	0.56 (0)	3.0 (4.2)	0.22 (0.20)
RMZBN-100w3h			760	0.81 (0)	4.1 (5.0)	0.66 (0.65)
MZBN-100w3hd	16.9	8.3 (8.8)	649	0.78 (0.04)	5.2 (6.2)	0.22 (0.22)
RMZBN-100w3hd	12.7		748	1.08 (0.05)	6.2 (6.7)	0.58 (0.53)
MZBN-100w5h	15.9	12.6	625	0.96 (0.09)	7.2 (6.8/8.7)	0.23 (0.23)
RMZBN-100w5h	12.3		838	1.48 (0.12)	8.1 (7.1/8.8)	0.80 (0.80)

^aValues in parentheses are the basal spacing of as-synthesised materials.

^bThe data in parentheses are ^bmicropore volume, ^cpore size maxima obtained using NLDFT analysis and ^dstrong acidity values after evacuation at 250 °C

Figure 4.1 B and C show the XRD patterns of the MZBN-100 derivatives that were washed (magnetically stirred) in boiling water at atmospheric conditions and dried prior to calcination. For materials washed for 3 h (MZBN-100w3h and MZBN-100w3hd), both the as-synthesised and calcined samples exhibit a well resolved peak from mesostructural ordering at 2θ value of ca. 1.8°. The basal spacing for as-synthesised samples increases from 5.2 nm for MZBN-100 unwashed sample to 8.8 and 10.0 nm for MZBN-100w3hd and MZBN-100w3h samples, respectively. On calcination, the basal spacing (d_{100}) for MZBN-100w3hd and MZBN-100w3h reduces to 8.3 and 9.4 nm respectively, which is a contraction of ca. 6%.

The extent of contraction observed in the washed samples compares well to that of the unwashed MBZN-100 sample.

The basal spacing expansion of 70 and 90% for the samples washed for 3 h in 100 and 200 mL of water, respectively provides further evidence for sample modification caused by the washing step, and shows that more water (MZBN-100w3h) favours greater expansion. On the other hand, the as-synthesised sample washed for 5 h (MZBN-100w5h) exhibits an even higher basal spacing of 12.6 nm which is an increase in excess of 140%. It appears therefore that washing of the as-synthesised mesophase in boiling water causes significant lattice expansion of the MZBN-100 sample. Such expansion of mesoporous silicate mesophase during extended hydrothermal treatment has been previously reported in literature.²⁹⁻³³

The expansion/restructuring is caused by thermal effects that act on the relatively flexible as-synthesised aluminosilicate framework under hydrothermal conditions. The observed pore-size expansion involves base-induced intrapore mineralization and transport of aluminosilicate species and redeposition. Dissolution of the aluminosilicate species is made possible by the basic conditions. It is likely that the dissolved aluminosilicate species is transported and redeposited onto areas with a high surface curvature. Similar behaviour has been reported for surfactant templated mesoporous silica.³² In such a scenario, the restructuring involves significant dissolution of as-synthesized materials and the subsequent formation, via redeposition, of larger pore materials.

The TEM micrographs in Figure 4.2 provide further support that sample MBZN-100 is mesostructured which is in good agreement with the powder XRD patterns in Figure 4.1A. The TEM images show relatively well ordered

wormhole-type pore channels with substantial level of pore ordering that is consistent with XRD patterns of at least one peak.^{5, 34-36} pore channels, of size ca. 3.0 nm are observed throughout the particles and hardly any other phase is observed as might be expected for composite/mesoporous materials wherein distinct zeolite β crystallites exist.^{19-22, 24-28}

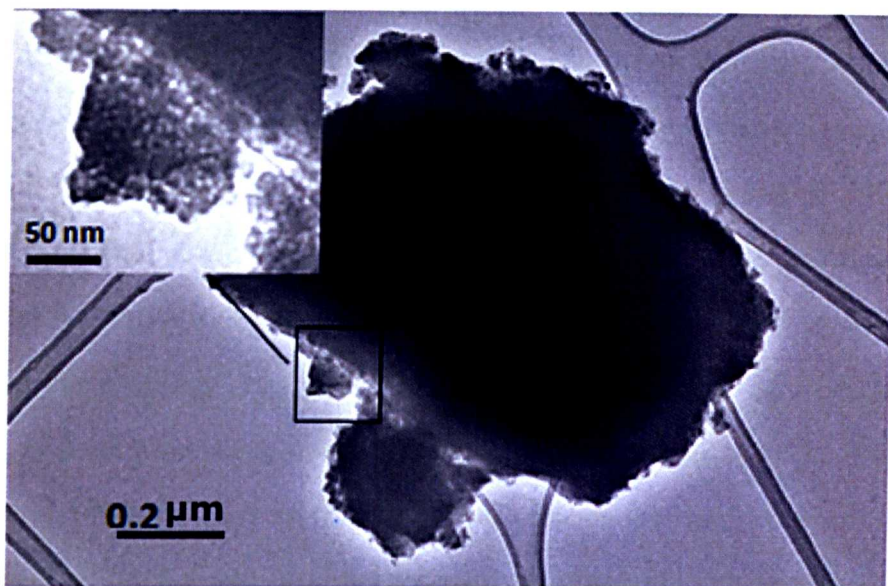


Figure 4.2 TEM micrographs of calcined MZBN-100 sample.

The present MZBN-100 sample synthesis uses a relatively low crystallisation temperature compared to previous reports that yield zeolite BEA. More importantly, the use of a higher Si/TEAOH ratio of 2.8 is significant since for the synthesis gels that yield zeolite BEA the ratio is usually ≤ 2.0 .^{23-25, 37, 38} Higher Si/TEAOH ratio is known to delay the growth of zeolite BEA crystallites³⁸ and the present results suggest that, under certain conditions, the delay can lead to formation of a mesostructured material via previously suggested mechanisms.^{18, 19, 21, 22, 39} The formation of mesopores in such a scenario is likely to be directed by partially aggregated TEA⁺ species. Xiao and co-workers²⁴ have previously observed

the formation of mesopores in micro/mesoporous silica generated from Si/TEA⁺/H₂O systems that contain partially aggregated TEA⁺ species and wherein the concentration of TEA⁺ is greater than 6 wt% in water. The nominal concentration of TEA⁺ species in our synthesis gel is ca. 14 wt% in water. Hence it is proposed that TEA⁺ species play a role in the initial formation of mesopores in sample MZBN-100.²⁰ This proposal is consistent with the TEA⁺ species being retained in the as-synthesised MZBN-100 mesophase as evidenced in Figure 4.3A; the as-synthesised mesophase shows IR peaks at 660 – 840 cm⁻¹ along with peaks between 1350 and 1500 cm⁻¹ that are attributable to the TEA⁺ species.³⁹ The Infra-red (IR) spectra in Figure 4.3A show that the lattice expansion which takes place during the washing step is accompanied by the removal of some of the TEA⁺ species from as-synthesised mesophase. IR peaks at 665, 704, 800, 833 and 1403 cm⁻¹ arising from the TEA⁺ species that are observed for as-synthesised MZBN-100 are not present for the washed samples. Other TEA⁺ peaks at 1635, 1655, 1695 cm⁻¹ and 1350 – 1500 cm⁻¹ also reduce in intensity. In addition, the as-synthesised MZBN-100 show three more peaks at ca. 1030 cm⁻¹ (with a shoulder at 1200 cm⁻¹), 790 and 580 cm⁻¹ of which the first two are characteristic of silicon oxides associated with asymmetric and symmetric Si-O stretching vibrations.⁴⁰

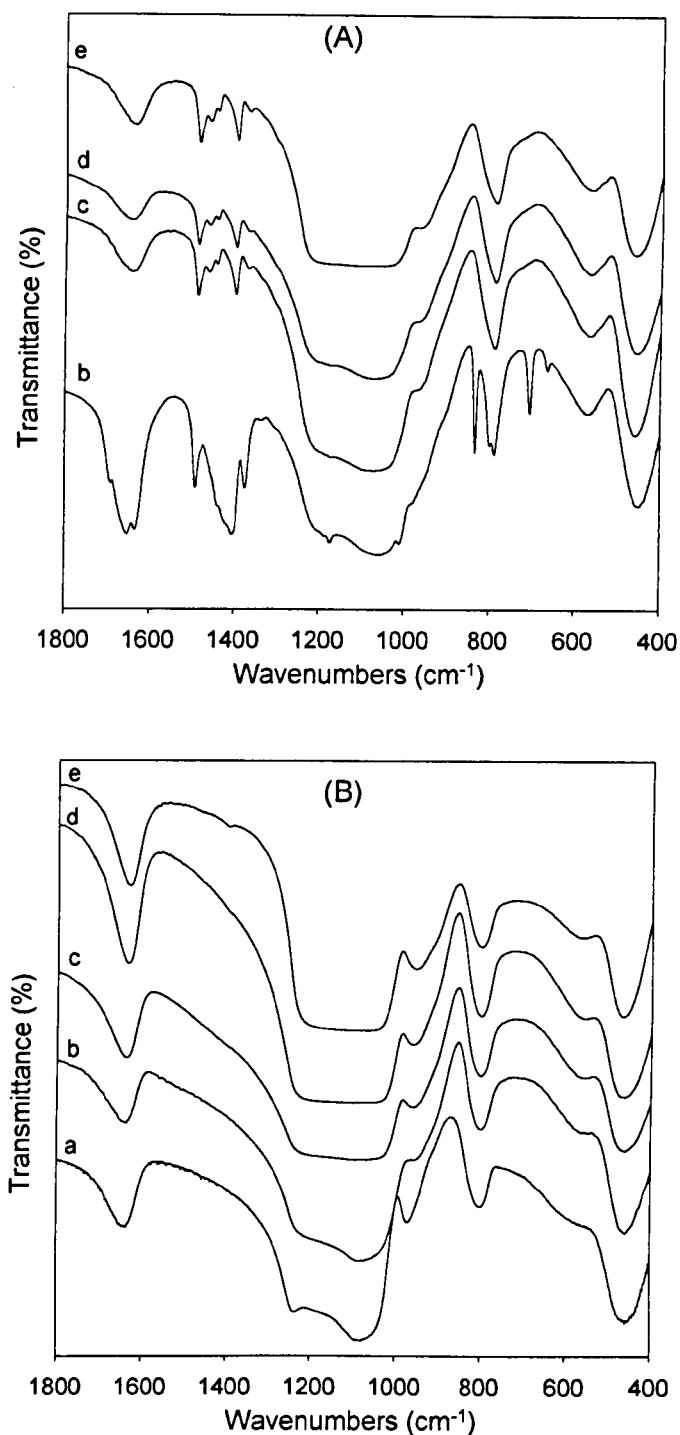


Figure 4.3 Infra-red spectra of (A) as-synthesised and (B) calcined aluminosilicate materials prepared from a zeolite BEA recipe; (b) MZBN-100, (c) MZBN-100w3h, (d) MZBN-100w3hd, (e) MZBN-100w5h, and for comparison (a) calcined Al-MCM-41.

The reduction in the TEA content in the washed sample is confirmed by TGA analysis as illustrated in Figure 4.4. The mass loss associated with the decomposition and burn-off of organic molecules (e.g. TEA) is between 120 and 350 °C. The mass loss due to burn off of organic matter is 38% for the as-synthesised MZBN-100 but reduces to 17% and 15% for samples washed for 3 h (MZBN-100w3h and MZBN-100w3hd, respectively). The sample washed for 5 h had lowest percentage reduction of 11%, which agrees well with IR spectra as well as powder XRD patterns and confirms that the washing step causes restructuring of MZBN-100.

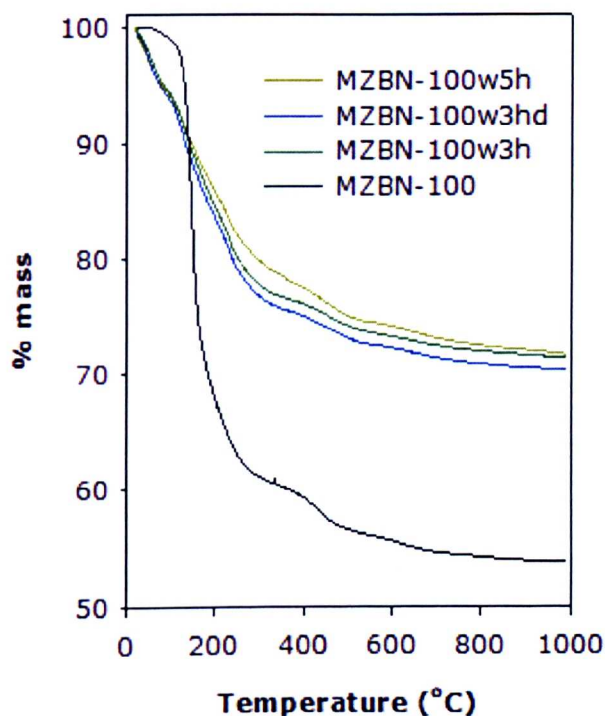


Figure 4.4 TGA curves of as-synthesised aluminosilicate mesophase materials prepared from a zeolite BEA recipe.

Framework Ordering

The IR spectra of as-synthesised MZBN-100 and the washed derivatives in Figure 4.3A allow probing of the nature of their frameworks. All the samples exhibit a well-developed band at 580 cm^{-1} that is indicative of six or five membered ring subunits of T-O-T (T = Si or Al) similar to subunits found in zeolites.^{9, 10, 41, 42} The IR peaks observed for the MZBN-100 samples are similar to those previously reported for mesoporous materials that possess zeolite building units.⁴³⁻⁴⁵ The zeolite building units do not appear to be adversely affected by washing prior to calcination. Furthermore, as shown in Figure 4.3B the IR peak at ca. 580 cm^{-1} is still observed for the calcined MZBN-100 sample although with reduced intensity. Further evidence for the presence of zeolite building units in the MBZN-100 sample was provided by comparing with conventional mesoporous materials (Al-MCM-41) as shown in Figure 4.3B (spectrum labelled a). The peak at ca. 580 cm^{-1} only remains as a weak shoulder in the IR spectrum of a conventional Al-MCM-41 sample (Figure 4.3B) The spectra in Figure 4.3 clearly show a distinction between the MZBN-X samples and conventional mesoporous materials (e.g. Al-MCM-41) that do not possess zeolite building units.

4.3.2 Silicate condensation in as-synthesised MZBN-100 sample and the washed derivatives

The extent of silicate condensation in the as-synthesised MZBN-100 and its washed derivatives was probed by ^{29}Si magic angle spinning (MAS) nuclear magnetic resonance (NMR). The ^{29}Si MASNMR spectra shown in Figure 4.5 exhibits three resonances at -90, -100, and -109 ppm which are assigned to silicon in $\text{Si}(\text{OSi})_2(\text{OH})_2$ (Q^2), $\text{Si}(\text{OSi})_3\text{OH}$ (Q^3) and $\text{Si}(\text{OSi})_4$ (Q^4) environments respectively. In addition there may also be Si in $\text{Si}(\text{OSi})_2(\text{OAl})(\text{OH})$ (-90 ppm) and $\text{Si}(\text{OSi})_3(\text{OAl})$ (-100 ppm) environments. Overall, the intensity of resonances indicates that most of the Si is in Q^3 and Q^4 environments with a greater proportion of Q^3 sites. The $\text{Q}^4/(\text{Q}^3+\text{Q}^2)$ ratio was used to estimate the extent of silicate condensation with a higher ratio signposting a more condensed framework. The calculated $\text{Q}^4/(\text{Q}^3+\text{Q}^2)$ for MZBN-100, MZBN-100w3hd, MZBN-100w3h and MZBN-100w5h was 0.48, 0.70, 0.79 and 0.92, respectively. The increasing trend with longer washing time is evidence for additional silicate condensation resulting in increased levels of condensation. The changes in the extent of silicate condensation are consistent with lattice expansion shown in Figure 4.1 and removal of TEA^+ species in IR spectra (Figure 4.3) and TGA curves (Figure 4.4) that occurs during the washing in boiling water. These changes involve expansion of the forming aluminosilicate framework whereby dissolved Si and Al species enable further growth and condensation.

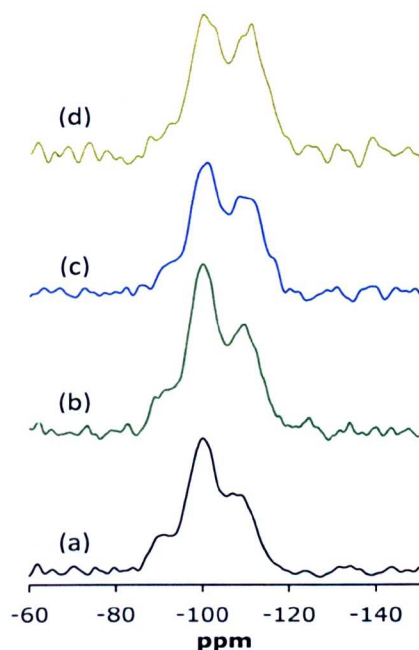


Figure 4.5 ^{29}Si MASNMR spectra of as-synthesised aluminosilicate materials prepared from a zeolite BEA recipe at 100 °C; (a) MZBN-100, (b) MZBN-100w3hd, (c) MZBN-100w3h, (d) MZBN-100w5h.

4.3.3 Aluminium content and acidity

The Al content of the samples is given as Si/Al ratio in Table 4.1. Sample MZBN-100 has a Si/Al ratio of 18.6, which was lower than the synthesis gel ratio of 25. The lower experimental Si/Al ratio is attributed to the preferential incorporation of Al into the aluminosilicate material which is a common phenomenon for direct (i.e. sol-gel) synthesised micro/mesoporous (zeolite or zeotype) aluminosilicates.^{23, 37, 38, 46-49} In all cases washing as-synthesised MBZN-100 resulted in increased Al content as evidenced by the decrease in the Si/Al ratio from 18.6 to 17.2, 16.9 and 15.9 for MZBN-100w3h, MZBN-100w3hd and MZBN-100w5h, respectively. The Si/Al ratio percentage increase of 8%, 9% and 15% after washing in boiling for 3 h, 3 h (200mL of water) and 5 h, respectively, is attributed to

expansion of aluminosilicate framework via dissolution and re-deposition of Al.

Figure 4.6 shows ^{27}Al magic angle spinning NMR spectra of as-synthesised and calcined MZBN-100 samples and their derivatives after washing for variable times. The spectrum of the as-synthesised MZBN-100 (Figure 4.6A) shows a sharp and symmetrical resonance centred at 53 ppm which arises from tetrahedrally coordinated Al in the mesoporous aluminosilicate framework with good symmetry. This implies that all Al in the as-synthesised MZBN-100 sample existed within the framework and that there was no extra-framework (octahedrally coordinated) Al. The spectrum of calcined MZBN-100 also exhibits one resonance at 53 ppm, which indicates that calcination did not cause any dealumination. Based on these findings, the aluminosilicate MBZN-100 sample was therefore stable after calcination. This makes the MZBN aluminosilicates very attractive in a manner similar to that of zeolites and very different from conventional mesoporous aluminosilicates.^{4, 5, 34-36, 50, 51}

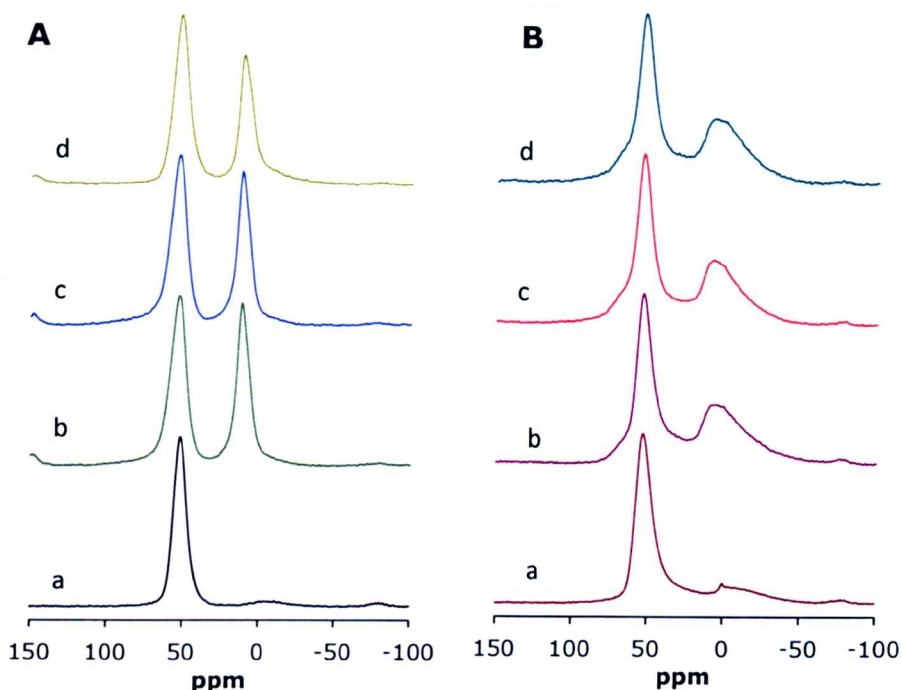


Figure 4.6 ^{27}Al MASNMR spectra of (A) as-synthesised and (B) calcined mesoporous aluminosilicate materials prepared from a zeolite BEA recipe; (a) MZBN-100, (b) MZBN-100w3hd, (c) MZBN-100w3h, (d) MZBN-100w5h.

In contrast, washing of as-synthesised MZBN-100 caused the formation of extra-framework Al as indicated by the peak centred at ca. 10 ppm for samples MZBN-100w3hd, MZBN-100w3h and MZBN-100w5h. However, upon calcination most of the extra-framework Al in the washed as-synthesised samples is re-inserted into the tetrahedral framework as shown in figure 4.6B. The overall picture that emerges from the ^{27}Al MASNMR spectra is that the Al in calcined samples is predominantly within framework positions. Such framework Al is expected to generate acid sites as shown by the acidity data in table 4.1. The samples have comparable acidity, with slightly higher acid content for the unwashed MZBN-100 sample. This is consistent with the NMR spectra in figure 4.6, i.e., that sample MZBN-100 has the highest content of framework Al. Although the

washed samples have a higher overall Al content (i.e., lower Si/Al ratio), some of the Al is in extra-framework sites that do not generate acid sites. What is, however, unexpected is that in all cases the total acidity and strong acidity values are similar, i.e., that the samples mainly possess strong acid sites. This is different from conventional mesoporous aluminosilicates, which usually possess a much lower proportion of strong acid sites.^{47, 52} the strong acidity is attributed to the presence of zeolite building units in the MZBN-100 samples in a manner similar to that observed for composite micro/mesoporous materials.²²

4.3.4 Morphology of the as-synthesised and calcined MZBN-100 sample

Figure 4.7 shows SEM images for the as-synthesised and calcined MZBN-100 sample. The images clearly show minimal framework modification after calcination. The SEM images for both as-synthesised and calcined MZBN-100 samples show flaky aggregated particles.^{53, 54} Calcination appears to cause an increase in the surface roughness of the particles. The smooth surface morphology of the as-synthesised aluminosilicate may be attributed to the presence of organic and occluded water molecules which are removed on calcination. Indeed, the calcined MZBN-100 samples show surface roughness which may be attributed to removal of surfactants and occluded water. The resultant morphology could also be ascribed to creation of larger mesopores and macropores or expansion of existing ones that link into each other to form larger mesopores or macropores.

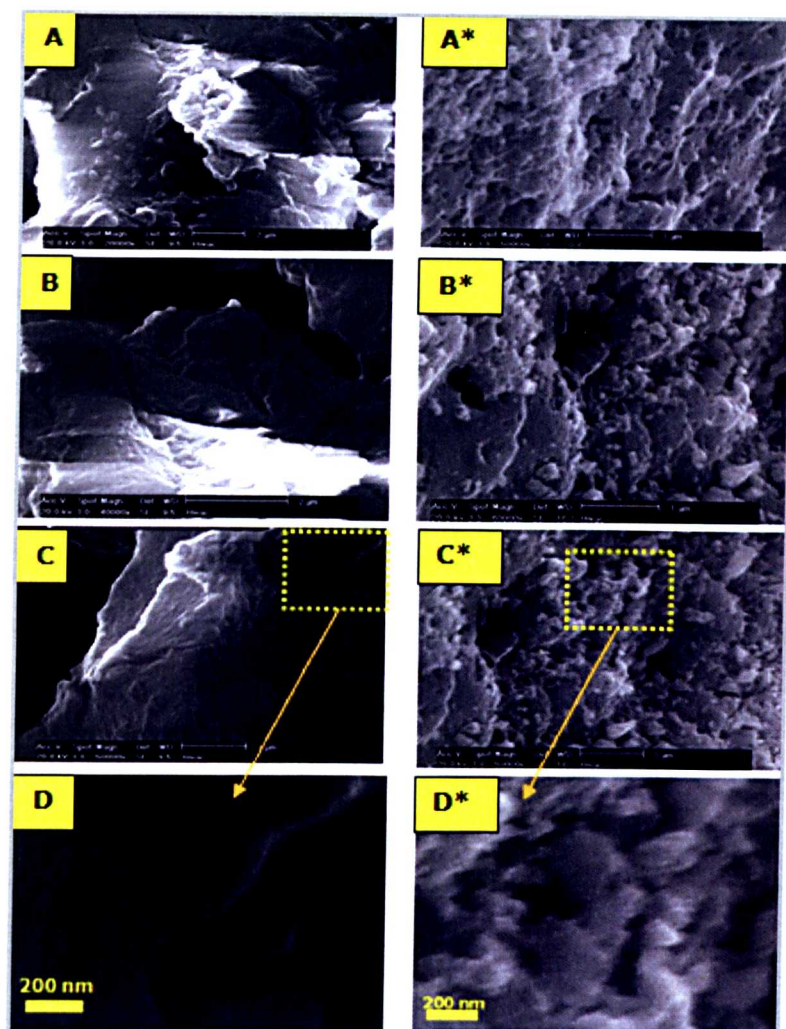


Figure 4.7 Scanning electron microscopy images of MZBN-100 samples; as-synthesised (A, B, C and D) calcined (A*, B*, C* and D*).

4.3.5 Porosity

The nitrogen sorption isotherms for the calcined MZBN-100 and its derivatives washed prior to calcination are shown in Figure 4.8A and the textural properties are summarized in Table 4.1. The adsorption-desorption isotherm for unwashed MBZN-100 sample is typical type IV isotherm with a mesopore filling step in the relative pressure (P/P_0) range 0.4 – 0.8 thus confirming the presence of mesoporosity.⁵⁵ An additional feature of the physisorption isotherms is the presence of hysteresis between the

adsorption and desorption branches that could be attributed to capillary condensation at partial pressures (P/P_0) greater than 0.4. The pore size distribution curves (obtained via BJH analysis of adsorption isotherm data) in Figure 4.8B show relatively uniform pores of size ca. 2.5 nm for sample MZBN-100. Analysis of pore size distribution using a Non Local Density Functional Theory (NLDFT) method (Figure 4.8C) indicated pore size of ca. 3.5 nm for sample MZBN-100. The disparity between the two methods is not unexpected since the BJH model is known to underestimate the pore size of mesoporous materials.⁵⁶⁻⁵⁸ Nevertheless, the pore size (2.5 – 3.5 nm) calculated from the nitrogen sorption data is similar to that (ca. 3.0 nm) obtained from the TEM images (Figure 4.2)

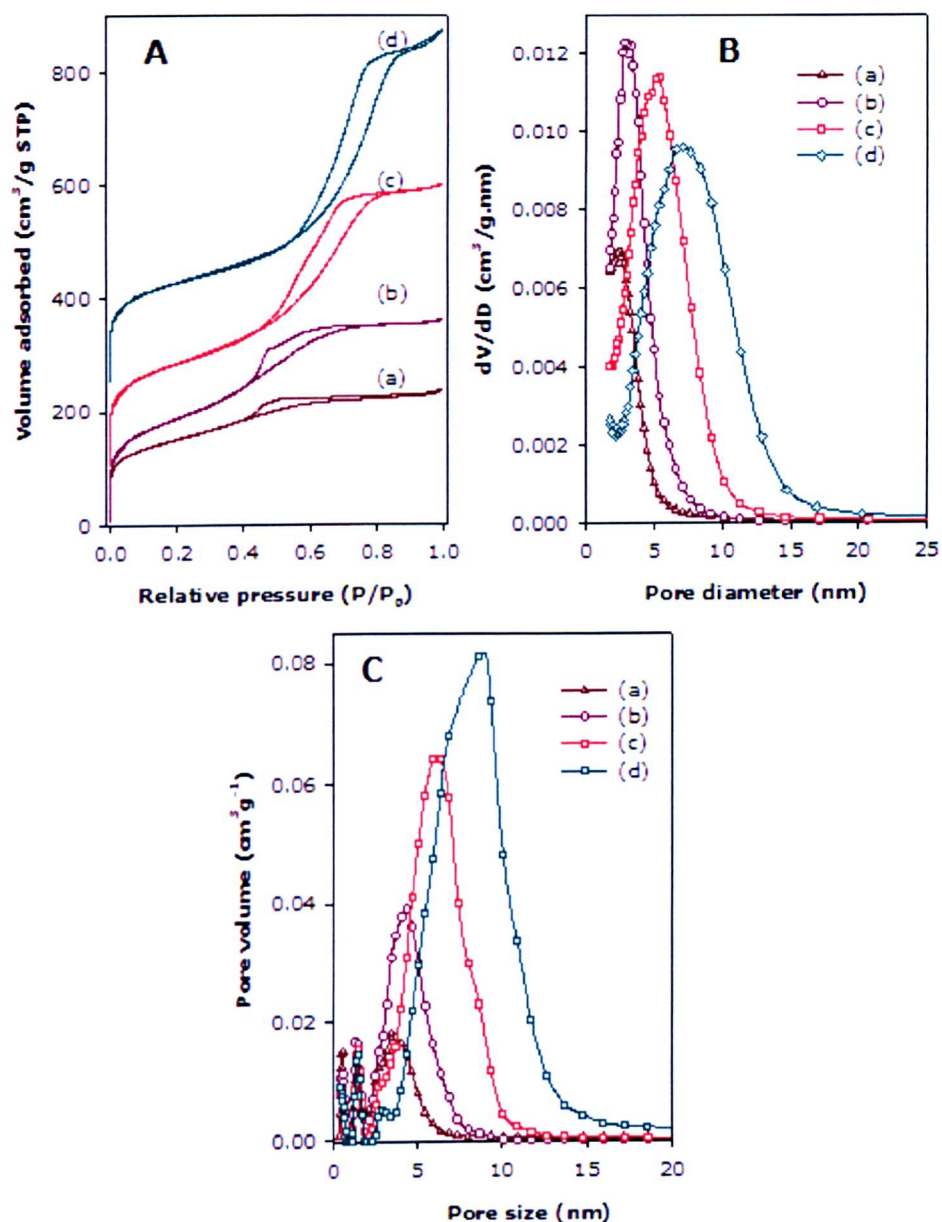


Figure 4.8 Nitrogen sorption isotherms (A) and corresponding pore size distribution curves obtained via the BJH (B) or NLDFT (C) models for mesoporous aluminosilicate materials prepared from a zeolite BEA recipe; (a) MZBN-100, (b) MZBN-100w3h, (c) MZBN-100w3hd (d) MZBN-100w5h. For clarity (a) isotherms c and d are offset (y-axis) by 100 cm³/g and 250 cm³/g, respectively.

Noteworthy is the lower value of the surface area ($527 \text{ m}^2/\text{g}$) and pore volume ($0.37 \text{ cm}^3/\text{g}$) of calcined MZBN-100 sample than expected for mesoporous materials.^{5, 34, 59} The relatively low textural properties of sample MZBN-100 may be attributed to the presence of zeolite units within the aluminosilicate framework, which increases framework density as previously reported.^{44, 60-63} The extent of microporosity in sample MZBN-100 is important given that it was prepared from a zeolite recipe. The micropore volume ($0.06 \text{ cm}^3/\text{g}$) contributes 16% to the total pore volume (Table 4.1), which suggests that sample MZBN-100 is predominantly mesoporous. The low level of microporosity is confirmed by NLDFT pore size distribution (Figure 4.8C), which shows very few pores with diameter smaller than 2.0 nm. These observations are at variance with what might be expected for a composite micro/meso material with a separate zeolite component.^{26-28, 43}

The nitrogen sorption isotherms of samples washed prior to calcination exhibit well developed mesopore filling step in the relative pressure (P/P_0) range of 0.4 – 0.8. The mesopore filling step is shifted to higher partial pressure depending on the washing duration (Figure 4.8A). Furthermore, the height of the mesopore filling step increases for longer washing duration, which is an indication of greater mesoporosity. The changes in porosity caused by washing are two-fold: (i) increase in pore size as shown in Figure 4.8B and 4.8C, and (ii) greater mesoporosity along with associated increases in surface area and pore volume. The pore size increases from ca. 2.5 nm for sample MZBN-100 to ca. 3.0 nm and 5.2 nm for MZBN-100w3h and MZBN-100w3hd, respectively, and 7.2 nm for MZBN-100w5h. It is interesting that sample MZBN-100w3h has a smaller pore size (compared to MZBN-100w3hd) despite a larger basal spacing.

This may suggest that sample MZBN-100w3h has thicker pore walls and that low amounts of water during the washing step (sample MZBN-100w3hd) favour expansion of pore size over formation of thicker walls as the aluminosilicate framework is restructured.

The increase in pore size is accompanied by a small rise in surface area (i.e. from 527 m²/g for MZBN-100 to between 625 and 667 m²/g for the washed samples) and much larger increase in pore volume from 0.37 cm³/g to between 0.56 and 0.96 cm³/g. It is also noteworthy that after washing the proportion of microporosity generally decreases, and in some cases (e.g., sample MZBN-100w3h) reduces to nil. The washing step therefore provides a route to modifying the textural properties of the present aluminosilicate samples.

4.3.6 Effect of Hydrothermal Synthesis Temperature

In order to assess the effect of crystallisation temperature and gain further insight into the mechanism of formation of the MZBN-x materials, the synthesis was performed at temperatures higher than 100 °C (i. e. 135 and 150 °C) and lower than 100 °C (i.e. 80, 50 and 25 °C)

Synthesis at temperatures higher than 100 °C

Figure 4.9 shows the nitrogen sorption isotherms (A) and corresponding PSD curves by both BJH (B) and NLDFT (C) methods. Calcined MBZN-135 (unwashed and washed prior to calcination) samples exhibit type IV isotherms with mesopore filling step in the relative pressure (P/P_0) range 0.4 – 0.9. The steep capillary condensation step is indicative of a narrow mesopore size distribution, which is confirmed by the PSD curves shown in Figure 4.9B and 4.9C.

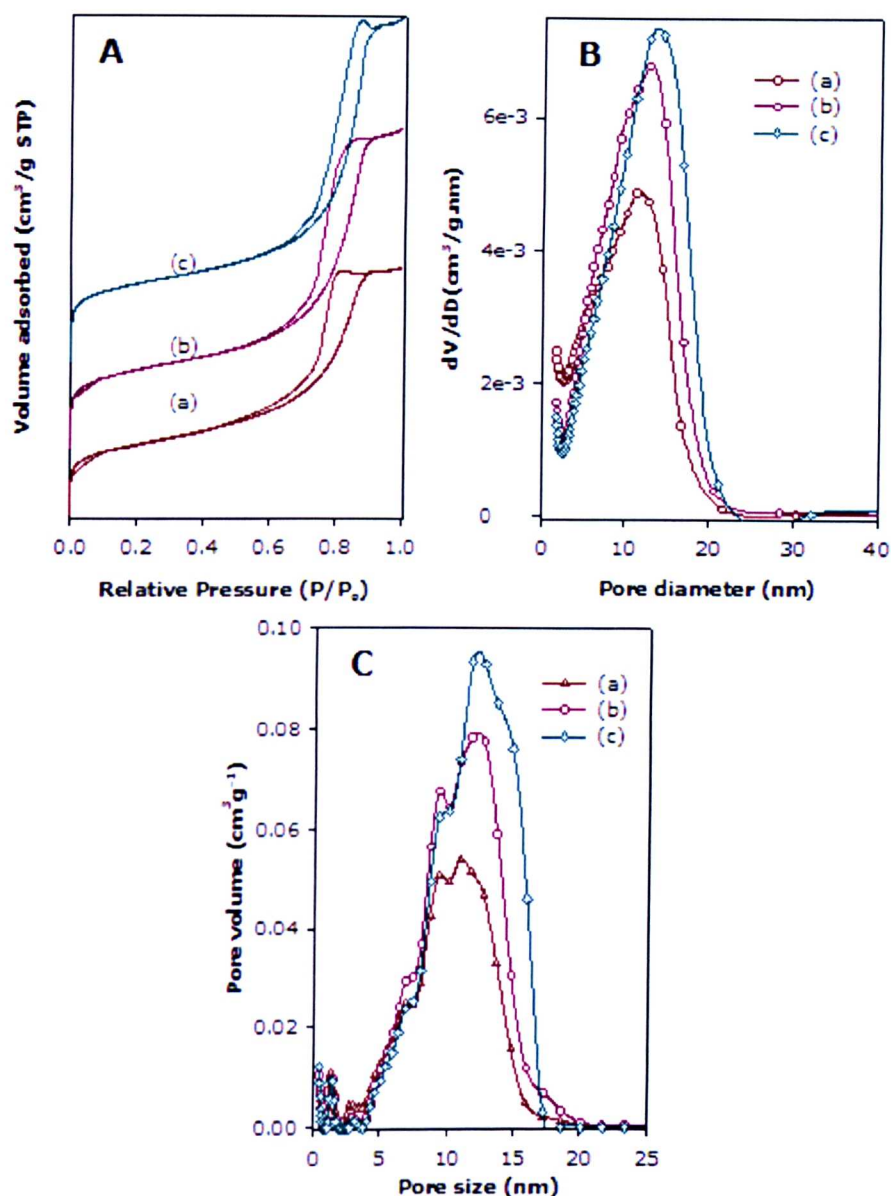


Figure 4.9 Nitrogen sorption isotherms (A) and corresponding pore size distribution curves obtained via the BJH (B) or NLDFT (C) models for mesoporous aluminosilicate materials prepared from a zeolite BEA recipe at 135 °C; (a) MZBN-135, (b) MZBN-135w3h, (c) MZBN-135w5h. For clarity in (A) isotherms b and c are offset (y-axis) by 100 cm^3/g and 250 cm^3/g , respectively.

The textural properties and elemental composition of MZBN-x samples prepared at higher crystallisation temperature are presented in Table 4.2.

The elemental composition remains relatively stable before and after washing. The unwashed MZBN-135 has a surface area of 468 m²/g (Table 4.2), which is comparable to that of sample MZBN-100 but double the pore volume (0.70 cm³/g compared to 0.37 cm³/g). This is due to the fact that the pore size of MZBN-135 (11.8 nm) is, as shown in Figure 4.9B and Figure 4.9C at least three times as large as that of MZBN-100. Washing of sample MZBN-135 prior to calcination only slightly increases the pore size to ca. 14.0 nm (Figure 4.9 and Table 4.2). The proportion of micropore volume (ca. 0.1 cm³/g) for MZBN-135 samples is ca. 12% of total pore volume, which is comparable to that of MZBN-100. Crystallisation at 135 °C therefore directly generates large pore mesoporous materials even without the washing step. It is, however, noteworthy that despite the higher temperature, the final phase is still a mesoporous rather than zeolitic microporous phase. It may be proposed that the higher crystallisation temperature increases the rate of formation of zeolite building units and speeds up their incorporation into a growing mesostructured aluminosilicate network 'templated' by TEA⁺ species via a scaffolding mechanism.¹⁸ Once formed, the growing aluminosilicate framework undergoes expansion (in a manner similar to that proposed above in section 4.3.1 for the MZBN-100 sample) during the extended crystallisation at 135 °C to generate a stable mesoporous framework with larger pores. IR spectra (Figure 4.10) indicated that the extent to which zeolite units are present in sample MZBN-135 (IR peak at ca. 580 cm⁻¹) is similar to that of sample MZBN-100 (Figure 4.3).

Table 4.2 Elemental composition and textural properties of zeotype aluminosilicate materials aged at 135 and 150 °C.

Sample	Si/Al ratio	Surface area (m ² g ⁻¹) ^a	Pore volume (cm ³ g ⁻¹) ^b	Pore size (nm) ^c
MZBN-135	13.2	468 (188)	0.70 (0.09)	11.8
MZBN-135w3h	15.0	514 (238)	0.91 (0.11)	12.4
MZBN-135w5h	14.7	498 (229)	0.97 (0.11)	13.8
MZBN4-135	16.0	509 (198)	0.43 (0.09)	5.2
MZBN4-135w3h	15.8	600 (161)	0.84 (0.07)	7.0
MZBN4-135w5h	15.2	559 (161)	0.81 (0.07)	7.4
MZBN-150	14.7	592 (428)	0.64 (0.20)	6.5
MZBN-150w3h	14.8	553 (462)	0.54 (0.22)	11.3
MZBN-150w5h	15.1	476 (394)	0.50 (0.19)	-

^aValues in parentheses are micropore surface area. ^bvalues in parentheses are micropore volume. ^c The values shown are pore size maxima obtained using BJH adsorption data.

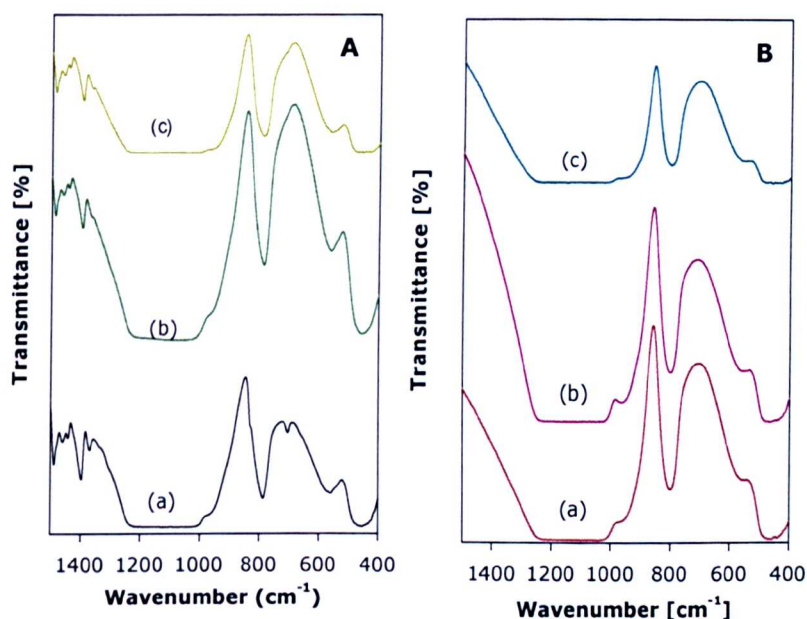


Figure 4.10 FT-IR spectra of (A) as-synthesised and (B) calcined aluminosilicate materials prepared at 135 °C; (a) MZBN-135, (b) MZBN-135w3h and (c) MZBN-135w5h.

The powder XRD patterns for the samples synthesised at 150 °C (designated MZBN-150) are shown in Figure 4.11. The patterns are typical for zeolite beta, which means that a zeolite rather than mesostructured material is formed at 150 °C.⁶⁴ Furthermore, the patterns of all the MZBN-150 samples (the unwashed and washed prior to calcination) in terms of peak intensity as well as resolution are comparable to each other. This is a good indication that the structural integrity of the zeolite beta units in the as-synthesised MZBN-150 are unchanged after both washing in boiling water and calcination.

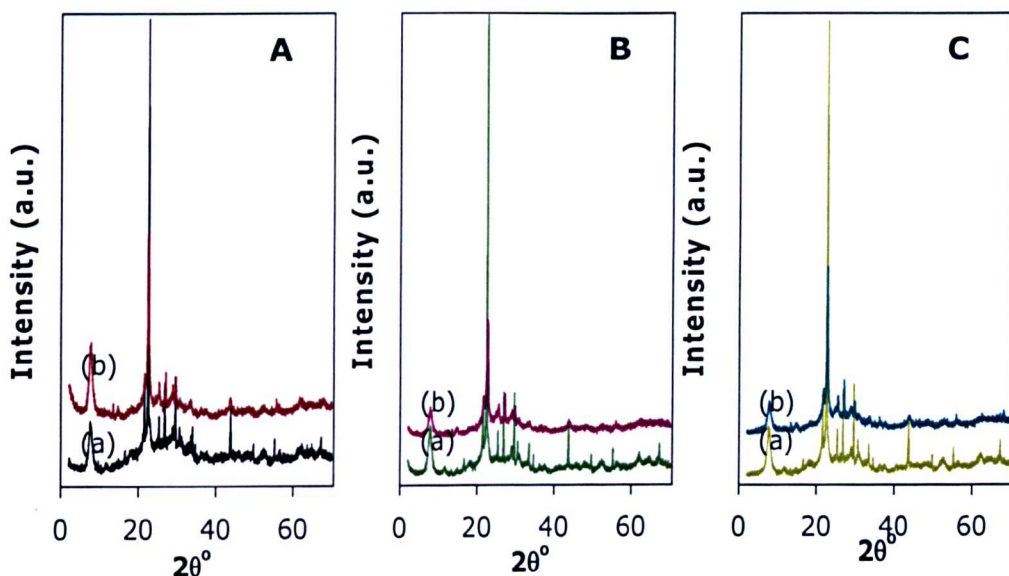


Figure 4.11 Powder XRD patterns of (a) as-synthesised and (b) calcined MZBN-150 aluminosilicate materials prepared from a zeolite BEA recipe at 150 °C; (A) directly calcined (sample MZBN-150), (B) washed for 3 h before calcination (MZBN-150w3h) and (C) washed for 5 h before calcination (MZBN-150w5h).

The MZBN-150 sample has a surface area of 592 m²/g (Table 4.2) and pore volume of 0.64 cm³/g. Washing of MZBN-150 sample prior to calcination

slightly reduces the surface area, pore volume and mesoporosity (Table 4.2). It is noteworthy that the micropore volume (ca. $0.2 \text{ cm}^3/\text{g}$) for MZBN-150 samples is 30 – 40% of the total pore volume, which is a much higher proportion than that of samples prepared at 100 and 135 °C.

Figure 4.12A shows the nitrogen sorption isotherms and corresponding PSD curves by BJH analysis (Figure 4.12B) and NLDFT method (Figure 4.12C). The sorption isotherm of calcined MZBN-150 is quite similar for the samples washed prior to calcination (MZBN-150w3h and MZBN-150w5h). All the three samples exhibit isotherms which are characterised by a well-developed micropore filling in the relative pressure (P/P_0) less than 0.02 due to micropore filling. Worth noting is a sharp increase in nitrogen uptake at high relative pressure ($P/P_0 > 0.9$) as shown in Figure 4.12A, indicative of a significant amount of interparticle mesoporosity.⁴⁶ The PSD curves in Figure 4.12B obtained via BJH analysis show mesopore size maxima for unwashed calcined MZBN-150 centred at ca. 6.5 nm which increases by ca. 74% after washing in boiling water for 3 h.

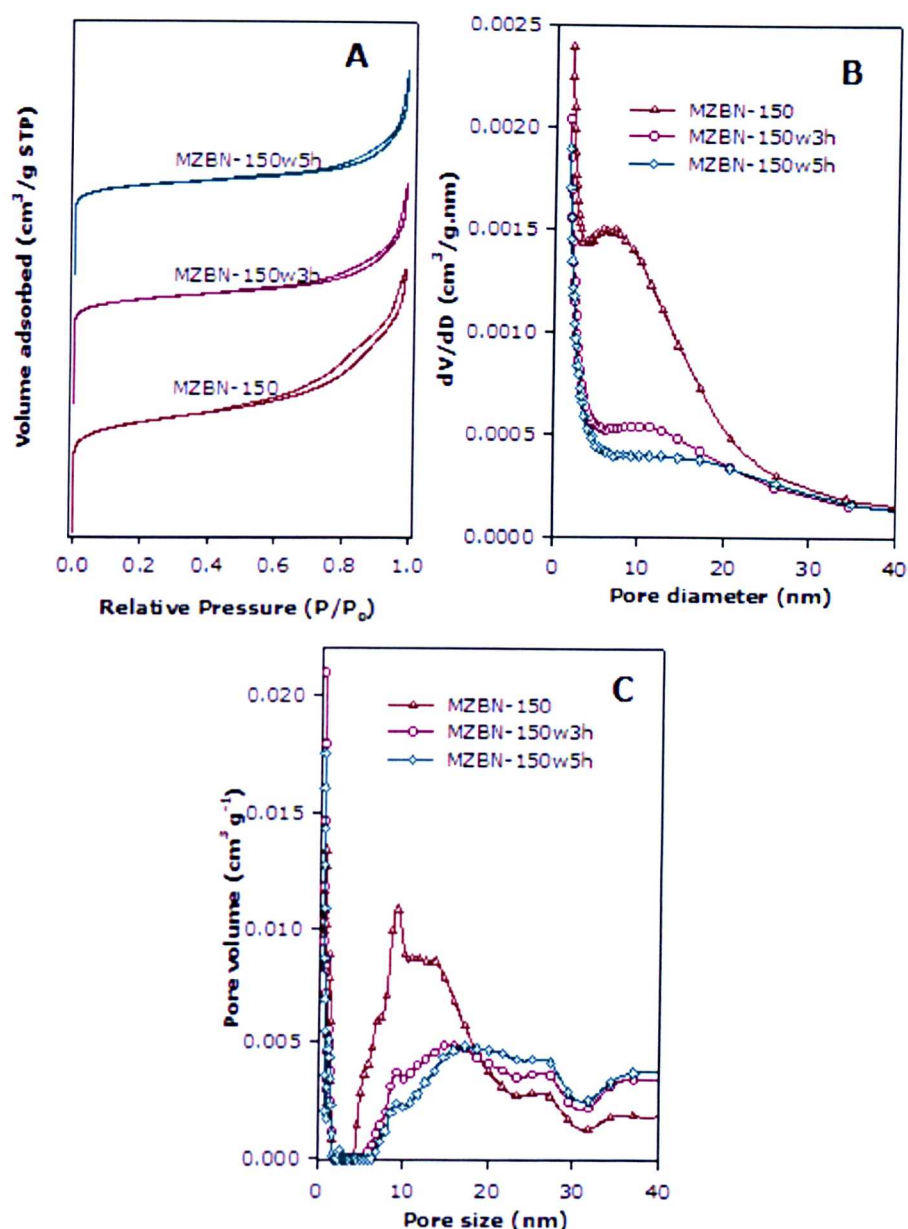


Figure 4.12 Nitrogen sorption isotherms (A) and corresponding pore size distribution curves obtained via the BJH (B) or NLDFT (C) models for mesoporous aluminosilicate materials prepared from a zeolite BEA recipe at 150 °C as indicated inset. For clarity isotherms in (A) for MZBN-150w3h and MZBN-150w5h are offset (y-axis) by 200 cm^3/g and 400 cm^3/g , respectively.

The significant proportion of microporosity in MZBN-150 samples was confirmed by NLDFT pore size distribution (Figure 4.12C). It appears therefore that crystallisation at a much high temperature (i.e., 150 °C) shifts the final material towards being microporous rather than mesoporous. Indeed the porosity of the MZBN-150 samples is similar to that of aggregated zeolite β nanocrystals.⁶⁵ It is therefore likely that crystallisation at 150 °C speeds up the rate of formation of zeolite β nanocrystals. Furthermore, the IR spectra of samples MZBN-150 (Figure 4.13) are fully consistent with the formation of a zeolitic material with several IR peaks between 400 and 600 cm^{-1} arising from well-formed zeolite β crystallites.^{9, 23, 37, 38, 41, 42} The data from the samples prepared at 135 and 150 °C, when compared to sample MZBN-100, demonstrate that there needs to be a balance between the Si/TEAOH ratio and crystallisation temperature in order to obtain mesoporous materials.

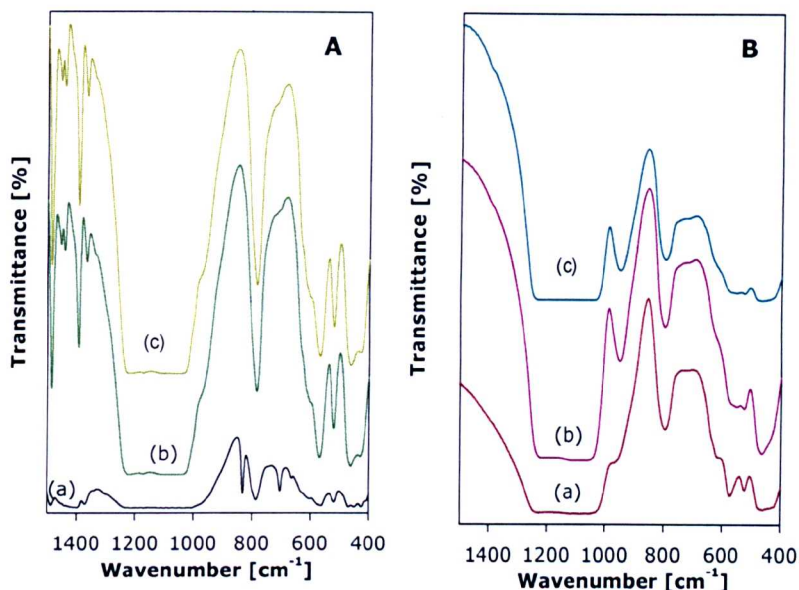


Figure 4.13 FT-IR spectra of (A) as-synthesised and (B) calcined aluminosilicate materials prepared from a zeolite BEA recipe at 150 °C; (a) MZBN-150, (b) MZBN-150w3h and (c) MZBN-150w5h. For clarity the spectra (a) MZBN-150w3h and (b) MZBN-150w5h offset (y-axis) by 0.1% and 0.4% transmittance, respectively.

Synthesis at temperatures lower than 100 °C

The need to balance Si/TEAOH ratio and crystallisation temperature in order to maintain mesoporosity of aluminosilicates synthesised is further supported by the fact that MZBN-X (where X = 50 or 80 °C) are all mesostructured. The textural properties and elemental composition of samples prepared at 25, 50 and 80 °C are shown in Table 4.3.

Table 4.3 Elemental composition and textural properties of various aluminosilicate materials denoted MZBN-x (as-prepared), MZBN-xw3h (washed for 3 h then calcined) and MZBN-xw5h (washed for 5 h then calcined) where x is the crystallisation temperature (25, 50 or 80 °C).

Sample	Si/Al ratio	Surface area (m ² g ⁻¹)	Pore volume (cm ³ g ⁻¹) ^b	Pore size (nm) ^c
MZBN-25	13.9	497 (228)	0.35 (0.11)	
MZBN-25w3h	12.1	644 (247)	0.47 (0.11)	
MZBN-25w5h	11.0	495 (141)	0.53 (0.06)	
MZBN-50	14.7	563 (242)	0.36 (0.11)	
MZBN-50w3h	13.1	660 (115)	0.68 (0.05)	4.2 (1.4 / 5.6)
MZBN-50w5h	14.0	538 (071)	0.52 (0.03)	3.5 (1.4 / 5.6)
MZBN-80	14.6	569 (170)	0.43 (0.08)	2.6 (4.5)
MZBN-80w3h	14.3	651 (180)	0.88 (0.08)	6.5 (6.8)
MZBN-80w5h	15.0	568 (158)	0.80 (0.07)	6.3 (6.8)

The values in parentheses represent: ^a micropore surface area, ^b micropore volume and ^cpore size maxima obtained using NLDFT analysis.

The FT-IR spectra in Figure 4.14 show that the MZBN-50 and MZBN-80 samples prepared at 50 and 80 °C, respectively, are quite similar to the samples prepared at 100 °C (MZBN-100). For example, the FT-IR peak at ca. 580 cm⁻¹ in Figure 4.3 and Figure 4.14, which indicates the presence of zeolite units, is comparable in samples prepared at 50°C (MZBN-50), 80 °C (MZBN-80) and 100 °C (MZBN-100).

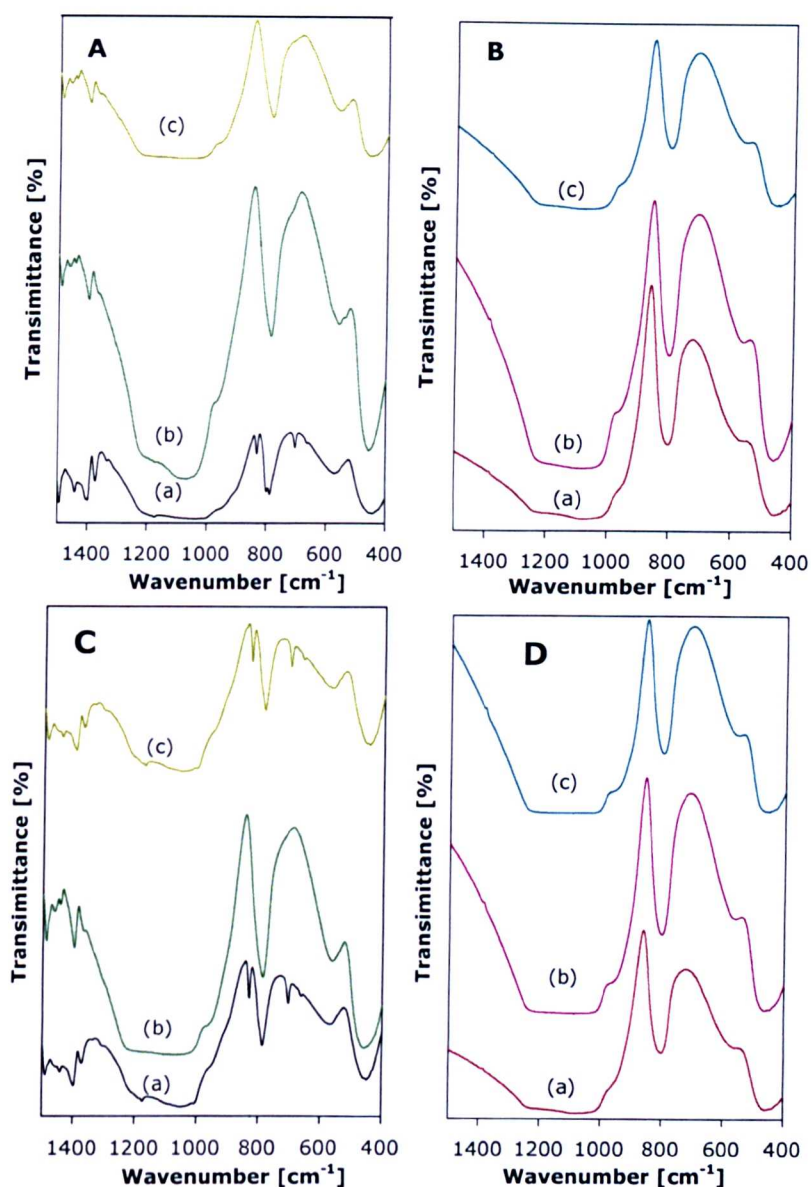


Figure 4.14 FT-IR spectra of (A and C) as-synthesised and (B and D) calcined aluminosilicate materials prepared from a zeolite BEA recipe at 50 and 80 °C, respectively: (a) MZBN-x, (b) MZBN-xw3h and (c) MZBN-xw5h (where x = 50 or 80 °C). For clarity the spectra (b) and (c) offset (y-axis) by 0.02% and 0.04% transmittance, respectively.

Nitrogen sorption isotherms and corresponding PSD curves for samples synthesised at temperatures lower than 100 °C are shown in Figure 4.15. All the samples exhibit mesopore filling in the relative pressure (P/P_0) range of 0.4 to 0.8 as shown in Figure 4.15A and 4.16A for MZBN-50 and

MZBN-80 samples, respectively. This is confirmed by the PSD curves shown in Figure 4.15B, 4.15C, 4.16B and 4.16C.

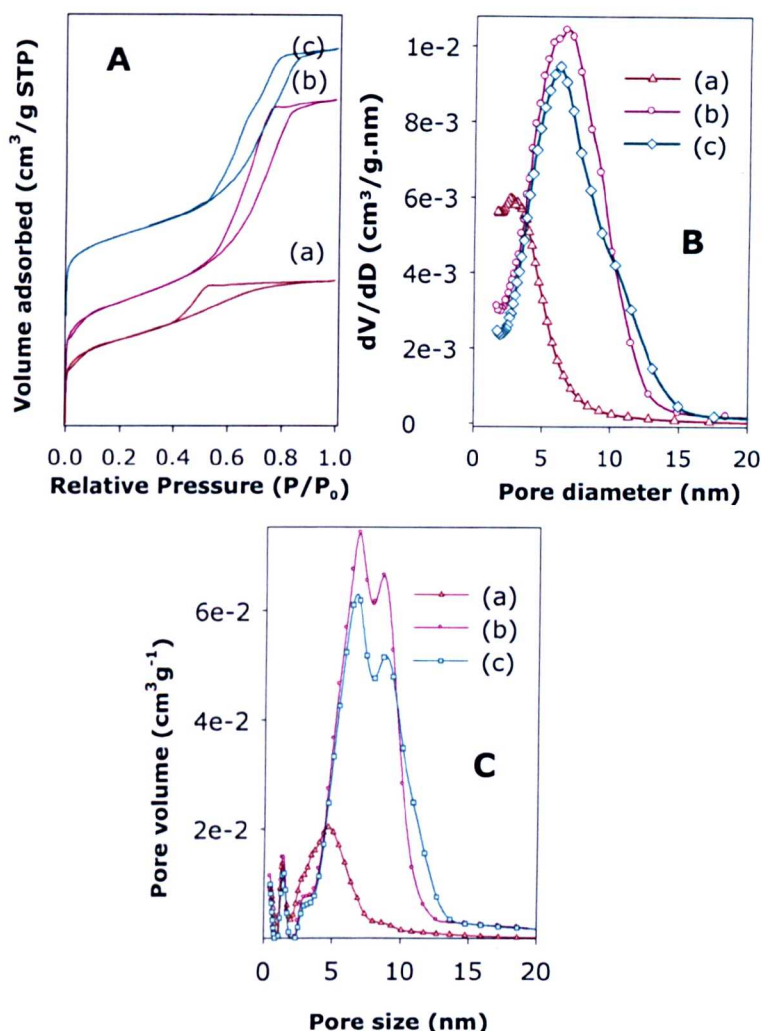


Figure 4.15 Nitrogen sorption isotherms (A) and corresponding pore size distribution curves obtained via the BJH (B) or NLDTF (C) models for mesoporous aluminosilicate materials prepared from a zeolite BEA recipe at 80 °C; (A) MZBN-80, (B) MZBN-80w3h and (C) MZBN-80w5h. For clarity in (A) isotherms b and c are offset (y-axis) by 50 cm³/g and 200 cm³/g, respectively.

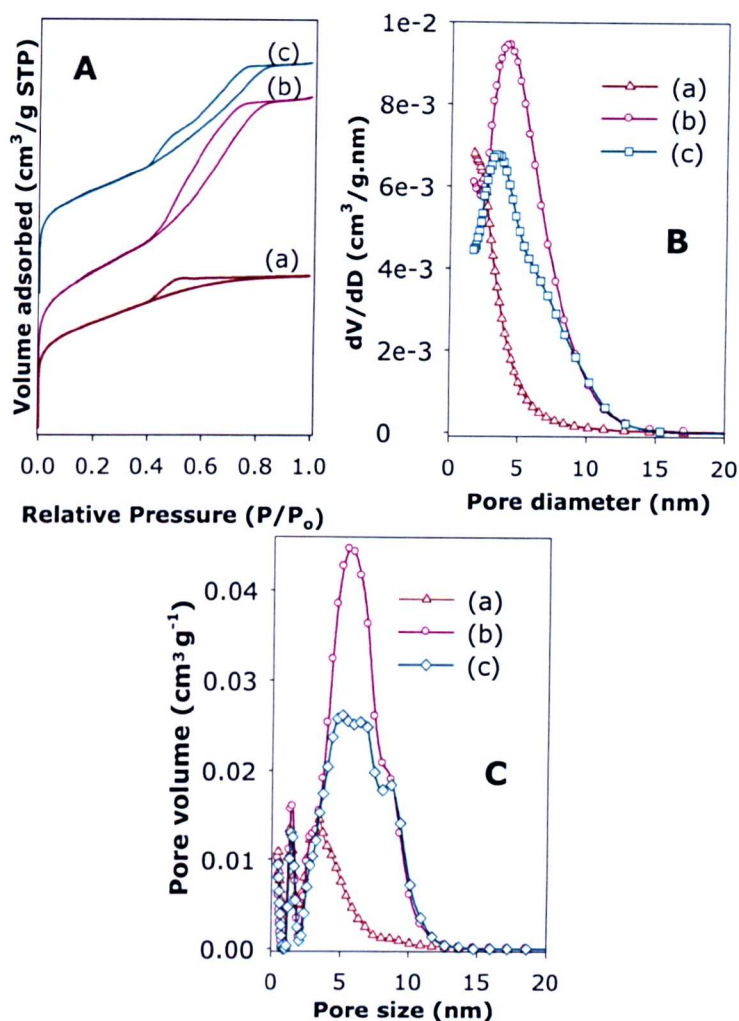


Figure 4.16 Nitrogen sorption isotherms (A) and corresponding pore size distribution curves obtained via the BJH (B) or NLDFT (C) models for mesoporous aluminosilicate materials prepared from a zeolite BEA recipe at 50 °C; (a) MZBN-50, (b) MZBN-50w3h and (c) MZBN-50w5h. For clarity in (A) isotherms b and c are offset (y-axis) by 50 cm^3/g and 200 cm^3/g , respectively.

Figure 4.17 shows nitrogen sorption isotherms with corresponding PSD curves for samples prepared at 25 °C that evidences the generation of porous materials with a wide pore size distribution. This is accompanied by negligible nitrogen uptake at relative pressures between 0.3 and 0.8 indicative of a population of non-uniformly sized pores (Figure 4.17A).

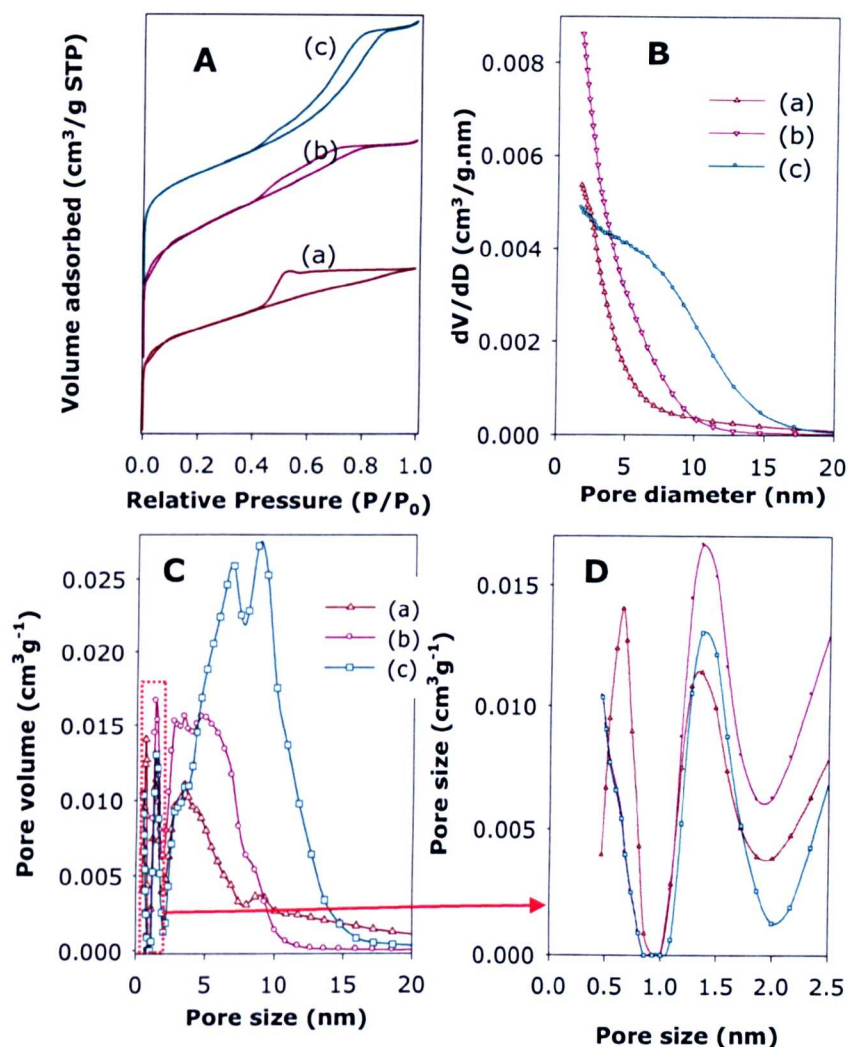


Figure 4.17 Nitrogen sorption isotherms (A) and corresponding pore size distribution curves obtained via the BJH (B) or NLDFT (C) models for mesoporous aluminosilicate materials prepared from a zeolite BEA recipe at 25 °C; (a) MZBN-25, (b) MZBN-25w3h and (c) MZBN-25w5h. For clarity in (A) isotherms b and c are offset (y-axis) by 50 cm³/g and 200 cm³/g, respectively.

The BJH pore size distribution curves of the sample synthesised at 25 °C (MZBN-25) and its washed derivatives presented in Figure 4.17B did not show any Gaussian pore size distribution in the mesopore range. This was contrary to the other samples synthesised at higher crystallisation temperatures which had distinct pore size maxima. However, NLDFT data (Figure 4.17C and 4.17D) confirmed that washing of MZBN-25 prior to calcination broadens the PSD even further to pore sizes greater than 2.5 nm. However, the pore size centred at ca. 1.4 nm (Figure 4.17D) did not change on washing. The unwashed calcined MZBN-25 gave a surface area of 497 m²/g (Table 4.3) with up to ca. 54% micropore surface area proportion and pore size maxima (Figure 4.17C) centred at ca. 0.6, 1.1 and 3.4 nm.

The Si/Al ratio of sample MZBN-25 decreases on washing (as shown in Table 4.3), from 13.9 by 13% (washed for 3 h) and 21% (washed for 5h). The calcined MZBN-25 sample and the washed derivatives had the lowest Si/Al ratio (highest Al content) compared to samples prepared at higher temperature. In addition, the results of FTIR studies of as-prepared MZBN-25 represented by plot (a) in Figure 4.18 show a weak 'noisy' and weak IR band at ca. 580 cm⁻¹. This could be ascribed to minimal presence of zeolite building units unlike in the case of the samples synthesised at higher temperatures.

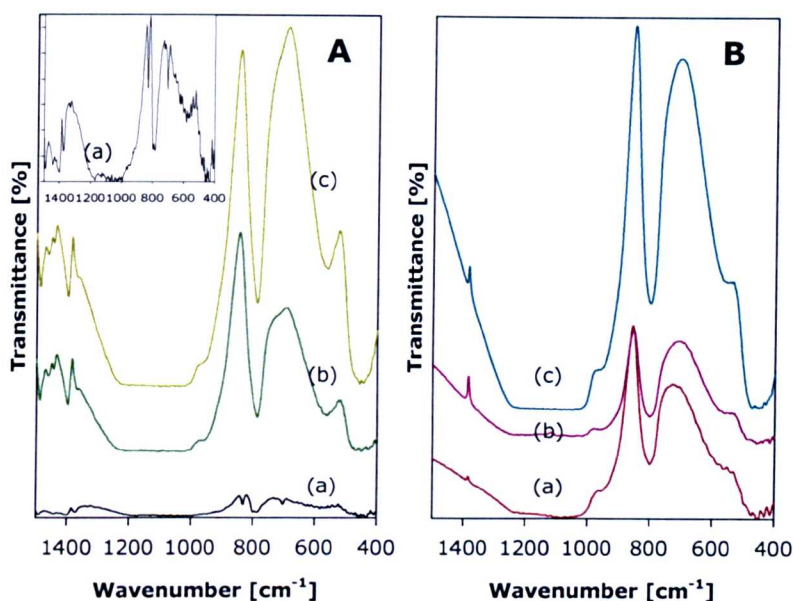


Figure 4.18 FT-IR spectra of (A) as-synthesised and (B) calcined aluminosilicate materials prepared from a zeolite BEA recipe at 25 °C; (a) MZBN-25, (b) MZBN-25w3h and (c) MZBN-25w5h. For clarity the spectra (b) and (c) offset (y-axis) by 0.02% and 0.04% transmittance, respectively.

The variable temperature synthesis data, therefore, suggests that mesostructured aluminosilicate materials may be obtained from zeolite BEA recipe for synthesis temperatures between 50 and 135 °C. The pore size generally increases with synthesis temperature, although it can also be modified by washing prior to calcination. A higher crystallisation temperature of 150 °C generates a predominantly microporous zeolite β material. The crystallisation temperature does not, however, have any significant effect on the Si/Al ratio as shown in Table 4.1, 4.2 and 4.3. The synthesis conditions were modified in order to assess the effect of Si /TEAOH ratio on mesostructural framework ordering as discussed in section 4.3.8.

4.3.7 Hydrothermal Stability of calcined MZBN-100 and its derivatives washed prior to calcination

Higher hydrothermal stability of zeolites is one of the key advantages over mesoporous silicates. Hydrothermal stability is a critical property for mesoporous aluminosilicates because many of their applications may require use in hot aqueous media^{2, 51, 66} The hydrothermal stability of MZBN-100 samples was assessed by refluxing in water for 6 or 120 h. Figure 4.19 shows the nitrogen sorption isotherms with corresponding PSD curves on the right hand side of the samples before and after 6 h refluxing in water. It is clear that all the samples exhibit high hydrothermal stability; the isotherms of the refluxed samples exhibit a well-developed mesopore filling step characteristic of well-ordered mesoporous materials. Furthermore in all cases the height of the mesopore filling step increases after refluxing. The hydrothermal treatment therefore enhances mesoporosity, which is a rather unusual observation since most mesostructured aluminosilicates undergo some diminution of mesoporosity when refluxed in water.^{9, 13, 45, 51, 67-69}

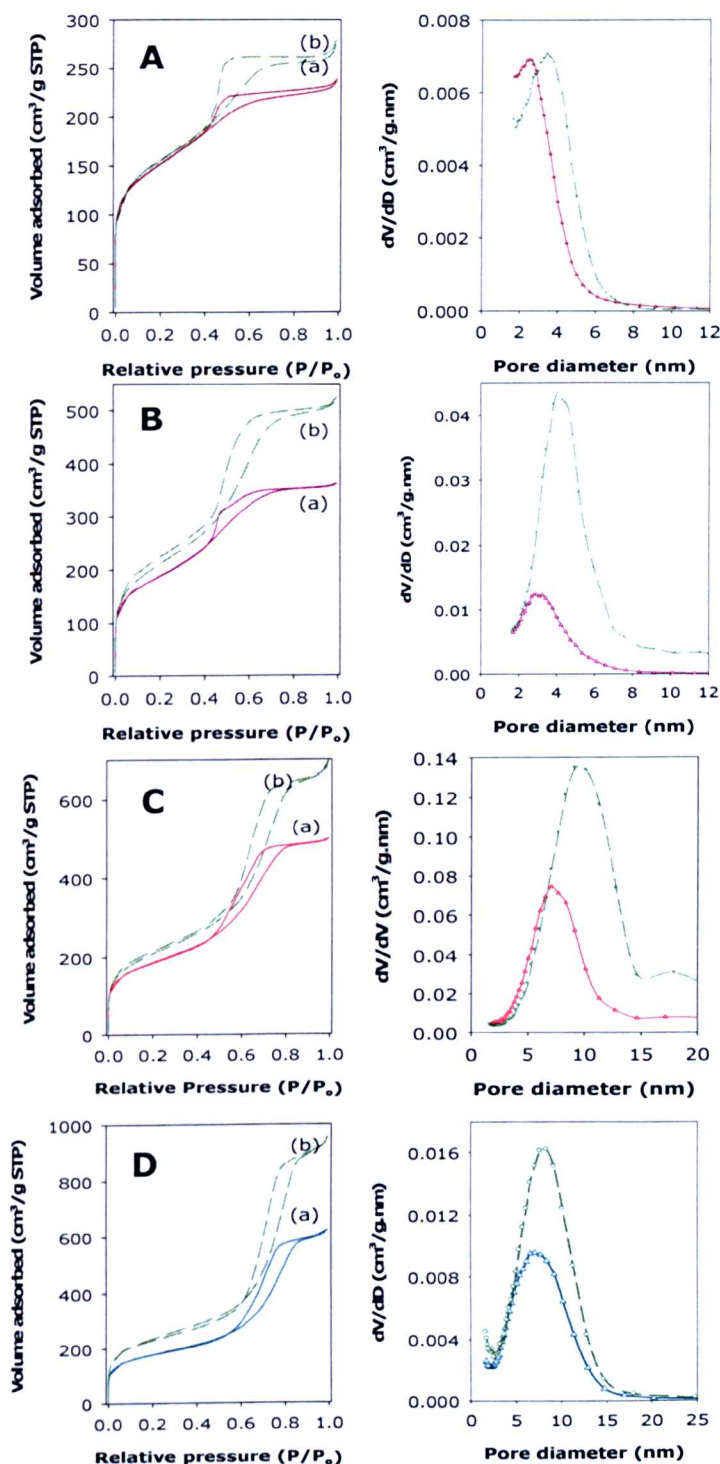


Figure 4.19 Nitrogen sorption isotherms (on left hand side) and corresponding PSD curves obtained via BJH model (on the right hand side) of calcined MZBN-100 samples before (a) and after (b) refluxing in water; (A) MZBN-100, (B) MZBN-1003wh, (C) MZBN-100w3hd and (D) MZBN-100w5h. The refluxed samples are designated with prefix R.

The textural parameters of the samples after hydrothermal treatment are given in Table 4.1. In all the cases, the hydrothermal treatment results in an increase in pore size while still retaining a narrow pore size distribution as shown in Figure 4.19. Similarly, pore size distribution curves by NLDFT shown in Figure 4.20 provide further evidence of well controlled distribution of pore sizes after refluxing. It is worth noting that the sum effect of washing the as-synthesised material in combination with refluxing after calcination is that the pore size of sample MZBN-100 can be tailored between 2.5 and 8.8 nm.

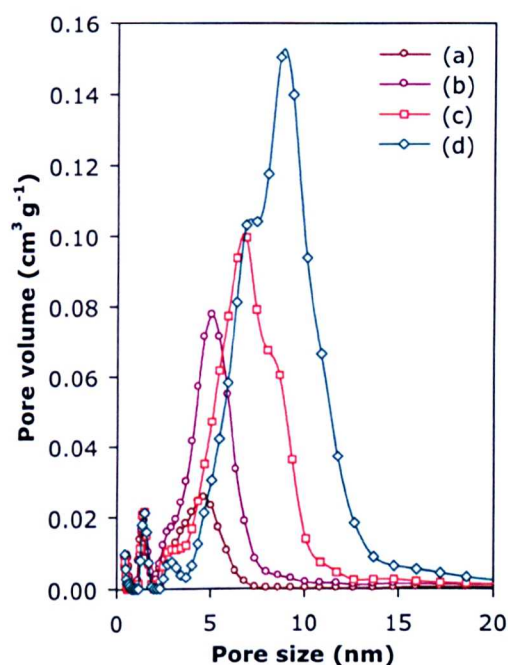


Figure 4.20 Non Local Density Functional Theory (NLDFT) pore size distribution curves for MZBN-100 mesoporous aluminosilicate materials prepared from a zeolite BEA recipe at 100 °C after refluxing; (a) RMZBN-100, (b) RMZBN-100w3hd, (c) RMZBN-100w3h, (d) RMZBN-100w5h.

The surface area increases after refluxing with sample MZBN-100w5h exhibiting the greatest increase (35%) from 625 to 838 m²/g. The pore

volume also shows increases of 16% for MZBN-100, ca. 40% for MZBN-100w3h and MZBN-100w3hd and 54% for MZBN-100w5h. The proportion of microporosity is not affected by refluxing.

Extending the hydrothermal testing (refluxing) time to 120 h has no effect on the mesoporosity of the materials as shown in Figure 4.21. Sample MZBN-100 refluxed for 120 h had a surface area of 506 m²/g and pore volume of 0.4 cm³/g, with micropore volume of 0.03 cm³/g. These values are similar to those of the parent MZBN-100, which attests to the high hydrothermal stability of the MZBN-x aluminosilicate materials.

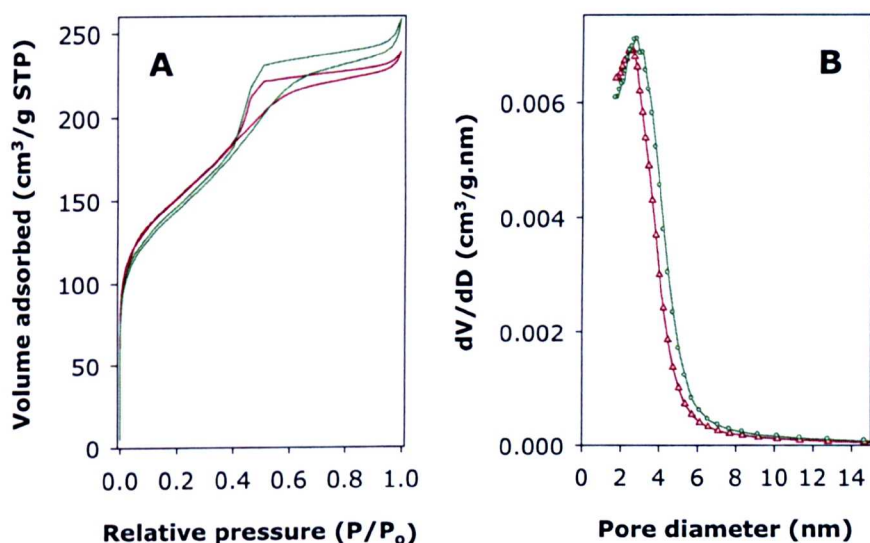


Figure 4.21 Nitrogen sorption isotherms (A) and corresponding pore size distribution curves obtained via BJH model (B) of calcined mesoporous aluminosilicate material MZBN-100 before (dark red) and after refluxing in water for 120 h.

The Si/Al ratio of the samples reduces after refluxing as shown in Table 4.1. The Al content per gram of material increases for the refluxed samples by ca. 30% due to removal of amorphous silica during the refluxing. Removal of amorphous silica (which is not part of the mesoporous

aluminosilicate structure) would explain both the increase in Al content and the textural changes. If such silica is within the pores, removal would lead to an apparent increase in pore size and pore volume as observed. The ^{27}Al MASNMR spectra of the MZBN-100 samples do not show remarkable change after refluxing (Figure 4.22), exhibiting a sharp resonance at ca. 53 ppm, from tetrahedrally coordinated Al in the aluminosilicate framework, and a low intensity resonance at ca. 5 ppm from octahedrally coordinated non-framework Al. The ratio of tetrahedral to octahedral Al is unaffected by the refluxing. This indicates that refluxing does not cause any dealumination, meaning that MZBN-type materials are stable to hydrothermal treatment (refluxing), which is unlike conventional mesoporous aluminosilicates.^{4, 35, 46-48, 50}

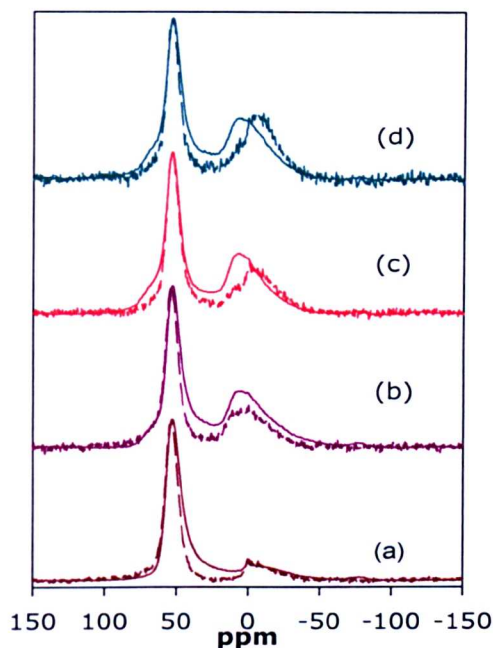


Figure 4.22 ^{27}Al MASNMR spectra of calcined mesoporous aluminosilicate materials prepared from a zeolite BEA recipe before (solid line) and after (refluxing in water for 6 h (dashed line); samples before refluxing (a) MZBN-100, (b) MZBN-100w3hd, (c) MZBN-100w3h, (d) MZBN-100w5h. While after refluxing a prefix R is used for designation: for example MZBN-100 after refluxing is denoted RMZBN-100.

The acidity of the refluxed samples increases significantly and in most cases more than doubles as shown in Table 4.1. The increase in acidity per weight of sample is not unexpected given that the Al content increases and the fact that the refluxing causes no dealumination. However, the increase in acidity is much higher than the rise in Al content, which indicates that some of the acid sites may have been blocked by silica before refluxing. Removal of the silica not only increases the acid content per given weight of sample but also unblocks some acid sites. Overall, the data of the refluxed samples show that the MZBN-type materials are very stable to hydrothermal treatment.

4.3.8 Effect of SiO₂ : TEAOH ratio on mesostructural framework

The role of organic molecules in zeolite synthesis can be classified into at least three categories, namely: space filling, structure directing and templating. For example, Lok and co-workers suggested that organic cation not only fit into the cages, but also on many instances occupy the channel space of the molecular sieves.⁷⁰ The as synthesised sample prepared in this section was aged at crystallisation temperature of 135 °C (designated as MZBN4-135). The choice of this temperature was due to the fact that samples previously prepared at 135 °C (MZBN-135) with SiO₂ : TEAOH ratio of 2.8 showed minimal structural modification on washing in boiling water.

The nitrogen sorption isotherms for MZBN-135 and MZBN4-135 samples with SiO₂ : TEAOH ratio of 2.8 and 4, respectively are shown in Figure 4.22. As expected all the aluminosilicates (unwashed calcined MZBN4-135 and its washed derivatives; MZBN4-135w3h and MZBN4-135w5h) exhibit type IV isotherms. The nitrogen sorption isotherms of MZBN4-135 prior to washing exhibit well developed mesoporosity with mesopore filling in the relative pressure (P/P_0) range 0.4 to 0.8. The mesopore filling step shifted to a higher partial pressure on washing for 3 h (MZBN4-135wh3) and 5 h (MZBN4-135w5h) to 0.5 to 0.9 and 0.6 to 0.9, respectively. The pore size distribution profiles in Figure 4.23 are consistent with type H1 hysteresis, which indicate multi-layer adsorption with capillary condensation step. Such narrow pore size distribution profile (labelled b in Figure 4.23) show that the material has cylindrical pore geometry and a high degree of pore size uniformity.⁵⁵ The pore volume of unwashed calcined MZBN4-135 (0.43 cm³/g) was lower by 39% when compared with MZBN-135.

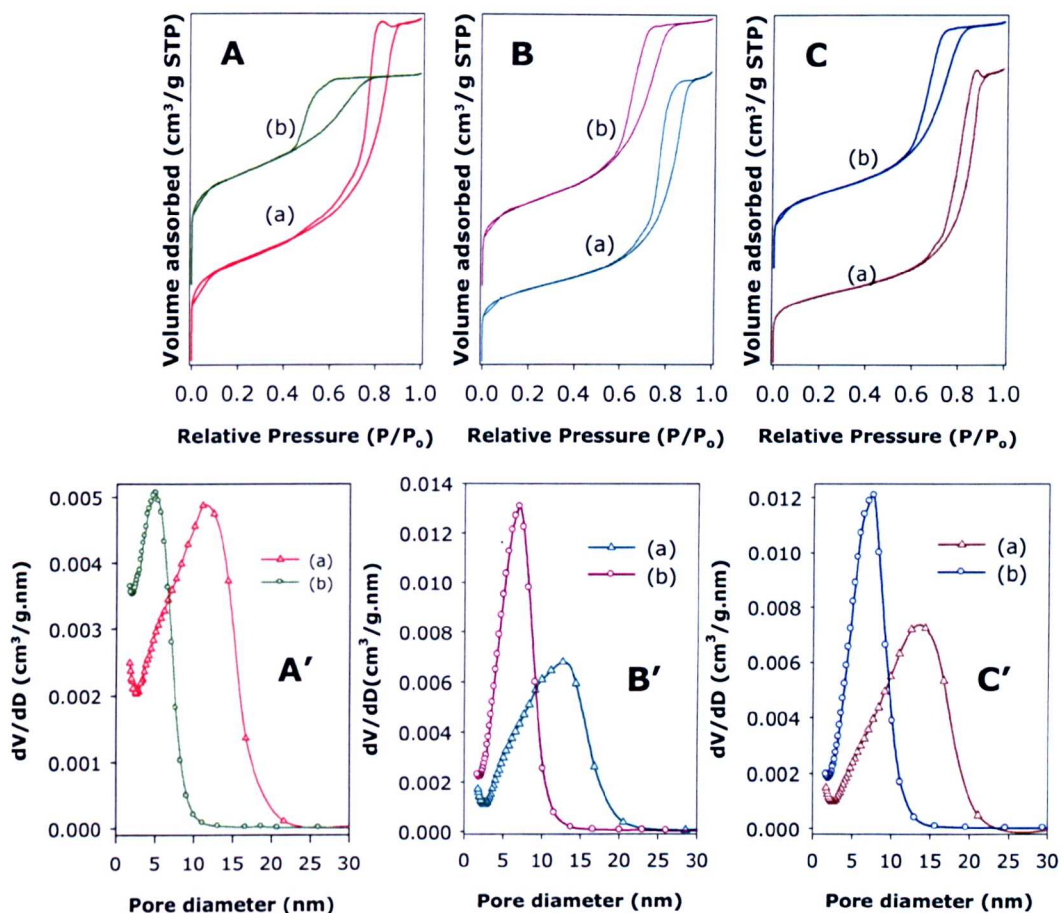


Figure 4.23 Nitrogen sorption isotherms (a, b and c) and corresponding pore size distribution curves (a', b' and c') for calcined aluminosilicate materials for unwashed (A and A') and washed for 3 h (B and B') and 5 h (C and C') prior to calcination from a zeolite BEA recipe at 135 °C with SiO₂ : TEAOH ratio of (a) 2.8 and (b) 4, respectively.

The textural properties and elemental composition of calcined MZBN4-135 and its derivatives washed prior to calcination are presented in Table 4.2. Generally, the samples prepared at SiO₂ : TEAOH ratio of 4 had higher surface area than their equivalents prepared at SiO₂ : TEAOH ratio of 2.8. For example, sample MZBN4-135 had a surface area of 498 m²/g which is 6% higher compared with MZBN-135. Also worth pointing out is the lower

pore size for MZBN4-135 series with the unwashed sample being lower by more than half at 5.2 nm.

The as-synthesised mesophase shows FI-IR peaks (Figure 4.24) at 660 to 840 cm^{-1} that are ascribed to the TEA^+ species.³⁹ In addition, there is a band at ca. 580 cm^{-1} characteristic of the five-ring T-O-T structure in zeolite where T = Si or Al^{43, 71} that explicitly indicates formation of zeolitic building units.

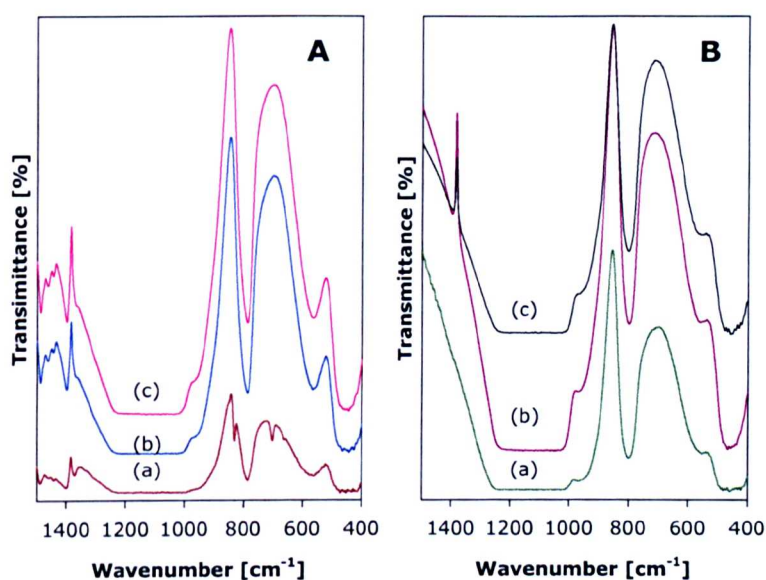


Figure 4.24 FT-IR of (A) as-synthesised and (B) calcined aluminosilicate materials prepared from a zeolite BEA recipe at 135 °C with SiO_2 : TEOH ratio 4; (a) MZBN4-135, (b) MZBN4-135w3h and (c) MZBN4-135w5h. For clarity spectra (b) and (c) are offset (y-axis) by 0.02% and 0.04% transmittance respectively.

4.4 Summary

Mesoporous aluminosilicates with tuneable porosity have been successfully prepared under conditions similar to those typically used for the preparation of zeolites. The synthesis route was modified by a low crystallisation temperature and a high Si/TEOH ratio. The prepared aluminosilicates exhibit mesostructural ordering as evidenced by TEM

micrographs and powder XRD patterns. Generally, the data for refluxed samples show that the MZBN-type materials are very stable to hydrothermal treatment and also exhibit strong acidity. This contrasts with most amorphous mesoporous aluminosilicates which have several limitations including poor hydrothermal stability, weak acidity and low ion exchange capacity.^{35, 51}

The textural parameters of the present mesoporous aluminosilicates varied on washing prior to calcination which allowed pore size and pore size distribution modification. For example, the pore size of MZBN-100 series was tailored to between 2.5 and 14.0 nm while the surface area increased after refluxing with MZBN-5h exhibiting the greatest increase from 625 to 838 m²/g. The surface area of a sample prepared at crystallisation temperature of 135 °C was comparable to the sample prepared at 100 °C though the former exhibited higher pore volume. In contrast the sample prepared at 150 °C had characteristics similar to those of zeolite beta.

Overall the data obtained from the prepared materials show that the MZBN-type samples are very stable to hydrothermal treatment. Therefore, the synthesis procedure reported in this chapter avoids the use of surfactant template and directly generates acid sites on calcination. Such acidic sites coupled with hydrothermal stability are critical for applications in catalysis.

4.5 Bibliography

1. M. E. Davis, *Chem. Euro. J.*, 1997, **3**, 1745-1750.
2. M. E. Davis, *Nature*, 2002, **417**, 813-821.
3. C. C. Freyhardt, M. Tsapatsis, R. F. Lobo, K. J. Balkus and M. E. Davis, *Nature*, 1996, **381**, 295-298.
4. J. S. Beck, J. C. Vartuli, W. J. Roth, M. E. Leonowicz, C. T. Kresge, K. D. Schmitt, C. T. W. Chu, D. H. Olson, E. W. Sheppard, S. B. McCullen, J. B. Higgins and J. L. Schlenker, *J. Am. Chem. Soc.*, 1992, **114**, 10834-10843.
5. G. Øye, J. Sjöblom and M. Stöcker, *Adv. Coll. Int. Sci.*, 2001, **89-90**, 439-466.
6. A. Karlsson, M. Stöcker and R. Schmidt, *Microporous Mesoporous Mater.*, 1999, **27**, 181-192.
7. K. Richard Kloetstra and J. C. Jansen, *Chem. Commun.*, 1997, 2281-2282.
8. D. Trong On and S. Kaliaguine, *Angew. Chem.*, 2001, **113**, 3348-3351.
9. Y. Liu, W. Z. Zhang and T. J. Pinnavaia, *J. Am. Chem. Soc.*, 2000, **122**, 8791-8792.
10. Y. Liu, W. Z. Zhang and T. J. Pinnavaia, *Angew. Chem.-Int. Edit.*, 2001, **40**, 1255-1258.
11. J. Čejka, A. Corma and S. Zones, eds., *Zeolite and Catalysis; Synthesis, Reactions and Applications*, WILEY-VCH Verlag GmbH & Co. KGaA, Weinheim, 2010.
12. S. C. Christiansen, D. Zhao, M. T. Janicke, C. C. Landry, G. D. Stucky and B. F. Chmelka, *J. Am. Chem. Soc.*, 2001, **123**, 4519-4529.
13. R. Mokaya, *Chem. Commun.*, 2001, 633-634.

14. L.-Q. Wang and G. J. Exarhos, *J. Phys. Chem. B*, 2002, **107**, 443-450.
15. Y. Xia and R. Mokaya, *Microporous Mesoporous Mater.*, 2006, **94**, 295-303.
16. Y. Xia and R. Mokaya, *J. Phys. Chem. B*, 2006, **110**, 9122-9131.
17. Y. Xia, R. Mokaya and J. J. Titman, *J. Phys. Chem. B*, 2004, **108**, 11361-11367.
18. J. C. Jansen, Z. Shan, L. Marchese, W. Zhou, N. von der Puil and T. Maschmeyer, *Chem. Commun.*, 2001, 713-714.
19. J. Wang, J. C. Groen, W. Yue, W. Zhou and M. O. Coppens, *Chem. Commun.*, 2007, 4653-4655.
20. J. Wang, J. C. Groen and M. O. Coppens, *J. Phys. Chem. C*, 2008, **112**, 19336-19345.
21. J. Wang, J. C. Groen, W. Yue, W. Zhou and M. O. Coppens, *J. Mater. Chem.*, 2008, **18**, 468-474.
22. J. Wang, W. B. Yue, W. Z. Zhou and M. O. Coppens, *Microporous Mesoporous Mater.*, 2009, **120**, 19-28.
23. B. Gautier and M. Smaihi, *New J. Chem.*, 2004, **28**, 457-461.
24. F.-S. Xiao, L. Wang, C. Yin, K. Lin, Y. Di, J. Li, R. Xu, D. S. Su, R. Schlögl, T. Yokoi and T. Tatsumi, *Angew Chem. Int. Ed.*, 2006, **45**, 3090-3093.
25. H. Wang and T. J. Pinnavaia, *Angew. Chem. Int. Ed.*, 2006, **45**, 7603-7606.
26. J. Song, L. Ren, C. Yin, Y. Ji, Z. Wu, J. Li and F.-S. Xiao, *J. Phys. Chem. C*, 2008, **112**, 8609-8613.
27. L. F. Wang, Z. Zhang, C. Y. Yin, Z. C. Shan and F. S. Xiao, *Microporous Mesoporous Mater.*, 2010, **131**, 58-67.

28. F. N. Gu, F. Wei, J. Y. Yang, N. Lin, W. G. Lin, Y. Wang and J. H. Zhu, *Chem. Mater.*, 2010, **22**, 2442-2450.
29. A. Sayari, P. Liu, M. Kruk and M. Jaroniec, *Chem. Mater.*, 1997, **9**, 2499-2506.
30. R. Mokaya, *J. Phys. Chem. B*, 1999, **103**, 10204-10208.
31. L. Y. Chen, T. Horiuchi, T. Mori and K. Maeda, *J. Phys. Chem. B*, 1999, **103**, 1216-1222.
32. C.-F. Cheng, W. Zhou and J. Klinowski, *Chem. Phys. Lett.*, 1996, **263**, 247-252.
33. D. Khushalani, A. Kuperman, G. A. Ozin, K. Tanaka, N. Coombs, M. M. Olken and J. Garcés, *Adv. Mater.*, 1995, **7**, 842-846.
34. J. Y. Ying, C. P. Mehnert and M. S. Wong, *Angew. Chem. Int. Ed.*, 1999, **38**, 56-77.
35. A. Taguchi and F. Schüth, *Microporous Mesoporous Mater.*, 2005, **77**, 1-45.
36. S. Pega, C. Boissière, D. Grosso, T. Azaïs, A. Chaumonnot and C. Sanchez, *Angew. Chem. Int. Ed.*, 2009, **48**, 2784-2787.
37. M. A. Camblor, A. Mifsud and J. Pérez-Pariente, *Zeolites*, 1991, **11**, 792-797.
38. M. A. Camblor and J. Pérez-Pariente, *Zeolites*, 1991, **11**, 202-210.
39. Y. Ji, C. Wang, Y. Zou, J. Song, J. Wang, F. Li and F.-S. Xiao, *J. Phys. Chem. C*, 2008, **112**, 19367-19371.
40. A. Corma, J. Pérez-Pariente, V. Fornés, F. Rey and D. Rawlence, *Appl. Catal., A* 1990, **63**, 145-164.
41. Z. T. Zhang, Y. Han, L. Zhu, R. W. Wang, Y. Yu, S. L. Qiu, D. Y. Zhao and F. S. Xiao, *Angew. Chem. Int. Ed.*, 2001, **40**, 1258-1262.

42. Z. T. Zhang, Y. Han, F. S. Xiao, S. L. Qiu, L. Zhu, R. W. Wang, Y. Yu, Z. Zhang, B. S. Zou, Y. Q. Wang, H. P. Sun, D. Y. Zhao and Y. Wei, *J. Am. Chem. Soc.*, 2001, **123**, 5014-5021.
43. Y. Xia and R. Mokaya, *J. Mater. Chem.*, 2004, **14**, 863-870.
44. N. Alam and R. Mokaya, *J. Mater. Chem.*, 2008, **18**, 1383-1391.
45. J. Liu, X. Zhang, Y. Han and F. S. Xiao, *Chem. Mater.*, 2002, **14**, 2536-2540.
46. S. Biz and M. G. White, *J. Phys. Chem. B*, 1999, **103**, 8432-8442.
47. R. Mokaya and W. Jones, *J. Mater. Chem.*, 1998, **8**, 2819-2826.
48. Y. Xia and R. Mokaya, *J. Phys. Chem. B*, 2003, **107**, 6954-6960.
49. R. Mokaya, *J. Phys. Chem. B*, 2000, **104**, 8279-8286.
50. C. T. Kresge, M. E. Leonowicz, W. J. Roth, J. C. Vartuli and J. S. Beck, *Nature*, 1992, **359**, 710-712.
51. Y. Liu and T. J. Pinnavaia, *J. Mater. Chem.*, 2002, **12**, 3179-3190.
52. R. Mokaya and W. Jones, *Phys. Chem. Chem. Phys.*, 1999, **1**, 207-213.
53. B. Mihailova, V. Valtchev, S. Mintova, A. C. Faust, N. Petkov and T. Bein, *Phys. Chem. Chem. Phys.*, 2005, **7**, 2756-2763.
54. A. Alberti, G. Cruciani, E. Galli, S. Merlino, R. Millini, S. Quartieri, G. Vezzalini and S. Zanardi, *J. Phys. Chem. B*, 2002, **106**, 10277-10284.
55. K. S. W. Sing, D. H. Everett, R. A. W. Haul, L. Moscou, R. A. Pierotti, J. Rouquerol and T. Siemieniewska, *Pure Appl. Chem.*, 1985, **57**, 603-619.
56. P. I. Ravikovitch, S. C. O. Domhnaill, A. V. Neimark, F. Schueth and K. K. Unger, *Langmuir*, 1995, **11**, 4765-4772.

57. C. Lastoskie, K. E. Gubbins and N. Quirke, *J. Phys. Chem.*, 1993, **97**, 4786-4796.
58. M. Kruk, M. Jaroniec and A. Sayari, *J. Phys. Chem. B*, 1997, **101**, 583-589.
59. D. Trong On, D. Desplantier-Giscard, C. Danumah and S. Kaliaguine, *Appl. Catal., A*, 2001, **222**, 299-357.
60. M. Choi, H. S. Cho, R. Srivastava, C. Venkatesan, D.-H. Choi and R. Ryoo, *Nat. Mater.*, 2006, **5**, 718-723.
61. R. Srivastava, M. Choi and R. Ryoo, *Chem. Commun.*, 2006, 4489-4491.
62. V. N. Shetti, J. Kim, R. Srivastava, M. Choi and R. Ryoo, *J. Catal.*, 2008, **254**, 296-303.
63. Y. Fang and H. Hu, *J. Am. Chem. Soc.*, 2006, **128**, 10636-10637.
64. J. B. Higgins, R. B. LaPierre, J. L. Schlenker, A. C. Rohrman, J. D. Wood, G. T. Kerr and W. J. Rohrbaugh, *Zeolites*, 1988, **8**, 446-452.
65. R. Mokaya, W. Jones, S. Moreno and G. Poncelet, *Catal. Lett.*, 1997, **49**, 87-94.
66. A. Corma, *Chem. Rev.*, 1997, **97**, 2373-2420.
67. A. Stein, *Adv. Mater.*, 2003, **15**, 763-775.
68. D. H. Pan, P. Yuan, L. Z. Zhao, N. A. Liu, L. Zhou, G. F. Wei, J. Zhang, Y. C. Ling, Y. Fan, B. Y. Wei, H. Y. Liu, C. Z. Yu and X. J. Bao, *Chem. Mater.*, 2009, **21**, 5413-5425.
69. R. Mokaya, *Angew. Chem. Int. Ed.*, 1999, **38**, 2930-2934.
70. B. M. Lok, T. R. Cannan and C. A. Messina, *Zeolites*, 1983, **3**, 282-291.

71. D. Trong On and S. Kaliaguine, *Angew. Chem. Int. Ed.*, 2002, **41**, 1036-1040.

Chapter Five

Chapter 5.0: Supercritical CO₂ mediated Incorporation of Palladium Nanoparticles into Zeolite Templated Carbons: Structural Characterisation and Hydrogen Storage Properties..... 151

5.1 Abstract	151
5.2 Introduction	152
5.3 Results and discussions	156
5.3.1 Structural Analysis of Pd-free carbons	156
5.3.2 Thermal stability of templated carbons	159
5.3.3 Textural Properties and porosity of templated carbons.....	160
5.3.4 Effect of carbonisation environment	164
5.3.5 Effect of Pd loading in zeolite templated carbons.....	168
5.3.5.1 Structural and thermal analysis of Pd-doped carbons.....	169
5.3.5.2 Textural Properties and porosity of Pd-doped carbons.....	173
5.3.5.3 Electron microscopy analysis of Pd-free and Pd-doped carbons	175
5.4 Hydrogen uptake measurements of Pd-free and Pd-doped carbons	1800
5.5 Summary	185
5.6 Bibliography.....	187

Chapter 5.0: Supercritical CO₂ mediated Incorporation of Palladium Nanoparticles into Zeolite Templated Carbons: Structural Characterisation and Hydrogen Storage Properties

5.1 Abstract

The use of zeolite Y (ZY) as a template to generate high surface area carbons, via a chemical vapour deposition (CVD) performed at 800, 850 or 900 °C, is explored in this chapter. The so-called zeolite templated carbons (ZTCs) are found to exhibit high surface area (up to ca. 2200 m²/g) and pore volume (up to 1.25 cm³/g) depending of the CVD temperature. The textural properties and level of zeolite-like ordering was highest for the carbon prepared at 800 °C thereafter reducing at higher CVD temperature. The extent of graphitisation followed the reverse trend. This chapter also explored the possibility of improving the hydrogen uptake of ZTCs via supercritical fluid (SCF)-mediated metal incorporation of Pd nanoparticles. SCF-mediated metal implantation offers advantages over conventional methods such as solvent-based impregnation or ion exchange methods due to the liquid-like densities and gas-like properties of SCFs. Moreover, SCFs have no surface tension, which facilitates effective penetration into the pore channels of the ZTCs. The SCF-mediated Pd incorporation enabled the decoration of high surface area ZTCs prepared at 800 °C with 0.2 – 4.0 mg of well dispersed Pd nanoparticles. The Pd-doped ZTCs exhibit enhanced hydrogen storage density (14.3 – 20.5 μmol H₂/m²), which is much higher than that of Pd-free zeolite templated carbon (12.0 μmol H₂/m²).

5.2 Introduction

In the 21st century a key area of intensive materials research is the quest for viable alternative power generation and energy storage systems. The dwindling supply of fossil fuels and reliance on hydrocarbon-based energy has been responsible for atmospheric pollution. The gases released by fossil-based energy sources include carbon dioxide, which is a known cause of global warming. Therefore, energy sources that are sustainable and concomitantly produce negligible pollution are needed. In terms of mobile applications, hydrogen is one of the leading contenders as an energy carrier for the future because of its high energy content and clean burning. However, the greatest impediment to the use of hydrogen as an energy carrier is the development of safe and practical storage systems.

Porous carbons due to their tuneable micro-texture and surface functionality coupled with different forms (powders, fibres, forms, composites among others) are potentially useful hydrogen storage materials.^{1, 2} Additionally, carbonaceous nanostructured materials have very unique surface textures and porosities that can be highly modulated through synthetic procedure to give high surface area and well-ordered pore systems.

Highly porous carbons may be prepared via a number of synthesis procedures including activation (physical and chemical)³⁻⁵ or template carbonisation.^{6,7, 8, 9-11} In the template carbonisation methodology, an inorganic porous template characterised by unique nanospace such as a zeolite matrix is used to define and template the porosity of the resultant carbon sample. The advantage of using materials with well-defined texture and pore size distribution for hydrogen storage lies in the possibility of

relating the hydrogen uptake properties to the textural properties of the adsorbent.

In the recent past years, the intensive research interest focused on the use of porous carbon materials as hydrogen reservoirs has established a correlation between the surface area (associated with microporosity) and hydrogen storage.^{10, 12-16} In addition, some studies have proposed that micropores between 0.6 and 0.8 nm are the most efficient for hydrogen storage.^{12, 13, 15-17}

The success of any future hydrogen economy depends on the ability to develop inexpensive materials with sufficient hydrogen capacity. In particular, the remarkable potential of carbon-based nanomaterials in hydrogen storage is yet to be realised. Several synthesis methods have shown promise in generating carbons with significant hydrogen storage. Zeolites have proved to be excellent templates for the fabrication of microporous carbons with uniform micropores and small mesopores. Indeed, the great variety of zeolites (and other related inorganic templates) and the rich abundance of carbon precursors offers the opportunity to design novel materials with desired pore size and surface area. For example, of relevance to the work in this chapter, a hydrogen uptake of 6.9 wt% (at -196 °C and 20 bar), which is amongst the highest ever reported for carbonaceous materials, has been achieved by zeolite-templated carbons prepared via chemical vapour deposition (CVD) of carbon precursor into zeolites followed by removal of the zeolite framework to generate the final carbons.¹⁰

This chapter reports on investigations of the effect of pyrolysis environment of CVD-derived zeolite-templated carbons by carrying out chemical vapour

[153]

deposition at variable temperatures (800 to 900 °C) under either flowing nitrogen or argon. Subsequently, the chapter reports on the possibility of enhancing the hydrogen uptake capacity of the zeolite templated carbons (ZTCs) by incorporation of metal nanoparticles. The introduction of noble metal nanoparticles (metals such as Ni, Pt, and Pd) into the porous carbons forms a hybrid material that combines the properties of carbon and the metal with the aim of altering the hydrogen uptake.

It has been suggested that dispersed metal nanoparticles within a high surface area substrate (such as a porous carbon) generates a composite material that takes up hydrogen via two processes; (i) adsorption of hydrogen on the surface of the pores of porous material and (ii) hydrogenation on the metal nanoparticles by forming metal hydrides.¹⁸ The later process (hydrogenation) is due to chemisorption of atomic hydrogen on the metal nanoparticles, which can then initiate a mechanism referred to as hydrogen 'spillover'.¹⁹⁻²² Furthermore Nalm and co-workers have established that hydrogen spillover does not only improve hydrogen capacity but also increases initial hydrogen adsorption kinetics.²³

However, the very existence of a spillover mechanism has been strongly debated with some experimental results reporting findings that revealed very low hydrogen capacities after metal doping.^{24, 25} Nevertheless, the spillover of atomic hydrogen is a well-established process in heterogeneous catalysis.²⁶⁻²⁹ The details of spillover as applied in hydrogen storage processes are yet to be clearly understood due to the disparity in experimental data.²⁶⁻²⁹

Synthesis of metal nanoparticles and subsequent dispersion into high surface area carbons can either be carried out by chemical or physical

methods, including wet impregnation,^{19, 30} thermal evaporation³¹ and sputter coating.³² However, these methods suffer from relatively poor size and dispersion control of anchored metal particles. Therefore an effective preparation procedure that enhances the formation of well dispersed metal nanoparticles is highly sought after and remains an important area of research focus.

The limitations of conventional metal implantation techniques may be overcome by using supercritical carbon dioxide (scCO₂) as an anchoring medium. scCO₂ is an excellent and easily obtained as it has a convenient critical point (31.1 °C and 73.8 bar). Supercritical fluid technology is well established in the literature as earlier discussed with scCO₂ having gas-like diffusivity and extremely low viscosity. In particular, the readily accessible conditions of scCO₂ coupled with its abundance, low cost, non-flammability and non-toxicity makes it attractive as a green medium/solvent in current and emerging chemical processes.^{33, 34}

In this chapter, the use of acetonitrile as the carbon precursor to generate templated carbons was based on its ready availability as a by-product of acrylonitrile synthesis. Likewise the choice of zeolite as template was based on the fact that zeolites possess unique properties for replication processes given that the dimensions of their cages and channels are quite similar to the size of the precursor organic molecules that on carbonisation constitute the carbon replica.

The results obtained in this chapter illustrate the potential of nanocasting techniques in generating porous carbons with similar pore size which is a sought after property in porous materials research. Zeolite Y was used as a hard template and acetonitrile as carbon precursor in an attempt to

inversely replicate the zeolite structure in high surface area carbons. The carbon precursor was introduced into the zeolite pores via CVD at variable temperatures under either nitrogen or argon environment. A carbon sample prepared at CVD temperature of 800 °C under argon was then used as a substrate for Pd loading as detailed in section 3.4. The obtained samples both Pd-free and Pd-loaded are fully characterised with respect to their porosity and hydrogen uptake.

5.3 Results and discussions

5.3.1 Structural Analysis of Pd-free carbons

Figure 5.1 shows powder XRD patterns of acetonitrile-derived zeolite/carbon composites and the final zeolite templated carbons prepared via CVD under an argon environment at variable temperature. The XRD patterns of zeolite/carbon composites (Figure 5.1A) are characterised by many sharp peaks due to zeolitic framework ordering. These sharp peaks are comparable to those of the zeolite Y (ZY) template, which suggests that the zeolite framework remains intact at all the carbonisation temperatures.³⁵⁻³⁷

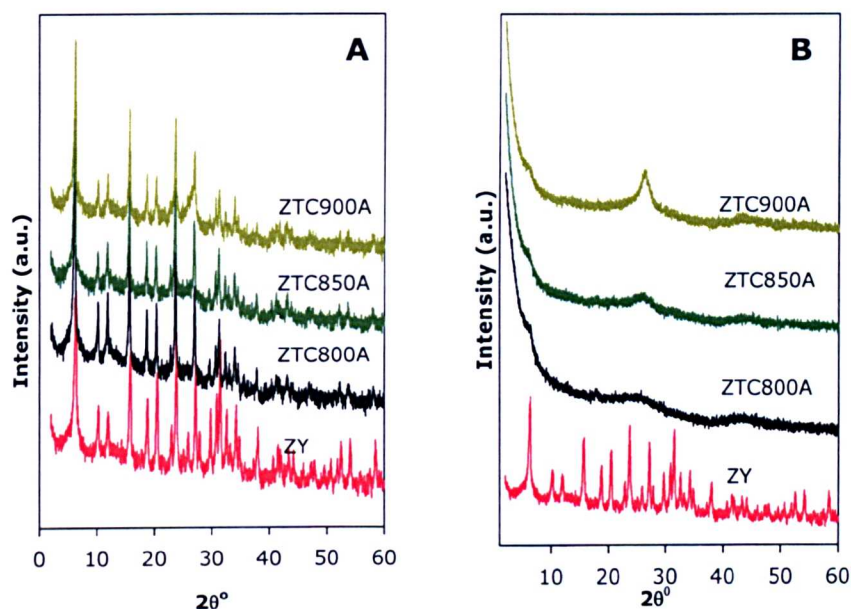


Figure 5.1 Powder XRD patterns of zeolite/carbon composites (A) and zeolite-templated carbons (B) prepared under argon flow at variable temperatures (800, 850 and 900 °C). Also, zeolite Y (ZY) template spectrum is included.

The resultant carbon samples after dissolution of the zeolite template showed XRD patterns (Figure 5.1B) that vary according to the CVD temperature. The sample carbonised at 800 °C (ZTC800A) showed a poorly resolved peak at $2\theta = 6^\circ$ which could be ascribed to as being similar to the (111) planes of zeolite Y. This suggests that structural regularity similar to that of zeolite Y has been replicated in the carbon but only to a limited extent since the peaks have much a lower intensity compared to the zeolite template. The samples carbonised at 850 and 900 °C showed a weak shoulder at $2\theta = 6^\circ$ which is suggestive of lesser zeolite replication at higher temperatures.

The XRD patterns thus show that long-range zeolite-like ordering was not significantly replicated in the carbons except for ZTC800A. On the other hand, all three carbon samples showed a broad diffraction feature at ca. $2\theta = 26^\circ$ which could be ascribed to the (002) diffraction from graphitic/turbostratic carbon. The intensity of this peak increases at higher CVD temperature. In particular, the intensity and sharpness of the (002) peak for sample ZTC900A is high and thus clearly, greater graphitisation occurs at 900 °C. The d_{002} carbon spacing obtained for this peak is 0.394 nm which is ca. 18% higher than the ideal value for graphite ($d_{002} = 0.335$ nm),³⁶ indicating the turbostratic nature of the template carbons.

Based on the XRD patterns, it is quite evident that CVD temperatures play a key role in replication of zeolite-like ordering and graphitisation. The differences in the XRD patterns may be explained by the varying rate of acetonitrile carbonisation either within the pore channels or on the surface of the zeolite template. Thus at 800 °C carbonisation is relatively slow allowing acetonitrile to permeate into the interior of the zeolite pores and carbonise therein. On removal of the zeolite framework, the resulting carbon materials exhibit zeolite-like pore channel structural regularity and are generally non-graphitic because the carbon deposited within the zeolite pores is most unlikely to undergo graphitisation as a result of steric hindrance occasioned by the relatively small size of zeolite pore channels.³⁸ On the other hand, a higher carbonisation temperature (e.g. for ZTC900A) leads to accelerated carbonisation of the acetonitrile precursor on and within the surface or near surface region of the zeolite particles. Deposition of carbon near the surface of the zeolite particles hinders further access of acetonitrile to the interior pore channels. The formation of carbon is

mainly on the outer surface of the zeolite particles with no lower levels of zeolite-like pore channel regularity.

5.3.2 Thermal stability of templated carbons

The burn off temperature of carbons is determined by their level of graphitisation. The TGA curves represented in Figure 5.2 are thus in good agreement with the XRD patterns in Figure 5.1B and clearly show that the burn off temperature of carbon (i.e. onset of mass loss) increases for carbons prepared at higher CVD temperature. The corresponding differential gravimetric (DTG) profiles in Figure 5.2B show that the maximum carbon mass loss centred at ca. 600 °C for ZTC800A shifting to 635 and 660 °C for ZTC850A and ZTC900A, respectively. The shift in the temperature of maximum mass loss of carbon is in line with a higher degree of graphitisation for carbon sample prepared at 900 °C.

The thermal gravimetric analysis of the zeolite/carbon composites (shown in Figure 5.2A with dotted curves for ZTC800A (b'), ZTC850A (c') and ZTC900A ³⁹) indicated carbon content of 25%, 27% and 30%, respectively. The zeolite ZY template (Figure 5.2A (a)) showed no mass loss after 580 °C which confirms its suitability as reliable template for the high temperature templating process. The TGA profiles for the carbons after dissolution of zeolite template showed < 1.0% residual weight which confirms that the resultant carbons were virtually zeolite free.

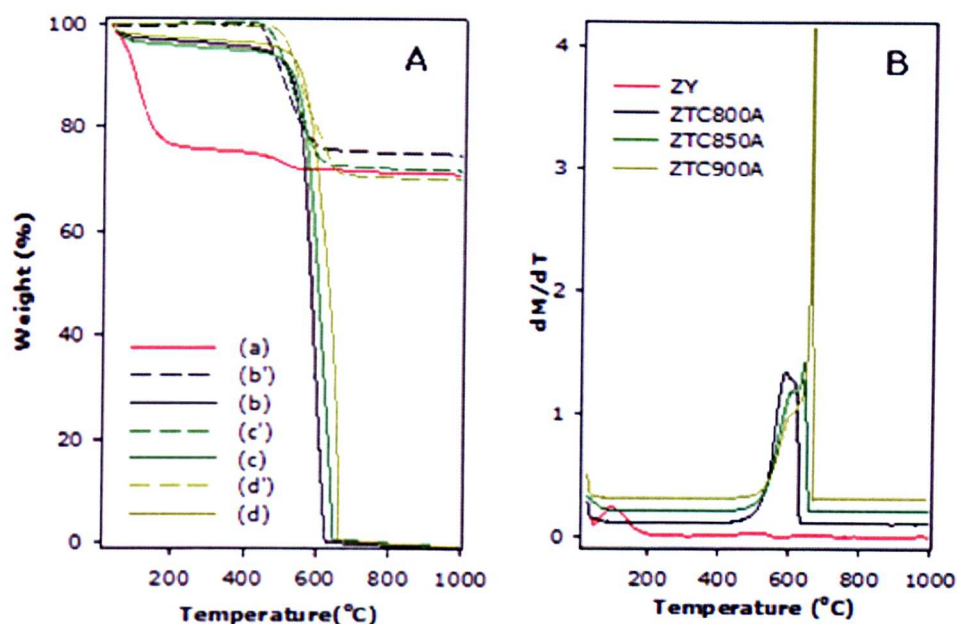


Figure 5.2 Thermogravimetric analysis (TGA) curves (A) and differential thermogravimetric (DTG) profiles (B) of zeolite templated carbons. The TGA curves (A) represented by dotted lines (b', c' and d') and solid lines (b, c and d) are for zeolite/carbon composites and carbon materials, respectively. For clarity, DTG profiles (B) of ZTC800A, ZTC850A and ZTC900A are offset (y-axis) by 0.1, 0.2 and 0.3 (%/min), respectively.

5.3.3 Textural Properties and porosity of templated carbons

Figure 5.3 shows nitrogen sorption isotherms and corresponding pore size distribution (PSD) curves of the carbons. The sorption isotherm for zeolite (ZY) template is shown for comparison purposes. All the carbon samples exhibit isotherms typical of microporous materials and show high adsorption capacities at relative pressure (P/P_0) below 0.02). All the isotherms also exhibit significant adsorption at $P/P_0 > 0.2$ due to the presence of pores slightly larger than micropores. On the other hand, the

nitrogen sorption isotherm of the zeolite template (ZY) is clearly Type I as shown in Figure 5.3A, and exhibits no adsorption at P/P_0 greater than 0.02.

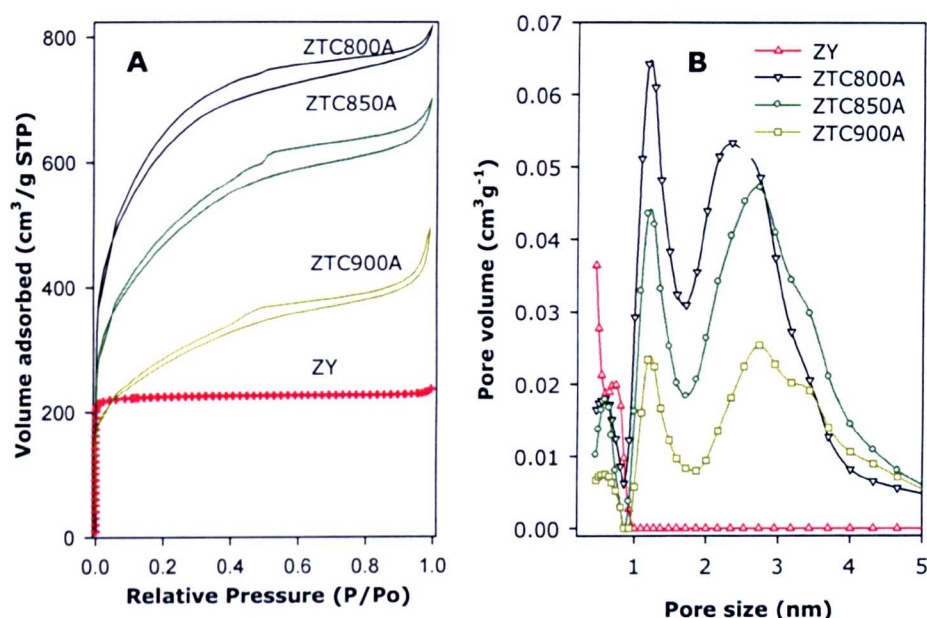


Figure 5.3 Nitrogen sorption isotherms (A) and corresponding pore size distribution curves (B) of zeolite Y (ZY) and zeolite templated carbons (ZTC800A, ZTC850A and ZTC900A) prepared at 800, 850 and 900 °C, respectively, via CVD.

Table 5.1 summarises the textural properties of the zeolite templated carbons. All the carbon samples have higher surface area than the zeolite template. In particular, ZTC800A* has surface area of 2174 m²/g which translates into ca. 200% increase over the zeolite template. Similarly the pore volume remarkably increases with ZTC800A* showing an increase of up to 240% compared with the zeolite template. It is noteworthy that the proportion of micropore surface area and pore volume (obtained by applying t-plot analysis to adsorption data) is significantly high at ca. 75% and 61% respectively.

Table 5.1 Textural properties of zeolite templated carbons prepared via chemical vapour deposition (CVD) at variable temperatures under different inert environment using acetonitrile as carbon precursor. The sample are denoted ZTCxy where x is temperature of carbonisation (800, 850 or 900 °C) and y is either nitrogen (N) or argon (A) flow.

Sample	Surface area (m ² /g) ^a	Pore volume (cm ³ /g) ^b	Pore size (nm) ^c	H ₂ uptake	
				(wt%) ^d	density (ρ) ^e
ZY	728 (718)	0.37 (0.23)	0.6	-	-
ZTC800A	2046 (1480)	1.21 (0.70)	0.6/1.2/2.4	4.9	12.0
ZTC800A*	2174 (1638)	1.26 (0.77)	0.6/1.2/2.4	5.1	11.7
ZTC850A	1594 (916)	1.04 (0.48)	0.6/1.2/2.7	3.3	10.4
ZTC900A	866 (381)	0.71 (0.18)	0.6/1.2/2.7	2.0	11.5
ZTC800N	1837 (1406)	1.07 (0.38)	0.6/1.2/2.4	3.8	10.3
ZTC850N	1717 (1074)	1.10 (0.50)	0.6/1.2/2.7	3.5	10.2
ZTC900N	973 (384)	0.74 (0.18)	0.6/1.2/2.7	2.1	10.8

The values in the parenthesis refer to: ^at plot micropore area, ^b t-Plot micropore volume, and ^c maxima of the PSD obtained using NLDFT model analysis. ^d Represents hydrogen uptake capacity at -196 °C and 20 bar and ^e is the hydrogen uptake density in μmol.H₂m⁻² (ρ).

The carbons have relatively similar pore size distribution (PSD) as shown in Figure 5.3B. We note that the PSD of all the carbons and the zeolite template were determined via a non-local density function theory (NLDFT) model using adsorption data. Despite the fact that the NLDFT model applied to nitrogen sorption has previously been reported to overestimate pore size, it is an invaluable comparative analytical tool.^{4, 12, 40} All the carbons exhibit a tri-modal PSD with maxima centered at ca. 0.6, 1.2 and 2.4 nm for ZTC800A, while for ZTC850A and ZTC900A the largest pore size shifts to 2.7 nm. In addition the distribution of the largest pores slightly

varies with carbonisation temperature; the sample carbonised at 900 °C has a broader and lower intensity maximum centered at 2.7 nm.

The presence of pores in the micropore range is expected given that the wall thickness of the zeolite Y framework is ca. 1.0 nm.³⁷ For all the carbons the peak centred at 1.2 nm is therefore most probably directly templated by the zeolite framework. The difference in the expected value of 1.0 nm of zeolite framework could be attributed to the shrinkage of carbon during carbonization and /or incomplete filling of the voids of zeolite pores.⁴¹ It is noteworthy that the proportion of these pores gradually reduced at higher sample preparation temperature. This is consistent with a lowering in the extent of zeolite replication at higher temperature as discussed above. The pores centered at 0.6 nm may be ascribed to initially well-ordered carbons upon dissolution in HF breaking off to create pores that are similar to the parent zeolite. The largest pores centered at 2.4 nm (for ZTC800A and ZTC850A) and 2.7 nm (for ZTC900A) are clearly too large to be directly templated by the zeolite. The formation of these small mesopores may lie in the extent of infiltration of the carbon precursor into the zeolite pores channels. The degree of infiltration of a carbon precursor into the channels and/or cages is expected to greatly affect the pore structure of the resultant carbons with incomplete pore filling generating larger pores (> 2 nm) than those that are directly templated (ca. 1.2 nm). Furthermore, during the carbonization of acetonitrile at 800 – 900 °C, small gaseous molecules such as CO₂ and H₂ are released, which on exiting can generate micropores or cause the enlargement of directly templated pores.³⁵ Thus the sample carbonised at 900 °C exhibited the largest pore size as expected due to the increased number of small molecules being

released and a lower level of carbon infiltration into the zeolite template. Based on these findings, it is evident that the increase in CVD temperature affects the porosity of the templated carbons which is similar to the data reported by Zhao and co-workers.⁴¹ Independently Johnson and co-workers reported similar PSD and attributed the pore systems to filled and unfilled zeolite pores in the composite material.³⁵

5.3.4 Effect of carbonisation environment

In order to elucidate the effect of carbonisation environment, a second set of zeolite templated carbons were prepared under the flow of nitrogen gas instead of argon. Figure 5.4 shows powder XRD patterns of zeolite/carbon composite and subsequent resultant carbons prepared at 800 (ZTC800N), 850 (ZTC850N) and 900 °C (ZTC900N). The XRD patterns for the zeolite/carbon composite are comparable to those in Figure 5.1A and therefore, under nitrogen, the zeolite framework remains intact after the carbonisation process. Upon dissolution of the zeolite framework in HF acid followed by refluxing in HCl, the resultant carbons exhibit similar trends (Figure 5.4B) in their XRD patterns as for samples carbonised under argon (Figure 5.1B). Thus, the XRD patterns in Figure 5.4B, where there is no clearly resolved peak at 2θ value of 6° are suggestive of lack of zeolite-like framework in the resultant carbons, and in particular for sample ZTC900N. It is noteworthy that the peak at $2\theta = 26^\circ$, ascribed to (002) diffraction of turbostratic carbon is observed with increased intensity especially for sample ZTC900N. The higher extent of graphitisation particularly for ZTC900N is confirmed by TGA and DTG data in Figure 5.5; similar to what is observed for samples prepared under argon, the burn off temperature increases for carbons prepared at higher CVD temperature. The TGA

profiles in Figure 5.1A are comparable to those in Figure 5.3A; with carbon mass loss in the same temperature range. However, the zeolite/carbon composites (Figure 5.5A) exhibited a higher carbon fraction of ca. 36% for ZTC900N compared to 27% for ZTC900A. A likely reason for this is that nitrogen offers a more favourable (compared to argon) environment for the deposition of carbon from the acetonitrile precursor.

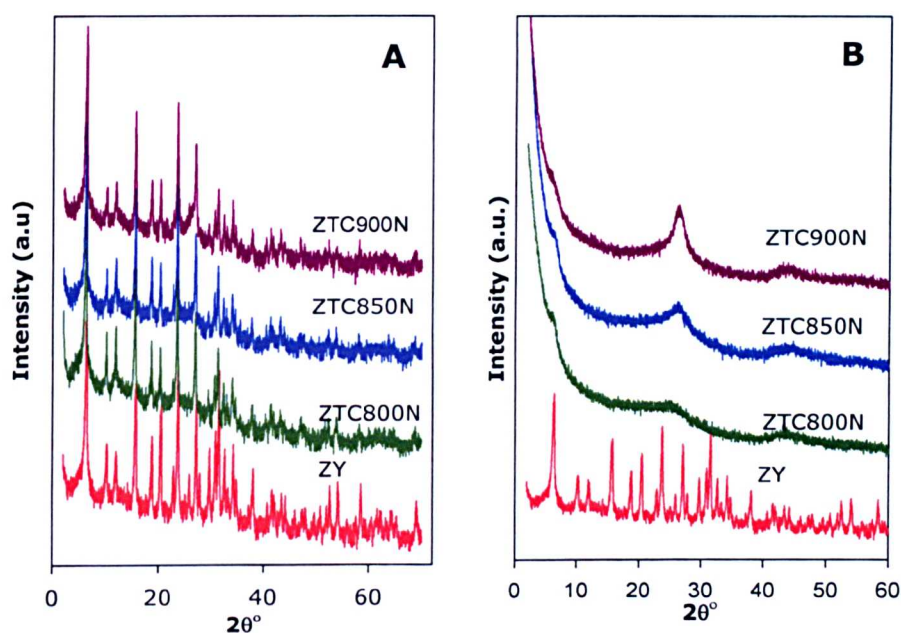


Figure 5.4 Powder XRD patterns of zeolite/carbon composites (A) and corresponding zeolite templated carbons (B) prepared via CVD under nitrogen flow.

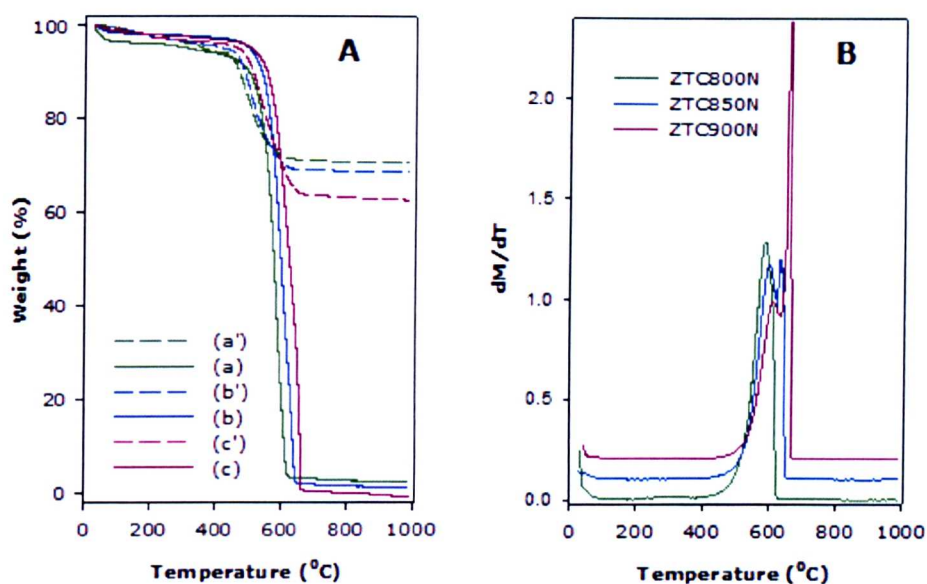


Figure 5.5 Thermogravimetric analysis (TGA) curves (A) and differential thermogravimetric (DTG) profiles (b) of zeolite templated carbon materials prepared at variable temperatures (800, 850 or 900 °C); the TGA curves (A) represented by dotted lines (a', b' and c') and solid lines (a, b and c) are composite and pure carbon materials, respectively.

Figure 5.6 shows the nitrogen sorption isotherms of samples prepared under nitrogen, and the textural properties are summarised in Table 5.1. All the carbons exhibit isotherms indicative of the presence of micropores and small mesopores. There is significant adsorption at P/P_0 below 0.02 indicating the presence of significant microporosity. Similar to samples prepared under argon, the presence of large micropores and small mesopores is evidenced by adsorption in the relative pressure (P/P_0) range between 0.1 and 0.6. The presence of micropores and small mesopores is confirmed by the PSD curves in Figure 5.6B. In contrast, to the carbons prepared under argon, the samples prepared under nitrogen exhibit small mesopores that are slightly larger at 2.7 nm for ZTC805N and ZTC900N.

Nevertheless, the proportion of pores of size below 2.0 nm, which are highly sought after for hydrogen storage, are similar for both sets of samples thus confirming similarity of the tri-modal pore channel systems.

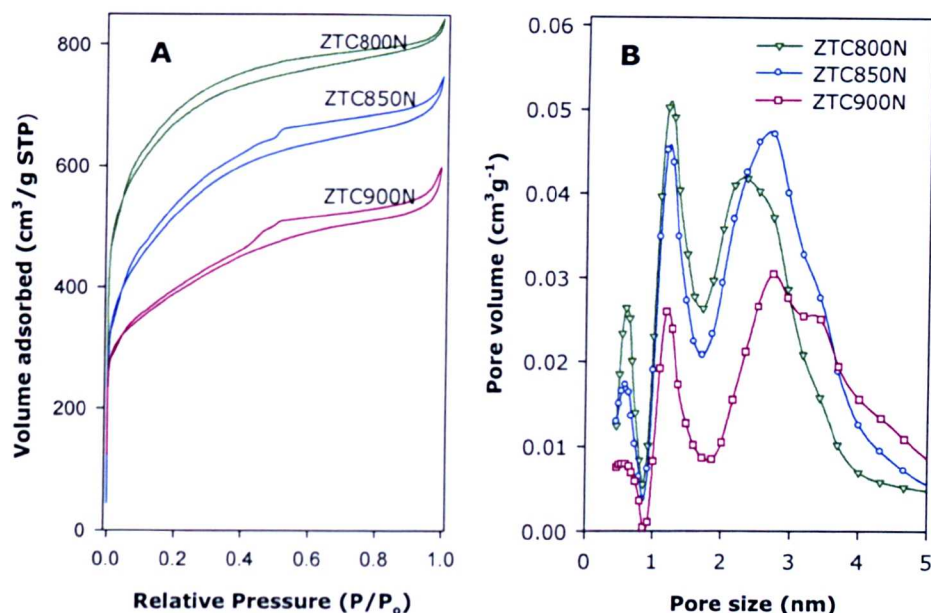


Figure 5.6. Nitrogen sorption isotherms (A) and corresponding pore size distribution curves (B) of zeolite templated carbons (ZTC800N, ZTC850N and ZTC900N) carbonised at 800, 850 and 900 °C, respectively.

As shown in Table 5.1, the surface area and pore volume for the carbons generated under nitrogen are comparable to those of their analogues prepared under argon flow. Therefore it is reasonable to generalise that the environment for carbonisation does not appear to have any significant effect on the textural and structural ordering of the templated carbons. However, optimisation of the reaction parameters is important in developing materials with tailored porosity for hydrogen adsorption. To assess reproducibility of the templating process, an extra carbon sample denoted ZTC800A* was carbonised at 800 °C under the flow of argon.

Based on the textural properties summarised in Table 5.1, it is evident that under our synthesis conditions, the two carbons prepared at 800 °C exhibit similar data within experimental error. Therefore the results presented clearly represent great potential for modulating the porosity of carbon samples by varying the CVD temperature. The generated porous carbons exhibit the highest reported surface area and pore volume for such synthesis at 800 °C in a one-step CVD process using zeolite Y as a hard template.

5.3.5 Effect of Pd loading in zeolite templated carbons

As previously discussed in section 5.2 similar materials (the so-called zeolite templated carbons) exhibiting high surface area have been reported to show attractive hydrogen uptake properties.^{9, 10} This section reports on work done aimed at enhancing the hydrogen uptake capacity via incorporation of metal nanoparticles in the zeolite templated carbons. It is believed that the presence of metals such as Ni, Pt, and Pd can enhance hydrogen uptake capacity on porous carbons due to the overlap of the potential fields generated at the carbon pore walls and increased polarizability of the adsorbent surface due to the presence of metal particles at nanometre scale.⁴²

The choice of ZTC800A and ZTC800A* for Pd incorporation, which in this section are for clarity denoted ZTC8 and ZTC8*, respectively, was based on their excellent textural properties; the two samples exhibited the highest surface area and pore volume and the highest proportion of microporosity (Table 5.1). Furthermore, these carbon samples prepared at 800 °C exhibited some zeolite-like properties as evidenced by a weak XRD peak at $2\theta = 6^\circ$ in Figure 5.1. The preparation of Pd-ZTCx samples is detailed in

section 3.4; in summary the Pd doping process involved the use of supercritical carbon dioxide as a medium for the carbon/palladium composites. This method of doping is environmentally benign, fast and convenient, and generates no waste. Furthermore, given that supercritical fluids have high diffusivity;^{34, 43} they are expected to overcome diffusion and mass transfer limitations inherent in conventional solvents.

5.3.5.1 Structural and thermal analysis of Pd-doped carbons

Comparison of the ZTC and Pd(hfa)₂ mixture before and after the reaction in supercritical CO₂ revealed a significant change in colouration from a mix of crystalline yellow and black to uniformly black throughout the mixture, which was indicative of a substantial reaction. Powder XRD patterns presented in Figure 5.7A exhibit at least four well resolved peaks for Pd-loaded samples, whereas for Pd-free samples only one peak at $2\theta = 6^\circ$ is observed.

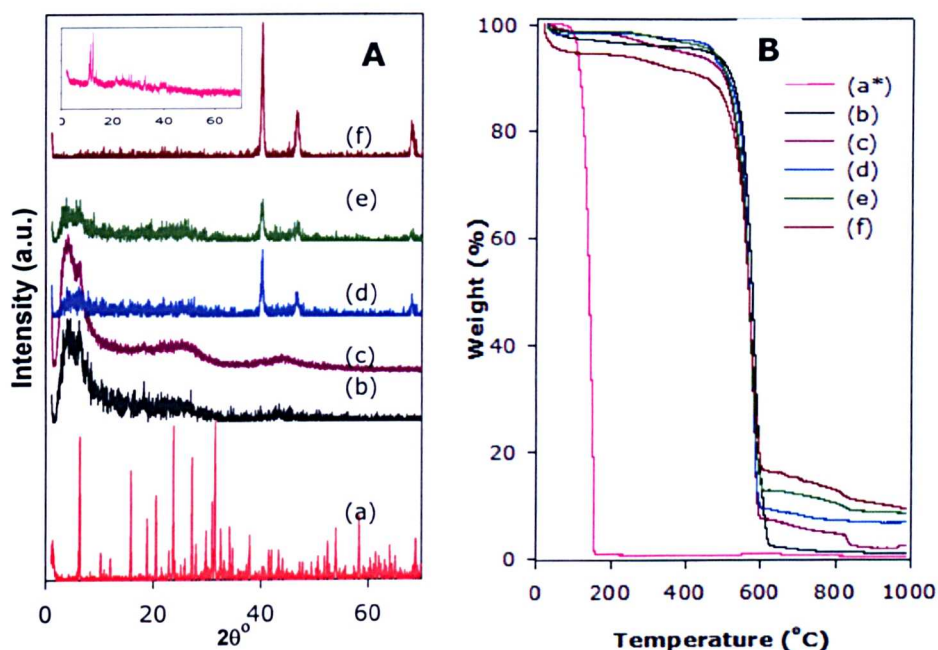


Figure 5.7 Powder XRD patterns (A) and TGA curves (B) of Pd-free and Pd-doped carbons; where a and a* represent zeolite Y template (ZY) and (Pd-(hfa)₂) while b, c, d, e and f are Pd-free (ZTC8), Pd-doped (ZTC8Pd-0.2, ZTC8Pd-0.4, ZTC8Pd-0.8 and ZTC8Pd-2.0), respectively. Also, represented inset in (A) is the XRD pattern of Pd-(hfa)₂.

It is worth noting that the zeolitic peak at $2\theta = 6^\circ$ is still maintained after Pd impregnation, though with a shoulder which could be due to an experimental artefact. The peaks at $2\theta = 39^\circ$, 47° and 68° in the pattern of the Pd-loaded samples are [111], [200] and [220] diffractions from FCC Pd crystals corresponding to d-spacing of 0.224, 0.193 and 0.137 nm, respectively. The powder XRD patterns for Pd-loaded samples are consistent with those reported by Howdle and co-workers in palladium-aerogel nanocomposites prepared via supercritical fluids.³³ Also, the XRD pattern of the Pd-(hfa)₂ precursor (inset Figure 5.7A) exhibits very weak sharp peaks in the 2θ range $> 20^\circ$. This further confirms that the sharp

and well defined peaks in the XRD patterns of the Pd-doped samples do indeed arise from Pd nanoparticles occluded in the carbons.

Figure 5.7B shows TGA data for the Pd precursor (Pd-(hfa)₂), Pd-free and Pd-doped carbons; the mass loss was monitored between room temperature and 1000 °C at a heating ramp rate of 10 °C/min under static air conditions. The TGA curves indicate a significant mass loss at ca. 600 °C of 80% and 95% for ZTC8Pd-2.0 and ZTC8, respectively, which corresponds to combustion of carbonaceous material. The residual weight exhibited by Pd-doped sample confirmed that Pd was successfully incorporated into carbon substrate. The fact that the Pd-doped carbons exhibited residual mass at 1000 °C is further evidence for the occlusion of Pd. The residual mass varied according to the carbon/Pd ratio in the following order: ZTC8Pd-2.0 (17.9%), ZTC8Pd-0.8 (13.6%), ZTC8Pd-0.4 (10.2%), and ZTC8Pd-0.2 (7.7%). Clearly, the residual mass is rather larger than the actual amount of Pd added to the carbon, which raises the possibility that some thermally stable Pd-C may be generated during the thermal analysis. Detailed investigation of this possibility is rather outside the scope of this thesis.

The mass loss at temperatures below 100 °C is due to removal of any residual water or other volatile components. It is worth noting here that the TGA curve of Pd(hfa)₂ (Figure 5.7B curve a*) indicates complete decomposition of the Pd precursor with ca. 1.0% residual mass at 135 °C. This is attributed to the fact that the Pd(hfa)₂ is thermally labile at low temperatures and has a low sublimation temperature.^{44, 45} Generally, the TGA data for the Pd-doped carbons is in good agreement with the XRD

patterns given that the sample with highest loading (ZTC8Pd-2.0) showed patterns with highest intensity Pd peaks.

In order to assess the effect of higher Pd loading than for sample ZTC8Pd-2.0, the Pd content was doubled to generate a sample designated as ZTC8*Pd-4.0. The XRD patterns and TGA curves of Pd-free (ZTC8*) and Pd-doped (ZTC8*Pd-4.0) are presented in Figure 5.8. The XRD pattern of sample ZTC8*Pd-4.0 (Figure 5.8A, pattern b) exhibits intense peaks $2\theta = 39^\circ$, 47° and 68° , which are (111), (200) and (220) diffractions from FCC Pd crystals. Although the intensity of the Pd peaks for sample ZTC8*Pd-4.0 in Figure 5.8A are comparable to those of ZTC8Pd-2.0 in Figure 5.7A, TGA data (Figure 5.8B) indicates that the former has a higher residual mass of 27.1% (compared to 17.0% for the latter).

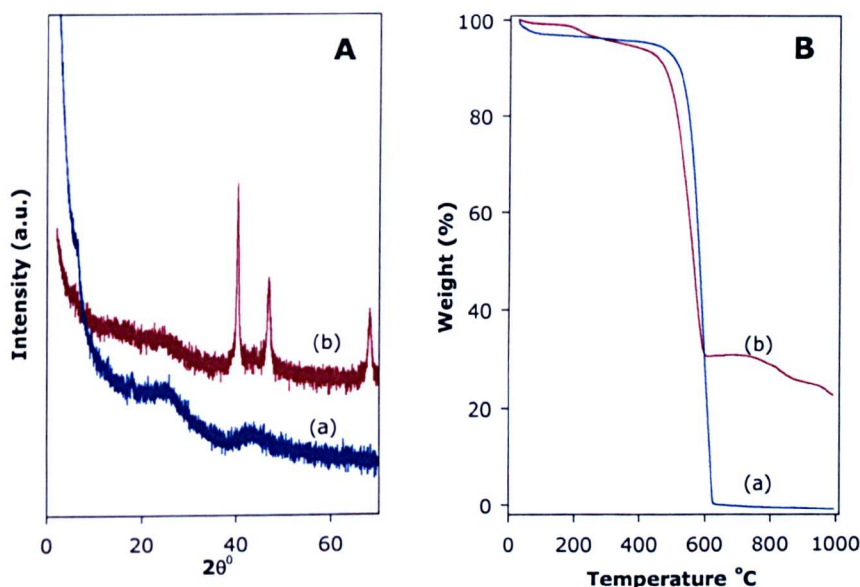


Figure 5.8 Powder XRD patterns (A) and TGA curves (B) of Pd-free carbon in which (a) and (b) refer to Pd-free (ZTC8*) and Pd-loaded (ZTC8*Pd-4.0) carbons, respectively.

5.3.5.2 Textural Properties and porosity of Pd-doped carbons

The nitrogen sorption isotherms of the Pd loaded samples are shown in Figure 5.9A.

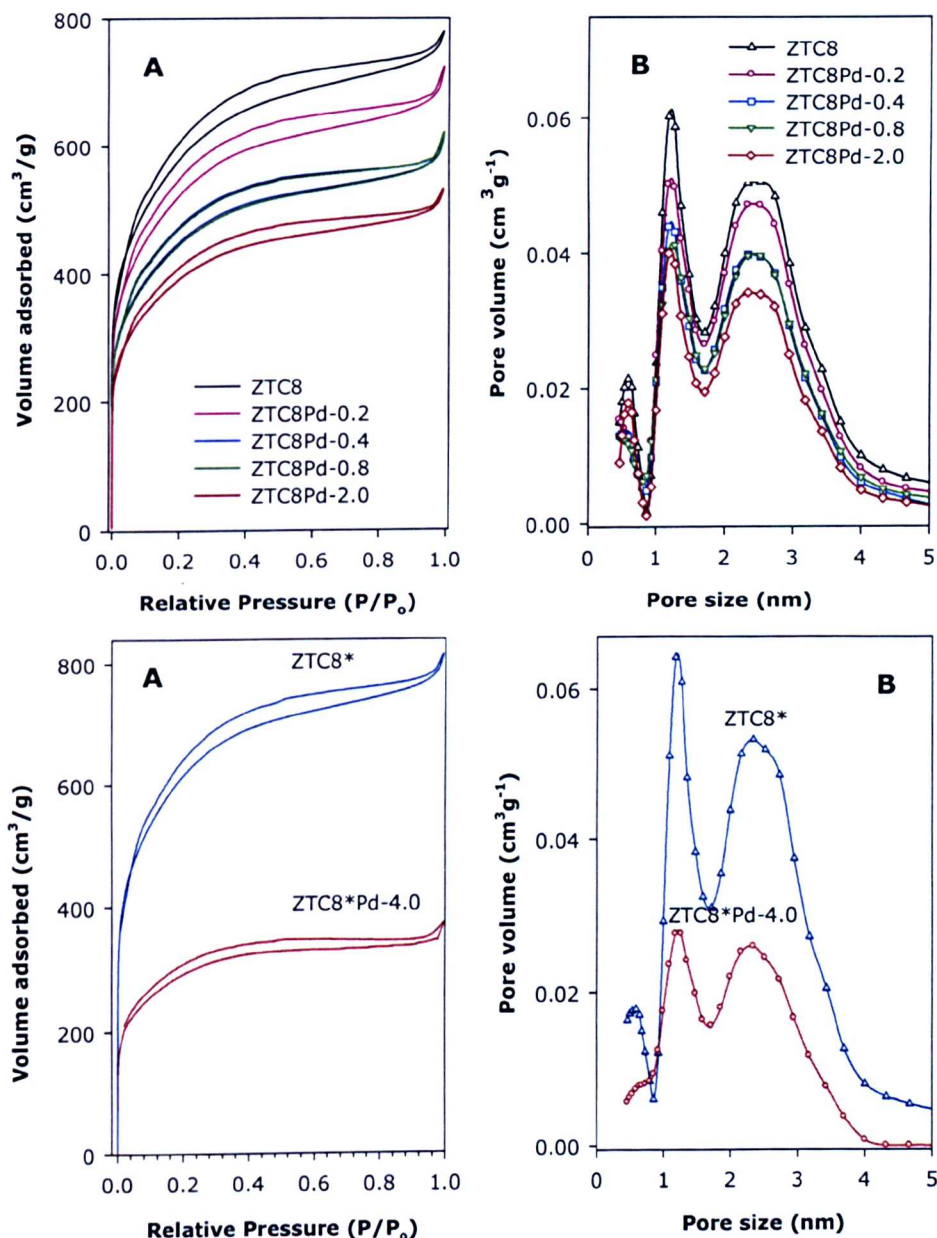


Figure 5.9 Nitrogen sorption isotherms (A) and corresponding pore size distribution curves (B) of Pd-free zeolite templated carbons and Pd-loaded carbons.

The isotherms of all the Pd loaded samples are very similar to those of the Pd-free ZTC8/ZTC8* samples, and in all cases therefore indicate the presence of micropores and small mesopores.⁴⁶ The effect of Pd appears only to be in a lowering of the overall amount of nitrogen sorbed perhaps due to blocking of some pores, but with no effect on pore size or pore size distribution. This is confirmed by the PSD shown in Figure 5.9B. The Pd-loaded samples exhibit tri-modal pore size distribution centred at 0.6, 1.2 and 2.4 nm.

The textural properties and hydrogen uptake data for the Pd-free and Pd-loaded samples are summarised in Table 5.2. As expected, the surface area and pore volume of the zeolite templated carbons reduces on Pd-doping, and in general the extent of the reduction increases at higher Pd loading. The decrease in surface area appears to be roughly similar to the reduction in pore volume. The surface area decreases by 10% and 53% whereas the pore volume reduces by 8% and 54% for ZTC8Pd-0.2 and ZTC8*Pd-4.0, respectively. The changes in micropore surface area and micropore pore volume mirror those of the total surface area and pore volume. The proportion of micropore surface area for most of the samples is 72 - 75% except for samples ZTC8Pd-2.0 and ZTC8*Pd-4.0 with the largest amounts of Pd, which it is 31% and 65%, respectively.

Table 5.2 Textural properties and hydrogen capacity of zeolite templated carbon with or without palladium.

Sample	Surface	Pore	Pore size	H ₂ uptake	
	area	volume	(nm) ^c	(wt%) ^d	density
	(m ² /g) ^a	(cm ³ /g) ^b			(ρ) ^e
ZTC8	2046 (1480)	1.21 (0.70)	0.6/1.2/2.4	4.9(5.8)	12.0
ZTC8*	2174 (1638)	1.26 (0.77)	0.6/1.2/2.4	5.1(6.5)	11.7
ZTC8Pd-0.2	1858 (1351)	1.12 (0.63)	0.6/1.2/2.4	5.3(7.3)	14.3
ZTC8Pd-0.4	1390 (1031)	0.82 (0.48)	0.6/1.2/2.4	5.1(6.4)	18.3
ZTC8Pd-0.8	1597 (1187)	0.99 (0.55)	0.6/1.2/2.4	5.1(6.6)	16.0
ZTC8Pd-2.0	1582 (1166)	0.96 (0.55)	0.6/1.2/2.4	4.7(6.1)	14.9
ZTC8*Pd-4.0	1022 (314)	0.58 (0.14)	0.6/1.2/2.4	4.2(5.0)	20.5

The values in parenthesis refer to: ^a t-plot micropore area, ^b t-plot micropore volume, ^c maxima of the PSD obtained using NLDFT model analysis, ^d maximum hydrogen uptake (wt %) estimated from Langmuir plots. Data in ^e is hydrogen uptake density in μmol.H₂m⁻² (ρ).

5.3.5.3 Electron microscopy analysis of Pd-free and Pd-doped carbons

The TEM images in Figure 5.10 for sample ZTC8* (i.e. before Pd incorporation) are consistent with the XRD data in showing only low levels of zeolite-like ordering. There are clearly observable void spaces (Figure 5.10B) indicative of incomplete filling of the zeolite template pores in a manner similar to that observed by Johnson and co-workers on the effect of micropore topology on the structure and properties of zeolite polymer replicas.³⁵ The TEM images are also, in agreement with XRD patterns, consistent with there being minimal graphitisation for this sample that was prepared at 800 °C.

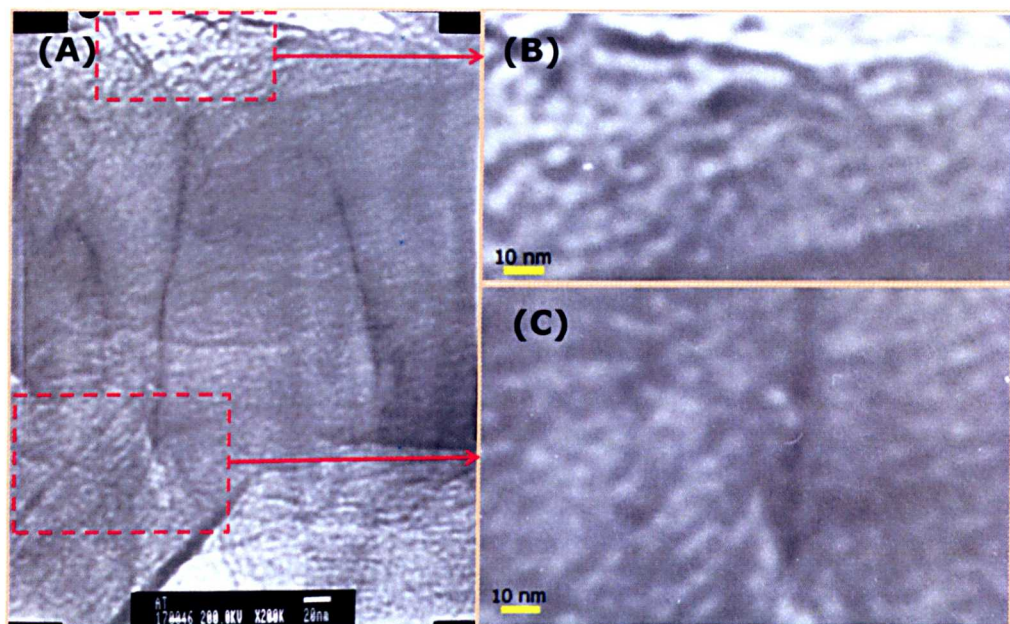


Figure 5.10 TEM micrographs of zeolite templated carbon ZTC8* carbonised at 800 °C in argon flow.

TEM images for the Pd-loaded sample with the highest amount of Pd are shown in Figure 5.11. Irregularly-dispersed spherical Pd nanoparticles of size 4 – 6 nm are clearly observed. We note that Wai and co-workers, using supercritical CO₂, decorated multi-walled carbon nanotubes (MWCNTs) with Pd nanoparticles with a size range of 5 - 10 nm.⁴⁷ The selected area electron diffraction (SAED) pattern of the Pd nanoparticles in Figure 5.11C shows concentric rings without any clear spots, which is suggestive of nanoparticles composed of agglomerated fine crystallites. The SAED data is in good agreement with the XRD patterns in Figure 5.8A with well-resolved diffraction peaks corresponding to Pd.

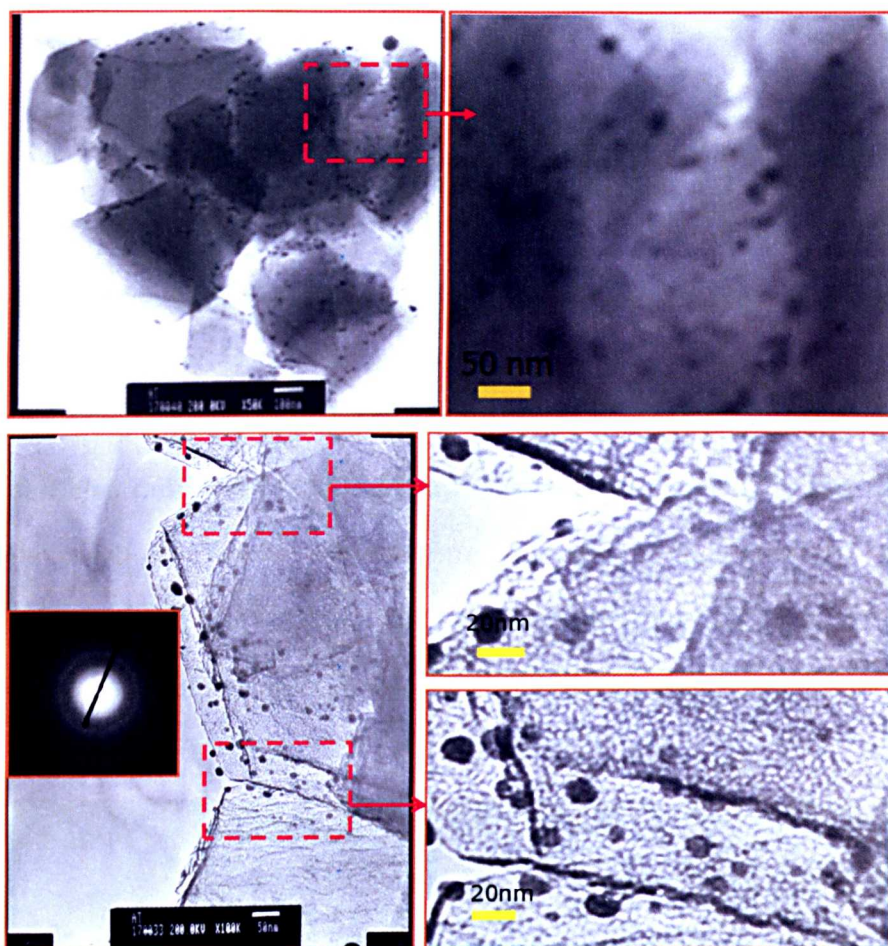


Figure 5.11 TEM images of the highest doped carbon (ZTC8*Pd-4.0) illustrating fairly well dispersed Pd nanoparticles with possibility of agglomeration.

TEM images with Pd-loaded samples with intermediate amounts of Pd are given in Figures 5.12, 5.13 and 5.14. The TEM images clearly show the increase in amount of Pd. Indeed, for sample ZTC8Pd-0.2, we observed hardly any Pd particles. This shows that this amount of added Pd is too low to allow any significant deposition of Pd nanoparticles that are large enough to be observed by our TEM. For sample ZTC8Pd-0.4 with 0.4 mg Pd, it is possible to observe (Figure 5.13) some Pd nanoparticles. For

sample ZTC8Pd-0.8 with 0.8 mg the Pd particles are easily observed and appear, in general, to be well distributed throughout the carbon particles (Figure 5.14). The size of the Pd nanoparticles is rather smaller (3-5 nm) than those of sample ZTC8*Pd-4.0 (Figure 5.11). Thus the variable Pd incorporation is evident with less visible Pd nanoparticles on decreasing the doping amount and vice versa as illustrated in Figure 5.11 to 5.14. Thus on reducing the amount of Pd(hfa)₂ precursor, the loading density of Pd nanoparticles onto the carbon substrate decreases. Therefore, the findings in this section clearly demonstrate successful incorporation of Pd nanoparticles into the carbons by hydrogen reduction of organometallic precursors using supercritical CO₂ as a reaction medium.

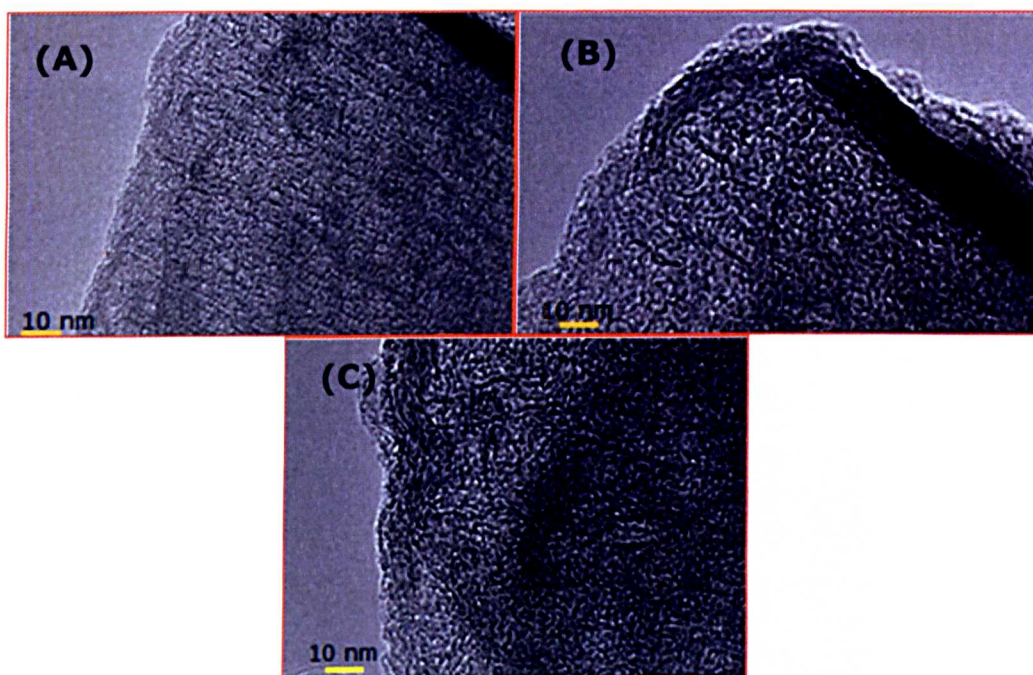


Figure 5.12 TEM images of ZTC8Pd-0.2 with 0.2 mg Pd loading.

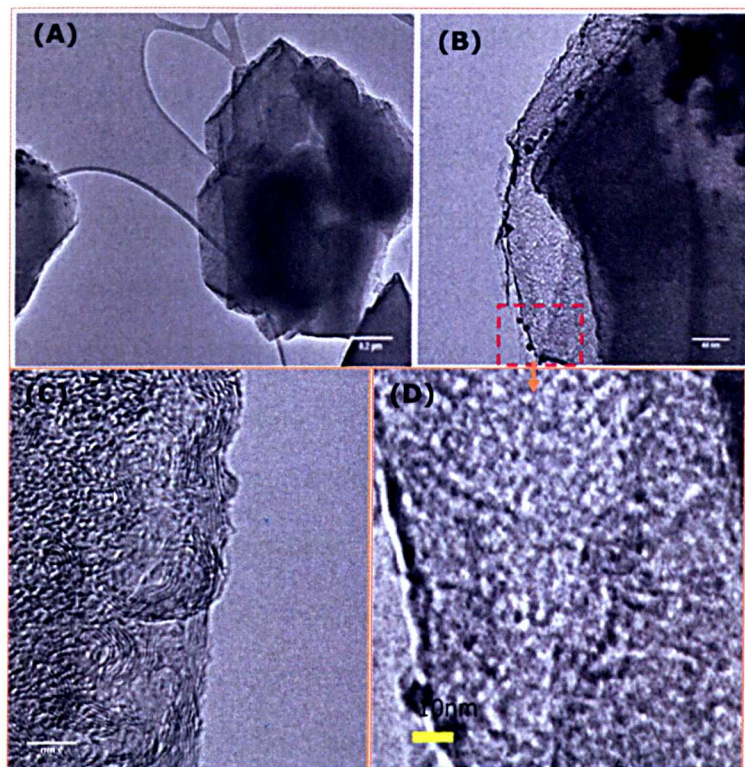


Figure 5.13 TEM micrographs of ZTC8Pd-0.4 with 0.4 mg Pd loading.

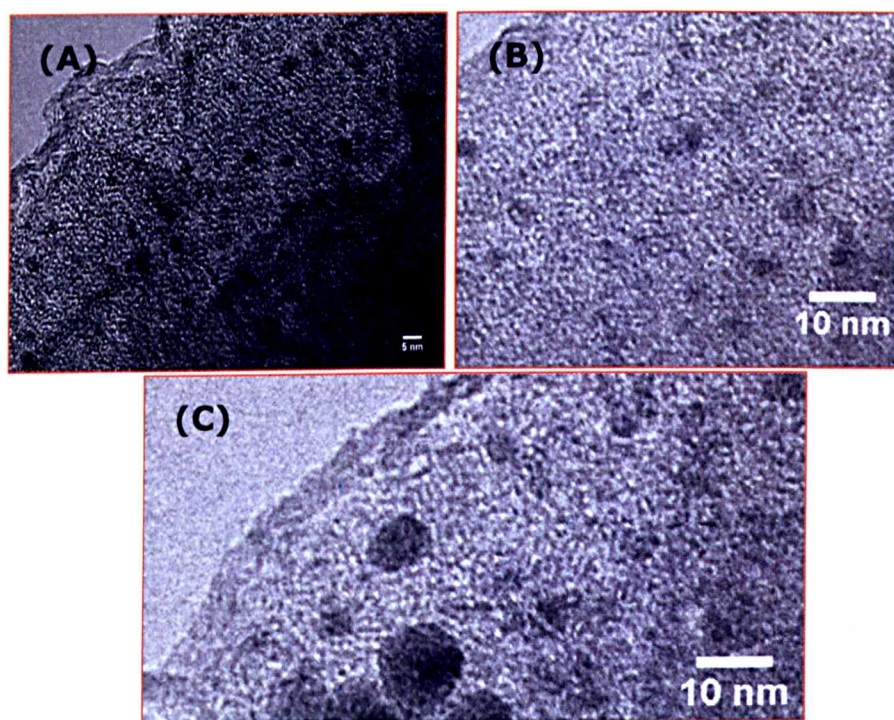


Figure 5.14 TEM images of ZTC8Pd-0.8 with 0.8 mg Pd loading.

5.4 Hydrogen uptake measurements of Pd-free and Pd-doped carbons

The safe and reversible storage of hydrogen is one of the main challenges that must be overcome before the realization of 'Hydrogen Economy'. This challenge is currently the focus of intensive research as recently highlighted by the review of Berg and Areán focusing on materials that are being developed and modified for hydrogen storage.¹ A key aspect of current research is the ability to correctly determine the hydrogen uptake of any materials that are developed. Hydrogen uptake is mainly determined via volumetric or gravimetric methods. In this work, a gravimetric method has been used and all issues that may affect the obtained results have been addressed.^{48, 49} The hydrogen uptake isotherms were calculated based on a carbon density of 1.5 g/cm³, and a hydrogen density of 0.04 g/cm³ was used for buoyancy correction of adsorbed hydrogen.^{50, 51} The hydrogen uptake capacity (at 77K and a pressure of 20 bar) for Pd-free and Pd-doped carbons was obtained as described in section 3.7.2. The hydrogen storage capacity data is summarised in Table 5.2 and the corresponding hydrogen uptake isotherms are shown in Figures 5.15 and 5.16. Also presented in Figure 5.16B is a graph showing hydrogen uptake normalised per unit surface area (i.e. hydrogen uptake density in $\mu\text{mol H}_2/\text{m}^2$). The hydrogen uptake isotherms (Figure 5.15 and Figure 5.16A) show that the adsorption branch for all the samples matches the desorption branch with no hysteresis suggestive that the hydrogen sorption is fully reversible. In addition, the isotherms exhibit no saturation in the 0 – 20 bar pressure range indicative of the possibility of higher hydrogen uptake if the pressure is increased beyond 20 bar.

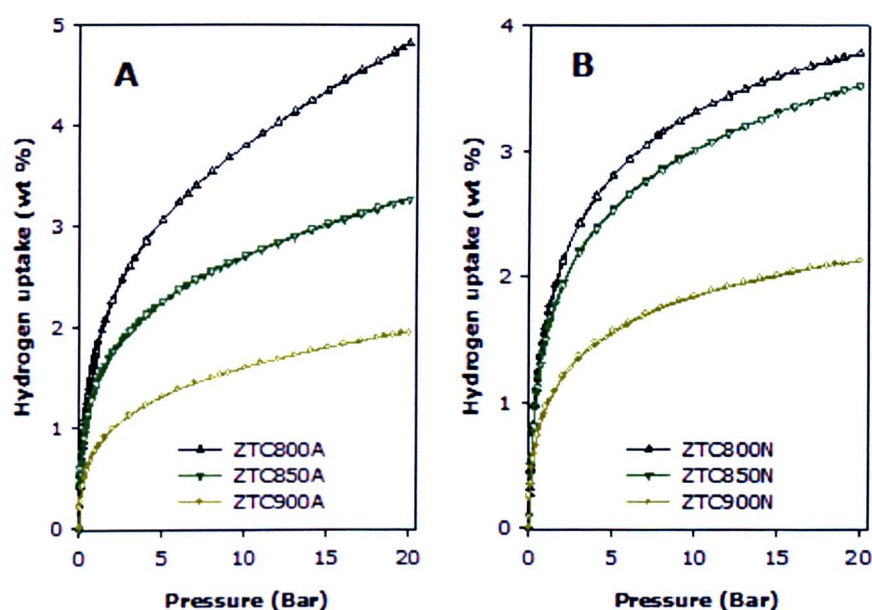


Figure 5.15 Hydrogen uptake isotherms at 77K and pressure range of 0 – 20 bar for zeolite templated carbons prepared at 800, 850 or 900 °C under argon (A) and nitrogen (B) gas flow.

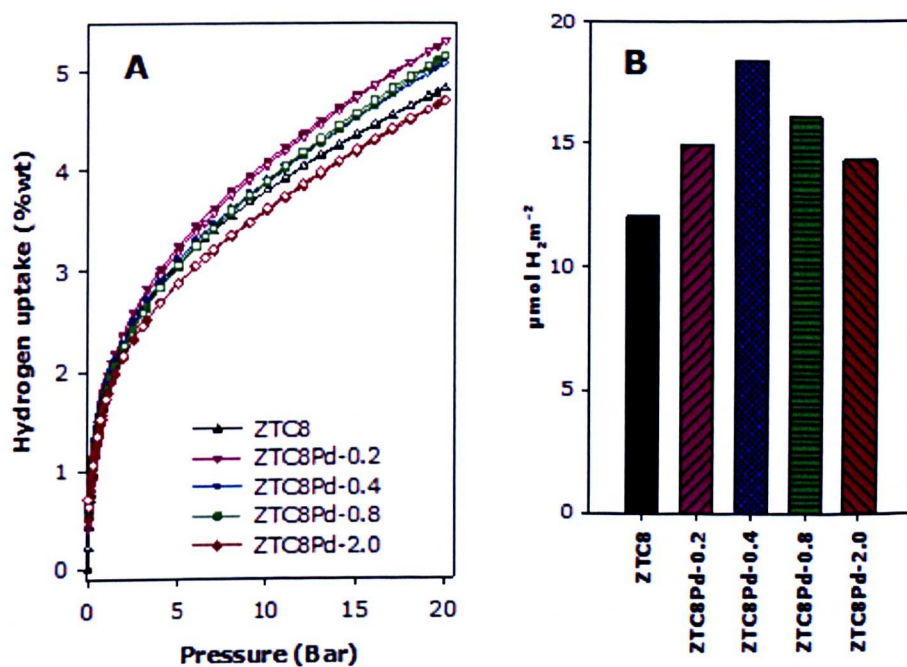


Figure 5.16 hydrogen uptake isotherms (A) and hydrogen uptake density (B) of Pd-free (ZTC8) and Pd-loaded carbons.

Hydrogen uptake of 4.9% (at 20 bar and 77K) for the Pd-free ZTC8 carbon that has a surface area of 2046 m²/g is expected based on the known performance of zeolite templated carbons. This hydrogen uptake is rather higher than that which would be predicted based on Chahine rule of 1 wt% uptake per 500m²/g of surface area.^{4, 52} An estimated maximum hydrogen uptake capacity of 5.8 wt% (Table 5.2) was computed by fitting the experimental data using the Langmuir model^{10, 53} The data obtained for the Pd-free carbon is therefore in good agreement with previous reports on zeolite templated carbons and more generally with the known relationship between hydrogen uptake and the surface area of porous materials.^{11, 54}

In general Pd-doped carbons showed higher hydrogen uptake capacity compared to the original Pd-free carbon. This is clearly illustrated in Figure 5.15B in which samples doped with Pd have a higher uptake per unit surface area; the improvement in uptake density over Pd-free carbons is up to 60% greater than the corresponding Pd-free sample. It is interesting to note that ZTC8Pd-0.2 gave the highest hydrogen uptake of 5.3 wt%, but due to its higher surface area, did not show the highest uptake density. This highlights the compromise between the optimum incorporation of Pd and the conservation of microporous structure. The hydrogen uptake data for the Pd-loaded zeolite templated carbons shows a trend similar to that observed by Yang and co-workers who found the order of hydrogen uptake in Ru-doped templated carbon to be 6% Ru > 8% Ru > 3% Ru. This was ascribed to both reduced surface area in the case of the highest loading and a lower amount of Ru metal in the case of the lowest loading.⁵⁵

To further probe the influence of Pd incorporation on the hydrogen uptake, the hydrogen adsorption energy; the so-called isosteric heat of adsorption (Q_{st}) of the samples was obtained and compared. The Q_{st} was calculated using the hydrogen adsorption isotherms measured at two independent temperatures (-186 and -196 °C) as illustrated in Figure 5.17.

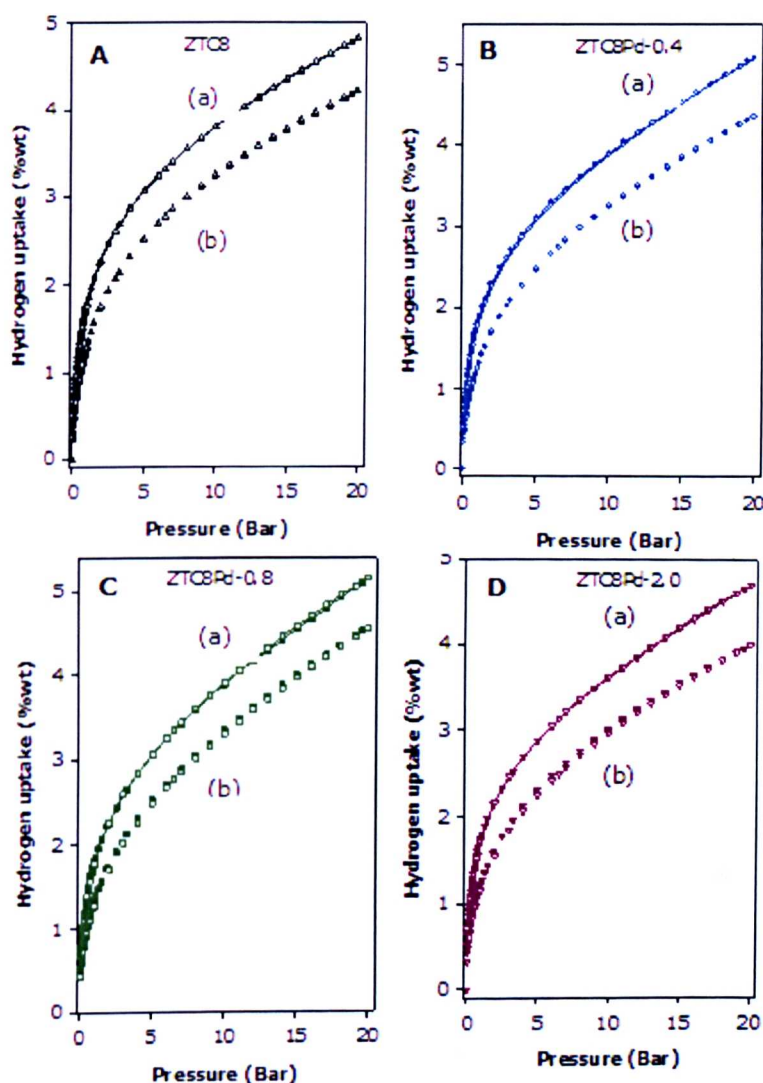


Figure 5.17 hydrogen uptake isotherms of pd-free or pd-doped samples obtained at 77k (a) or 87k (b). Filled symbols are for adsorption and empty symbols for desorption.

The adsorption branch of the hydrogen uptake isotherms in Figure 5.16 was used to determine isosteric heat of adsorption based on the Clausius-Clapeyron equation as discussed in section 3.7.2. The plots of isosteric heat of adsorption as a function of hydrogen uptake for the Pd-free and Pd-doped carbons presented in Figure 5.18 shows that the Q_{st} for Pd-doped samples are generally higher than Pd-free sample at low hydrogen uptake.

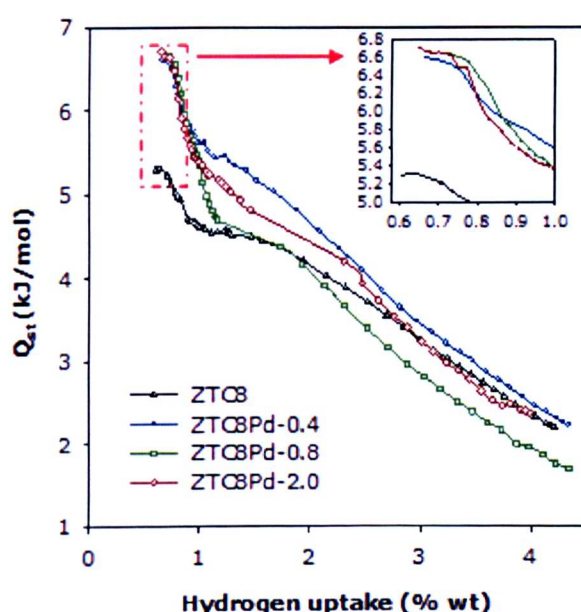


Figure 5.18 Isosteric heat of adsorption (Q_{st} kJ/mol) as a function of the quantity of hydrogen adsorbed for Pd-free (ZTC8) and Pd-loaded zeolite templated carbons.

Figure 5.18 clearly illustrates that the heat of adsorption decreases at higher hydrogen uptake.^{10, 14, 56, 57} The Q_{st} for Pd-free sample (ZTC8) is ca. 5.3 kJ/mol compared to the Pd-doped carbons with up to 6.7 kJ/mol. The higher values for Pd-doped carbons are indicative of greater hydrogen – substrate interaction. Overall, the Q_{st} values observed are slightly lower

than those reported for zeolite templated carbons with smaller pores (8.2 kJ/mol)¹⁰ and comparable to those of most activated carbons. (4 to 6.5 kJ/mol).⁵⁷⁻⁵⁹ The increase in Q_{st} of 18% may be attributed to the so-called 'spillover' effect whereby hydrogen molecules dissociate to atomic hydrogen on a metal catalyst and successively migrate from the metal to the surface of carbonaceous material.²⁰ Similar trends have been reported by Lueking and Yang in which enhancement of hydrogen storage properties were established via hydrogen spillover onto metal catalyst (transition metals such as Pt, Pd and Ni) supported carbon nanotubes.^{60, 61}

5.5 Summary

Zeolite Y has been used as a hard template to successfully generate a suite of carbons via inverse replication. The ingress of the carbon precursor into the zeolite Y pore channels was achieved via chemical vapour deposition at temperatures between 800 and 900 °C. The sample prepared at CVD temperature of 800 °C exhibited some zeolite-like structural ordering and the highest textural properties with surface area of ca. 2200 m²/g and pore volume of 1.26 cm³/g. On the contrary, the extent of graphitisation was highest for the sample prepared at CVD temperature of 900 °C. The CVD environment (argon or nitrogen) was found not to have any significant effect of the textural properties of the zeolite templated carbons, although nitrogen appeared to favour greater carbon deposition and slightly higher levels of graphitisation. Supercritical carbon dioxide was used as medium for the deposition of well dispersed Pd nanoparticles onto the sample prepared at 800 °C. The SCF-mediated Pd incorporation enabled the decoration of high surface area ZTCs prepared at 800 °C with 0.2 – 4.0 mg of well dispersed Pd nanoparticles. Whilst the surface area and pore volume

of the carbon decreased on Pd doping, with the decrease dependent on amount of Pd, there was no change in the pore size or pore size distribution. Crucially, we observed that Pd incorporation enhances hydrogen uptake presumably via the so-called spillover process. Although the surface area and pore volume decreased significantly (by up to 50%) on Pd incorporation, the hydrogen uptake remained largely unchanged. This in effect translated to a much higher hydrogen storage density for the Pd doped carbons. Thus, while the zeolite templated carbon (ZTC) used as substrate (with surface area of 2046 m²/g) had a hydrogen storage capacity (at 77K and 20 bar) of 4.9 wt%, the Pd-ZTCs had uptake of 4.7 – 5.3 wt% despite surface area in the range 1390 – 1858 m²/g. The Pd-ZTCs thus exhibit enhanced hydrogen storage density (14.3 – 20.5 μmol H₂/m²), which is much higher than that of Pd-free zeolite templated carbon (12.0 μmol H₂/m²). The hydrogen storage density goes through maxima at 0.4 mg Pd loading.

The findings in this section therefore provide excellent insight into the process of optimising the balance between metal loading and surface area so as to achieve the best composite for enhanced hydrogen uptake.

5.6 Bibliography

1. A. W. C. van den Berg and C. O. Arian, *Chem. Commun.*, 2008, 668-681.
2. K. M. Thomas, *Catal. Today*, 2007, **120**, 389-398.
3. A. Ahmadpour and D. D. Do, *Carbon*, 1996, **34**, 471-479.
4. M. Sevilla, N. Alam and R. Mokaya, *J. Phys. Chem. C*, 2011, **114**, 11314 - 11319.
5. M. Sevilla, A. B. Fuertes and R. Mokaya, *Energy Environ. Sci.*, 2011, **4**, 1400-1410.
6. R. Ryoo, S. H. Joo and S. Jun, *J. Phys. Chem. B*, 1999, **103**, 7743-7746.
7. B. Sakintuna and Y. Yürüm, *Ind. Eng. Chem. Res.*, 2005, **44**, 2893-2902.
8. T. Kyotani, *Bull. Chem. Soc. Jpn.*, 2006, **79**, 1322-1337.
9. Y. Xia, Z. Yang and R. Mokaya, *Nanoscale*, 2010, **2**, 639-659.
10. Z. Yang, Y. Xia and R. Mokaya, *J. Am. Chem. Soc.*, 2007, **129**, 1673-1679.
11. Z. X. Yang, Y. D. Xia, X. Z. Sun and R. Mokaya, *J. Phys. Chem. B*, 2006, **110**, 18424-18431.
12. N. Texier-Mandoki, J. Dentzer, T. Piquero, S.-E. Saadallah, P. David and C. Vix-Guterl, *Carbon*, 2004, **24**, 2744-2747.
13. I. Cabria, M. J. López and J. A. Alonso, *Carbon*, 2007, **45**, 2649-2658.
14. G. Yushin, R. Dash, J. Jagiello, J. E. Fischer and Y. Gogotsi, *Adv. Funct. Mater.*, 2006, **16**, 2288-2293.

15. C. Vix-Guterl, E. Frackowiak, K. Jurewicz, M. Friebe, J. Parmentier and F. Béguin, *Carbon*, 2005, **43**, 1293-1302.
16. Y. Gogotsi, C. Portet, S. Osswald, J. M. Simmons, T. Yildirim, G. Laudisio and J. E. Fischer, *Int. J. Hydrogen Energy*, 2009, **34**, 6314-6319.
17. Y. Gogotsi, R. K. Dash, G. Yushin, T. Yildirim, G. Laudisio and J. E. Fischer, *J. Am. Chem. Soc.*, 2005, **127**, 16006-16007.
18. C. Zlotea, F. Cuevas, V. r. Paul-Boncour, E. Leroy, P. Dibandjo, R. Gadiou, C. Vix-Guterl and M. Latroche, *J. Am. Chem. Soc.*, 2010, **132**, 7720-7729.
19. D. Giasafaki, A. Bourlinos, G. Charalambopoulou, A. Stubos and T. Steriotis, *Microporous Mesoporous Mater.*, 2012, **154**, 74-81.
20. C.-H. Chen and C.-C. Huang, *Microporous Mesoporous Mater.*, 2008, **109**, 549-559.
21. C.-Y. Chen, J.-K. Chang, W.-T. Tsai and C.-H. Hung, *J. Mater. Chem.*, 2011, **21**, 19063-19068.
22. X. R. Ye, Y. Lin and C. M. Wai, *Chem. Commun.*, 2003, 642-643.
23. R. Zacharia, K. Y. Kim, A. K. M. Fazle Kibria and K. S. Nahm, *Chem. Phys. Lett.*, 2005, **412**, 369-375.
24. N. P. Stadie, J. J. Purewal, C. C. Ahn and B. Fultz, *Langmuir*, 2010, **26**, 15481-15485.
25. R. Campesi, F. Cuevas, E. Leroy, M. Hirscher, R. Gadiou, C. Vix-Guterl and M. Latroche, *Microporous Mesoporous Mater.*, 2009, **117**, 511-514.
26. R. B. Levy and M. Boudart, *J. Catal.*, 1974, **32**, 304-314.
27. S. J. Teichner, *Applied Catalysis*, 1990, **62**, 1-10.

28. V. V. Bhat, C. I. Contescu and N. C. Gallego, *Nanotechnology*, 2009, **20**, 204011.
29. R. Prins, *Chem. Rev.*, 2012, **112**, 2714-2738.
30. J. L. Figueiredo, M. F. R. Pereira, P. Serp, P. Kalck, P. V. Samant and J. B. Fernandes, *Carbon*, 2006, **44**, 2516-2522.
31. C. Bittencourt, A. Felten, J. Ghijsen, J. J. Pireaux, W. Drube, R. Erni and G. Van Tendeloo, *Chem. Phys. Lett.*, 2007, **436**, 368-372.
32. Y. Zhang and H. Dai, *Appl. Phys. Lett.*, 2000, **77**, 3015-3017.
33. K. S. Morley, P. Licence, P. C. Marr, J. R. Hyde, P. D. Brown, R. Mokaya, Y. Xia and S. M. Howdle, *J. Mater. Chem.*, 2004, **14**, 1212-1217.
34. J. A. Darr and M. Poliakoff, *Chem. Rev.*, 1999, **99**, 495-542.
35. S. A. Johnson, E. S. Brigham, P. J. Ollivier and T. E. Mallouk, *Chem. Mater.*, 1997, **9**, 2448-2458.
36. T. Kyotani, T. Nagai, S. Inoue and A. Tomita, *Chem. Mater.*, 1997, **9**, 609-615.
37. Z. Ma, T. Kyotani and A. Tomita, *Carbon*, 2002, **40**, 2367-2374.
38. J. Rodriguez-Mirasol, T. Cordero, L. R. Radovic and J. J. Rodriguez, *Chem. Mater.*, 1998, **10**, 550-558.
39. A. Demessence, D. M. D'Alessandro, M. L. Foo and J. R. Long, *J. Am. Chem. Soc.*, 2009, **131**, 8784-8786.
40. C. Guan, K. Wang, C. Yang and X. S. Zhao, *Microporous Mesoporous Mater.*, 2009, **118**, 503-507.
41. F. Su, X. S. Zhao, L. Lv and Z. Zhou, *Carbon*, 2004, **42**, 2821-2831.

42. R. Ströbel, J. Garche, P. T. Moseley, L. Jörissen and G. Wolf, *J. Power Sources*, 2006, **159**, 781-801.
43. H. Wakayama and Y. Fukushima, *Ind. Eng. Chem. Res.*, 2005, **45**, 3328-3331.
44. V. Bhaskaran, M. J. Hampden-Smith and T. T. Kodas, *Chem. Vap. Deposition*, 1997, **3**, 85-90.
45. T. Hasell, C. D. Wood, R. Clowes, J. T. A. Jones, Y. Z. Khimyak, D. J. Adams and A. I. Cooper, *Chem. Mater.*, 2009, **22**, 557-564.
46. K. S. W. Sing, D. H. Everett, R. A. W. Haul, L. Moscou, R. A. Pierotti, J. Rouquerol and T. Siemieniewska, *Pure Appl. Chem.*, 1985, **57**, 603-619.
47. X. Ye, Y. Lin, C. M. Wang, M. H. Engelhard, Y. Wang and C. M. Wai, *J. Mater. Chem.*, 2004, **14**, 908-913.
48. N. B. McKeown, B. Gahnem, K. J. Msayib, P. M. Budd, C. E. Tattershall, K. Mahmood, S. Tan, D. Book, H. W. Langmi and A. Walton, *Angew. Chem. Int. Ed.*, 2006, **45**, 1804-1807.
49. N. B. McKeown, B. Gahnem, K. J. Msayib, P. M. Budd, C. E. Tattershall, K. Mahmood, S. Tan, D. Book, H. W. Langmi and A. Walton, *Angew. Chem.*, 2006, **118**, 1836-1839.
50. P. Kowalczyk, P. A. Gauden, A. P. Terzyk and S. K. Bhatia, *Langmuir*, 2007, **23**, 3666-3672.
51. Q. Y. Wang and J. K. Johnson, *J. Chem. Phys.*, 1999, **110**, 577-586.
52. M. Sevilla, R. Mokaya and A. B. Fuertes, *Energy Environ. Sci.*, 2011, **4**, 2930-2936.
53. Z. Zheng, Q. Gao and J. Jiang, *Carbon*, 2010, **48**, 2968-2973.
54. A. G. Wong-Foy, A. J. Matzger and O. M. Yaghi, *J. Am. Chem. Soc.*, 2006, **128**, 3494-3495.

55. L. Wang and R. T. Yang, *J. Phys. Chem. C*, 2008, **112**, 12486-12494.
56. G. Srinivas, Y. Zhu, R. Piner, N. Skipper, M. Ellerby and R. Ruoff, *Carbon*, 2010, **48**, 630-635.
57. P. Bénard and R. Chahine, *Langmuir*, 2001, **17**, 1950-1955.
58. L. Zhou, Y. Zhou and Y. Sun, *Int. J. Hydrogen Energy*, 2004, **29**, 475-479.
59. X. B. Zhao, B. Xiao, A. J. Fletcher and K. M. Thomas, *J. Phys. Chem. B*, 2005, **109**, 8880-8888.
60. A. D. Lueking and R. T. Yang, *Appl. Catal., A*, 2004, **265**, 259-268.
61. A. Lueking and R. T. Yang, *J. Catal.*, 2002, **206**, 165-168.

Chapter Six

Chapter 6.0 Two-Step Process Preparation of Ultrahigh Surface Area Porous Carbons Templated using Zeolite 13X for Enhanced Hydrogen Storage193

6.1 Abstract 193

6.2 Introduction..... 193

6.3 Results and Discussion.....195

6.3.1 Structural ordering and thermal stability..... 195

6.3.2 Porosity of zeolite templated carbons 199

6.3.3 Nanoscale ordering of zeolite templated carbons..... 202

6.3.4 Assessment of mechanical stability of FA-ZTCs 203

6.3.5 Hydrogen uptake storage..... 207

6.4 Summary 211

6.5 Bibliography..... 212

Chapter 6.0 Two-Step Process Preparation of Ultrahigh Surface Area Porous Carbons Templated using Zeolite 13X for Enhanced Hydrogen Storage

6.1 Abstract

In this chapter, the use of zeolite 13X as a template to generate ultrahigh surface area carbons, via a two-step process combining liquid impregnation and chemical vapour deposition is explored. In this method, the first step involves impregnation of zeolite 13X with furfuryl alcohol and the second step consists of chemical vapour deposition (CVD) of ethylene. Zeolite-like structural ordering was achieved for all the zeolite templated carbons (ZTCs) prepared at variable heating ramp rates. Likewise, the textural properties for all carbons were comparable with negligible variations. The templated carbons exhibit very high surface area and pore volume of up to 3332 m²/g and 1.66 cm³/g respectively. The carbon materials achieved a remarkable hydrogen uptake of 7.3 wt% at 20 bar and 77 K which is the highest ever recorded for carbon materials. This chapter also explored the mechanical stability of the carbons via compaction in which the resultant compacted sample showed minimal modification.

6.2 Introduction

In recent years, research on hydrogen storage has been guided mainly by the requirements set forth by the United States Department of Energy (DOE) in 2003.¹ Revisions to these requirements are on-going as the program moves towards its set targets based on improved forecasts that come from actual experience. For example, the revision done in 2010 decreased the storage target to 5 wt% (40 g/L) of hydrogen at ambient temperature and pressure < 100 bar. One of the most promising methods to store hydrogen is in solid state materials such as nanostructured porous

carbon materials, because porous carbons have attractive chemical, physical, thermodynamic and transport properties compared to other bulky materials.²

Nanostructured porous carbons with high surface area and well-ordered pore systems continue to be a very important category of porous materials at nanometre scale for possible application in hydrogen storage.³⁻⁷ Thus, work in the research group of Mokaya has shown that zeolite templated carbons store up to 6.9 wt% hydrogen at 20 bar and 77 K, one of the highest value reported to date.⁶ More recently, our group achieved hydrogen uptake capacity of 7.03 wt% under similar conditions for ultrahigh surface area polypyrrole-based activated carbons.⁸

Porous carbons are conventionally obtained by carbonisation of precursors of natural or synthetic origin, followed by chemical or physical activation procedures. However, traditional activation procedures lack control over porosity development, leading to materials with broad pore size distributions and completely disordered structures. On the other hand, hard templating with inorganic frameworks has been the most successful method so far in controlling the porosity of carbons.⁹⁻¹⁵ This method involves filling the pores of a solid with a different material, and chemical separation of the resulting material from the template. The success of this method has also been demonstrated for the preparation of replica polymers,^{16, 17} metals¹⁸ and semi-conductors,^{19, 20} among an ever increasing list of novel porous materials. This chapter will describe the use of suitable templates to prepare carbon materials with controlled architecture and relatively narrow pore size distribution. In particular, the target templated carbons that possess a significant proportion of

micropores below 1.0 nm and preferably in the range 0.6 – 0.8 nm as it is known from previous studies that such pores are the most efficient for hydrogen adsorption.^{8, 21-25}

Among the many templates that are currently under intensive research for synthesis of nanostructured carbons, much attention has been paid to zeolites.^{10, 25-28} Despite extensive investigations into nanocasting techniques, the use of a two-step synthesis, as demonstrated in this chapter, has not yet been fully exploited. This process involves Liquid Impregnation (LI) in which zeolite channels are first filled by furfuryl alcohol followed by polymerisation and partial carbonisation as the first stage. The second stage involves the use of ethylene as a carbon precursor for chemical vapour deposition (CVD). The selection of zeolite 13X selection as a hard template was based on the fact that most studies so far have focused on the use of zeolite Y (FAU-type structure),^{9, 12, 13, 29} zeolite beta^{6, 30} and zeolite EMC-2 (EMT-structure type).³¹

Separately, the effect of compaction on the textural properties is assessed since such materials are expected to withstand high pressure conditions in some industrial applications. Commercially available activated carbon AX21 was used in this work as baseline material in the assessment of textural properties before and after compaction.

6.3 Results and Discussion

6.3.1 Structural ordering and thermal stability

Figure 6.1 shows the powder XRD patterns of ZTCs obtained at variable heating ramp rate. For comparison, the XRD pattern for zeolite 13X and zeolite/carbon composite are also included. For all the carbons, the XRD patterns show a sharp peak, similar to that present in the zeolite 13X, at

$2\theta = 6.3^\circ$ with d-spacing of ca. 1.4nm which is comparable to that of zeolite 13X (d-spacing = 1.4 nm). This suggests that the resulting ZTCs exhibit structural pore ordering similar to that of zeolite 13X.^{26, 32, 33} In addition a very broad and weak reflection is observable at ca. $2\theta = 43^\circ$ which is attributed to (101) diffraction from graphitic/turbostratic carbon.³⁴

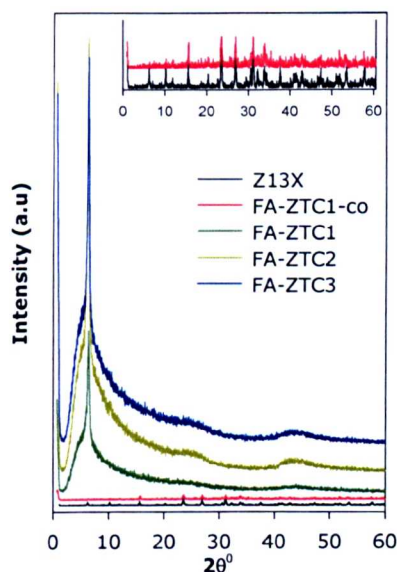


Figure 6.1 Powder XRD patterns of zeolite templated carbons (FA-ZTC1, FA-ZTC2 and FA-ZTC3) prepared at variable heating ramp rate (5, 10 and 15 °C/min respectively). Patterns for the zeolite/carbon composite (FA-ZTC1-co), zeolite 13X (Z13X) are also shown inset.

The weak peak observed at $2\theta = 43^\circ$ could be attributed to the presence a thin layer of turbostratic carbon deposited on the outer surface of the zeolite particles.^{26, 29, 35} However, worth noting is the near complete absence of an powder XRD reflection at $2\theta \approx 26^\circ$, usually ascribed to the (002) diffraction of graphitic carbon. The XRD patterns of zeolite 13X and the zeolite/carbon composite (Figure 6.1 and inset) are characterised by the appearance of many sharp peaks due to the framework topology of zeolite 13X. The presence of these peaks is evidence that the zeolite

framework is not destroyed upon carbonisation and heat treatment at temperatures of up to 900 °C. However, it is worth noting that the intensity of zeolite structural peaks is significantly reduced as expected in the composite particularly at low angle. This is due to the filling of zeolite pores causing reduction in phase contrast scattering. In contrast to the single step carbonisation investigated in section 5.5.1, it can clearly be observed from the XRD patterns in Figure 6.1 that the structural integrity of zeolite frameworks is more readily replicated in the carbons.

It is reasonable to infer that the FA-ZTC samples are essentially amorphous (i. e. non-graphitic) with respect to crystallographic ordering. This is evident from the absence of the peak at $2\theta \approx 26^\circ$, as well as the presence of a weak and broad peak at $2\theta = 43^\circ$. This is because at 700 °C (which is the CVD temperature used for synthesis of FA-ZTC samples) the carbonisation process is relatively slow and the ethylene in the second step is able to permeate into the zeolite/polyfurfuryl alcohol composite into any unfilled zeolite pores. The preferential internal deposition of carbon into zeolite particles has been reported by Mokaya and co-workers to enhance the replication of zeolite-like pore channel regularity in the resulting carbon materials.¹² Moreover, given the narrow nanochannels of zeolite 13X, it is impossible to form stacking structures within the pores and therefore the expectation is that the resultant carbons will comprise a single graphene sheet without any stacking and are thus are non-graphitic.³⁶ Overall, the XRD patterns indicate that the heating ramp rate had negligible effect on the structural ordering of the resultant carbons.

The thermal stability of the FA-ZTC samples was probed by Thermogravimetric Analysis (TGA). Figure 6.2 shows the TGA curves of the

zeolite template (Z13X), zeolite/carbon composite (FA-ZTC1-Co) and a representative carbon (FA-ZTC1).

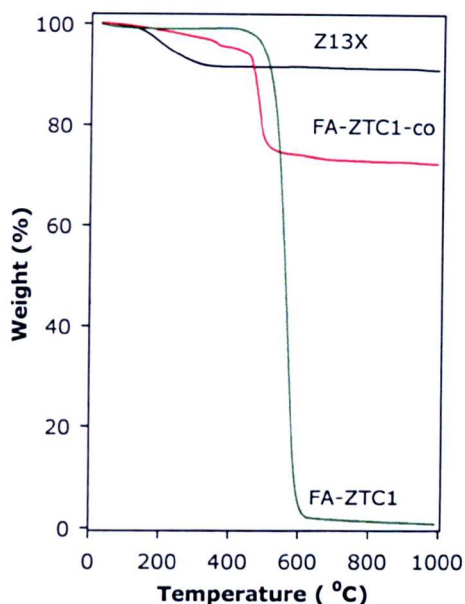


Figure 6.2 TGA curves for zeolite 13X (Z13X), zeolite/carbon composite (FA-ZTC1-co) and a representative zeolite template carbon (FA-ZTC1).

The TGA curve of the zeolite 13X template shows a weight loss event of ca. 10% in the temperature range 180 °C to 350 °C which is attributable to water. As expected after this early weight loss, the zeolite is stable up to 1000 °C. TGA curve for the zeolite/carbon composite (FA-ZTC1-co) exhibits a single weight loss between 400 and 560 °C due to the combustion of the carbon component. The percentage of carbon in the zeolite/carbon composite was determined to be ca. 28%. The assessment of a representative template free carbon sample (FA-ZTC1) by TGA showed that the carbons exhibit a residual weight of < 2% at 620 °C thus confirming that the resultant carbons are virtually zeolite-free. In addition, it is clearly observable that the carbon sample obtained is mainly one phase material given the sharp weight loss within a temperature range of < 5 °C.

6.3.2 Porosity of zeolite templated carbons

Nitrogen sorption isotherms and corresponding pore size distribution curves of the zeolite templated carbons prepared at variable heating ramp rate are shown in Figure 6.3. For comparison, the data for the zeolite 13X template and commercially available activated carbon (AX21) is also presented. The nitrogen sorption isotherms of all the prepared carbons are mainly type I, with a high nitrogen uptake in the low relative pressure domain ($P/P_0 < 0.01$). The isotherms reveal the super-microporous character of the prepared carbon materials ($1.0 \text{ nm} < \text{pore diameter} < 2.0 \text{ nm}$).

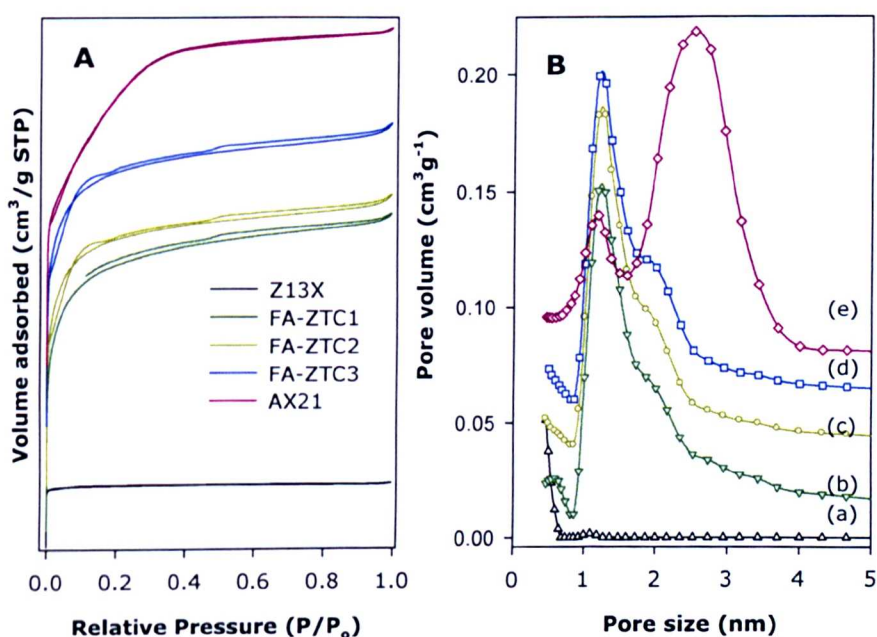


Figure 6.3 Nitrogen sorption isotherms (A) and pore size distribution curves (B) for (a) zeolite 13X, (b) FA-ZTC1, (c) FA-ZTC2, (d) FA-ZTC3 and (e) AX21. For clarity, the PSD curves (B); (b), (c), (d) and (e) are offset (y-axis) by 0.01, 0.04, 0.06 and 0.08 cm³/g, respectively.

The isotherms of all the FA-ZTCx samples exhibit hysteresis over a wide range of relative pressure ($P/P_0 = 0.01$ to 0.99) which has previously been reported for some zeolite templated carbons.^{12, 27, 37, 38} The isotherms are [199]

consistent with the data reported by Mokaya and co-workers for zeolite templated carbons that exhibit significant levels of zeolite-like ordering.^{6, 12}

The pore size distribution curves for the microporous carbons, calculated using Nonlocal Density Function Theory (NLDFT) are presented in Figure 6.3B. The carbons templated from zeolite 13X exhibit unimodal PSD maximum centred at 1.2 nm; the pore size maxima are summarised in Table 6.1. The obtained pore size of 1.2 nm is consistent with previous studies that have shown that zeolite templated carbons with higher levels of zeolite-like ordering do not possess pores larger than 1.5 nm.^{6, 15, 34}

On the contrary the AX21 sample has a bimodal pore size distribution centered at 1.1 and 2.5 nm with a higher proportion of the latter pores. Table 6.1 gives the textural parameters and hydrogen uptake of the FA-ZTCx zeolite templated carbons, along with data for the zeolite 13X template.

Table 6.1 Textural properties and hydrogen uptake of ultrahigh surface area porous carbons prepared by a two-step process using zeolite 13x. Also data for zeolite 13X is included for comparison.

Sample	Surface area (m ² /g) ^a	Pore volume (cm ³ /g) ^b	Pore size (nm) ^c	H ₂ uptake	
				(wt%) ^d	density (ρ) ^e
Z13X	658 (646)	0.33 (0.31)	1.0	-	-
FA-ZTC1	3332 (2837)	1.66 (1.18)	1.2	7.3	11.0
FA-ZTC2	3106 (2728)	1.50 (1.13)	1.2	6.6	10.6
FA-ZTC3	3169 (2760)	1.55 (1.15)	1.2	6.0	9.5

The values in the parenthesis refer to: ^amicropore surface area, ^bmicropore volume and ^cmaxima of the PSD obtained using NLDFT analysis. ^dhydrogen uptake capacity at 77 K and 20 bar and ^e(ρ) is the hydrogen uptake density in μmol.H₂ m⁻².

All the carbon samples possess high surface area and large pore volume of up to 3332 m²/g and 1.66 cm³/g, respectively, which is one of the highest to date for zeolite templated carbons. The high surface area of FA-ZTCs may be attributed to the presence of single nanographene sheets with surface available as described by Kyotani and co-workers.³⁶ Moreover, the graphene sheet at nanometre scale consists of a large number of edges, which contribute to an increase in specific surface area. Noteworthy is the proportion of micropore surface area and pore volume that is significantly high; typically up to 88% of the total surface area, while the micropore volume contributes up to 75% of the total pore volume. This agrees with the high level of zeolite-type pore ordering consistent with XRD patterns (shown in Figure 6.1) which favours high surface area and large pore volume with sizable proportion of microporosity.

6.3.3 Nanoscale ordering of zeolite templated carbons

Transmission Electron Micrograph (TEM) images recorded for FA-ZTC2 with a JEOL 2100F at a resolution of 0.14 nm operating at 200kV are presented in Figure 6.4.

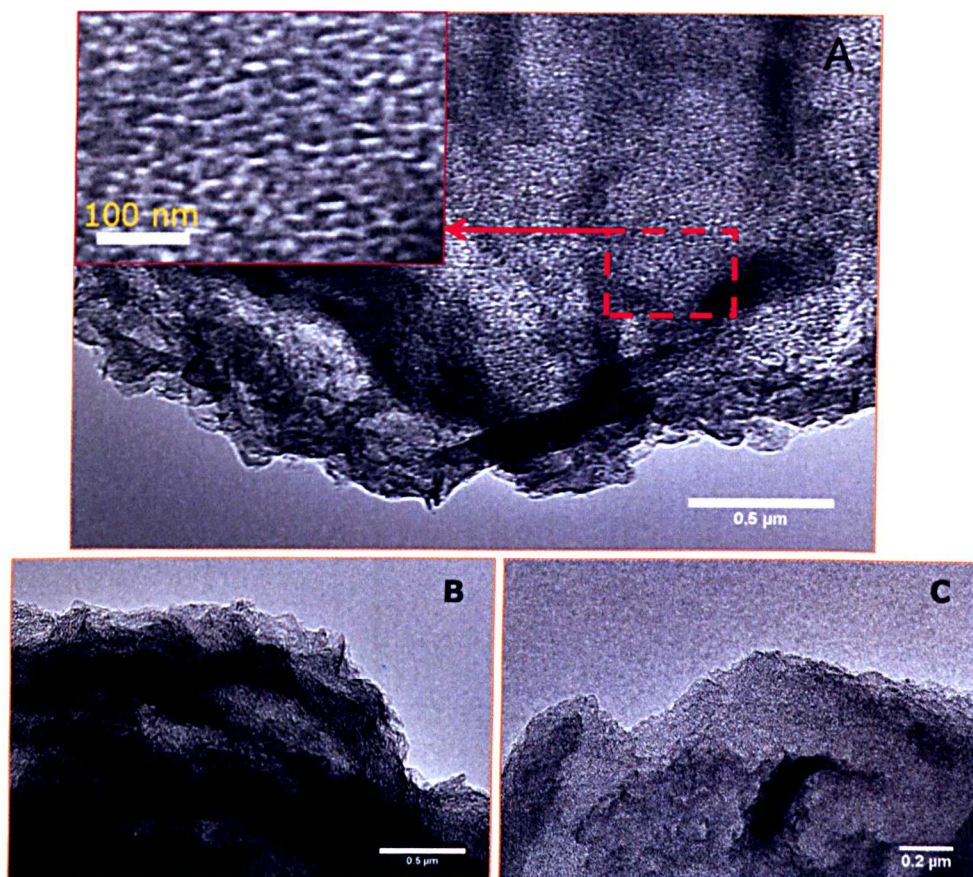


Figure 6.4 TEM images of zeolite templated carbon (sample FA-ZTC2).

The TEM micrographs clearly reveal well-ordered micropore channels, which is consistent with XRD patterns illustrated in Figure 6.1. The formation of well-ordered microporous carbon further confirms that the amount of carbon infiltrated into the zeolite channels via the two-step synthesis method was sufficient. Thus, the zeolite-like structural framework

is preserved in the synthesis process. Noteworthy is the absence of the outer layer covering the particles which rules out the possibility of graphitisation arising from carbon deposited on the external surface of the zeolite particle.

6.3.4 Assessment of mechanical stability of FA-ZTCs

The mechanical stability of the carbon (FA-ZTC3) prepared at highest heating ramp rate was investigated via compaction at 5 Tons and 10 Tons. In order to do a comparative study, commercially available activated carbon (AX21) was used as a baseline. Figure 6.5 shows powder XRD patterns of the carbonaceous material before and after compaction. The compacted carbons were ground into powder before analysis.

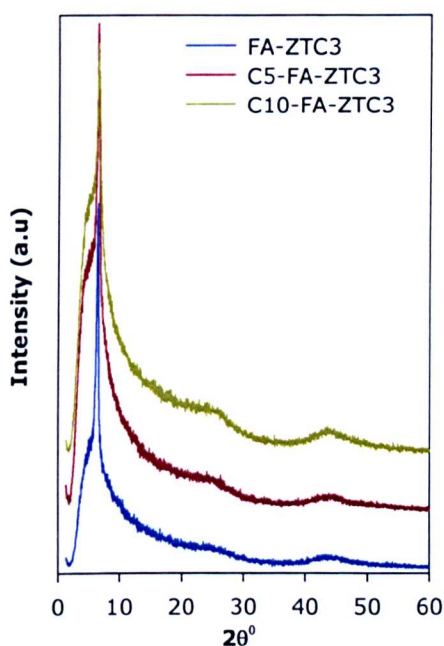


Figure 6.5 Powder XRD patterns of zeolite templated carbon (FA-ZTC3) before and after compaction (C5 and C10 for compaction at 5 and 10 Tons, respectively).

The powder XRD patterns depicted in Figure 6.5 show that the carbon framework of the zeolite templated carbon can withstand mechanical pressure for 10 mins under pressures as high as 10 Tons. The structural ordering remains the same after being exposed to such high compaction pressure.

Nitrogen sorption isotherms (A and C) and corresponding pore size distribution curves (B and D) for FA-ZTC3 and AX21, respectively before and after compaction are shown in Figure 6.6. Although the shape of the isotherms does not change after compaction, retaining a type I isotherm typical of microporous materials,³⁹ it is clearly observable in Figure 6.6A and B that compacted samples have reduced adsorption as compared to non-compacted samples.

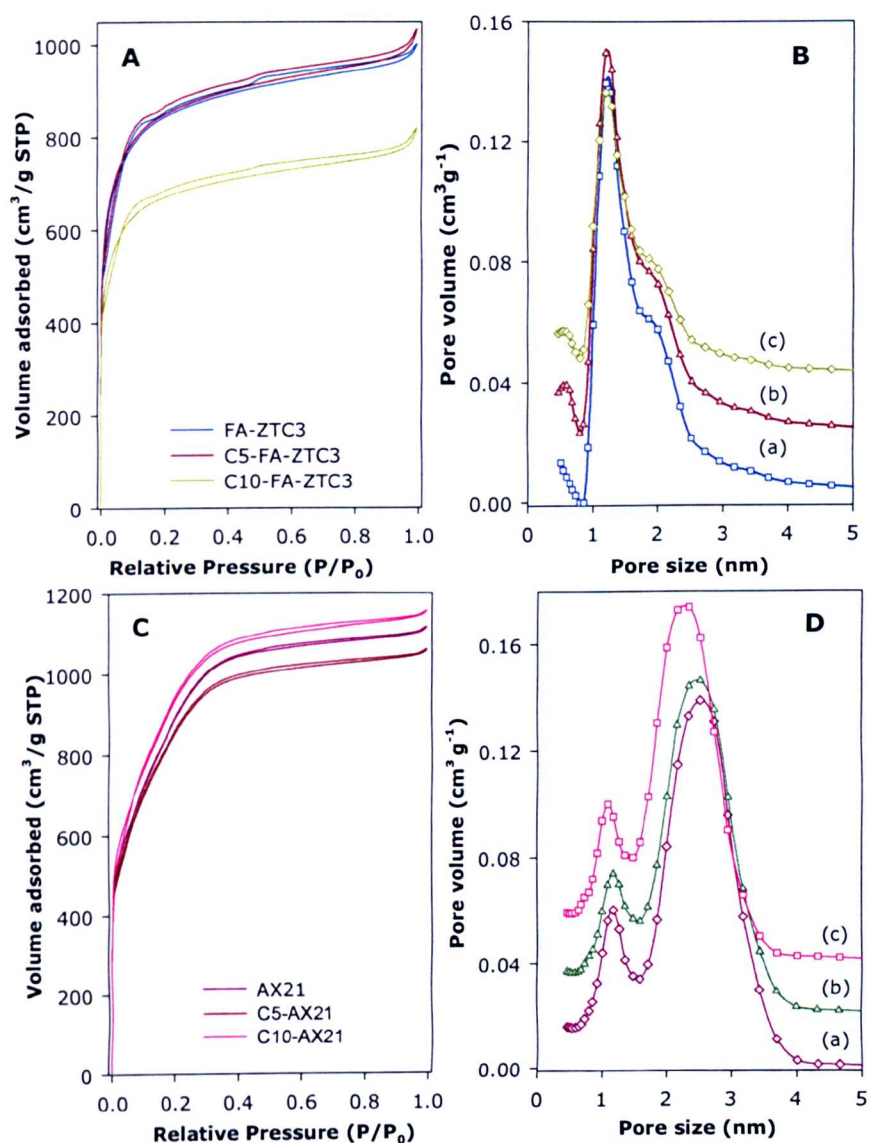


Figure 6.6 Nitrogen sorption isotherms of zeolite templated carbon (A) and commercially available activated carbon; AX21 (C) before and after compaction, (B) and (D) shows the corresponding PSD curves obtained via NLDFT model, respectively.

It is worth noting that, the zeolite templated carbon sample (C10-FA-ZTC3) compressed at 10 Tons shows the lowest nitrogen adsorption which is opposite to that of the commercially available activated carbon (C10-AX21). The PSD curves in Figure 6.6B and D clearly show that the pore size

remains largely unchanged after compaction. Textural properties summarised in Table 6.2 provide further evidence of negligible modifications in the zeolite templated carbons after compaction.

Table 6.2 Textural properties and hydrogen uptake (wt%) of FA-ZTC3 and AX21 before and after compaction.

Sample	Surface area (m ² /g) ^a	Pore volume (cm ³ /g) ^b	Pore size (nm) ^c	H ₂ uptake	
				(wt%) ^d	density (ρ) ^e
C5-AX21	2787 (2226)	1.64 (1.21)	1.1 (2.5)	6.2	11.1
C10-AX21	3059 (2454)	1.79 (1.32)	1.2 (2.5)	6.0	9.8
C5-FA-ZTC3	3192 (2769)	1.60 (1.15)	0.6/1.2	6.3	9.9
C10-FA-ZTC3	2782 (2430)	1.27 (0.91)	0.6/1.2	5.9	10.6

The values in the parenthesis refer to: ^amicropore surface area, ^bmicropore volume and ^cmaxima of the PSD obtained using NLDT analysis ^dhydrogen uptake capacity at 77K and 20 bar and ^ehydrogen uptake density (ρ) in μmol.H₂ m⁻².

The BET surface area of C10-FA-ZTC3 (2782 m²/g) and pore volume (1.27 cm³/g) confirms that, at a pressure of 10 Tons, the sample is slightly modified. This may be attributed to the blocking of some pores during the compaction process, which in turn reduces the exposed surface area as well as the pore volume. Also, worth noting is the proportion of microporosity in FA-ZTC3 and its compacted derivatives (C5-FA-ZTC3 and C10-FA-ZTC3) which is 87%. Likewise, the compacted zeolite templated carbons (C5-FA-ZTC3 and C10-FA-ZTC3) had significant proportion of micropore volume of up to 74% of the total volume.

6.3.5 Hydrogen uptake storage

The hydrogen uptake isotherms were obtained by gravimetric analysis at three independent temperatures; namely 77 K, 87 K and 298 K and at pressures up to 20 bar as shown in Figure 6.7 and 6.8.

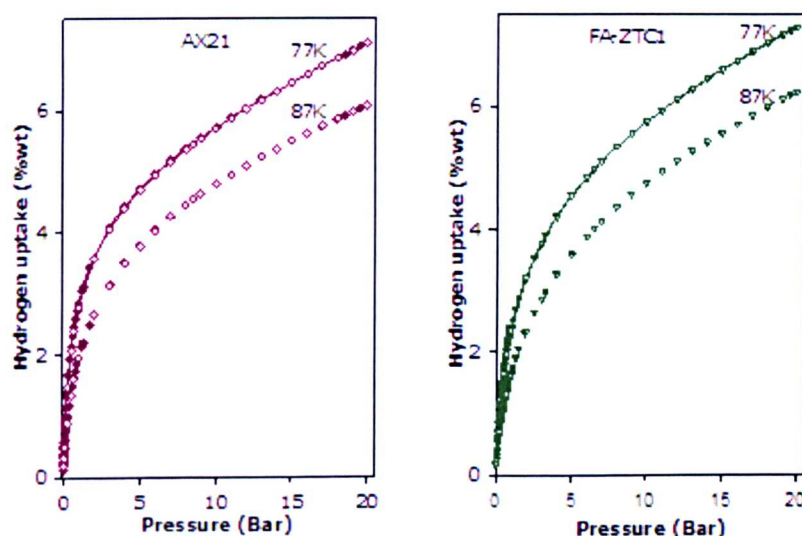


Figure 6.7 Hydrogen uptake isotherms at 77 k and 87 k for FA-ZTC1 and AX21.

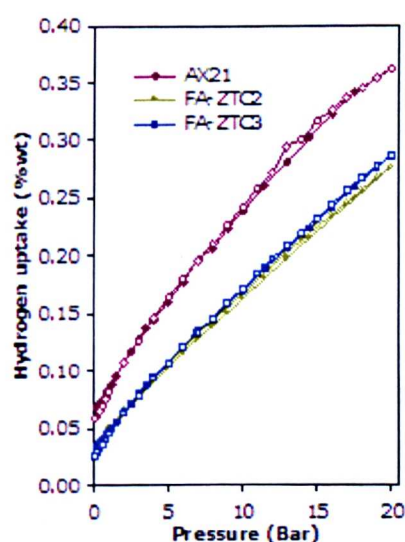


Figure 6.8 Hydrogen uptake isotherms for zeolite carbon samples (FA-ZTC2 and FA-ZTC3) and AX21 at 298 K.

The corresponding hydrogen uptake and hydrogen uptake density at 20 bar and 77 K are summarised in table 6.1. The obtained sorption isotherms and in particular figure 6.7 analysed at cryogenic temperatures shows the desorption branches (open symbols) matching the adsorption branches (filled symbols) of the isotherms without hysteresis. This indicates that hydrogen sorption is totally reversible. In addition, it is clearly observable in figure 6.7 that the isotherms do not attain hydrogen saturation at 20 bar which implies that higher capacities of hydrogen storage are possible above 20 bar. However, the scenario is different at 298 K as illustrated in figure 6.8 in which hydrogen sorption isotherms remain almost linear. It is clear the temperature strongly affects hydrogen uptake of carbon materials. This is expected given the nature of the physisorption process that governs the hydrogen uptake.

Sample FA-ZTC1, which has the highest surface area and micropore surface area of 3332 and 2837 m²/g, respectively, exhibits the highest hydrogen uptake capacity of 7.3 wt% at 20 bar and 77 K. It is worth noting that this uptake is the highest ever recorded for any carbon material.^{21, 40-48} This result surpasses the 6.9 wt% previously reported for a zeolite EMC-2 templated carbon,⁶ 7.03 wt% for a polypyrrole-derived activated carbon⁷ and 7.08 wt% for a doubly activated carbon.⁴⁹ The high uptake is attributed to well-controlled pore size centered at 1.2 nm as well as the high surface area. Furthermore, the amount of hydrogen uptake at ambient temperatures (298 K) of up to 0.36 %wt, is comparable to previously reported work by Thomas.⁵ A maximum hydrogen adsorption capacity of up to 9.22 wt% (equivalent to hydrogen uptake density of 13.8 μmol H₂/m² for FA-ZTC1 was obtained via extrapolation by fitting the adsorption data at 77 K with the Langmuir model.⁵⁰ The unprecedented high hydrogen

storage exhibited in this chapter provides further evidence that zeolite templated carbons remain as one of the key materials for gas storage media. Overall, the optimal pore size and pore size distribution, simultaneously generating high surface area, offer a great potential for enhanced hydrogen storage.

Effect of compaction on hydrogen uptake

Hydrogen uptake capacity for FA-ZTC3 and its compacted derivatives was determined under similar conditions to sample AX21 with its compacted derivatives. Figure 6.9 shows the hydrogen sorption isotherms for compacted and non-compacted carbonaceous materials.

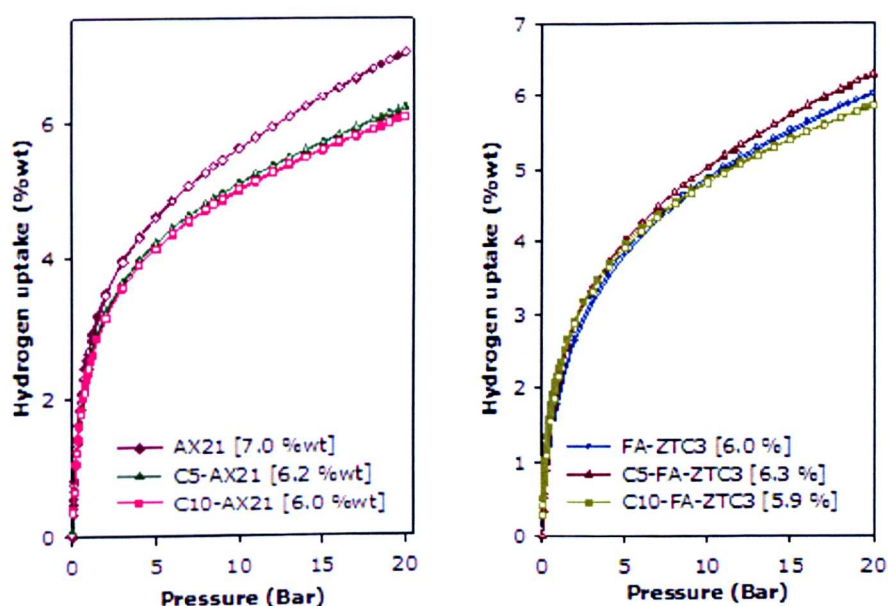


Figure 6.9 Hydrogen uptake isotherms at 77 K of FA-ZTC3 and AX21 before and after compaction.

The hydrogen sorption isotherms in figure 6.9 show a fully reversible hydrogen sorption process. The percentage changes in hydrogen uptake

[209]

capacity after compaction showed a decrease of 14% for AX21 and an increase of 5.0% for FA-ZTC3 (table 6.2). The small changes in the amount of hydrogen adsorbed at 20 bar before and after compaction may be attributed to the increased packing density of carbons after compaction at higher pressure without much change in porosity.^{51, 52} The changes in hydrogen uptake capacities may be attributed to modification of the specific interparticle pore volume upon compaction.

Generally, the FA-ZTCs recorded hydrogen uptake capacity that tends to generally outperform or is in line with the Chahine rule as illustrated in Figure 6.10.^{53, 54}

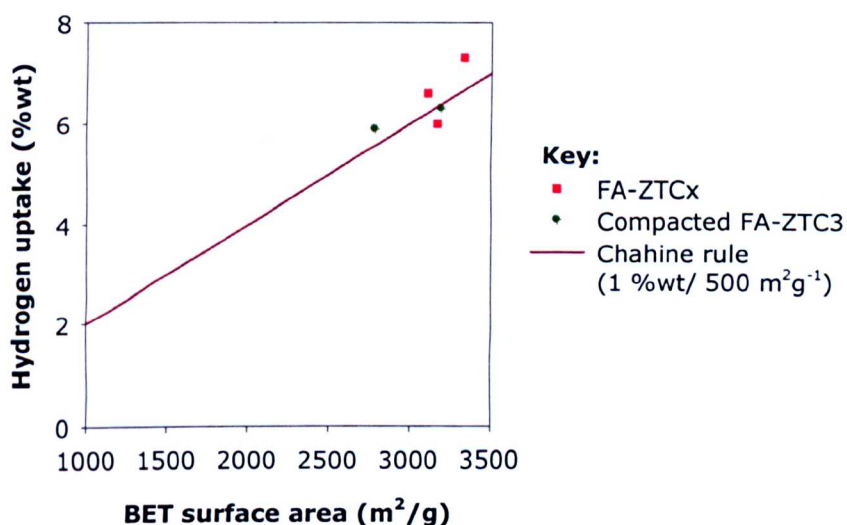


Figure 6.10 Correlation between BET surface area and hydrogen uptake capacity (%wt) for carbon samples.

Chahine rule is a widely accepted relationship which states that in general there is 1 wt% hydrogen adsorption for every 500 m^2/g of surface area which was first articulated in 1996.⁵⁵ This is equivalent to a hydrogen density of 10 $\mu\text{mol H}_2 \text{ m}^2$. Therefore, the FA-ZTCx carbons generally

showed superior hydrogen uptake as compared to the average for carbonaceous materials. The hydrogen uptake capacity is closely related to the surface area of the carbons which is in agreement with most previously reported data.^{34, 56} Overall, higher hydrogen uptake is attributed to the presence of optimal pore size range and that of an enclosed surface area with high proportion of micropores. FA-ZTCs have PSD with maximum centered at 1.2 nm. This agrees with Fischer and co-workers who concluded that pores larger than 1.5 nm make little contribution to hydrogen uptake at 77 K and pressure of up to 60 bar.⁵⁷

6.4 Summary

The nanocasting technique via a two-step synthesis process has been employed to generate a suite of porous carbons with zeolite-like structural ordering. It was found that the heating ramp rate has negligible effects on the textural properties while compaction of carbons resulted in slight modification of porosity. All the carbons prepared irrespective of whether unmodified or modified exhibit high surface area and large pore volume of up to 3332 m²/g and 1.66 cm³/g, respectively. The porosity in the prepared carbons consisted of mainly micropores with a unimodal pore size distribution centred at 1.2nm. A total hydrogen uptake capacity of up to 7.3 wt% at 20 bar and 77 K was achieved, which is the highest ever for a carbon material. This study provides a promising route to synthesis and post synthesis modification of carbon materials with tuneable porosity. The findings add new insights that are valuable for the development of carbonaceous materials with enhanced hydrogen storage capacity.

6.5 Bibliography

1. Fuel Cell Technologies Program Multi-Year Research, Development and Demonstration Plan; The DOE Hydrogen and Fuel Cells Program, <http://www1.eere.energy.gov/hydrogenandfuelcells/mypp/>, Accessed 2nd July 2012.
2. A. M. Seayad and D. M. Antonelli, *Adv. Mater.*, 2004, **16**, 765-777.
3. A. W. C. van den Berg and C. O. Areal, *Chem. Commun.*, 2008, 668-681.
4. R. Ströbel, L. Jörissen, T. Schliermann, V. Trapp, W. Schütz, K. Bohmhammel, G. Wolf and J. Garche, *Journal of Power Sources*, 1999, **84**, 221-224.
5. K. M. Thomas, *Catal. Today*, 2007, **120**, 389-398.
6. Z. Yang, Y. Xia and R. Mokaya, *J. Am. Chem. Soc.*, 2007, **129**, 1673-1679.
7. M. Sevilla, A. B. Fuertes and R. Mokaya, *Energy Environ. Sci.*, 2011, **4**, 1400-1410.
8. M. Sevilla, R. Mokaya and A. B. Fuertes, *Energy Environ. Sci.*, 2011, **4**, 2930-2936.
9. T. Kyotani, *Bull. Chem. Soc. Jpn.*, 2006, **79**, 1322-1337.
10. Y. Xia, Z. Yang and R. Mokaya, *Nanoscale*, 2010, **2**, 639-659.
11. A. A. Zakhidov, R. H. Baughman, Z. Iqbal, C. Cui, I. Khayrullin, S. O. Dantas, J. Marti and V. G. Ralchenko, *Science*, 1998, **282**, 897-901.
12. N. Alam and R. Mokaya, *Energy Environ. Sci.*, 2010, **3**, 1773-1781.
13. J. Lee, J. Kim and T. Hyeon, *Adv. Mater.*, 2006, **18**, 2073-2094.
14. R. Ryoo, S. H. Joo, M. Kruk and M. Jaroniec, *Adv. Mater.*, 2001, **13**, 677-681.

15. Y. Xia, G. S. Walker, D. M. Grant and R. Mokaya, *J. Am. Chem. Soc.*, 2009, **131**, 16493-16499.
16. R. V. Parthasarathy and C. R. Martin, *Nature*, 1994, **369**, 298-301.
17. S. A. Johnson, P. J. Ollivier and T. E. Mallouk, *Science*, 1999, **283**, 963-965.
18. C. R. Martin, *Adv. Mater.*, 1991, **3**, 457-459.
19. C. West and R. Mokaya, *Chem. Mater.*, 2009, **21**, 4080-4086.
20. J. D. Klein, R. D. Herrick, D. Palmer, M. J. Sailor, C. J. Brumlik and C. R. Martin, *Chem. Mater.*, 1993, **5**, 902-904.
21. N. Texier-Mandoki, J. Dentzer, T. Piquero, S.-E. Saadallah, P. David and C. Vix-Guterl, *Carbon*, 2004, **24**, 2744-2747.
22. I. Cabria, M. J. López and J. A. Alonso, *Carbon*, 2007, **45**, 2649-2658.
23. G. Yushin, R. Dash, J. Jagiello, J. E. Fischer and Y. Gogotsi, *Adv. Funct. Mater.*, 2006, **16**, 2288-2293.
24. Y. Gogotsi, R. K. Dash, G. Yushin, T. Yildirim, G. Laudisio and J. E. Fischer, *J. Am. Chem. Soc.*, 2005, **127**, 16006-16007.
25. M. Sevilla, N. Alam and R. Mokaya, *J. Phys. Chem. C*, 2011, **114**, 11314 - 11319.
26. T. Kyotani, Z. Ma and A. Tomita, *Carbon*, 2003, **41**, 1451-1459.
27. T. Kyotani, T. Nagai, S. Inoue and A. Tomita, *Chem. Mater.*, 1997, **9**, 609-615.
28. P. Enzel and T. Bein, *Chem. Mater.*, 1992, **4**, 819-824.
29. Z. Ma, T. Kyotani and A. Tomita, *Carbon*, 2002, **40**, 2367-2374.

30. A. Pacula and R. Mokaya, *J. Phys. Chem. C*, 2008, **112**, 2764-2769.
31. C. Ducrot-Boisgontier, J. Parmentier and J. Patarin, *Microporous Mesoporous Mater.*, 2009, **126**, 101-106.
32. F. O. M. Gaslain, J. Parmentier, V. P. Valtchev and J. Patarin, *Chem. Commun.*, 2006, 991-993.
33. Z. Yang, Y. Xia and R. Mokaya, *Microporous Mesoporous Mater.*, 2005, **86**, 69-80.
34. Z. X. Yang, Y. D. Xia, X. Z. Sun and R. Mokaya, *J. Phys. Chem. B*, 2006, **110**, 18424-18431.
35. Z. Ma, T. Kyotani and A. Tomita, *Chem. Commun.*, 2000, 2365-2366.
36. H. Nishihara, Q.-H. Yang, P.-X. Hou, M. Unno, S. Yamauchi, R. Saito, J. I. Paredes, A. Martínez-Alonso, J. M. D. Tascón, Y. Sato, M. Terauchi and T. Kyotani, *Carbon*, 2009, **47**, 1220-1230.
37. S. A. Johnson, E. S. Brigham, P. J. Ollivier and T. E. Mallouk, *Chem. Mater.*, 1997, **9**, 2448-2458.
38. F. Su, X. S. Zhao, L. Lv and Z. Zhou, *Carbon*, 2004, **42**, 2821-2831.
39. K. S. W. Sing, D. H. Everett, R. A. W. Haul, L. Moscou, R. A. Pierotti, J. Rouquerol and T. Siemieniewska, *Pure Appl. Chem.*, 1985, **57**, 603-619.
40. M. Armandi, B. Bonelli, C. O. Areán and E. Garrone, *Microporous Mesoporous Mater.*, 2008, **112**, 411-418.
41. P. Chen, X. Wu, J. Lin and K. L. Tan, *Science*, 1999, **285**, 91-93.
42. M. Hirscher and B. Panella, *J. Alloys Compd.*, 2005, **404-406**, 399-401.
43. C. Liu, Y. Y. Fan, M. Liu, H. T. Cong, H. M. Cheng and M. S. Dresselhaus, *Science*, 1999, **286**, 1127-1129.

44. M. Rzepka, P. Lamp and M. A. de la Casa-Lillo, *J. Phys. Chem. B*, 1998, **102**, 10894-10898.
45. L. Schlapbach and A. Züttel, *Nature*, 2001, **414**, 353-358.
46. E. Terrés, B. Panella, T. Hayashi, Y. A. Kim, M. Endo, J. M. Dominguez, M. Hirscher, H. Terrones and M. Terrones, *Chem. Phys. Lett.*, 2005, **403**, 363-366.
47. Y. Xia and R. Mokaya, *J. Phys. Chem. C*, 2007, **111**, 10035-10039.
48. W. C. Xu, K. Takahashi, Y. Matsuo, Y. Hattori, M. Kumagai, S. Ishiyama, K. Kaneko and S. Iijima, *Int. J. Hydrogen Energy*, 2007, **32**, 2504-2512.
49. H. Wang, Q. Gao and J. Hu, *J. Am. Chem. Soc.*, 2009, **131**, 7016-7022.
50. G. Srinivas, Y. Zhu, R. Piner, N. Skipper, M. Ellerby and R. Ruoff, *Carbon*, 2010, **48**, 630-635.
51. J. Juan-Juan, J. P. Marco-Lozar, F. Suárez-García, D. Cazorla-Amorós and A. Linares-Solano, *Carbon*, 2010, **48**, 2906-2909.
52. J. Alcañiz-Monge, G. Trautwein, M. Pérez-Cadenas and M. C. Román-Martínez, *Microporous Mesoporous Mater.*, 2009, **126**, 291-301.
53. P. Bénard and R. Chahine, *Scripta Materialia*, 2007, **56**, 803-808.
54. E. Poirier, R. Chahine and T. K. Bose, *Int. J. Hydrogen Energy*, 2001, **26**, 831-835.
55. R. Chahine and T. K. Bose, Characterization and optimization of adsorbents for hydrogen storage, *Proc. 11th World Hydrogen Energy Conf.*, Stuttgart, 1996, PP 1259 - 1263.
56. A. G. Wong-Foy, A. J. Matzger and O. M. Yaghi, *J. Am. Chem. Soc.*, 2006, **128**, 3494-3495.

57. Y. Gogotsi, C. Portet, S. Osswald, J. M. Simmons, T. Yildirim, G. Laudisio and J. E. Fischer, *Int. J. Hydrogen Energy*, 2009, **34**, 6314-6319.

Chapter Seven

7.0 Preparation of Templated and Activated Carbon Aerogels for Carbon Dioxide Capture.....218

7.1 Abstract.....218

7.2 Introduction.....218

7.2 Results and Discussion.....222

 7.2.1 Structure and porosity of CaCl₂-tempated carbon aerogels.... 222

 7.2.2 Thermogravimetric analysis 228

 7.2.3 Chemical activation of CaCl₂-templated carbon aerogels 229

 7.2.4 Effect of organic precursor on porosity on activated carbon aerogels..... 233

7.3 Measurement of Carbon dioxide uptake capacity.....240

7.4 Summary.....244

7.5 Bibliography.....245

7.0 Preparation of Templated and Activated Carbon Aerogels for Carbon Dioxide Capture

7.1 Abstract

This chapter describes the preparation of carbon aerogels by carbonising either resorcinol - formaldehyde (RF) or melamine - formaldehyde resins (MF) at high temperature (between 700 and 900 °C) under a nitrogen atmosphere. The influence of a metal salt template in the synthesis of MF resin is investigated and in particular its effect on the porosity of the resultant carbons. The control of activation parameters such as reaction temperature and amount of potassium hydroxide are investigated with the aim of tailoring the porosity of carbon materials. The templated carbons after activation exhibit ultrahigh surface area and large pore volume up to ca. 3343 m²/g and 2.65 cm³/g, respectively. All the carbons exhibit significant CO₂ uptake of up to 2.6 mmol/g at 298 K and 1 bar.

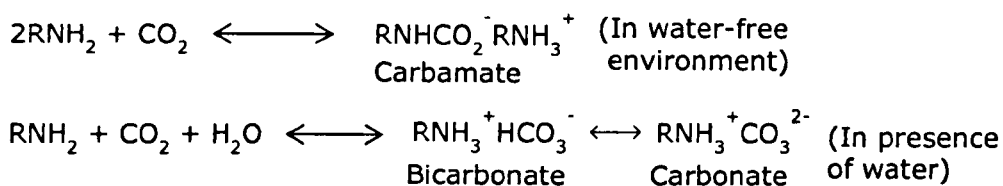
7.2 Introduction

The world's energy demand is currently supplied mostly by fossil fuels; namely petroleum, natural gas and coal, which are depleting rapidly due to ever increasing energy demands. Fossil fuel combustion generates pollutants, particularly carbon dioxide (a greenhouse gas) emissions associated with global warming.¹⁻⁵ This is threatening the stability of the Earth's climate. Hoffert *et al.* in their research based on climate models and paleoclimate data projected an increase in atmospheric carbon dioxide of up to 550 ppm by the end of this century.⁶ The increased dependency on fossils fuels therefore dictates the need to develop systems that will reduce CO₂ emissions.

Considerable research efforts are currently directed at finding the most effective way to reduce CO₂ emissions without compromising economic growth. This will require innovative changes in the technology of energy production, distribution, storage and conversion.⁷ The current industrial separation of CO₂ produced from combustion of fossil fuels is handled via amine scrubbing technology involving absorption and stripping with aqueous amine.^{8, 9} However, this technology suffers from several drawbacks (e.g. energy consumption, corrosion of the equipment or toxicity) and, in consequence, there is great interest in developing other capture methods. A good alternative is to use sorbents to capture CO₂ by means of pressure, temperature or vacuum swing adsorption.¹⁰ It is highly desirable, therefore, to develop novel sorption materials with enhanced adsorption capacity, good regeneration stability and enhanced selectivity for CO₂.^{4, 5, 11} In recent years, porous materials possessing high surface area and tuneable pore size distribution have shown excellent gas adsorption properties. In addition to the desirable properties discussed earlier for enhanced gas storage, porous materials can be functionalised in order to improve selectivity for CO₂ capture and storage.^{5, 11}

Unlike liquid alkaline solution absorption technology, which is well developed and used in almost all commercial processes for capturing CO₂, the development of porous solid CO₂ adsorbents still remains a great challenge. The current intensive research into the necessary technology for potential commercialisation is driven by the set goals of the Department of Energy (DOE). The specific goal set by the DOE is to have technologies developed by 2012 which can achieve 90% CO₂ capture at an increase in the cost of electricity of less than 20% and 10 % for post-combustion/oxy-combustion and pre-combustion, respectively.¹² In an attempt to tackle

limitations of CO₂ capture via conventional amine solutions, a wide range of novel materials including amine-modified silicas¹³⁻¹⁵ and zeolites¹⁶⁻¹⁸ have been widely investigated as CO₂ uptake media. In the former, surface modification enhances selectivity for CO₂ adsorption through the formation of carbamate or bicarbonate species according to the following pathways.



In recent years, much of the focus of research has been on the use of Metal Organic Frameworks (MOFs)¹⁹⁻²¹ and porous carbons²²⁻²⁴ as CO₂ capture materials owing to their exceptionally high surface areas and tuneable porosity. In particular, carbon-based porous materials are attractive because they are relatively easy to regenerate due to their moderate heats of sorption²⁵, and non-expensive preparation methods. They also, have good chemical stability²⁶ and are not as sensitive to water as the other CO₂-philic materials aforementioned. However, the adsorption of CO₂ on these porous materials is typically a weak physisorption process which can result in low uptake capacity coupled with poor selectivity and great sensitivity to temperature. The current intensive research efforts are therefore directed towards enhancing the adsorbate-adsorbent interactions and selectivity for CO₂ capture.

Several studies have reported on the enhancement of the CO₂ adsorption capacity of carbon-based adsorbents by chemical modification of carbon structure by means of impregnation with amines.²⁷⁻²⁹ Improvement in CO₂ uptake capacity has also been reported in other porous materials (e.g.

ordered mesoporous silicas) after post-synthesis modification via grafting amine groups onto their surfaces.^{14, 30-32} However, incorporation of amine groups is known to block pores which in turn hinder accessibility to interior porosity, but grafted amines also suffer from leaching and instability in any subsequent regeneration step.^{29, 33} Other strategies are based on the utilization of nitrogen-rich carbon compounds as precursors.³⁴

Porous carbons with tuneable, optimised pore structure and high surface area are highly sought after given their potential for gas adsorption as discussed in section 1.7. It is desirable to prepare carbon-based materials that combine efficient CO₂ uptake capacity and selectivity at moderate temperatures. Despite possessing excellent textural parameters such as high surface-to-volume ratios and continuous porosities, no detailed studies have been done on the use of KOH activated carbon aerogels on CO₂ capture. Recently, Robertson and Mokaya prepared carbon aerogels via sol-gel methods which exhibited high CO₂ uptake capacities of up to 13.2 wt% (3 mmol/g) at 298 K and atmospheric pressure.³⁵ Furthermore, carbon aerogels have a network structure of interconnected nanometre sized primary particles with micropores related to intraparticle structure, whereas mesopores and macropores related to interparticle structure.³⁶ This is one of the key advantages of carbon aerogels, affording control of the amount of micropores and mesopores independently. The work reported in this chapter is based on a systematic study of porous carbons involving fabrication of carbon aerogels with or without the use of an inorganic metal salt as a structure director (i.e., porogen). The synthesis included chemical activation of the aerogels in order to generate carbons with high surface area and pore volume.³⁷

Conventionally, carbon aerogels (CA) are prepared through the sol-gel polymerisation of resorcinol with formaldehyde in aqueous solution to produce the so called organic gels. These are then supercritically dried followed by pyrolysis in an inert atmosphere.³⁸ The structural properties of the resultant CA are greatly influenced by the type and amount of catalyst used in the polymerisation stage that determines the size, shape and connectivity of the primary network of particles. For example, Moreno-Castilla *et. al.*³⁷ and Fricke *et. al.*,³⁹ working independently used an acid catalyst in the sol-gel process to generate porous structures with network and pore features on the nanometre scale. In this present work, carbon aerogels derived from melamine-formaldehyde (MF) resins via pyrolysis followed by chemical activation are investigated. In particular, the effects of (i) using a metal salt as a porogen in the MF synthesis and (ii) varying the organic precursor on the properties of the CAs in relation to their CO₂ storage capacity are probed. The organic aerogels in all cases were recovered without supercritical drying.

7.2 Results and Discussion

7.2.1 Structure and porosity of CaCl₂-templated carbon aerogels

Powder XRD patterns of carbon aerogels (CAs) synthesised using melamine-formaldehyde resins with calcium chloride as porogen and pyrolysed at 700 to 900 °C are shown in Figure 7.1A. A broad peak at $2\theta = 26^\circ$ is the (002) diffraction from carbon layers with a turbostratic stacking structure. This suggests that the CAs possess small amounts of graphitic/turbostratic domains; the $d_{(002)}$ spacing obtained by the Scherrer equation is at 0.346 nm higher than for graphite (0.335 nm), which is consistent with low levels of graphitisation. The CAs exhibit sharp peaks at

$2\theta = 42^\circ$ to 48° . The intensity of these peaks decreases at higher carbonisation temperature. Indeed, the reduced intensity of these peaks for the sample carbonised at 900°C (Ca-CAMF900) allows observation of the (101) diffraction from turbostratic carbon.⁴⁰⁻⁴² The sharp peaks may be associated with inorganic residue arising from the use of CaCl_2 as porogen.

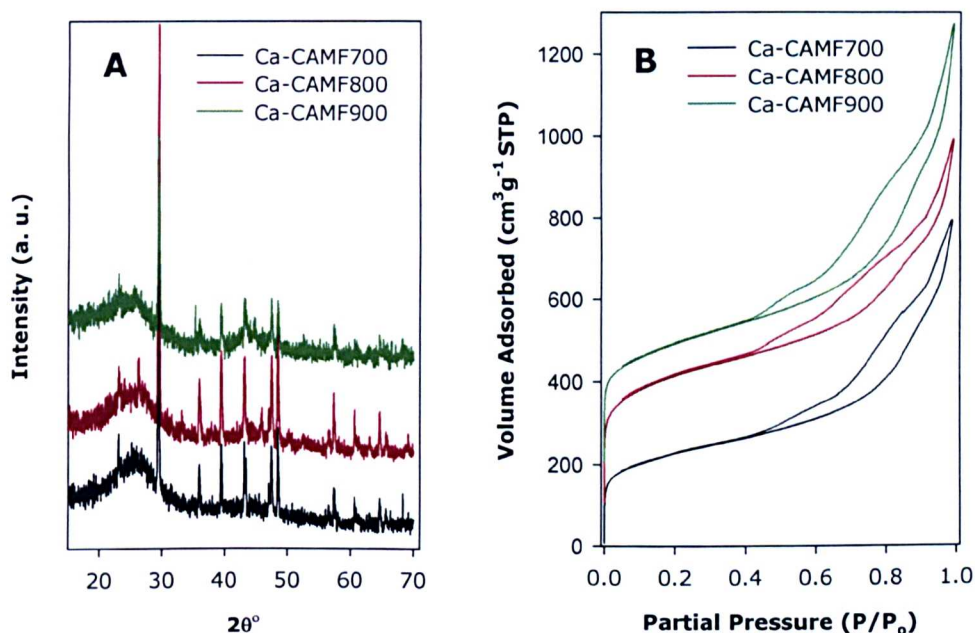


Figure 7.1. Powder XRD patterns (A) and nitrogen sorption isotherms (B) for Ca-CAMFx samples carbonised at 700, 800 or 900°C .

The porosity of the samples was probed using nitrogen sorption analysis. The nitrogen adsorption-desorption isotherms are shown in Figure 7.1B and the textural properties are summarised in Table 7.1. The nitrogen adsorption isotherms on all carbon aerogels are close to Type IV and display a hysteresis loop at relative pressure (P/P_0) above 0.5.⁴³ The shape of hysteresis loop (which is H4 Type) is indicative of the presence of narrow slit-like pores. Carbon aerogels pyrolysed at higher temperature (i.e., Ca-CAMF900 and Ca-CAMF800) have higher adsorption, and thus greater

porosity compared to sample Ca-CAMF700. The surface area of the CaCl_2 -templated carbon aerogels varies between 785 and 1090 m^2/g) and the pore volume between 1.22 and 1.66 cm^3/g . These textural properties are amongst the highest ever reported for carbon aerogels,^{38, 44, 45} and perhaps illustrate the positive influence of using a porogen. Unusually, the present carbon aerogels exhibit a high level of microporosity, which is a contributing factor to the high total surface area observed. The proportion of surface area associated with micropores is 48%, 56% and 55% for Ca-CAMF700, Ca-CAMF800 and Ca-CAMF900, respectively, and thus relatively similar irrespective of the pyrolysis temperature. The proportions are consistent with nitrogen sorption isotherms in Figure 7.1B which show appreciable adsorption at relative pressure (P/P_0) < 0.02. On the other hand, the proportion of micropore volume is rather lower at 14%, 20% and 13% for Ca-CAMF700, Ca-CAMF800 and Ca-CAMF900, respectively. Overall the textural data suggest that the pyrolysis temperature has an influence with the aerogel prepared at 800 °C exhibiting the most well developed porosity.

Table 7.1 Textural properties and CO₂ uptake at 298 K and 1 bar for CaCl₂-templated carbon aerogels before and after activation

Sample	Surface area (m ² g ⁻¹) ^a	Pore volume (cm ³ g ⁻¹) ^b	Pore size (nm) ^c	^d CO ₂ Uptake	
				(wt %)	mmol/g
Ca-CAMF700	785 (375)	1.22 (0.18)	10	8.93	2.03
Ca-CAMF800	1090 (611)	1.37 (0.28)	9	9.01	2.06
Ca-CAMF900	1014 (557)	1.66 (0.21)	10	7.26	1.66
14AC-Ca-CAMF800-6	1504 (1272)	0.83 (0.60)	-	10.75	2.44
14AC-Ca-CAMF800-7	2782 (1258)	2.04 (0.58)	-	7.27	1.65
14AC-Ca-CAMF800-8	3343 (803)	2.65 (0.36)	-	10.78	2.59

The values in the parenthesis refer to: ^amicropore surface area, ^bmicropore volume, ^cmaxima of pore size obtained using the BJH model, ^d CO₂ uptake at 298 K and 1 bar.

The pore size distribution (PSD) of the carbon aerogels determined via BJH and NLDFT models using nitrogen adsorption data is shown in Figure 7.2 and the pore size data is summarised in Table 7.1. Pore size distribution (PSD) curves obtained for the carbon aerogels via BJH analysis of adsorption data (Figure 7.2A) show a relatively wide range of pore sizes with the maximum centred at ca. 10.0 nm for Ca-CAMF700 and Ca-CAMF900 and 9.0 nm for Ca-CAMF800. Therefore according to BJH analysis, the carbon aerogels have similar pore size distribution dominated by pores of size ca. 10 nm. The PSD obtained via BJH model also shows the presence of micropores, with their proportion being highest for sample Ca-CAMF800 which is consistent with the extent of microporosity (Table 7.1). Given the limitations of BJH analysis in probing the presence of micropores, we also performed pore size analysis using the NLDFT model (Figure 7.2B). The NLDFT analysis (Figure 7.2C) confirms the presence of

micropores of size ca. 1.2 nm. The carbon aerogels also possess small mesopores of size ca. 3.0 nm. Nevertheless, NLDFT PSD indicates that the predominant pores are large mesopores of size ca. 10 nm. In this case the BJH and NLDFT analysis indicate a similar pore size for these large 10 nm pores. NLDFT PSD also indicates the presence of even larger pores of size 26 nm.⁴⁶

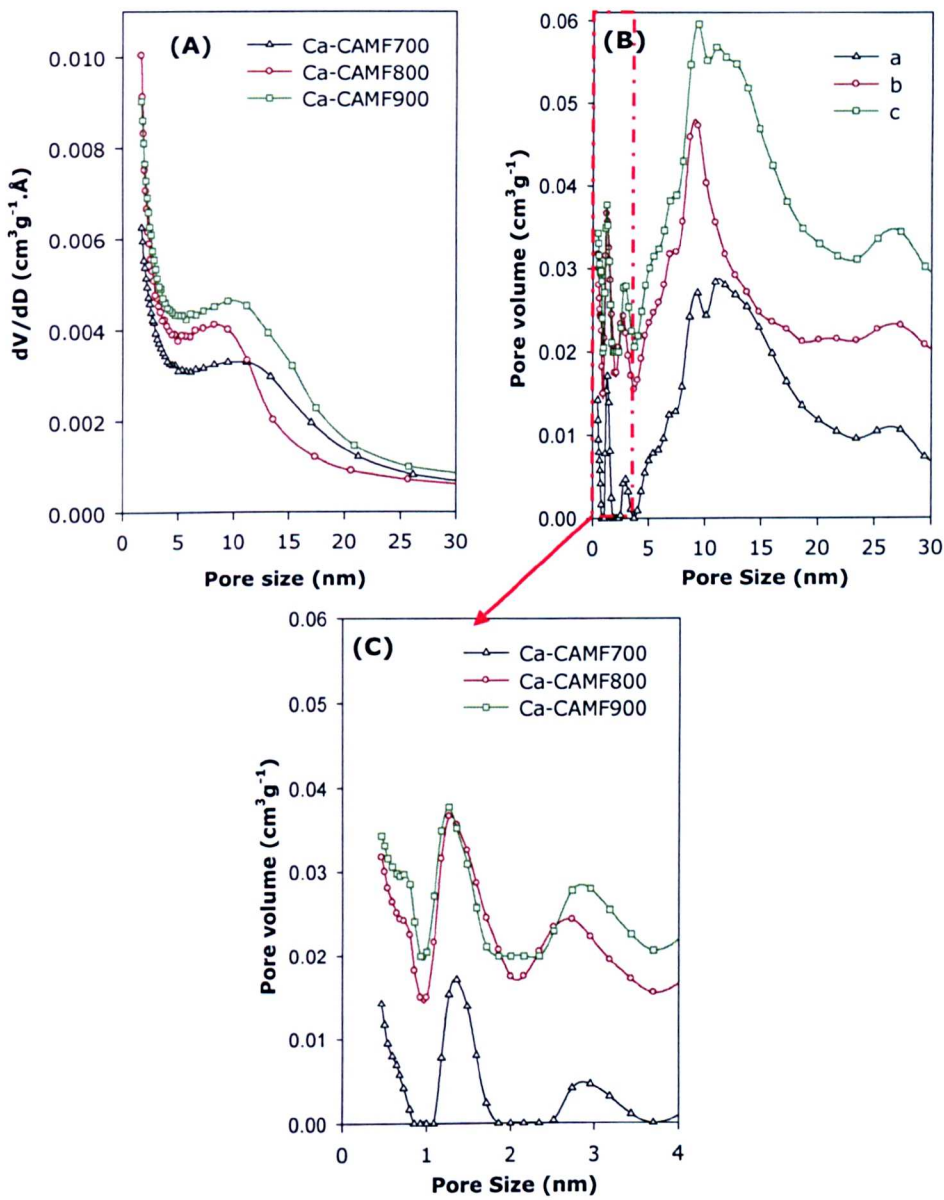


Figure 7.2 PSD curves obtained using (A) BJH or (B) NLDFT analysis for CaCl_2 -templated Ca-CAMFx carbon aerogels (where x is pyrolysis temperature; 700, 800, or 900 °C); a, b and c in (b) refers to Ca-CAMF700, Ca-CAMF800 and Ca-CAMF900, respectively.

7.2.2 Thermogravimetric analysis

The thermal stability and combustion properties of carbon aerogels were evaluated using Thermogravimetric analysis (TGA) in static air. The TGA curves and corresponding differential thermogravimetric analysis (DTG) profiles are shown in Figure 7.3. All the samples are stable at temperatures under 450 °C. Initial weight loss observed below 120 °C may arise from the evaporation of adsorbed water. A significant weight loss step occurs in the temperature range 480 to 600 °C which may be attributed to oxidation of carbon. Weight loss in this temperature range was previously reported by Devallencourt *et al.* which was attributed to melamine-formaldehyde condensate undergoing degradation with quantitative formation of volatile products e.g. HCN, CO and CO₂.⁴⁷ Furthermore, Ca-CAMF700 and Ca-CAMF800 exhibit weight loss above 600 °C. It is observed that Ca-CAMF900 does not exhibit any weight loss above 600 °C. This is consistent with the XRD patterns in Figure 7.1A which showed sharp peaks due to inorganic impurities for Ca-CAMF700 and Ca-CAMF800, which were much reduced in the pattern of Ca-CAMF900. This suggests that the weight loss above 600 °C for Ca-CAMF700 and Ca-CAMF800 is largely due to the removal of inorganic residues. Indeed, the carbon aerogels show residue mass of 15%, 8% and 6% for samples pyrolysed at 700, 800 and 900 °C, respectively. The decrease in the residual mass with increase in pyrolysis temperature is suggestive of fewer impurities in Ca-CAMF900 which is in agreement with the XRD patterns in Figure 7.1A.

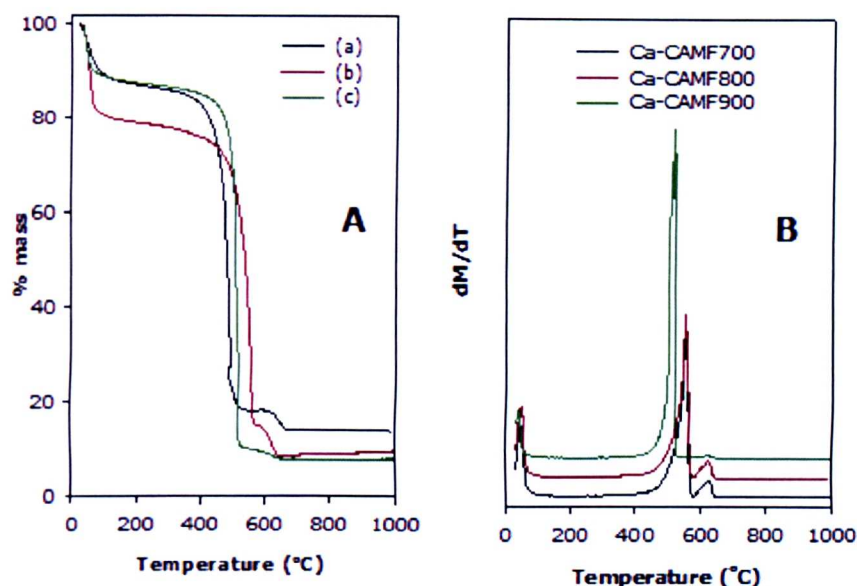


Figure 7.3 Thermogravimetric analysis curves (A) and corresponding derivative thermogravimetric analysis profiles (B) for carbon aerogels; (a) Ca-CAMF700, (b) Ca-CAMF800 and (c) Ca-CAMF900.

7.2.3 Chemical activation of CaCl_2 -templated carbon aerogels

Chemical activation of carbonaceous materials (e.g. coal, biomass-derived carbons etc.) constitutes an established route for the preparation of carbons with high surface area and large pore volume.⁴⁸⁻⁵⁰ Due to the enhanced porosity, the use of one-step chemically activated carbons, in particular using KOH as an activating agent, has been intensively investigated for gas storage. The chemical activation was performed on Ca-CAMF800 based on the well-controlled porosity as discussed in section 3.6.2. The activated samples were prepared with KOH (temperature range of 600 to 800 °C and KOH/carbon ratio of 4).

The powder XRD patterns of activated carbon aerogels and the parent sample (Ca-CAMF800) are shown in Figure 7.4A. The (002) diffraction from

turbostratic carbon at ca. $2\theta = 26^\circ$ which is present in Ca-CAMF800 is hardly observed for the activated carbon aerogels. This is indicative of amorphisation during the chemical activation process. Thus the activated carbon aerogels do not possess any significant graphitic/turbostratic carbon domains. Also, the absence of any peak in the 2θ range between 20 and 60° implies that any graphitic domains present are widely distributed and very small in size. Therefore, the activated samples are essentially amorphous with no evidence of graphitisation based on the XRD patterns.

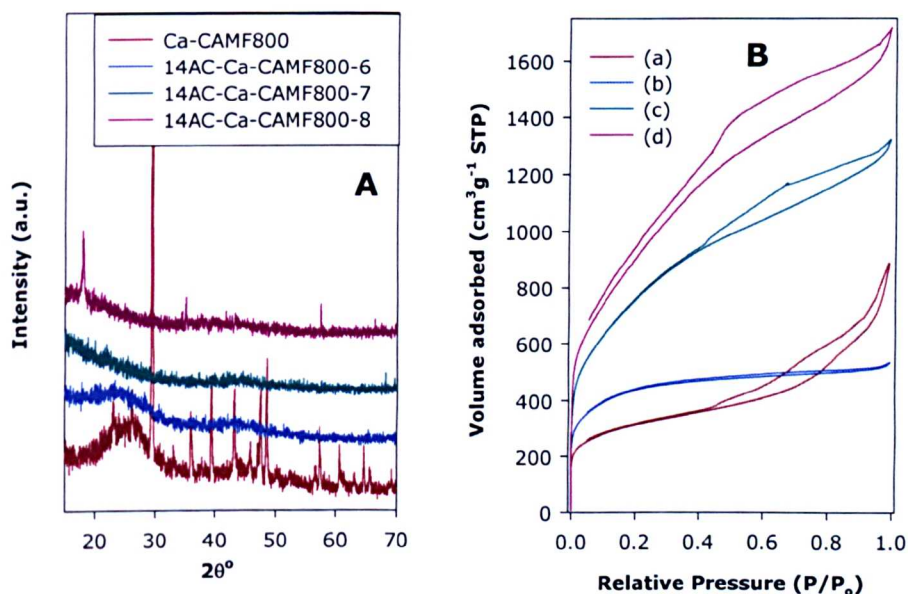


Figure 7.4 Powder XRD patterns (A) and nitrogen sorption isotherms (B) for (a) Ca-CAMF800, and after activation; (b) 14AC-Ca-CAMF800-6, (c) 14AC-Ca-CAMF800-7 and (d) 14AC-Ca-CAMF800-8.

The nitrogen sorption isotherms of carbon aerogels activated at 600, 700 and 800 $^\circ\text{C}$ are shown in Figure 7.4B. For comparison purposes, the isotherm for Ca-CAMF800 is also presented. In all cases, activation leads to an increase in the amount of nitrogen adsorbed, i.e., an increase in porosity. The shape of the isotherms also changes after activation [230]

depending on the activation temperature (i.e., extent of activation). Activation at 600 °C leads to a modest increase in nitrogen adsorption and an apparent loss of large pores. The isotherm of sample 14AC-Ca-CAMF800-6 suggests the presence of significant microporosity. At higher activation temperature, there is an increase in both the microporosity and mesoporosity. The changes are evidence of variations in the porous structure of the resultant activated carbon aerogels. Thus, the isotherm of 14AC-Ca-CAMF800-6 exhibits a fairly sharp adsorption 'knee' in the relative pressure (P/P_0) > 0.2 while for 14AC-Ca-CAMF800-7 and 14AC-Ca-CAMF800-8, the 'knee' is much broader and has a positive gradient. The difference in the isotherms is due to the increase in pore size and broadening of pore size distribution as the adsorption knee broadens. A similar trend was previously reported by Sevilla and co-workers on chemical activation of polypyrrole-based carbons.²⁶ It is noteworthy that the isotherms of the parent and activated carbon aerogels appear to be similar at very low relative pressure ($P/P_0 < 0.01$), which is an indication that all the samples possess some microporosity.

The pore size distribution (PSD) of the activated carbon aerogels, determined via the NLDFT model, is shown in Figure 7.5. Activation at 600 °C removes the 10 nm pores present in the parent carbon but retains 1.2 and 3 nm pores. This means that the resulting activated carbon is much more microporous than the parent sample. A similar trend is observed for activation at 700 and 800 °C except that there is much larger increase in the proportion of pores of size ca. 3 nm. Overall, therefore the activation shifts the porosity of the carbon aerogel towards smaller pores. The porosity of the activated aerogels may therefore be categorised into three well-ordered pore systems, namely: (i) ultramicropores (ca. 0.6 nm), (ii)

supermicropores (ca. 1.2 nm) and (iii) mesopores whose size and proportion gradually increases with rise in activation temperature. Thus micropores are present in both the parent and activated samples, which show that the activation process did not entirely alter porosity.

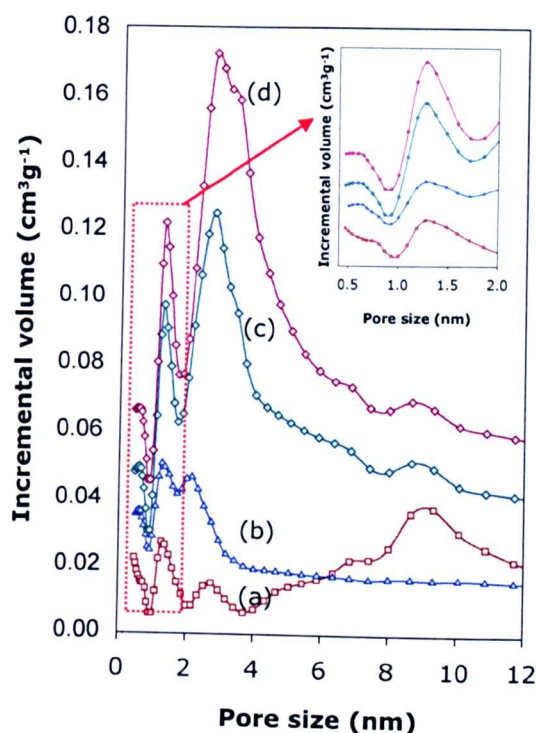


Figure 7.5 Pore size distribution (PSD) curves for (a) parent carbon aerogel (Ca-CAMF800), and after activation (b) 14AC-Ca-CAMF800-6, (c) 14AC-Ca-CAMF800-7 and (d) 14AC-Ca-CAMF800-8.

The textural parameters (i.e., surface area and pore volume) summarised in Table 7.1 indicate that the activated carbon aerogels have high surface area up to 3343 m²/g representing an increase of ca. 207% over the parent aerogel. The surface area of the activated aerogels clearly increases with activation temperature. The pore volume reduces for the sample activated at 600 °C, which is consistent with the shift to microporosity discussed above, and then increases for samples activated at 700 and 800

°C to reach the extraordinarily large value of 2.65 cm³/g for 14AC-Ca-CAMF800-8. The differences in pore size distribution discussed above are reflected in the proportion of the micropore surface area and volume; the sample activated at 600 °C is highly microporous with ca. 85% (i.e. 1272 m²/g) of the total surface area (i.e. 1504 m²/g) arising from micropores. The proportion of micropore surface area decreases to 45% and 24% for 14AC-Ca-CAMF800-7 and 14AC-Ca-CAMF800-8, respectively. Likewise the proportion of micropore pore volume decreases with increase in activation temperature from 72% for 14AC-Ca-CAMF800-6 to 14% for 14AC-Ca-CAMF800-8. The changes in textural properties are consistent with the creation of mesopores of size ca. 3 nm and whose proportion increases at higher activation temperature. The greater mesoporosity is most likely caused by increased gasification of carbon aerogels by evolution of CO₂ from the decomposition of K₂CO₃ that takes place at temperatures of 700 °C and above.^{51, 52}

7.2.4 Effect of organic precursor on porosity on activated carbon aerogels

A set of activated carbon aerogels prepared from a melamine-formaldehyde (MF) carbon aerogel (designated as CAMF) in absence of metal salt as a porogen and carbonised at 1050 °C were also evaluated in this study. In order to investigate the effect of organic precursor, a resorcinol-formaldehyde (RF) carbon aerogel pyrolysed at the same temperature (1050 °C) and designated as CACR was prepared and activated. Both sets of samples, i.e., MF and RF-derived were similarly activated at various temperatures to generate two sets of samples. We note that our group recently showed that chemical activation of pyrolysed RF-derived carbon aerogels increased their surface area by a factor of

390% and that the resulting activated carbons exhibit high CO₂ uptake capacity of up to 13.2 wt% (3 mmol/g) at 298 K and 1.0 bar.³⁵

Comparison of MF and RF aerogels before pyrolysis revealed a significant colour difference between the two resins. The former is colourless while the latter is dark red in colour. Upon carbonisation, the resultant carbon aerogels derived from MF were shinier in appearance than those from RF. The powder XRD patterns of the carbon aerogels before and after activation are shown in Figure 7.6. The powder XRD patterns of all the carbon aerogels, before and after activation, exhibit two broad peaks centred at $2\theta = 25^\circ$ and 43° assigned to (002) and (101) diffraction from carbon domains with graphitic characteristics. Noteworthy is the presence of sharp peaks that may be attributed to the presence of impurities. The broad nature of these peaks suggests that the carbon aerogels are amorphous with disorganised turbostratic structure. Furthermore, it is clearly observable in Figure 7.6A, that the patterns of RF-derived carbon aerogels are comparable showing negligible changes after activation. On the contrary, the MF-derived carbon aerogels presented in Figure 7.6B show significant changes upon activation. The (002) peak for the parent CAMF sample has higher intensity compared to the activated samples. Moreover, the (002) peak broadens and decreases in intensity with increase in activation temperature. Therefore, the parent sample (CAMF) contains more graphitic character compared to activated samples. Thus activation leads to amorphisation of the carbon aerogels. The differences in the effect of activation on RF and MF derived carbon aerogels suggest that the latter are more activatable.

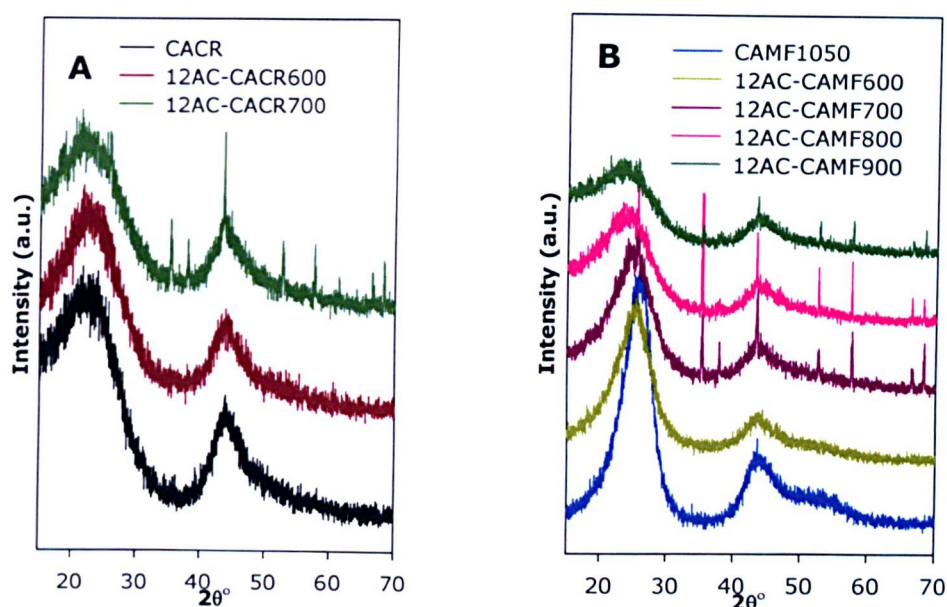


Figure 7.6. Powder XRD patterns of carbon aerogels derived from (A) resorcinol-formaldehyde resin (denoted as CACR) and (B) melamine-formaldehyde resin (denoted as CAMF), before and after activation.

Figure 7.7 shows the nitrogen sorption isotherms of carbon aerogels derived from RF resins (A) and MF resins (B) before and after activation. The sorption isotherms of RF-derived carbons (Figure 7.7A) are Type I exhibiting substantial adsorption at $P/P_0 < 0.01$ indicative of micropore filling. In addition these RF-derived carbons exhibit very high adsorption at relative pressure (P/P_0) 0.9 to 1.0, which arises from interparticle voids. There is a modest increase in nitrogen adsorption after activation due to a similarly modest rise in porosity. There is no clear trend between activation temperature and increase in porosity. The isotherms of mf-derived carbon aerogels show (Figure 7.7B) a clear influence of the activation process and activation temperature. The parent carbon aerogel (CAMF) has very low porosity, which gradually increases with activation temperature. Low temperature activation (600 °C) mainly generates micropores. At higher

activation temperature (700 – 900 °C) there is greater formation of micropores along with some supermicropores/small mesopores at the highest activation temperature (900 °C). The isotherm for 12AC-CAMF600 (activated at 600 °C) exhibits reasonable adsorption below relative pressure (P/P_0) = 0.01 due to capillary filling of micropores. On the other hand, the isotherms for samples activated at higher temperature (12AC-CAMF900) show a fairly sharp 'knee' in the 0.1 to 0.4 relative pressure (P/P_0) range, indicating the presence mainly of micropores and a small proportion of mesopores.

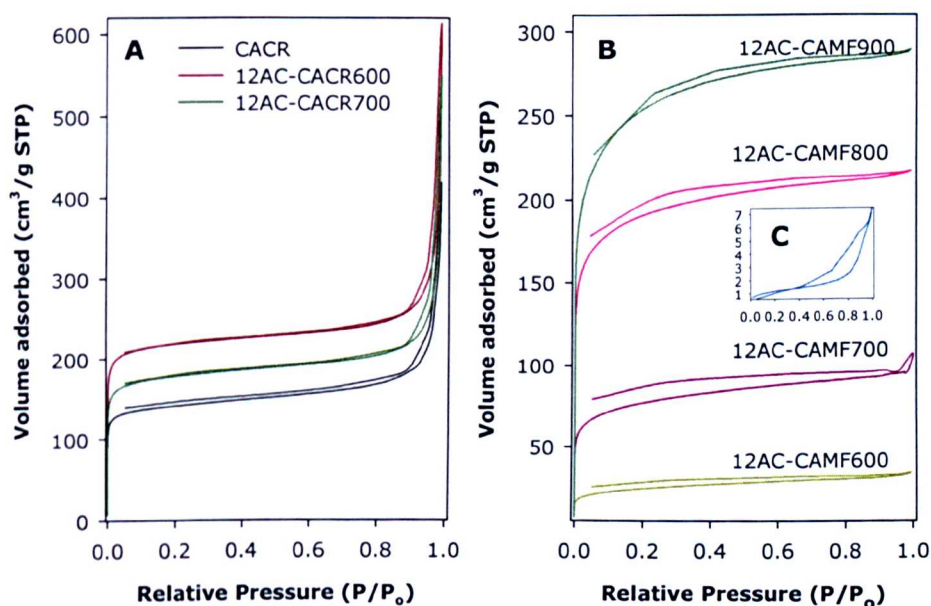


Figure 7.7. Nitrogen sorption isotherms of carbon aerogels derived from resorcinol-formaldehyde resins (A) and melamine-formaldehyde resins (B) before and after activation. (C) shows the sorption isotherm of CAMF.

The pore size changes are confirmed by PSD curves obtained using NLDFT, which are presented in Figure 7.8 and the pore size summarised in Table 7.2. The PSD of carbon aerogels derived from RF resins, which have pores of size 0.6 and 1.2 nm, remain largely unchanged after activation; the

main variation is the large increase in proportion of 0.6 nm pores for the sample activated at 600 °c. The RF generated carbons thus exhibit PSD maxima at 0.6 and 1.2 nm which correspond to ultramicropores and supermicropores, respectively. On the other hand, MF generated carbons show gradual increase in porosity at higher activation temperature. The parent carbon (CAMF) has very low porosity (Figure 7.7C). On activation at 600 °C, 1.1 nm pores are generated. At higher activation temperature, 0.6 nm pores are also generated along with a much higher proportion of pores in the range 1.2 – 2.0 nm and small mesopores up to 4.0 nm in size. Thus the 'average' pore size of the activated aerogels increases at higher activation temperature.

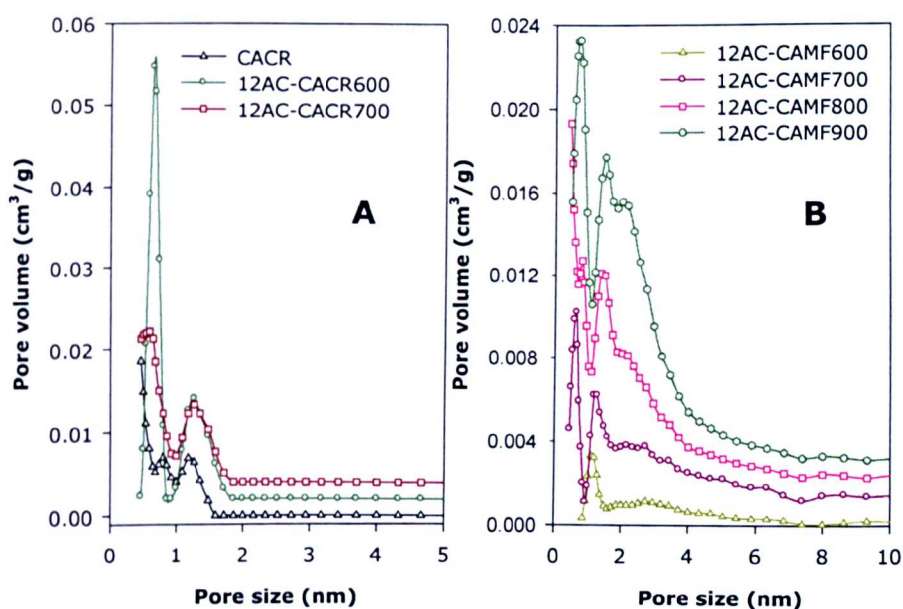


Figure 7.8 PSD curves of carbon aerogels derived from resorcinol-formaldehyde resins (A) and melamine-formaldehyde resins (B) before and after activation at variable temperature.

The textural parameters summarised in Table 7.2 indicate that activated carbon aerogels possess higher surface area and pore volume than the

parent carbons. The surface area and pore volume of RF derived carbons do not show significant variation; the parent sample, CACR, exhibits a surface area of 465 m²/g, which on activation, increases to 718 m²/g for carbon activated at 600 °C and then decreases to 589 m²/g for the sample activated at 700 °C. The proportion of surface area associated with micropores remains fairly constant at 82% for the parent carbon, 89% for sample activated at 600 °C, and 86% for the 700 °C sample. The proportion of micropore volume varies from 28% for the parent sample (CACR) to 33% for 12AC-CACR600. In contrast, surface area and pore volume of MF derived carbon aerogels are substantially affected by a change in activation temperature. The parent carbon aerogel (CAMF) exhibits negligible porosity with a surface area and pore volume of 4 m²/g and 0.01 cm³/g, respectively. However, upon activation the surface area increases with increase in activation temperature. First, the surface area increases from 4 m²/g to 84 m²/g for 12AC-CAMF600 and then gradually to 860 m²/g for 12AC-CAMF900. The proportion of micropore surface area and pore volume is high for all the samples, and actually increases for carbons activated at high temperature. Thus 12AC-CAMF700 has 78% of surface area and 63% of pore volume arising from micropores, while for 12AC-CAMF900 the corresponding values are 86% and 78%, respectively.

Table 7.2 Textural properties and CO₂ uptake at 298 K and 1 bar of carbon aerogels before and after activation.

Sample	Surface area (m ² g ⁻¹) ^a	Pore volume (cm ³ g ⁻¹) ^b	Pore size (nm) ^c	CO ₂ Uptake	
				(wt %) ^d	(mmol/g) ^e
CACR	465 (383)	0.64 (0.18)	0.6/1.2	9.81	2.22
12AC-CACR600	718 (641)	0.95 (0.31)	0.6/1.2	10.52	2.40
12AC-CACR700	589 (508)	0.85 (0.24)	0.6/1.2	9.83	2.24
12AC-CAMF600	84 (59)	0.05 (0.03)	1.1	4.58	1.04
12AC-CAMF700	260 (203)	0.16 (0.10)	0.6/1.2	6.43	1.46
12AC-CAMF800	637 (550)	0.33 (0.26)	0.8/1.5	8.66	1.96
12AC-CAMF900	860 (736)	0.45 (0.35)	0.8/2.2	9.15	2.06

The values in the parenthesis refer to: ^a micropore surface area, ^b micropore volume, ^c maxima of PSD curves obtained via NLDFT analysis. ^d and ^e are CO₂ uptake data expressed in wt% and mmol/g, respectively. at 298 K and 1 bar.

Some of the present carbon aerogels are derived from organic gels that are prepared by sol-gel polycondensation of resorcinol with formaldehyde as initially proposed by Pekala.⁵³ In recent years, and as demonstrated in the preceding sections in this chapter, the main focus has been on the use of new precursors and new solvents with a view to enhancing controllable properties and thus target particular applications. Carbon aerogels retain popularity mainly due to their low cost and unique tuneable properties. In this chapter, the carbon aerogels exhibit a wide range of properties with well controlled porosity before and after activation. Therefore, based on their porosity, the potential of the present carbon aerogels in the capture of various gases was explored.

7.3 Measurement of Carbon dioxide uptake capacity

Apart from textural properties (that have been discussed in detail in section 7.2), the presence of nitrogen as dopant in carbon has been known to play a vital role in the capture of acidic gases like CO₂.⁵⁴ For example, Lu and co-workers prepared nitrogen containing carbon monolith by direct pyrolysis of the copolymer of resorcinol, formaldehyde and lysine which showed a CO₂ uptake capacity of 3.13 mmol/g at 298 K and 1.0 bar.⁵⁵ In this study, MF derived carbon aerogels are expected to contain variable amounts of nitrogen given that they are prepared from a nitrogen rich precursor (melamine). The development of an efficient and simple high performance porous solid for CO₂ capture is a great challenge.

Assessment of CO₂ adsorption was carried out using a thermogravimetric analyser (TA Q600) as detailed in section 3.7.2. Figure 7.9 displays representative CO₂ adsorption capacities as a function of time for CaCl₂-templated carbon aerogels and their activated analogues. The maximum CO₂ capacity achieved at 298 K and ca. 1.0 bar is summarised in Table 7.1.

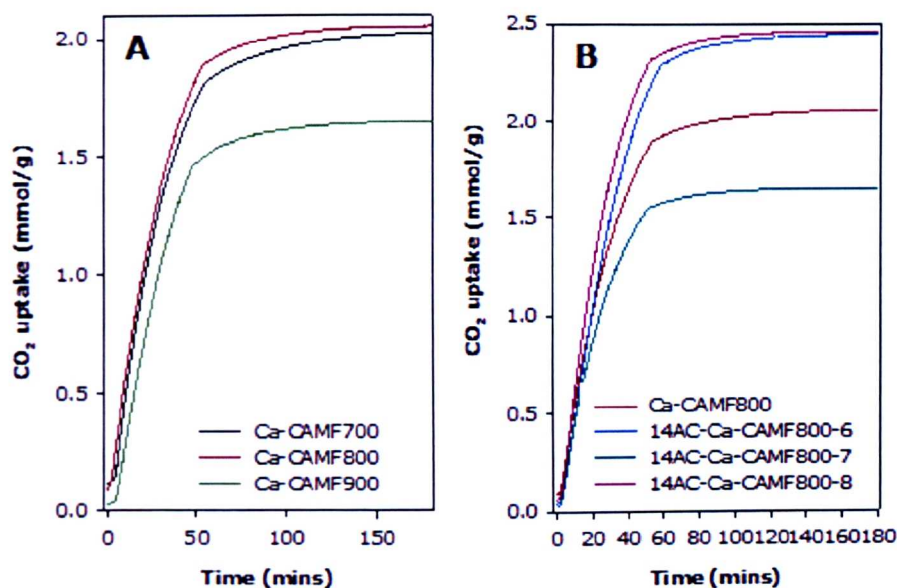


Figure 7.9 CO₂ adsorption at 298 K and 1 bar on CaCl₂-templated carbon aerogel (Ca-CAMF800) derived from mf resins; (A) before and (B) after activation. For comparison purposes the uptake of Ca-cAMF800 is included in (C).

Figure 7.9 demonstrates rapid CO₂ uptake for the first few minutes followed by a gradual increase to equilibrium after ca. 60 min. For CaCl₂-templated (Ca-CAMFx) carbon aerogels, the CO₂ uptake at 298 K and 1 bar varies between 1.66 and 2.06 mmol/g (Table 7.1) with pyrolysis at 700 and 800 °C generating better CO₂ absorbers. For carbon aerogels prepared without any porogen, CAMF (from MF resin) had virtually no porosity while CACR (from RF resin) had a surprisingly high CO₂ uptake of 2.22 mmol/g. The high CO₂ uptake of CACR is attributed to the presence of only small pores of size 0.6 and 1.2 nm (Figure 7.8A). In general, the CO₂ uptake for activated carbons is higher than that of the parent sample, and varies between 1.04 and 2.59 mmol/g. It is significant, that all the samples exhibit higher CO₂ adsorption capacity than the required (1.00 mmol/g) at ambient conditions.⁵⁶ Activation of the CaCl₂-templated aerogel, Ca-

CAMF800, at 600 and 800 °C improves the CO₂ uptake capacity from 2.06 mmol/g to 2.44 and 2.59 mmol/g, respectively. It is clear that for this series of samples, the increase in CO₂ uptake is proportionately much lower than the rise in surface area. This is because most of the porosity generated during activation is in the mesopore range and thus not efficient for CO₂ uptake. Thus, overall the trends for CO₂ uptake do not show a clear relationship with the textural properties (surface area and pore volume). For example, the CaCl₂-templated sample which was activated at 800 °C had highest surface area of 3343 m²/g and large pore volume of 2.65 cm³/g but does not show a proportionately high CO₂ uptake. Clearly, this is due to the fact that this sample is highly mesoporous with very low microporosity (Table 7.1). A number of studies have shown that only pores less than five times that of the molecular size of the adsorbate (ca. 1.5 nm for CO₂) are effective for gas adsorption at atmospheric pressure.^{57, 58} Activation of CACR and CAMF aerogels mainly generates an increase in microporosity, which is reflected in the fact that the CO₂ uptake generally increases for the activated carbons despite the modest rises in total surface area and pore volume (Table 7.2).

The effect of type of organic precursor on CO₂ uptake capacities is shown in Figure 7.10. RF derived carbons show insignificant variations in textural properties, so do the CO₂ uptake capacities as summarised in Table 7.2. However, it is noteworthy that the RF derived samples have high CO₂ uptake, which is attributed to their high levels of microporosity and presence of 0.6 and 1.2 nm pores. In particular the sample activated at 600 °C (12AC-CACR600), and which shows a preponderance of 0.6 nm pores (Figure 7.8) also shows enhanced CO₂ uptake. This is in agreement with what has been demonstrated by Seaton and co-workers that only

micropores less than 1.5 nm are effective towards CO₂ capture at atmospheric pressure.⁵⁹ It is also evident that the surface area plays a lesser role in CO₂ capture; for example, sample 12AC-CACR600 (2.40 mmol/g) exhibit only 8.0% greater CO₂ uptake than CACR (2.22 mmol/g) despite having surface area that is 54% higher.

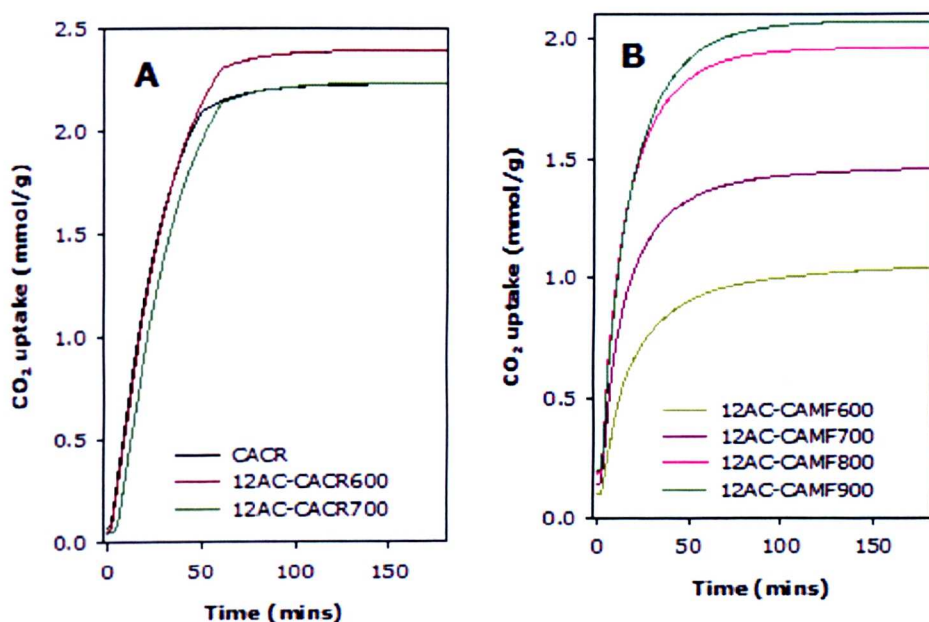


Figure 7.10 CO₂ uptake by carbon aerogels determined at 298 K and 1 bar.

Some effect of both surface area and pore size is evident from the carbon dioxide uptake data in Figure 7.10B and Table 7.2. The sample with the lowest surface area (12AC-CAMF600) shows low CO₂ adsorption of ca. 1.04 mmol/g. The surface area dependence on CO₂ uptake for the aerogels activated at 700, 800 and 900 °C is relatively weak with adsorption of 1.46, 1.96 and 2.06 mmol/g, respectively. Worth noting is the lower CO₂ uptake by CAMF-X samples as compared to CACR series which may be attributed to presence of lower pore volume exhibited by the former. This

confirms that pores of size below 1.5 nm are necessary for enhanced CO₂ uptake capacity.

7.4 Summary

The sol-gel method of synthesis of carbon aerogels and subsequent chemical activation has been successfully used to generate a range of highly porous carbon aerogels exhibiting high surface area and pore volume of up to 3343 m²/g and 2.65 cm³/g respectively. The carbon aerogels derived from a melamine-formaldehyde resin (MF) with a metal salt (CaCl₂) as porogen showed the highest surface area compared to those generated without a metal salt. All prepared carbon aerogels showed some level of microporosity which is shown to be critical in enhancing CO₂ uptake capacity. Thus, the materials prepared in this study achieved CO₂ uptake capacities of up to 2.59 mmol/g at 298 K and 1 bar.

The diverse range of textural properties which includes high surface area and controllable pore size is useful in a number of applications such as electro-chemical applications and gas sorption. The preparation of aerogels is shown to depend upon the synthesis conditions (with or without a metal salt as a porogen), pyrolysis temperature and chemical activating parameters.

7.5 Bibliography

1. J. A. Turner, *Science*, 1999, **285**, 687-689.
2. C.-J. Winter, *Int. J. Hydrogen Energy*, 2009, **34**, 1-52.
3. G. W. Crabtree, M. S. Dresselhaus and M. V. Buchanan, *Phys. Today*, 2004, **57**, 39-44.
4. D. M. D'Alessandro, B. Smit and J. R. Long, *Angew. Chem. Int. Ed.*, 2010, **49**, 6058-6082.
5. Q. Wang, J. Luo, Z. Zhong and A. Borgna, *Energy Environ. Sci.*, 2011, **4**, 42-55.
6. M. I. Hoffert, K. Caldeira, G. Benford, D. R. Criswell, C. Green, H. Herzog, A. K. Jain, H. S. Kheshgi, K. S. Lackner, J. S. Lewis, H. D. Lightfoot, W. Manheimer, J. C. Mankins, M. E. Mauel, L. J. Perkins, M. E. Schlesinger, T. Volk and T. M. L. Wigley, *Science*, 2002, **298**, 981-987.
7. M. I. Hoffert, K. Caldeira, A. K. Jain, E. F. Haites, L. D. D. Harvey, S. D. Potter, M. E. Schlesinger, S. H. Schneider, R. G. Watts, T. M. L. Wigley and D. J. Wuebbles, *Nature*, 1998, **395**, 881-884.
8. R. Steeneveldt, B. Berger and T. A. Torp, *Chem. Eng. Res. Des.*, 2006, **84**, 739-763.
9. G. T. Rochelle, *Science*, 2009, **325**, 1652-1654.
10. J. A. Wurzbacher, C. Gebald and A. Steinfeld, *Energy Environ. Sci.*, 2011, **4**, 3584-3592.
11. Y. Xia, Z. Yang and R. Mokaya, *Nanoscale*, 2010, **2**, 639-659.
12. J. D. Figueroa, T. Fout, S. Plasynski, H. McIlvried and R. D. Srivastava, *Int. J. Greenhouse Gas Control*, 2008, **2**, 9-20.
13. R. S. Franchi, P. J. E. Harlick and A. Sayari, *Ind. Eng. Chem. Res.*, 2005, **44**, 8007-8013.
14. J. C. Hicks, J. H. Drese, D. J. Fauth, M. L. Gray, G. Qi and C. W. Jones, *J. Am. Chem. Soc.*, 2008, **130**, 2902-2903.

15. V. Zelenak, D. Halamova, L. Gaberova, E. Bloch and P. Llewellyn, *Microporous Mesoporous Mater.*, 2008, **116**, 358-364.
16. P. J. E. Harlick and F. H. Tezel, *Microporous Mesoporous Mater.*, 2004, **76**, 71-79.
17. W. Jia and S. Murad, *J. Chem. Phys.*, 2005, **122**, 234708-234711.
18. X. Xu, X. Zhao, L. Sun and X. Liu, *J. Nat. Gas Chem.*, 2008, **17**, 391-396.
19. R. Banerjee, H. Furukawa, D. Britt, C. Knobler, M. O’Keeffe and O. M. Yaghi, *J. Am. Chem. Soc.*, 2009, **131**, 3875-3877.
20. A. R. Millward and O. M. Yaghi, *J. Am. Chem. Soc.*, 2005, **127**, 17998-17999.
21. A. Demessence, D. M. D’Alessandro, M. L. Foo and J. R. Long, *J. Am. Chem. Soc.*, 2009, **131**, 8784-8786.
22. Y. Xia, R. Mokaya, G. S. Walker and Y. Zhu, *Adv. Energy Mater.*, 2011, **1**, 678-683.
23. S. Himeno, T. Komatsu and S. Fujita, *J. Chem. Eng. Data*, 2005, **50**, 369-376.
24. V. Jiménez, A. Ramírez-Lucas, J. A. Díaz, P. Sánchez and A. Romero, *Environ. Sci. Technol.*, 2012, **46**, 7407-7414.
25. H. Marsh and F. Rodríguez-Reinoso, in *Activated Carbon*, Elsevier Science Ltd, Oxford, 2006, pp. 383-453.
26. M. Sevilla, R. Mokaya and A. B. Fuertes, *Energy Environ. Sci.*, 2011, **4**, 2930-2936.
27. M. M. Maroto-Valer, Z. Tang and Y. Zhang, *Fuel Process. Technol.*, 2005, **86**, 1487-1502.
28. M. Plaza, C. Pevida, B. Arias, J. Feroso, A. Arenillas, F. Rubiera and J. Pis, *J. Therm. Anal. Calorim.*, 2008, **92**, 601-606.

29. M. G. Plaza, C. Pevida, A. Arenillas, F. Rubiera and J. J. Pis, *Fuel*, 2007, **86**, 2204-2212.
30. R. Vaidhyanathan, S. S. Iremonger, G. K. H. Shimizu, P. G. Boyd, S. Alavi and T. K. Woo, *Science*, 2010, **330**, 650-653.
31. C. Chen, S.-T. Yang, W.-S. Ahn and R. Ryoo, *Chem. Commun.*, 2009, 3627-3629.
32. Y. Tang and K. Landskron, *J. Phys. Chem. C*, 2010, **114**, 2494-2498.
33. C. Pevida, M. G. Plaza, B. Arias, J. Fermoso, F. Rubiera and J. J. Pis, *Appl. Surf. Sci.*, 2008, **254**, 7165-7172.
34. C. Pevida, T. C. Drage and C. E. Snape, *Carbon*, 2008, **46**, 1464-1474.
35. C. Robertson, MSc Project, The University of Nottingham, 2011.
36. N. Yoshizawa, H. Hatori, Y. Soneda, Y. Hanzawa, K. Kaneko and M. S. Dresselhaus, *J. Non-Cryst. Solids*, 2003, **330**, 99-105.
37. C. Moreno-Castilla, F. J. Maldonado-Hódar and A. F. Pérez-Cadenas, *Langmuir*, 2003, **19**, 5650-5655.
38. T. F. Baumann, M. A. Worsley, T. Y.-J. Han and J. H. Satcher Jr, *J. Non-Cryst. Solids*, 2008, **354**, 3513-3515.
39. R. Brandt, R. Petricevic, H. Pröbstle and J. Fricke, *J. Porous Mater.*, 2003, **10**, 171-178.
40. Y. Xia and R. Mokaya, *Adv. Mater.*, 2004, **16**, 1553-1558.
41. Y. Xia and R. Mokaya, *Chem. Mater.*, 2005, **17**, 1553-1560.
42. C. H. Kim, D.-K. Lee and T. J. Pinnavaia, *Langmuir*, 2004, **20**, 5157-5159.

43. K. S. W. Sing, D. H. Everett, R. A. W. Haul, L. Moscou, R. A. Pierotti, J. Rouquerol and T. Siemieniewska, *Pure Appl. Chem.*, 1985, **57**, 603-619.
44. Y. Hanzawa, K. Kaneko, N. Yoshizawa, R. W. Pekala and M. S. Dresselhaus, *Adsorption*, 1998, **4**, 187-195.
45. T. Horikawa, Y. Ono, J. i. Hayashi and K. Muroyama, *Carbon*, 2004, **42**, 2683-2689.
46. C. Guan, K. Wang, C. Yang and X. S. Zhao, *Microporous Mesoporous Mater.*, 2009, **118**, 503-507.
47. C. Devallencourt, J. M. Saiter, A. Fafet and E. Ubrich, *Thermochimica Acta*, 1995, **259**, 143-151.
48. D. Lozano-Castelló, D. Cazorla-Amorós and A. Linares-Solano, *Fuel Process. Technol.*, 2002, **77-78**, 325-330.
49. J. A. Maciá-Agulló, B. C. Moore, D. Cazorla-Amorós and A. Linares-Solano, *Carbon*, 2004, **42**, 1367-1370.
50. M. Wu, Q. Zha, J. Qiu, Y. Guo, H. Shang and A. Yuan, *Carbon*, 2004, **42**, 205-210.
51. H. Teng and L.-Y. Hsu, *Ind. Eng. Chem. Res.*, 1999, **38**, 2947-2953.
52. M. J. Illán-Gómez, A. García-García, C. Salinas-Martínez de Lecea and A. Linares-Solano, *Energy Fuels*, 1996, **10**, 1108-1114.
53. R. W. Pekala, *J. Mater. Sci.*, 1989, **24**, 3221-3227.
54. T. C. Drage, A. Arenillas, K. M. Smith, C. Pevida, S. Piippo and C. E. Snape, *Fuel*, 2007, **86**, 22-31.
55. G.-P. Hao, W.-C. Li, D. Qian and A.-H. Lu, *Adv. Mater.*, 2010, **22**, 853-857.
56. R. A. Khatri, S. S. C. Chuang, Y. Soong and M. Gray, *Energy Fuels*, 2006, **20**, 1514-1520.

57. A. Vishnyakov, P. I. Ravikovitch and A. V. Neimark, *Langmuir*, 1999, **15**, 8736-8742.
58. J. M. Martín-Martínez, R. Torregrosa-Maciá and M. C. Mittelmeijer-Hazeleger, *Fuel*, 1995, **74**, 111-114.
59. M. Heuchel, G. M. Davies, E. Buss and N. A. Seaton, *Langmuir*, 1999, **15**, 8695-8705.

Chapter Eight

8.0 Conclusions and Outlook

Porous inorganic and carbonaceous materials have been systematically investigated in this thesis. In particular, the thesis demonstrates the development of novel porous materials in the nanometre scale with tuneable porosity, and presents new strategies for tailoring functional materials. Five synthesis strategies have been investigated, i.e. hydrothermal synthesis of aluminosilicates, nanocasting techniques wherein hard templates are used, sol-gel synthesis routes to inorganic and carbon materials, supercritical CO₂ mediated incorporation of metal nanoparticles into a porous substrate and chemical activation of carbon.

In chapter 4, a new type of ordered mesoporous aluminosilicates, which exhibit some zeolitisation, were successfully prepared using template molecules and synthesis conditions that are normally used for the preparation of microporous BEA type zeolite (i.e., zeolite beta). The porosity of the aluminosilicates was further modified by applying simple washing/refluxing (in water) steps performed either on the as-synthesised mesophase or calcined material. This allowed the preparation of materials that possess tuneable porosity with surface area of 500 to 850 m²/g, pore volume in the range 0.35 – 1.5 cm³/g and pore size between 2.5 and 14.0 nm. Owing to high hydrothermal stability and strong acid sites exhibited by the aluminosilicates, the materials show great promise for use in heterogeneous catalysis or other related industrial applications.

Chapter 5 reports the preparation of zeolite-like carbons prepared using zeolite Y as a hard template and acetonitrile as carbon precursor via replication nanocasting process in which the carbon was grown within the

zeolite particles via chemical vapour deposition (CVD) at 700 – 900 °C. It was shown that the level of zeolite-like ordering and textural properties were highest for the carbon prepared at CVD temperature of 800 °C, which exhibited surface area of 2200 m²/g and pore volume of 1.25 cm³/g. Overall, the carbons exhibited a moderate level of zeolite-like ordering and a tri-modal pore size distribution with pores in the micropore (pore maxima at 0.6 and 1.2 nm) and small mesopore (2.4 – 2.7 nm) range. Supercritical CO₂-mediated incorporation of Palladium nanoparticles into the zeolite templated carbons (ZTCs) was successfully demonstrated. Pd-doped ZTCs exhibited enhanced hydrogen uptake density, which increased by ca. 50% compared to the parent Pd-free ZTC. The flexible nature of the method employed in this work would allow incorporation of a wide range of different metal precursors to include nanoparticles of Ni, Rh and Cu and as such offers potential for further research. Furthermore, future research efforts could be tailored towards probing the exact quantity of Pd nanoparticles impregnated into the carbon substrates.

In chapter 6, using a two step synthesis route, the preparation of zeolite templated carbons with ultrahigh surface area is demonstrated. The two step process involves a first step of liquid impregnation of furfuryl alcohol (FA) onto the pores of a zeolite 13X template followed by some mild heat treatment to polymerise the FA, and then in step 2 chemical vapour deposition of ethylene gas into the FA-containing zeolite to ensure maximum filling of the zeolite pores with carbon. The resultant carbon materials, after etching of the zeolite framework, exhibit zeolite-like structural ordering and ultrahigh surface area of up to 3332 m²/g and pore volume of 1.66 cm³/g. The carbons were found to be mechanically stable; their porosity remained unchanged on mechanical compaction and

pressures of up to 10 tons. The carbons were observed to have remarkably high hydrogen sorption capacity of up to 7.3 wt% (at 77 K and 20 bar), which is the highest ever reported for any carbon material.

Chapter 7 systematically studied the sol-gel synthesis of aerogels which on subsequent carbonisation under inert environment yielded carbon aerogels. A metal salt (CaCl_2) was successfully used to generate carbon aerogels with very high surface area (up to $1100 \text{ m}^2/\text{g}$). In order to enhance porosity, the carbon aerogels were chemically activated with KOH. Activated carbon aerogels exhibited ultrahigh surface area and large pore volume of up to $3343 \text{ m}^2/\text{g}$ and $2.65 \text{ cm}^3/\text{g}$ respectively, and were found to have excellent CO_2 uptake of up to 2.59 mmol/g under ambient conditions. Future research efforts could be focussed on probing how the nitrogen content varies with experimental conditions. This may provide further insights into differences in structure and porosity of RF-derived and MF-derived materials.